MULTIWAVELENGTH STUDIES OF NOVA SYSTEMS

A Thesis

Submitted for the Degree of

Doctor of Philosophy

by

M. Pavana

to

The Department of Physics

Pondicherry University

Puducherry - 605 014, India

September 2020

Multiwavelength studies of nova systems

M. Pavana

Indian Institute of Astrophysics

Indian Institute of Astrophysics

Bangalore - 560 034, India

Title of the thesis	:	**Multiwavelength studies of nova systems**
Name of the candidate	:	**M. Pavana**
Address	:	Indian Institute of Astrophysics, Block-II, Koramangala Bengaluru - 560034, India
Email	:	pavana@iiap.res.in
Name of the supervisor	:	**Prof. G. C. Anupama**
Address	:	Indian Institute of Astrophysics, Block-II, Koramangala Bengaluru - 560034, India
Email	:	gca@iiap.res.in

Certificate

This is to certify that the thesis titled **Multiwavelength studies of nova systems** submitted to the Pondicherry University is a bonafide work done by M. Pavana, under my supervision and that no part of it has been included previously for the award of any degree, either in this University or any other institution.

Supervisor
Prof. G C Anupama,
Indian Institute of Astrophysics,
Bangalore.

Declaration

I, M. Pavana, declare that this thesis titled, **Multiwavelength studies of nova systems** and the work presented in it are carried out by me at the Indian Institute of Astrophysics, Bangalore, under the supervision of Prof. G. C. Anupama. This work has not been submitted for a degree or any other qualification either in this University or any other institution.

PhD student
M. Pavana,
Indian Institute of Astrophysics,
Bangalore.

Acknowledgements

I express my sincere gratitude to my supervisor Prof. G. C. Anupama for the unwavering support throughout my PhD study, and also the working group members Prof. T. P. Prabhu, Prof. U. S. Kamath, Prof. D. K. Sahu, Dr. Shubham Srivastav, Dr. Ramya M. Anche, Dr. Avinash Singh, Dr. Brajesh Kumar, Dr. Ashish Raj and Anirban Dutta for their valuable inputs during the group meetings. I would like to thank my collaborators for they have made me a part of collective scientific progress. I also thank the doctoral committee members Prof. V. V. Ravi Kanth Kumar and Prof. Aruna Goswami who gave valuable comments in the course of my PhD that helped me improve the quality of my work.

One of the essential things to carry out productive and efficient research is the environment required. I thank Prof. P. Sreekumar, Prof. Jayant Murthy, Prof. Annapurni Subramaniam and Prof. G. C. Anupama for providing such an environment in IIA. I want to thank IIA for all the facilities provided to carry out my research successfully. I would also like to extend my gratitude to the Board of Graduate Studies, academic and administrative staff of IIA. Also, Prof. V. V. Ravi Kanth Kumar (head of the Physics department), academic staff of the Physics department and administration staff of Pondicherry University. The observations carried out towards obtaining the astronomical data for this work would not have been possible without the support staff at different facilities. I would like to thank the staff at VBO, Kavalur such as Anbazhagan (Engineer-in-charge, VBO), Selva Kumar, Venkatesh, Appakutty, Dinakaran, Velu, Ganesan, Sivakumar, Surendharnath, Vimal, Ramesh, and Ramachandran. I would also like to thank the support staff at IIA CREST and IAO campuses such as Kiran, Pramod, Sujith, Lakshmi, Rakesh, Aneswar, Angchuk, Urgyan, Yourgyal, Kunga and also the operators at GMRT and SALT facility. I am very grateful to all the current, and past post-doctoral fellows, PhD students and the Bhaskara staff who were like a family throughout my PhD and have directly or indirectly helped me reach this stage. Also, grateful to have had supportive roommates Sangeetha, Bhoomika, Pruthvi and Sharmila in Bhaskara. I would also like

to extend my gratitude to Tanya, Megha and Anirban Bhowmick for their constant support during the final phase of my PhD journey.

This acknowledgement will be incomplete if I don't thank the people who were responsible for me getting into astronomy in the first place. The first thing that triggered me about knowing astronomy was in school when Sharma Sir taught *The Universe* lesson. He used to give answers to all of my questions very patiently. However, I was always more inclined towards mathematics. Although I leaned towards mathematics and electronics during my intermediate, my lecturers (Ramanujan Sir, Shobha madam, Uma madam, Sudha madam) dragged me towards Physics during the end of my bachelor's. Even though astrophysics was nowhere on my radar, it was a serendipitous intervention by the Universe. I would also like to thank my friends in and outside IIA who were part of this journey. To name a few, Sowmya, Mamatha, Akshitha, Jayanth, Mumtaz, Sunil, Akanksha and Avinash. Thank you for being there for me as an emotional support whenever I needed during this roller coaster journey.

Any of my achievement be it small or big would not have been possible without the support of my parents and brother, who stood by me throughout my life. As a closing point of my acknowledgement, I would like to extend my gratitude towards the most important person in my life, my significant other Hemanth Pruthvi who has been there for me during the lowest points.

"Astrophysics is the study of the way the universe functions, its underlying mysterious facts and events intrigued me to explore the same, and I think there is a little more important to one's understanding of the nature, and knowing one's role in it than just understanding", is what I thought as I began this endeavour. Alas! Was I wrong? It is not a mere window to the universe or a path to the natural truth. It is also a mirror for self-reflection. This has not just been the journey to study and understand astronomical objects, but also a journey to the discovery of self, and such profound experience should occur only less than twice in anyone's lifetime.

To my family, friends and mentors...

List of Publications

Refereed Journal Articles

1. *AstroSat Soft X-ray observations of symbiotic recurrent nova V3890 Sgr during its 2019 outburst*.
   K. P. Singh, V. Girish, **M. Pavana**, Jan-Uwe Ness, G. C. Anupama and M. Orio, 2020, MNRAS, under review.

2. *Spectroscopic and geometrical evolution of the ejecta of the classical nova ASASSN-18fv*.
   M. Pavana, A. Raj, T. Bohlsen, G. C. Anupama, Ranjan Gupta and G. Selvakumar, 2020, MNRAS, 495, 2, pp.2075-2087, doi:10.1093/mnras/staa1219.

3. *Optical spectroscopic and polarization properties of 2011 outburst of the recurrent nova T Pyxidis*.
   M. Pavana, Ramya M. Anche, G. C. Anupama, A. N. Ramaprakash and G. Selvakumar, 2019, A&A, 4(04):1, doi:10.1051/0004-6361/201833728.

4. *Breaking the Habit: The Peculiar 2016 Eruption of the Unique Recurrent Nova M31N 2008-12a*.
   M. Henze et al. [including **M. Pavana**], 2018, ApJ, 857, 1, 68, 29 pp., doi:10.3847/1538-4357/aab6a6.

5. *V2676 Oph: Dust formation in moderATel.,y fast nova*.
   A. Raj, **M. Pavana**, U. S. Kamath, G. C. Anupama and F. M. Walter, 2018, Acta Astronomica, 68, 1, p. 79-88, doi:10.32023/0001-5237/68.1.4.

6. *Kilonova Luminosity Function Constraints based on Zwicky Transient Facility Searches for 13 Neutron Star Mergers*.
   Kalsiwal et al. [including **M. Pavana**], arXiv:2006.11306, 2020, ApJ, under review.

7. *GROWTH on GW190425: Searching thousands of square degrees to identify an optical or infrared counterpart to a binary neutron star merger with the Zwicky Transient Facility and Palomar Gattini IR*. M. Coughlin et al. [including **M. Pavana**]. 2019, ApJL, 885, 1, article id. L19, 13 pp., doi:10.3847/2041-8213/ab4ad8.

8. *Multi-messenger Observations of a Binary Neutron Star Merger*. B. P. Abbott et al. [including **M. Pavana**], 2017, ApJL, 848, 2, article id. L12, 59 pp., 2017, doi:10.3847/2041-8213/aa91c9.

Refereed Conference Proceedings

1. *Geometry of nova ejecta*.
   M. Pavana, G. C. Anupama, Ramya M. Anche, U. S. Kamath, and G. Selva Kumar, 2019, International Astronomical Union Symposium 357 proceedings.

2. *Probing the Interplay between AGN Outflows and their Host Galaxies: - Optical Integral Field Unit and Radio Imaging*.
   P. Shastri et al. [including **M. Pavana**], 2015, IAU General Assembly, Meeting #29, id.2257811.

Telegrams and circulars

1. *Optical spectroscopy of the classical nova PNV J17580848-3005376*.
   M. Pavana, Pramod Kumar S, and G. C. Anupama, 2020, ATel., 13877.

2. *Optical spectroscopy of the Galactic nova AT 2019tpb/ASASSN-19aad*.
   M. Pavana, G. C. Anupama, and Pramod Kumar S., 2019, ATel., 13245.

3. *A long look at V3890 Sgr during its SSS phase with the AstroSat SXT*.
   K. P. Singh, V. Girish, G. C. Anupama and **M. Pavana**, 2019, ATel., 13145.

4. *AstroSat SXT observations of V3890Sgr*.
   K. P. Singh, V. Girish, G. C. Anupama and **M. Pavana**, 2019, ATel., 13102.

5. *GMRT observations of the recurrent nova V3890 Sagittarii*.
   M. Pavana, N. Roy, G. C. Anupama, K. P. Singh and V. Girish, 2019, ATel., 13092.

6. *Optical spectroscopy of the recurrent nova V3890 Sagittarii*.
   M. Pavana, G. C. Anupama, and Pramod Kumar S., 2019, ATel., 13060.

7. *M31N-2008-12a follow-up with GROWTH-India telescope*.
   S. Srivastav, **M. Pavana**, U. Stanzin, T. Stanzin, G. C. Anupama, and V. Bhalerao, 2018, ATel., 12203.

8. *Recurrent Nova M31N-2008-12a: Optical Spectroscopy of the 2018 Outburst*.
   M. Pavana, B. S. Kiran, D. S. Sujith and G. C. Anupama, 2018, ATel., 12195.

9. *BVRI polarimetry of PNV J16484962-4457032*.
   S. Muneer, G. C. Anupama, V. S. Rao, Sagayanathan. K., A. Raj and **M. Pavana**, 2018, ATel., 11333.

10. *Spectroscopy of nova ASASSN-17hx*.
    M. Pavana, G. C. Anupama, G. Selvakumar and B. S. Kiran, 2017, ATel., 10613.

11. *Optical and near-IR spectroscopy of nova Oph 2017 (TCP J17394608-2457555)*.
    A. Raj, **M. Pavana**, G. C. Anupama, A. Bhowmick, R. Dar and Pramod Kumar S., 2017, ATel., 10420.

12. *Optical spectroscopy of M31N-2008-12a during its recent outburst*.
    M. Pavana and G. C. Anupama. 2016, ATel., 9865.

13. *LIGO/Virgo S190425z - HCT spectroscopy*.
    M. Pavana, G. C. Anupama, B. S. Kiran and V. Bhalerao, 2019, GRB Coordinates Network, Circular Service 24200, #1.

14. *LIGO/Virgo G298048: HCT observations.*.
    M. Pavana, B. S. Kiran, G. C. Anupama, V. Bhalerao on behalf of the GROWTH collaboration report, 2017, GRB Coordinates Network 21554, #1.

List of Presentations

- *Geometry of nova ejecta*.

  M. Pavana, G. C. Anupama, Ramya M. Anche, U. S. Kamath, and G. Selva Kumar, International Astronomical Union Symposium 357, 2019, Hilo, Hawaii, US. Oral presentation.

- *Modelling the ejecta of Galactic Nova, ASASSN-16ma*.

  M. Pavana and G. C. Anupama, 37^{th} Annual meeting of Astronomical Society of India, 2019, Bengaluru, India. Oral presentation.

- *What triggers Kpc scale Radio Outflows in Seyfert Galaxies*.

  M. Pavana on behalf of the S7 team, Jet Triggering Mechanisms in Black Hole Sources, 2016, TIFR campus, Mumbai, India. Oral presentation.

- *Studying Radio Outflows in the S7 Seyfert Sample*.

  M. Pavana on behalf of the S7 team, Extragalactic Relativistic Jets: Cause and Effect, ICTS-IIA program, ICTS campus, Bengalru, India. Poster presentation.

Abstract

Novae are interacting binary star systems consisting of a Roche-lobe filling secondary on or near the main sequence, losing hydrogen-rich material through the inner-Lagrangian point onto an accretion disc surrounding the white dwarf primary. The mass losing secondary in some recurrent novae is a late giant star. Nova systems serve as valuable astrophysical laboratories in the studies of physics of accretion onto the compact, evolved objects, thermonuclear runaways on semi-degenerate surface which give insight into nuclear reaction networks, and line formation and transfer processes in moving atmospheres.

This work presents study of sixteen novae belonging to different spectral classes. The detailed temporal evolution of seven of these sixteen novae are discussed. The optical data were primarily obtained from the 2 m Himalayan Chandra Telescope (HCT) and 2.3 m Vainu Bappu Telescope (VBT).

Different types of novae can be distinguished using their spectra. The spectral evolution of these systems are studied and are used to derive the evolution of the radiation source and use them in testing the theoretical models of nova outburst. The physical conditions in the ejecta and their evolution are also be derived using the spectral evolution of these systems as they exhibit a varying range of physical conditions like ionization parameters and densities with time. The observations of high resolution spectra of some novae are used to get an insight into the geometry of the nova shell.

Two novae are also studied in UV and X-ray regimes and one of them in radio wavelength regime too. The multiwavelength observations are used to study the physical properties of the nova ejecta following the outburst, while the quiescence data are used to understand the accretion and binary properties of the nova system. The optical spectroscopic evolution of few classical and recurrent novae like 2011 outburst of T Pyx, V339 Del, 2016 eruption of M31N 2008-12a, V5856 Sgr, V612 Sct, V906 Car are presented. Multiwavelength temporal evolution of 2018 outburst of M31N 2008-12a and the 2019 outburst of V3890 Sgr are discussed. The ejecta geometry of several novae such as V477 Sct, V2362 Cyg, V5587 Sgr, V5588 Sgr, T

Pyx, V2676 Oph, V339 Del, V1369 Cen, V2944 Oph, V5856 Sgr, M31N 2008-12a, V3665 Oph, V906 Car, V5857 Sgr and V3890 Sgr are discussed.

The ejected mass of the CNe are estimated to be in the range of 10^{-4} to 10^{-6} $M_{\odot}$ and for RNe in the order of 10^{-6} $M_{\odot}$ except for M31N 2008-12a where the value is in the order of 10^{-8} $M_{\odot}$. Most of the novae have overabundance values of nitrogen, oxygen and helium compared to solar values sensitive to the evolutionary phase of the system. In Fe II class of novae, the abundance of iron is also more than the solar abundance value.

The morphology of the ejecta for three different spectral class of novae Fe II, He/N and hybrid are found to be similar. All the novae in the sample have bipolar structures with cones and with or without equatorial rings. In He/N and one of the hybrid novae in the sample, enhanced bipolar emission is seen. The spatial distribution of elemental lines in all the novae is identical irrespective of the spectral class. The high ionization forbidden lines always arise from the outer regions due to the optical thin ejecta in the outer regions. The helium lines are always from the inner regions of the ejecta. Fe II emission, if present, is from the equatorial rings, and the hydrogen Balmer lines arise from all the components in the ejecta.

Notations and Abbreviations

Å	Angstrom
$'$	arc minute
$''$	arc second
^{o}	degree
E(B-V)	colour excess
T_e	Electron temperature
i	Inclination angle
$M_\odot$	mass of the Sun
mag	magnitude
M_{WD}	Mass of the white dwarf
τ	Optical depth
pc	parsec
R_{WD}	Radius of the white dwarf
λ	wavelength
t_2	time required to decline to 2 mag since maximum
t_3	time required to decline to 3 mag since maximum
t_{on}	turn-on time for supersoft source phase
t_{off}	turn-off time for supersoft source phase
AAVSO	American Association of Variable Star Observers
ASASSN	All Sky Automated Survey for SuperNovae
AGNs	Active Galactic Nuclei
CASA	Common Astronomy Software Application
CCD	Charge Coupled Device
CNe	Classical novae
CSM	Circumstellar Material
CZT	Carl Zeiss Telescope
CVs	Cataclysmic Variables
FWHM	Full width at Half Maximum

GIT	Global Relay of Observatories Watching Transients Happen (GROWTH)-India Telescope
GMRT	Giant Metrewave Radio Telescope
HCT	Himalayan Chandra Telescope
HESP	Hanle Echelle Spectrograph
HFOSC	Himalaya Faint Object Spectrograph Camera
HRS	High Resolution Spectrograph
IAO	Indian Astronomical Observatory
IFOSC	IUCAA Faint Object Spectrometer and Camera
IGO	IUCAA Girawali Observatory
IIA	Indian Institute of Astrophysics
IR	Infrared
IRAF	Image Reduction and Analysis Facility
ISM	Interstellar medium
IUCAA	Inter-University Centre for Astronomy and Astrophysics
JCBT	Jagadish Chandra Bhattacharya Telescope
JD	Julian Date
MMRD	Maximum absolute magnitude relation with decline time
MS	Main-sequence
NIR	Near-Infrared
NLTE	Non-local thermodynamic equilibrium
OMR	Opto Mechanics Research spectrograph
PNe	Planetary Nebulae
RG	Red giant
RNe	Recurrent novae
SALT	South African Large Telescope
SDSS	Sloan Digital Sky Survey
S/N	Signal to noise ratio

SMARTS	Small and Moderate Aperture Research Telescope System
SG	Sub-giant
SNe	Supernovae
SSS	Supersoft Source phase
SXT	Soft X-ray Telescope
TIRSPEC	TIFR Near Infrared Spectrometer and Imager
TNR	Thermonulcear Runaway
uGMRT	upgraded Giant Metrewave Radio Telescope
UAGS	Universal Astro Grating Spectrograph
UV	Ultraviolet
UVOT	Ultraviolet/Optical Telescope
VBT	Vainu Bappu Telescope
VBO	Vainu Bappu Observatory
VLA	Very Large Array
WD	White Dwarf
XRT	X-ray Telescope

Contents

1

Introduction

Cataclysmic Variables (CVs) are interacting binary systems consisting of a white dwarf (WD) primary and a Roche-lobe filling secondary, with the WD accreting hydrogen-rich material from the secondary. Nova systems are CVs that undergo sudden outbursts powered by thermonuclear runaway (TNR) on the surface of the WD. Novae consist of three main components, the primary WD, the secondary (main sequence or red giant) and an accretion disc. The hydrogen-rich material from the secondary accretes onto the primary through an inner Lagrangian point. Due to very high angular momentum, the in-fall of the matter onto a WD surface takes place in the form of spiral around the primary forming the accretion disc. The material accreted from the secondary over a long period forms a layer of nuclear fuel on the WD surface. The surface gravity of the WD compresses the bottom of this layer of nuclear fuel resulting in electron degeneracy. This degeneracy prevents the material from expanding even though there is a rise in temperature from both nuclear fusion and compression. As the temperature at the bottom of this accreted layer reaches $\sim$7 $\times$ 10^7 K Fermi temperature, and the rate of increase in the temperature is so high that it leads to a TNR. This results in the release of a massive amount of energy. This energy is imparted to the accretion disc inducing it to expand and to be ejected from the system. The matter is expelled either in the form of a discrete shell, an optically thick wind or as a combination of both (Anupama & Kamath, 2012). Nova eruptions

are suggested to be inherently recurrent, with the WD and the secondary sustaining each outburst, and accretion reestablishing or continuing shortly afterwards.

Novae act as laboratories for understanding the physics of nuclear burning and accretion. They are also candidate progenitors of Type Ia supernova (della Valle & Livio, 1996; Starrfield et al., 2004). The nova explosions eject metal-enriched gas which is the source of heavy elements for the Interstellar Medium (ISM). Thus, they also contribute to the Galactic chemical evolution (Starrfield et al., 2016). Studying novae envelopes will help in the analysis of emission line spectra of objects like active galactic nuclei (AGN), supernovae (SNe) and planetary nebulae (PNe). Studies on novae provide an opportunity of real-time analyses of these objects whose evolution occurs over longer timescales and provides snapshots at a fixed epoch for each object. Novae are known to emit in all the bands of the electromagnetic spectrum from radio to gamma-ray. Observations of these systems in multiwavelength regime will enable us to understand their characteristics such as different physical parameters (like velocity, temperature, luminosity, etc.), the gas ejection mechanisms, the shocks in the ejecta/wind, presence of various components (thermal/non-thermal), different phases (optical thick/thin), dust formation, and properties of the progenitor.

1.1 Nova systems

Nova outbursts are the consequence of an explosion on the surface of WDs in interacting binary systems. It consists of an accreting primary WD and a secondary companion which fills the Roche-lobe. For a detailed review, refer to King (1989) and references therein.

1.1.1 The primary: White dwarf

After the exhaustion of its nuclear fuel, a Sun-like star results in a WD. The size of the WD is that of the Earth while its mass is close to that of the Sun. As the Sun-like star reaches the end of the nuclear burning stage, outer material in the form of a

planetary nebula is expelled, and the remaining core becomes increasingly reaching temperatures $>$ 100000 K, forming a young WD. Most of the hydrogen eventually burns out into helium and heavier metals, exhausting the nuclear fuel. Once there are no nuclear reactions in the core, it radiates the remaining energy and cools down for the next billion years. Typically, the evolution of low and intermediate-mass stars ($M \lesssim$ 8–10 $M_\odot$) on the main-sequence branch are known to form WDs (Shapiro & Teukolsky, 1986). The electron degenerate pressure keeps the WD from collapsing under its gravity. In electron degenerate cases, the high-density matter similar to WD core is prevented from further contraction leading to having more than one electron with same four quantum numbers violating Pauli exclusion principle, so electrons are forced to occupy higher energy states as all the lower energy states are occupied. Hence, when the mass of the WD is less than the Chandrasekhar mass limit (1.44 $M_\odot$), the gravitational energy is insufficient to cause further collapse or to combine the electrons and protons into neutrons. Thus, the electron-degenerate pressure supports the WD against further gravitational collapse (Shapiro & Teukolsky, 1986; Camenzind, 2007).

The mass of the progenitor plays a role in the chemical composition of the WD. The intermediate massive progenitor star ($\lesssim$ 8 $M_\odot$) results in a CO WD as the nuclear fusion of heavy elements in the core stops at O. A massive progenitor star (8 $M_\odot \lesssim M \lesssim$ 10 $M_\odot$) results in an ONe WD as the fusion continues beyond O to form heavier elements such as Ne (and Mg). This implies that the ONe WDs ($>$1.1–1.3 $M_\odot$) are typically more massive than that of the CO WDs ($\lesssim$ 1.2 $M_\odot$). The lowest mass WDs are the ones with He core of mass $\lesssim$ 0.5 $M_\odot$. WD atmosphere is a thin layer composed of lighter elements like H and He, as the heavy elements move toward the centre. A mass ($M_{\rm WD}$)-radius ($R_{\rm WD}$) relation for the WD was derived by Nauenberg (1972) as

$$R_{\rm WD} = 0.78 \times 10^9 \left(\left(\frac{M_{\rm Ch}}{M_{\rm WD}} \right)^{2/3} - \left(\frac{M_{\rm WD}}{M_{\rm Ch}} \right)^{2/3} \right)^{1/2} [\rm cm] \qquad (1.1)$$

Here, the radius shrinks as the mass increases and it approaches zero at the Chandrasekhar mass limit.

1.1.2 The secondary star

Novae are typically known to have either a main-sequence or red giant (RG) secondary. Strong stellar winds are featured in the systems where the secondary star is a more evolved one such as RG. Such systems are termed as symbiotic systems and they exhibit different mass-transfer mechanisms compared to CVs in general. However, some such system could still advance to nova eruptions. Darnley et al. (2012) suggested a new classification system for novae based on the evolutionary state of the secondary star such as MS-Nova (main sequence secondary star), SG-Nova (sub-giant secondary star) and RG-Nova (red giant secondary star).

In a nova, the secondary is the Roche-lobe filling star hence its properties can be derived from the Roche-lobe properties. Hence, the radius of the secondary (R_2) can be written as

$$\frac{R_2}{a} = \frac{2}{3^{4/3}} \left(\frac{q}{1+q} \right)^{1/3} \tag{1.2}$$

where a is the binary separation and q is the mass ratio of two stars M_2/M_1. The orbital period of the binary system (P) from the Kepler's third law can be given as

$$P^2 = \frac{4\pi^2 a^3}{GM} \tag{1.3}$$

where G is the universal gravitational constant, and $M = M_1 + M_2$. Hence, the density of the secondary can be deduced as

$$\bar{\rho} = \frac{3M_2}{4\pi R_2^3} \cong \frac{3^5\pi}{8GP^2} \cong 110\, P_{\rm hr}\ [\mathrm{g\ cm^{-3}}] \tag{1.4}$$

1.1.3 Mass-transfer mechanism

The mass-transfer mechanism in novae is from the secondary star to the WD via Roche-Lobe OverFlow (RLOF), where the outer layers of the secondary are accreted by the gravitational pull of WD. It is a cloud of gas (Fig. 1.1) surrounding a star

within which the orbiting material is bound gravitationally to the star. The binary system potential arising from the gravitational and centrifugal forces is referred as Roche potential (Φ_R). The equipotential surface is given by

$$\Phi_R(\mathbf{r}) = -\frac{GM_1}{|\mathbf{r}-\mathbf{r}_1|} - \frac{GM_2}{|\mathbf{r}-\mathbf{r}_2|} - \frac{1}{2}(\omega \times \mathbf{r})^2 \tag{1.5}$$

where $\omega = 2\pi/P$ is the angular frequency of the binary and the third term in the equation is the centrifugal force due to the rotation of the binary. The mass ratio q directs the shape of the equipotential. Such region encompassing each star is referred to as Roche-lobe. Once the star fills its Roche-lobe, RLOF occurs through inner Lagrangian point L_1 where there is potential balance from both the stars in the binary system.

As the WD size is small when compared to that of the binary separation a, and the gas influx has an angular momentum that is predominantly in the plane, the matter from the secondary does not reach the surface of primary WD directly. The matter spirals following an orbit around the primary. There is dissipation of energy from the gas stream causing the movement of matter in a circular orbit in the plane of the primary. This continuous flow of matter results in the interaction between the particles in the gas and some energy dissipation in the form of heat followed by radiation from the accreted matter. The energy loss leads to the spiralling of the accreted stream inwards towards the WD losing angular momentum. This eventually forms an *accretion disc* around the WD. The lost angular momentum is transferred to the outer parts of the disc resulting to spread outwards. The luminosity of the disc is

$$L_{\rm disc} = \frac{GM_{\rm WD}\dot{M}}{2R_{\rm WD}} = \frac{1}{2}L_{\rm acc} \tag{1.6}$$

Here, $R_{\rm WD}$, $M_{\rm WD}$, $\dot{M}$ and $L_{\rm acc}$ are the radius of WD, mass of WD, accretion rate and the accretion luminosity respectively. The remaining accretion luminosity is contributed by the boundary layer between the accretion disc and the surface of the

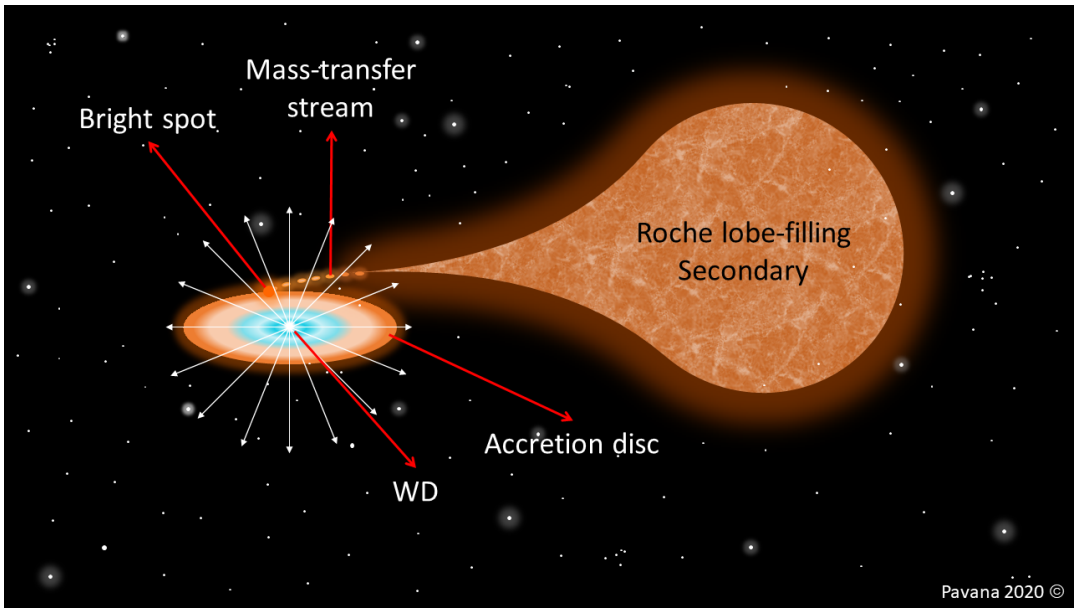

Figure 1.1: Schematic representation of a nova undergoing outburst.

star. The temperature of the disc at a radius r is given by

$$T_{\rm disc} = \left(\frac{3GM_{\rm WD}\dot{M}}{8\pi\sigma R_{\rm WD}^3}\right)^{1/4}\left(\frac{R_{\rm WD}}{r}\right)^{3/4}\left(1-\sqrt{R_{\rm WD}/r}\right)^{1/4} \tag{1.7}$$

Here, σ is the Stefan-Boltzmann constant.

1.2 Nova outburst mechanism

The outburst characteristics of novae depend on several factors such as the mass of the WD, its luminosity, chemical composition of both the accreting and WD core material, mass accretion rate, evolutionary history of the WD and cause, and time of the mixing of accreted layers with WD core (Starrfield et al., 2016). The outburst is a consequence of the accumulation of hydrogen-rich material accreted from secondary on to the surface of the electron degenerate primary WD. This kind of agglomeration over a long period results in the increase of pressure in the inner regions of the disc closer to the WD surface. This leads to the compression of the accreted layers in the bottom and heating of these layers by strong surface gravity of WD. As a

consequence of this mechanism a critical pressure (P_{crit}) is reached, given by

$$P_{\rm crit} = \frac{GM_{\rm WD}M_{\rm ign}}{4\pi R_{\rm WD}^4} \tag{1.8}$$

$$R_{\rm WD} \propto M_{\rm WD}^{-1/3} \tag{1.9}$$

$$M_{\rm ign} \propto \left(\frac{dM}{dt}\right)^{-1} \tag{1.10}$$

where $M_{\rm ign}$ is the ignition mass. The temperature and density increase to the extent of the onset of proton-proton (p–p) chain reaction. The thermal energy due to the nuclear reactions inhibits expansion and the temperature increases, resulting in the increase of the rate of nuclear reactions. This is referred to as TNR (Hellier 2001 and references therein). The H-burning goes through p–p chain reactions when the temperatures reach $\sim 10^6$ K and the reactions are

$$\begin{aligned} {}^1{\rm H}_1 + {}^1{\rm H}_1 &\rightarrow {}^2{\rm H}_1 + e^+ + \nu_e \\ {}^2{\rm H}_1 + {}^1{\rm H}_1 &\rightarrow {}^3{\rm He}_2 + \gamma \\ {}^3{\rm He}_2 + {}^3{\rm He}_2 &\rightarrow {}^4{\rm He}_2 + 2{}^1{\rm H}_1 \end{aligned} \tag{1.11}$$

When the temperature of the accreted matter reaches $\sim 10^7$ K, the CNO (Carbon-Nitrogen-Oxygen) cycle (Fig. 1.2) starts. The temperature further increases, enhancing nuclear reactions. As a consequence of very high energy at the bottom of the accreted layer, convection occurs, resulting in the exposure of unburnt nuclei to the nuclear burning region. Once the temperature reaches $\sim 10^8$ K, the matter is no longer degenerate, it starts expanding and cools down (Hellier 2001; Starrfield et al. 2016 and references therein).

The optical photosphere of the expanding envelope reaches its visual maximum at the peak of TNR, then the maximum bolometric luminosity is also reached in a timescale of hours. This time difference between the maximum bolometric luminosity and visual maximum depends on the expansion rate (Warner, 1995). Bath & Shaviv (1976) suggested that all the novae have Eddington luminosity at maximum

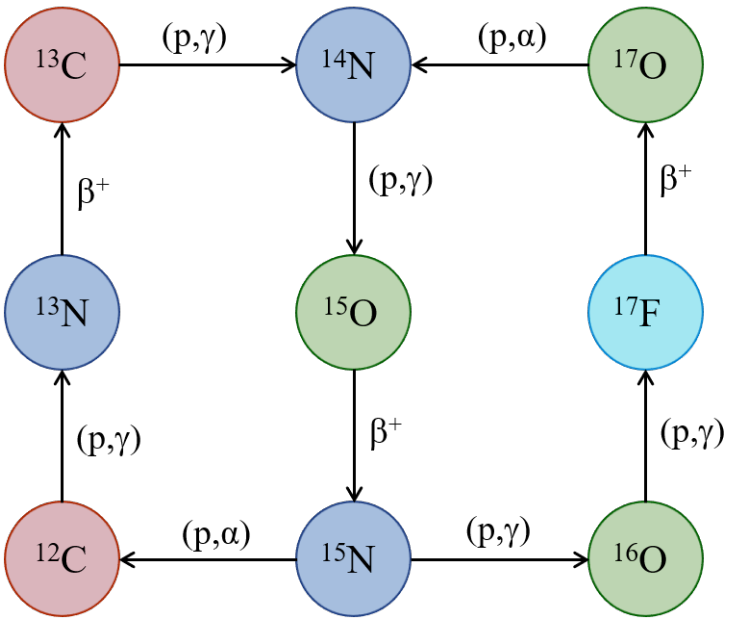

Figure 1.2: Schematic representation of CNO cycle reactions

light similar to a 1–2 $M_\odot$ object. The Eddington luminosity is the maximum luminosity of a star of given mass by balancing the outward radiation pressure and inward gravitational force and is given by

$$L_{\mathrm{Edd}} = \frac{4\pi G c M_{\mathrm{WD}}}{\kappa_T} \tag{1.12}$$

where c is the velocity of light, κ_T is the Thompson opacity for scattering by free electrons. Very fast novae (refer Sec. 1.4) seem to be super-Eddington in nature (Warner, 1995).

The physical expansion of the nova ejecta is divided into well-defined stages as fireball expansion, optically thin gas expansion and dust formation by Gehrz (1988). However, not all novae undergo dust formation. As the system rises to maximum, the expanding envelope appears to move along with the photosphere, and this is referred to as **fireball stage**. The photospheric emission is the one that is observed. The ejecta below this photosphere is an accelerating optically thick gas. The photosphere rapidly expands reaching a visual maximum and disconnects from the top of the ejecta. The radius of the photosphere shrinks into the deeper layers, while the outer layer is the optically thin gas that is expanding continuously post optical maximum

(Hachisu & Kato, 2014). Due to constant H-burning on the surface of primary WD, material is ejected either in the form of optically thick winds, or shells. The hot ejecta that is expanding will engulf both primary and secondary entering into a temporary short common-envelope phase and the binary motion aids in the ejection of matter. At constant bolometric luminosity, the evolution of the outburst becomes slower as the H-burning continues to occur on the surface of the WD for a few years, while nova slowly evolves back to quiescence state.

1.3 Classical and recurrent novae

The novae with one recorded outburst are termed as classical novae (CNe). They exhibit high outburst amplitude that ranges from 6 to 19 magnitude. The outburst amplitude is the magnitude difference between the pre-nova and nova outburst phase. This value is mainly associated with the mass-transfer rate from the secondary star onto the WD surface. The TNR on the WD surface powers the outbursts.

The novae with multiple recorded outbursts are termed as recurrent novae (RNe), unlike classical novae these have recurrence period of 1 to 80 years. These outbursts are also powered by TNR on the surface of the WD. Some of the RNe, in reality, are typical CVs with a main-sequence secondary, however, a majority of them are ones hosting an evolved companion (Darnley et al., 2012). The high frequency of the occurrence of these outbursts is ascribed to the high mass-transfer rate due to the stellar wind from a giant companion and the massive primary WD (Darnley et al., 2012). Due to the massive primary WD ($M \gtrsim 1.3$ $M_{\odot}$), these are known to be potential progenitors of type Ia supernovae.

1.4 Observational properties of novae

The observational properties of novae aid to interpret the physics underlying their outbursts. It also helps to understand the emission from the outburst, the energetics involved and the morphology.

1.4.1 Optical light curve properties

Most of the CNe have typical light curve evolution, as shown in Fig. 1.3 (McLaughlin 1960; Warner 1989 and references therein for detailed review). On the onset of a nova outburst, the magnitude rises by almost 9-10 magnitudes from its quiescent level in a few days. Depending on the speed-class of novae, most of them halt close to the rise for around two days or less. This is referred to as pre-maximum halt. This is followed by a final rise to maximum, and the maximum phase again depends on the speed-class of novae. Then the system undergoes an early decline till 3.5 mag from the peak. The timescale of this phase ranges from a few days to a few months. This phase is followed by a transition phase which is either a slow or smooth decline or other varied behaviour such as a sudden decrease in the brightness due to dust formation which absorbs the optical radiation and emits at infrared (IR) wavelengths; periodic or quasi-periodic oscillations for few days of amplitude up to 1.5 mag; plateau of constant 3–6 mag for few months followed by sharp decline (Warner, 2008; Strope et al., 2010); jittering above the base level of the light curve usually prominent from the start of the decline, unlike the oscillations. This phase is then followed by a final decline that is usually very slow, on timescales of years and goes back to the pre-nova magnitude.

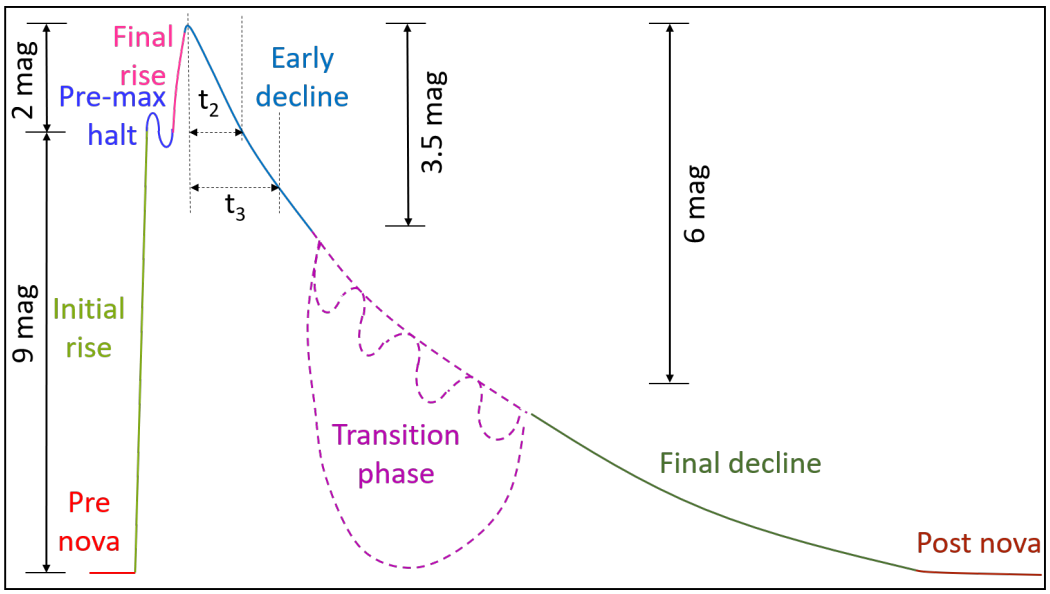

Figure 1.3: Light curve evolution of nova showing different stages (Warner, 2008).

Table 1.1: Classification of nova light curves by Payne-Gaposchkin (1964).

Speed class	t_2 **(day)**	$\mathbf{d}V/\mathbf{d}t$ **(mag day^{-1})**
Very fast	$<$10	$>$0.20
Fast	11–25	0.18–0.08
Moderately fast	26–80	0.07–0.025
Slow	81–150	0.024–0.013
Very slow	151–250	0.013–0.008

The light curves of novae are distinguished by parameters like rise time to visual maximum, maximum light, rate of rise, rate of decline, behaviour of the rise and decline. The decline rate is used to classify novae in general. It is based on the values t_2 and t_3 that is duration of days for the system to decrease from peak to 2 and 3 mag respectively. Novae were classified initially into fast and slow by McLaughlin. Later, Cecilia Payne-Gaposchkin classified them into five different speed-classes (Payne-Gaposchkin, 1964) based on the decline time t_2 and decline rate as given in Table 1.1. The classification of nova light curves based on their shape and speed was initially attempted by Duerbeck (1981). However, another classification scheme based on the shape of the light curves during the decline from maximum and transition phase was proposed by Strope et al. (2010). This classification scheme is introduced using 93 well-sampled light curves. Seven classes (Fig. 1.4) are defined as follows: *S* for smooth light curves, *P* for plateaus, *D* for dust dips, *C* for cusp-shaped secondary maximum, *O* for oscillations that are quasi-sinusoidal, *F* for flat-topped light curves and *J* for jitters or flares. A universal decline law was proposed by Hachisu & Kato (2006) based on the theoretical modelling of nova light curves. They suggested that these light curves could be fit by broken power laws with different slopes at early and late phases. It was suggested that the time of break in this power law slope is closely related to that of the mass of WD.

To measure Galactic and extragalactic distances, novae have been used as standard candles for several years based on the Maximum-Magnitude-Rate of Decline (MMRD) relationship. It was first introduced by Zwicky (1936). It was later explored and improved by many astronomers such as Cao et al. (2012); della Valle & Livio (1995); Livio (1992) and references therein. The MMRD relation is given by Fig. 1.5 from Cao et al. (2012).

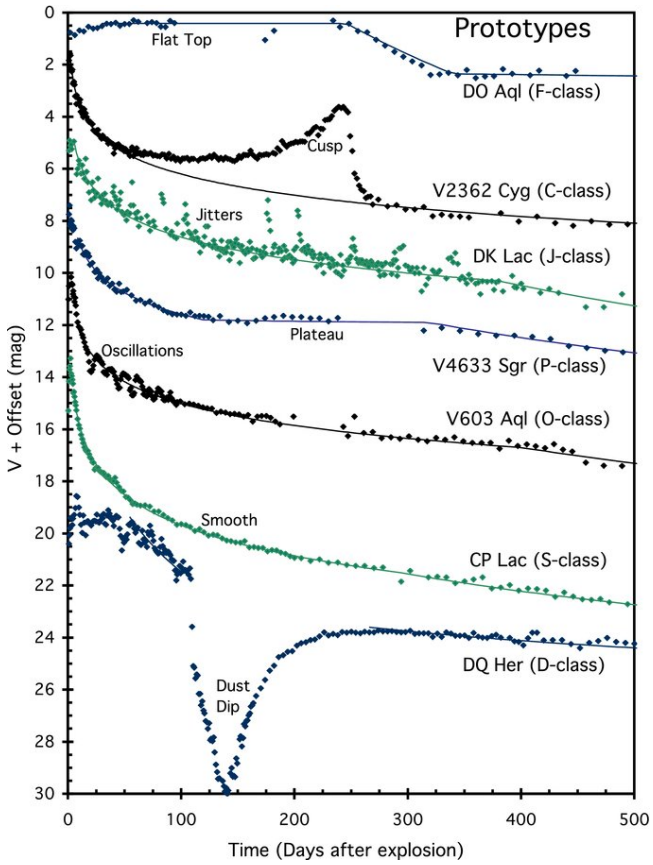

Figure 1.4: Prototypes showing seven distinct nova light curves as classified by Strope et al. (2010). Figure taken from Strope et al. (2010).

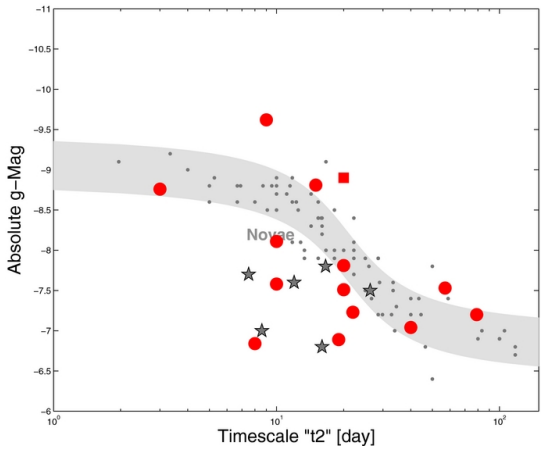

Figure 1.5: Maximum-Magnitude-Rate of Decline (MMRD) empirical relation taken from Cao et al. (2012) where the grey region represents the relation from della Valle & Livio (1995), small dark gray dots refer to nova sample in della Valle & Livio (1995), six grey stars belong to sample to faint fast novae from Kasliwal et al. (2011), red circles are M31 novae from Cao et al. (2012) and the red square refer to a bright recurrent nova M31N 2010-12a.

1.4.2 Optical spectral analysis

Spectral analysis is one of the important methods in astronomy to estimate the chemical composition, temperatures, velocities, densities, etc., of astronomical objects. In the case of transient astronomy, it has played a vital role in identifying the different types of transients based on the emission or absorption lines present. In the case of novae, spectral analysis is essential to understand as they show the signature of an expanding material as well as TNR reaction, they are influenced by the expansion of photosphere, wind and surface nuclear reactions. The spectral evolution of novae from pre-maximum phase to the late phase spectra (refer to Anupama & Kamath 2012 and references therein for a detailed review) is described as below:

1. Pre-maximum spectrum: This phase is featured by a strong continuum with broad, blue-shifted absorption lines (P-Cygni profiles) similar to that of early-type stars of B5 to F5 type. It is a characteristic of an expanding optically thick cooling ejecta.

2. Principal spectrum: This phase appears at about 0.6 mag below maximum, characterized by strong absorption lines similar to that of A to F supergiants with enhanced CNO emission compared to the previous phase. The velocities are larger than that of the previous phase. The emission lines appear post maximum and the strongest lines present are H, Ca II, Fe II, N, He and O. By the end of early decline, there is appearance of [O I] and [N II] emission lines.

3. Diffuse enhanced spectrum: This occurs shortly after the visual maximum and the spectrum is quite similar to the principal spectrum. However, with velocities twice as that of the principal spectrum.

4. Orion spectrum: This phase appears at $\sim$2–4 mag from maximum and is featured by highly blue-shifted absorption lines and emission lines of O I, He I, N II and H I. The name of this phase is derived from a similarity in nature to the stellar wind absorption lines in luminous OB stars.

5. Nebular spectrum: As the photosphere expands further, the density in the nova ejecta decreases and the spectra evolve to those of nebular regions forming high ionization lines. This phase is dominated by broad forbidden emission lines of [O I] and [N II] initially, followed by [O III] and probably [Ne III] and [Ne V] lines along with those from principal spectrum. If the ionizing radiation reaches a temperature of over 10^6 K then eventually coronal lines emerge up to [Fe IV].

6. Post-nova or quiescence spectrum: This usually appears after a few years to decades from the outburst. Eventually, spectra of individual components of the ejecta such as secondary or accretion disc are revealed. The spectrum is typically dominated by permitted lines of H, He, C, N and O, and a strong continuum.

Williams (1992) introduced a new spectral classification of novae based on post-outburst emission spectra. Novae were mainly divided in to **Fe** II and **He/N** classes based on the presence of prominent non-Balmer lines either Fe II or He and N lines.

1. Fe II class novae: These show several low ionization Fe II lines along with CNO lines in the far red of the spectrum excited by recombination and fluorescence scattering. The emission lines are narrow with round peaked profiles, and also some P-Cygni profiles signature of optically thick expanding ejecta. The expansion velocity of the ejecta range from 1000 to 3500 km s^{-1}. The spectra of these systems indicate that they are formed from a large circumbinary gas envelope emerging from secondary star (Williams, 2012).

2. He/N class novae: These show high ionization lines of He and N formed in the discrete shell of ejected gas. They are broad with flat-topped peaked rectangular profiles with expansion velocity > 2500 km s^{-1}. Such profiles trace back their origin to emission gas with high velocity and episodic ejection (Williams, 2012).

It was noted that few novae showed a transition from one class to another or showed features of both classes simultaneously, and they were classified as **hybrid** class

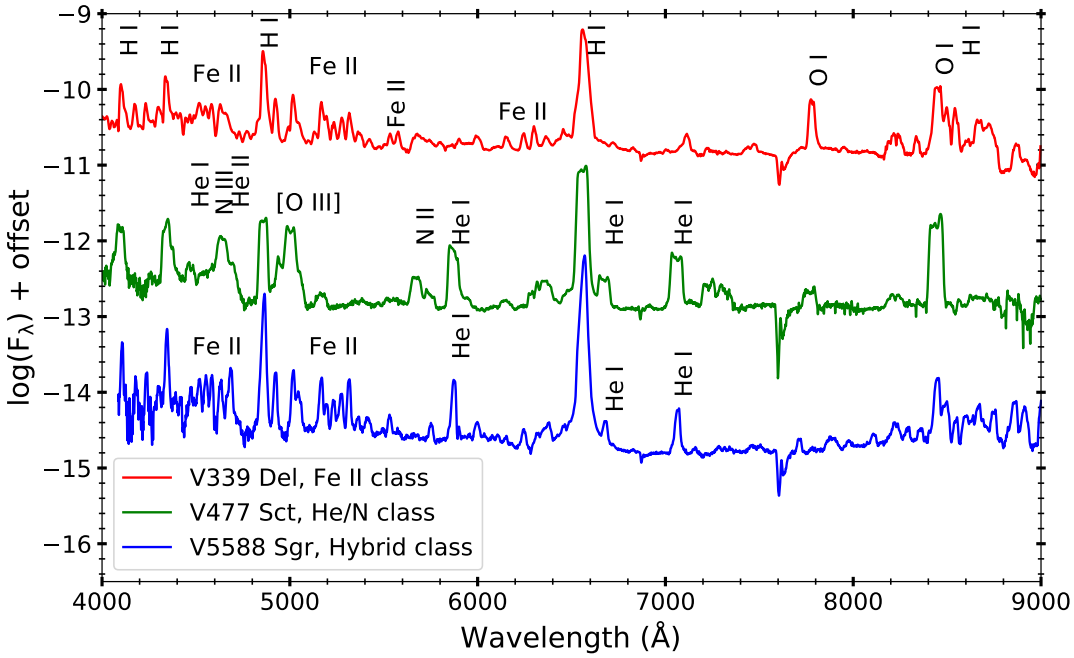

Figure 1.6: Emission line spectra of novae belonging to different spectral classes as marked.

(Williams, 1992, 2012). The classification scheme based on emission line spectra is depicted using the data from this work in Fig. 1.6.

1.4.3 Emission from other wavelengths

Novae are known to emit over the entire electromagnetic spectrum right from radio to gamma-rays (refer Bode & Evans 2008 for detailed review). The advancement in technology has resulted in the launch of high energy space telescopes which has paved the way for studying and understanding nova systems. Multi-wavelength studies of novae have become essential to understand the outburst and its properties.

Gamma-ray emission

Novae as potential gamma-ray emitters were first proposed by Clayton & Hoyle (1974). It was suggested that gamma-rays in novae appear due to the electron-positron annihilation. The gamma-rays are emitted due to nuclear radioactivity. Here, some of the radioactive nuclei which are synthesized during TNR undergo either electron capture or unstable β^+ emitting positrons. These decay into nuclei

with excited states which de-excite to ground states emitting photons at higher energies. The emitted positrons annihilate with electrons and also produce gamma-ray emission. Thus providing a signature of nucleosynthesis during outbursts and information on physical conditions of the environment.

The first nova outburst detected in gamma-rays was V407 Cyg in 2010 with *Fermi*-LAT (Abdo et al., 2010). This high energy emission is due to the relativistic particles produced during eruption accelerated by strong shocks. In the last decade, few novae have been observed to emit in gamma-rays by *Fermi*-LAT. However, the mechanism involving the emission at this high energy is not well understood. In the case of systems having evolved secondary such as RNe, shocks between the nova ejecta and pre-existing circumstellar medium (CSM) are considered to be producers of particle acceleration and eventually emit gamma-rays (Abdo et al., 2010). In the case of CNe, internal shocks are suggested to lead to the production of gamma-ray emission (Li et al., 2017; Aydi et al., 2020).

X-ray emission

After the initial outburst, a fraction of H-burning envelope remains continuously burning on the WD surface. This nuclear burning region is obscured by optically thick ejecta. As the expansion continues, the ejecta becomes optically thin to the emission from the surface of the WD. During this phase, optical photospheric radius decreases and energy distribution switch towards the shorter wavelength leading to peak emission in soft X-ray band. This phase is referred to as the supersoft source (SSS) phase (Krautter, 2008). This burning on the WD surface is anticipated to sustain at constant bolometric luminosity consuming remaining H-rich envelope. In due course, the majority of the H-rich matter is burned into heavier elements resulting in the depletion of nuclear reactions. Hence, the SSS phase ends as the soft X-ray emission disappears, and the system goes back to quiescence. The time since outburst for SSS phase to be detectable is referred to as SSS turn-on time ($t_{\rm on}$). When the ejected matter is massive, it expands slowly leading to the longer duration for it to become optically thin and SSS phase to become visible. Hence, SSS turn-on is

given as $t_{on} \propto M_H^{1/2} v_{ej}^{-1}$ by Krautter et al. (1996). The time since outburst for the SSS phase to disappear is referred to as SSS turn-off time (t_{off}). For massive WDs where $M_{WD} > 1$ $M_\odot$, little accreted matter is required to reach TNR when compared to less massive WDs. So, the fraction of remaining H-burning envelope on the WD surface is comparatively small and takes a shorter time to completely exhaust it, resulting at the end of the SSS phase. A relation for t_{off} is given by MacDonald (1996) as $t_{off} \propto M_{WD}^{-6.3}$. A detailed review on X-ray emission in novae is available in Krautter (2008) and references therein.

The other sources of X-ray emission other than thermal emission from remnant material on hot WD as described above are, emission from the CSM surrounding nova due to shocks within the wind or shock between the pre-existing material from previous outbursts or (and) an evolved companion wind and the ejecta, restoration of accretion through accretion disc or magnetically restricted accretion in the case of magnetized WD, and hard X-ray emission from a highly magnetized WD due to accretion shocked material or Compton downgrading of gamma-rays.

Ultraviolet emission

Novae show strong emission in ultraviolet (UV) range during the fireball stage. The UV rays are blocked due to the recombination of the iron elements, which is referred to as **Fe-curtain** stage. During this phase, all the wavelengths shorter than 1700 Å are blocked due to absorption by many heavy elemental lines of iron group such as Fe I/Fe II, Ti I/Ti II and Cr I/Cr II. These recombination lines are formed due to the decrease in temperature as the expansion proceeds. The optical depth of the ejecta in UV regime decreases after a few weeks from the outburst and the flux increases. As the pseudo-photosphere shrinks, the temperature increases resulting in an increase of ionization of the ejecta and decrease in opacity further. This is referred to as **lifting of the Fe-curtain**. Many spectral lines like Mg II, C II, and semi-forbidden N II and N III appear in UV spectrum. Once the ejecta is completely ionized and transparent, the nebular phase starts near the UV maximum. Highly ionized nebular and coronal lines like Ne VII and Fe VII to Fe XIV lines appear. A

detailed review of the evolution of the UV spectrum can be found in Shore (2008) and references therein.

Infrared emission

During the fireball stage and when the expansion of pseudo-photosphere happens, the free-free and line emission in optical and IR from the hot expanding ejecta dominate the flux. After this phase, the evolution of IR flux undergoes a sudden rise due to dust formation in circumstellar environment. Among CO and ONe novae, CO are known to form dust more likely than ONe. In the case of ONe, they evolve into coronal emission phase where the near-Infrared (NIR) and mid-IR emission lines are highly ionized for many years. The typical timescale of dust formation ranges from 30 to 80 days since outburst in novae. As the ejecta expands, gas temperature decreases below the condensation temperature of dust, resulting in the formation of dust grains in the circumstellar environment. This temperature is about 1000 to 1200 K. The dust formation leads to a sudden decrease in optical or UV and increase in IR light. This is due to absorption of optical radiation by dust grains which re-emit in IR wavelengths. A detailed review of the evolution of IR emission can be found in Gehrz (2008) and references therein.

Radio emission

Many novae are detected at radio wavelengths (Bode et al. 1987; Roy et al. 2012 and references therein). The primary process responsible for radio emission is thermal bremsstrahlung due to ionized ejecta. In few novae, non-thermal synchrotron emission is also detected. Radio observations aid in studying the structure and morphology of the expanding ejecta. The density distribution of the ejecta can be understood by studying the evolution of thermal radio emission from optically thick to thin phase along with observations from other wavelengths. Also, radio observations are used to determine the radio surface brightness during the optical thick phase and electron temperature. From the absorption line velocities and angular expansion rates, the distance to novae can also be determined. The first novae detected in radio

were CNe HR Del and FH Ser by Hjellming & Wade (1970). A detailed review of radio emission in novae can be found in Seaquist (2008) and references therein.

1.5 Thesis structure

This work involves the study of a few novae to understand their properties and also to interpret their behaviour with the aim of better understanding classical and recurrent nova systems in general. Few novae in this study show peculiar behaviour when compared to the typical nature of nova systems. One of the most important things addressed in this work is the morphology of the ejecta of different spectral class of novae in the sample. The main motivation of this study is to understand the following:

1. The evolution of physical conditions in the nova systems.
2. The spatial distribution of the ionized atoms in the structure of different novae.
3. The extent, distribution and emissivity distribution of different components and their evolution in the systems that are used to understand the ejection mechanism (wind or shell or both).
4. Obtaining models for a different classes of novae that would eventually lead to obtaining an exhaustive model for nova systems.

In Chapter 1, a general review on novae such as the theory of outburst, observational properties in all the bands, and classification schemes are discussed. In Chapter 2, the details of the telescopes and their instruments used to obtain multiwavelength data, and also the data reduction processes are presented. Chapter 3 deals with the detailed methodology and different analyses adopted to obtain the morphology of the ejecta of different novae. In Chapter 4, detailed analysis of Fe II class of novae namely V2362 Cyg, V5587 Sgr, V2676 Oph, V339 Del, V1369 Cen, V2944 Oph, V5856 Sgr, V3665 Oph and V5857 Sgr are discussed. The Chapter 5 deals with the detailed analysis of He/N class of novae namely V477 Sct, and M31N

2008-12a are discussed. In Chapter 6, detailed analysis of hybrid novae namely V5588 Sgr, T Pyx, V612 Sct, V906 Car and V3890 Sgr are presented. Finally, in Chapter 7 general summary and future work are discussed.

2

Data Acquisition and Reduction Techniques

The primary parameters that distinguish an astronomical object are its luminosity, radius, mass and chemical composition. Various techniques are used to derive these parameters such as photometry, spectroscopy, polarimetry and asteroseismology. Photometry refers to the measurement of flux over a broad wavelength band of radiation. Spectroscopy is the measure of intensity as a function of wavelength. Polarimetry involves the measurement of the degree of linear polarization and its direction. Asteroseismology deals with the study of oscillations of the stars to understand their interior structures. Various facilities covering different wavelength regime from radio to X-rays are used to study different nova systems. The details of the instruments used for the observation, and reduction processes carried out for different wavelengths are described in this chapter.

2.1 Spectroscopy

Spectroscopy is the measure of intensity as a function of wavelength. It is used in astronomy to understand the temperature, velocity and composition of a celestial object, and also to determine the mass, distance and many other quantities. It is the

technique that splits the electromagnetic radiation into its constituent wavelengths. There are three types of spectra, namely continuous, emission line and absorption line spectra. A continuous spectrum is an array of all the wavelengths produced by a hot dense object. An emission line spectrum consists of emission at specific wavelengths generated by a hot low-density gas. In contrast, an absorption line spectrum is due to cool gas absorbing light from a hot source before reaching an observer. The light from the source collected by a telescope is fed into a spectrograph which splits the light into its constituent wavelengths using a dispersing optical element such as a prism, grating or prism and grating (grism). The dispersed spectrum is then recorded by a detector, commonly Charge Coupled Devices (CCDs).

2.1.1 Spectrograph

The primary components of a basic spectrograph are

1. Slit: The slit is a mask with a narrow aperture placed in the focal plane of the telescope. It is used to limit the background noise, field and wavelength degeneracy. As the slit width decreases, the spectral resolution increases; however, there is a loss of light as the slit becomes narrower.

2. Collimator: It transforms diverging beam from the slit into a parallel beam, and directs it toward the dispersing element. The collimator can either be lens, mirror or both.

3. Dispersing element: The parallel beam of light from the collimator is dispersed into its constituent wavelengths using a prism, a grating or both. The prism disperses the light based on the principle that different wavelengths undergo different amount of refraction. This dispersion is disproportionately more in the blue regime than in the red. The grating disperses the light based on the principle of diffraction and interference. The dispersion is mostly linear in the case of the grating. The grism is such that the diffraction angle of the transmission grating is cancelled by the reflection angle of the prism such that

the dispersed beam is in-line with the incoming radiation. In high resolution spectroscopy, echelle grating is used as dispersing element.

4. Camera: It collects and converges the dispersed beam so that the spectrum is imaged onto the detector. It is either a lens or a mirror or catadioptric system.

5. Detector: The dispersed light is finally imaged by the spectrograph onto the detector forming a spectrum.

2.1.2 Echelle spectrograph

Echelle spectrograph is designed to obtain high resolution spectroscopic data. The light in this spectrograph is dispersed into two orthogonal directions using two dispersing elements resulting in the two-dimensional spectrum of the object. The incident beam undergoes dispersion using an echelle (coarse-ruled) grating followed by cross-dispersion using a prism or grating in the orthogonal direction. This spectrograph provides high dispersion without much loss in the spectral coverage. These can be used to operate in orders close to 100.

2.2 Charge Coupled Devices

These are the standard visible and near-ultraviolet imaging sensors used in astronomy since the 1980s. Most of the astronomical instruments use CCD for scientific observations. The invention of CCD was by Bell Laboratories researchers Willard S. Boyle and George E. Smith (Boyle & Smith, 1970; Amelio et al., 1970). It converts the light into a pattern of electronic charge in a silicon chip. This pattern is then converted into a video waveform, digitised and stored as an image file on a computer.

The fundamental principle in the operation of a CCD is the photoelectric effect. A photon incident on the pixel interacts with the valence electrons generating an electron-hole pair. More electron-hole pairs are produced as more photons fall on the pixels and the charge accumulates. A potential well is conserved using sub-pixel

sized electrodes called gates to prevent the recombination of the electron-hole pairs. The collected charge is held in the gate until it is readout. The CCD is clocked out and charge in each pixel is measured post the exposure. The charge that is collected in each pixel is electronically shifted along the columns after applying the voltages to the gates. The charge transfer is downwards along with the columns usually, and the clocking goes on till the charges in the rows are transferred to the final row to a readout where it is measured. The measurement is attained by amplifiers where the charge is measured as voltage and converted into a digital output which is then transmitted and stored in a computer.

There are several characteristics of CCDs that aid instrumentation in astronomy such as- a) they are sensitive to the wavelength in the optical and near-UV regime implying broad spectral response, b) the generation of charge in each pixel is proportional to the number of photons incident, c) they have a high dynamic range (ratio of highest to lowest charge values) helpful in astronomical objects with high variability in brightness, d) the noise levels in these can be reduced to a greater extent by cooling them using cryogenic materials, e) high quantum efficiency is seen in CCDs far more than that in photo-multiplier tubes and photographic emulsions, and f) usually, the detector response is stable for a very long time as they are cased in a protective enclosure.

2.3 Telescopes and instruments

The majority of the work presented in this thesis involves optical data using the 2 m Himalayan Chandra Telescope (HCT) and the 2.3 m Vainu Bappu Telescope (VBT). The other optical data were obtained from telescopes such as the 0.7 m GROWTH-India telescope (GIT), the 1 m Carl Zeiss Telescope (CZT), the 1.3 m Jagadish Chandra Bhattacharya Telescope (JCBT), the 2 m telescope at IUCAA Girawali Observatory (IGO) and the Southern African Large Telescope (SALT). The UV and X-ray data for 2018 outburst of M31N 2008-12a were obtained from *Swift* data archives. The radio and other soft X-ray data for V3890 Sgr were obtained

from Giant Metrewave Radio Telescope (GMRT) and AstroSat respectively. Further details of the instruments used in these telescopes are discussed in this section.

2.3.1 Himalayan Chandra Telescope

Most of the optical spectroscopic data used in this work were obtained using HCT located at Indian Astronomical Observatory (IAO), Hanle, India at an altitude of 4500 m above mean sea level in the north of Western Himalayas. The 2 m aperture telescope has an altitude-azimuth mount. It has a Ritchey-Chretien configuration with a primary mirror made of Corning Ultra Low-Expansion (ULE) ceramic to withstand low temperature. The low temperature, low humidity, low concentration of aerosols, less pollution and high altitude, provide favourable conditions for observations from this site. The telescope is remotely operated from CREST, Hoskote by a dedicated satellite link. There are three science instruments mounted at the f/9 Cassegrain focus: Hanle Faint Object Spectrograph and Camera (HFOSC[1]), TIFR Near-Infrared Spectrometer and Imager (TIRSPEC[2]) and Hanle Echelle Spectrograph (HESP[3]).

Hanle Faint Object Spectrograph and Camera

HFOSC is an optical imager and spectrograph mounted on the 2 m HCT. It covers a wavelength range of 350–920 nm with a set of 11 grisms of resolution ranging from 150–4500. It has a wider field of view of $10' \times 10'$ as the instrument is a focal reducer one. HFOSC is mounted on the on-axis port of the instrument mount cube of HCT. The CCD has 2048 $\times$ 4096 pixels with each pixel having a size of 15 $\times$ 15 μm. In this study, grism 7 and 8 were used which covers 350–800 and 520–920 nm with a resolution of 1300 and 2200 respectively.

[1]https://www.iiap.res.in/iao/hfosc.html
[2]https://www.tifr.res.in/ daa/tirspec/
[3]https://www.iiap.res.in/hesp/

Hanle Echelle Spectrograph

HESP[3] is a high resolution, fiber-fed cross-dispersed near-Littrow echelle spectrograph (Sriram et al., 2018) that is mounted on the 2 m HCT. It has wavelength coverage of 350–1000 nm with two resolution modes. Also, there is no gap in this coverage, and high throughput is obtained. The high resolution mode of 60000 spectral resolution is attained using the sliced fibre inputs while the low resolution mode is of 30000 resolution attained using the unsliced fibre inputs. The instrument consists of four subsystems such as Cassegrain, spectrograph, calibration and CCD units. The Cassegrain unit is attached to one of the side ports of telescope leading the light from telescope to spectrograph and auto-guider system. The spectrograph unit consists of an off-axis paraboloidal mirror collimator, echelle grating, two prisms and an f/2.7 camera mounted on an optical table. The calibration unit includes filters, calibration lamps (ThAr and ThArNe) and a Halogen lamp. The CCD is a 4K $\times$ 4K system with a pixel size of 15 $\times$ 15 μm.

2.3.2 Vainu Bappu Telescope

The next majority of the optical spectroscopic data used in this work was obtained from the Vainu Bappu Telescope (VBT). VBT is a 2.34 m with an equatorial mount located at the Vainu Bappu Observatory[4] (VBO), Kavalur, Tamilnadu, India. The observatory is located at 12° north enabling the observation of the southern sky, and at an altitude of 750 m above the mean sea level. The telescope has two foci namely prime focus f/3.5 with an image scale of 27 arcsec mm^{-1} and Cassegrain focus f/13 with a scale of 6.7 arcsec mm^{-1}.

Optometrics Research Spectrograph

The Optometrics Research Spectrograph (OMRS) is mounted on the Cassegrain focus of the telescope (Prabhu et al., 1998). It consists of 25 mm long slit with 40 μm minimum width and 950 μm maximum width. Its collimator is an off-axis

[4]https://www.iiap.res.in/Telescopes/VBO

paraboloid with a focal length of 1 m and an aperture of 110 mm with a tilt of 6°. The CCD is a 1K Tektronix detector with a pixel size of 24 μm. Four gratings are available and are chosen based on the requirement, and they are swtiched manually. The gratings available are 150 l/mm with resolution 21.2 Å and 8 Å at 5460 Å; 300 l/mm with resolution 10.6 Å and 4 Å at 7620 Å; 600 l/mm with 5.3 Å and 2 Å at 7500 Å; and 1200 l/mm with 2.7 Å and 1 Å at 7500 Å. The last two gratings were used for this study. It also includes six-position filter-wheel with a clear aperture and order separation filters such as Corning 4-71, Schott BG37, BG, 39, GG475 and RG695. For this work, the filter GG475 was used to obtain the spectrum of wavelength range 6000–8800 Å, and no filter was used to obtain the spectrum in the range of 3800–6500 Å. The wavelength calibration sources used were FeNe and FeAr lamps.

Echelle spectrograph

It is a fibre-fed echelle spectrograph, one of the instruments available in VBT. It is placed on the vibration isolation optical table in a separate chamber called coude laboratory and linked to the prime focus of the telescope through an optical fibre of 100 μ core size. It consists of an echelle grating with large blaze angles ranging from 63–70° operated in higher diffraction orders. It attains high resolution of 30000–105000 with a wavelength coverage of 400–1000 nm, with CCD of 12 μm pixel size and 4K $\times$ 4K. The slit can be adjusted from 30 to 100 μm, and an optimal resolution of 70000 can be achieved with a slit width of 60 μm. ThAr lamp was used as a wavelength calibration source.

2.3.3 Carl Zeiss Telescope - Universal Astro Grating Spectrograph

CZT is a 1.02 m aperture optical telescope at VBO, Kavalur, India. It has a Ritchey-Chretien F/13 optical configuration with a plate scale of 15.5 arcsec mm^{-1}. It has two foci, namely Cassegrain f/13 and Coude f/30. Currently, it is equipped

with two scientific instruments, stellar optical polarimeter and Universal Astro Grating Spectrograph (UAGS).

UAGS is a medium resolution spectrograph (Bhattacharyya, 1987) mounted at the Cassegrain focus of the telescope. The CCD is of 1K $\times$ 1K size. It has a catadioptric collimator system and two gratings. The gratings available are 651 grooves mm^{-1} at blaze angle of 8° with an efficiency of 80% peaking at 400 nm; and 1800 grooves mm^{-1} at blaze angle of 26°45$'$ with an efficiency of 81% peaking at 508.6 nm. The spectrograph has the arrangement to view the field with a diameter of 8$'$. The limiting unvignetted slit length is 10 mm that is 160$''$ at f/13 focus. Filters for order separation are mounted on a filter wheel placed after the slit.

2.3.4 Jagadish Chandra Bhattacharya Telescope - CCD imager

JCBT is 1.3 m telescope located at the VBO, Kavalur, India. It has a Ritchey-Chretien F/8 optical configuration, with a primary mirror of 1.3 m diameter.

The 2K $\times$ 4K UK Astronomy Technology Centre (UKATC) CCD is mounted on JCBT at the main port. The 15 μm pixel size corresponds to an image scale of 0.3$''$ pixel^{-1}, resulting a field of view of 10$'$ $\times$ 20$'$. It includes Bessell $BVRI$ filters.It has a back-illuminated, coated E2V broadband sensor chip, and it is cooled using liquid nitrogen.

2.3.5 IUCAA Girawali Observatory - IUCAA Faint Object Spectrometer and Camera

IGO is an astronomical observatory located at Girawali, Pune, Maharashtra, India and operated by the Inter-University Centre for Astronomy and Astrophysics (IUCAA). It has a telescope with primary mirror of 200 cm with f/3 and a secondary mirror which is 62 cm with f/10. It has one direct port and four side ports at its Cassagrain focus.

IUCAA Faint Object Spectrometer and Camera[5] (IFOSC) is one of the main instrument mounted on the Cassegrain port of the telescope. It has 2K $\times$ 2K back-illuminated thinned CCD with 13.5 μm pixels. The spatial sampling scale is 44 μm per arcsec with a field of view of 10.5$'$. It consists of $BVRI$ imaging and photometric capabilities along with several grisms with resolutions from 190 to 3700 covering a wavelength range of 350–850 nm. The calibration unit includes a set of lamps for flat field and spectral calibration. HeNe lamp is used as a wavelength calibration source. The grism C7 and C8 covering a wavelength range of 380–684 nm and 580–835 nm with resolution 1100 and 1600 were used for this work.

2.3.6 Southern African Large Telescope - High Resolution Spectrograph

SALT is situated at the South African Astronomical Observatory (SAAO) at Sutherland, Cape Town at an elevation of 1798 m. It is fixed at an elevation angle of 53° enabled to move only in azimuth. The aperture is of 11.1 $\times$ 9.8 m made up of 91 identical hexagonal segments. It includes instruments like SALT Imaging Camera (SALTICAM), Robert Stobie Spectrograph (RSS), a multi-purpose long-slit and multi-object imaging spectrograph and spectropolarimeter, and a fibre-fed High Resolution Spectrograph (HRS).

The SALT-HRS (Barnes & MacQueen, 2008; Bramall et al., 2010, 2012; Crause et al., 2014) is a dual-beam fibre-fed echelle spectrograph covering the wavelength range of 370–550 and 550–890 nm. It consists of VPH gratings as cross dispersers and refractive cameras. It uses pairs of large (350 μm and 500 μm; 1.6 and 2.2 arcsec) diameter optical fibres, for the source (star) and background (sky). The image slicers of resolving powers 14000 (unsliced 500 μm fibres), 40000 (sliced 500 μm fibres) and 65000 (sliced 350 μm fibres) are available. A single 2K $\times$ 4K CCD captures the blue orders and a 4K $\times$ 4K detector that uses a fringe-suppressing deep-depletion CCD is used as the red camera. Blue and red arms cover the whole wavelength coverage.

[5]http://igo.iucaa.in/igoweb/igo

2.3.7 GROWTH - India telescope

Global Relay of Observatories Watching Transients Happen (GROWTH)-India telescope (GIT)[6] is a 0.7 m robotic telescope at IAO, Hanle, India with an altitude-azimuth mount. The telescope is equipped with a thermo-electrically cooled, back-illuminated 4096 $\times$ 4108 Andor iKon-XL CCD. The 15 μm pixel size corresponds to an image scale of $0.7''$ pixel^{-1}, with a field of view of $\sim 0.7^{\circ} \times 0.7^{\circ}$. The telescope is funded under the international PIRE project Global Relay of Observatories Watching Transients Happen (GROWTH) by SERB-IUSSTF.

2.3.8 Giant Metrewave Radio Telescope

GMRT[7] is situated near Khodad village, Maharashtra, India and operated by the National Centre for Radio Astrophysics, Tata Institute for Fundamental Research. It consists of an array of 30 antennae spread over 25 km diameter, and each antenna is of 45 m diameter. 14 of the 30 antennae are placed in a central compact array with size 1.1 km while other antennae are in a Y shaped configuration resulting in a maximum baseline length of 25 km. Different feeds are mounted on the rotating turret at the focus. The available feeds are 150, 325, 610/235 and 1000–1450 MHz (sub-bands: 1060, 1170, 1280 and 1390 MHz). The GMRT Software Backend (GSB) supports a maximum bandwidth of 32 MHz. The upgraded-GMRT (uGMRT) has wideband feeds of 125–250 MHz, 250–500 MHz, 550–850 MHz and 1–1.5 GHz with a wideband backend of 400 MHz bandwidth.

2.3.9 The Neil Gehrels Swift Observatory

Swift is a multi-wavelength observatory launched into a low-Earth orbit consisting of three instruments covering γ-ray, X-ray, optical and ultraviolet wavelength regime. The instruments are co-aligned, and they are Burst Alert Telescope (BAT), X-ray Telescope (XRT) and Ultraviolet/Optical Telescope (UVOT).

[6] https://sites.google.com/view/growthindia/about
[7] http://www.ncra.tifr.res.in/ncra/gmrt

X-ray Telescope

XRT is a telescope with Wolter I configuration with an XMM EPIC CCD with 600 $\times$ 600 pixels, and an effective area of 135 cm^2 at 1.5 keV, covering the energy range of 0.2–10 keV. The detector operates in Photon Counting, integrated imaging and rapid timing modes, covering a field of view of $23.6' \times 23.6'$ with pixel scale $2.36''$ pixel $^{-1}$.

Ultraviolet/Optical Telescope

UVOT has a modified Ritchey-Chretien configuration with a 30 cm diameter and F/12.7 covering a wavelength range of 170–650 nm with a spectral resolution of 200 at 400 nm. The CCD has 2048 $\times$ 2048 pixels with a pixel scale of $0.48''$ and was used in photon counting mode. It consist of filters such as U centered at 346.5 nm, B at 439.2 nm, V at 546.8 nm, $uvw1$ at 260 nm, $uvm2$ at 224.6 nm and $uvw2$ at 192.8 nm (refer Poole et al. 2008 and Breeveld et al. 2011 for more details).

2.3.10 AstroSat

AstroSat[8] is the first Indian astronomy mission to cover X-ray, optical and UV regions simultaneously. It was launched in to a 650 km orbit in 2015. It consists of payload instruments such as the Large X-Ray Proportional Counter (LAXPC), Soft X-ray Telescope (SXT), Cadmium Zinc Telluride Imager (CZTI), Charge Particle Monitor (CPM), Ultra Violet Imaging Telescope (UVIT) and Scanning Sky Monitor (SSM).

SXT is equipped with focusing optics and a deep depletion CCD camera at the focal plane. It covers energy band of 0.3–10 keV. The optics consist of 41 concentric shells of conical foil mirrors close to the Wolter I telescope configuration. It has an effective area of about 120 cm^2 at 1 keV. The CCD is operated at -80 °C using thermoelectric cooling. The pixel size is 40 μm $\times$ 40 μm with pixel scale of $4.12''$

[8] http://astrosat.iucaa.in/

pixel^{-1} and field of view of $40'$. There are six data modes available, and Photon Counting mode is used for this study.

2.4 Reduction techniques

The above facilities were used to obtain the data used in this study. The raw data obtained consist of artifacts from the atmosphere and the instrumental response. To make the required measurements of the objects, it is necessary to correct the data using proper reduction processes.

2.4.1 Optical data

Optical data reduction was carried out using various tasks in Image Reduction and Analysis Facility[9] (IRAF).

To make sure that the Analog to Digital converter has a positive value, a bias level that is DC offset is added to the CCD signal. The bias level generates background counts due to the applied bias voltage. These counts were subtracted from the raw frames. Many bias frames were obtained throughout the observational nights with zero exposure, and all these frames were combined to obtain master bias frame. The bias subtracted science frames were obtained by subtracting the master bias from the raw frames. Bias subtraction was carried out using ZEROCOMBINE and IMARITH tasks in IRAF. To remove thermal noise generated in CCD, that is a function of temperature and exposure time, dark frames were obtained. The dark frames have exposure time corresponding to that of the object frame but without any light source. The dark frame was subtracted from the object frame to correct for the thermal noise. IMARITH task was used to carry out dark subtraction.

The response of the camera in a telescope to a source of uniform illumination is referred to as the flat field. The flat field frames were used to remove anomalies in the optical path like dust on the surface, sensitivity variances between pixels in the CCD

[9]IRAF is distributed by the National Optical Astronomy Observatory, which is operated by the Association of Universities for Research in Astronomy (AURA) under a cooperative agreement with the National Science Foundation.

and vignetting. This frame is nothing but an image of the uniformly illuminated field. The frames of the same filter were bias subtracted, normalized and combined to get a master flat. The bias subtracted object frames were divided by the master flat. Flat fielding was carried out using FLATCOMBINE and IMARITH tasks in IRAF. When high energy particles hit the CCD, it creates counts that are not of the target. Unlike stars which have Gaussian profile, cosmic rays have a sharp-peaked profile and usually within a single pixel. These were removed using IRAF tasks such as COSMICRAYS or CRMEDIAN.

1. Photometry: It is the process of measurement of flux from the astronomical objects. It can be represented in terms of magnitude as follows:

$$m_1 - m_2 = -2.5 \log \left(\frac{f_1}{f_2} \right) \tag{2.1}$$

where m_1 and m_2 refers to magnitudes of two sources and their fluxes in a particular bandpass is represented by f_1 and f_2 respectively. The magnitude scale in this relation is logarithmic. The zero point of the magnitude scale is set using the star Vega as a standard with magnitude assigned as 0, defining $zp = 2.5 \log f_{\text{Vega}}$. Hence, the magnitude relation with flux in the Vega system is

$$m_1 = -2.5 \log f_1 + zp \tag{2.2}$$

The total flux of the object is determined by the counts observed in respective filters. Thus, the magnitude in a particular filter with central wavelength λ is given by

$$m_\lambda = -2.5 \log \left(\frac{\text{counts}_\lambda}{\text{exposure time}} \right) + zp_\lambda \tag{2.3}$$

The first term on the right-hand side of the above equation gives the apparent brightness of the source and the second term is the zero point correction that is used to convert the instrumental magnitude to a standard system. Hence, to complete the process of photometry of novae, both these terms are essential. Photometry was carried out in this study for the RN M31N 2008-12a,

which is an extragalactic nova. As the object was faint, multiple frames with shorter exposures were obtained to avoid saturation of field stars in the frame with longer exposures. Once the pre-processing of the object frames such as bias subtraction and flat-fielding were complete, the frames of the same filters were aligned and co-added using the tasks in IRAF such as GEOMAP, GEOTRAN and IMARITH. Aperture photometry was carried out to determine the instrumental magnitude of the source. It was estimated by defining an aperture around the source and summing the counts due to the source in the CCD pixels over which the photons are spread. The aperture size was decided such that maximum light from the source is covered; however, the appropriate size was chosen to not involve the uncertainties in sky background and contamination from nearby objects. To carry out aperture photometry, DAOPHOT package in IRAF was used. It was performed at two apertures, viz., one closer to the full-width half-maximum (FWHM) of stellar profile and the other around three times the FWHM of the stellar profile. The magnitude difference from these two apertures was used as aperture correction, and the average correction is determined from all the stars in the field. The local standards in the field were calibrated using the zero-point magnitudes obtained from Darnley et al. (2016). Only those local standards whose magnitudes were estimated in Darnley et al. (2016) were used. The magnitude of the target was derived differentially using the calibrated magnitudes of the local standards.

2. Spectroscopy: Spectroscopic reduction is carried out using the standard tasks in IRAF. The object frames were initially subjected to pre-processing such as bias subtraction and flat-fielding followed by extraction of the spectrum. The one-dimensional spectrum was extracted from the two-dimensional spectrum using APALL task. The optimal aperture and background regions are chosen, and the aperture was traced along the dispersion axis using a cubic spline function. The counts were summed from various pixels using variance weighting to improve the signal to noise ratio. The arc lamp spectra were also extracted. The identification of lines in these spectra was carried out using IDENTIFY

task. The wavelength solutions estimated were applied using DISPCOR to the object frame and the standard star to obtain the wavelength calibrated spectra. The standard star spectrum was then used to obtain the sensitivity curves using the tasks STANDARD and SENSITIVITY for the instrument by comparing the flux values of the source with the known and catalogued values. These response curves were then used to correct the novae spectrum using CALIBRATE, and the continuum corrected object spectrum was obtained. These calibrated spectra in red and blue regions were combined and scaled to a weighted mean using the task SCOMBINE to obtain the final spectra. The zero points required to convert the spectra to the absolute flux scale were obtained from American Association of Variable Star Observers (AAVSO[10]) magnitudes in $UBVRI$ filters. The spectrum is then corrected for reddening using the task DEREDDEN. Most of the high resolution data were reduced using the same tasks as described above in the ECHELLE package of IRAF. Few HESP data were reduced using the HESP pipeline[11]. For the SALT data, pre-processing like over-scan correction, bias subtraction and gain correction was conducted using the science pipeline of SALT (Crawford et al., 2010). The remaining tasks, like aperture extraction and wavelength calibration, were carried out using the ECHELLE package in IRAF.

2.4.2 Radio data

The radio observations of V3890 Sgr were in standard continuum mode of GMRT with a bandwidth of 33 MHz split into 256 channels and using upgraded GMRT (uGMRT) at band 3 (250–500 MHz), band 4 (550–900 MHz) and band 5 (1000–1450 MHz). The sampling for recording data was 16 sec. The flux density and band-pass calibrators used were 3C286, 3C48 and 3C468.1 and phase calibrator were 1822-096 (J2000). The observing run of 1–3 hr duration was carried out on different epochs

[10]Kafka, S., 2020, Observations from the AAVSO International Database, https://www.aavso.org
[11]https://www.iiap.res.in/hesp/

for an object. The data were reduced and analyzed using Common Astronomy Software Application (CASA) package (McMullin et al., 2007). The processes such as loading, plotting, flagging, calibrating and imaging the data were carried out using standard tasks in CASA to reduce and analyze the data. The data editing (flagging) was to identify and discard several corrupt data (Radio Frequency Interference data). This was performed using the task FLAGDATA. This was followed by initial calibration to reduce the errors in the measurement of parameters like phase and amplitude of the voltage signals. Then the target was imaged using the task CLEAN. After imaging, a few rounds of phase-only self-calibration and couple of amplitude and phase self-calibration were carried out. The flux density of the target was estimated using the Gaussian fit at the source position.

2.4.3 *Swift* Ultraviolet/Optical and X-ray telescope data

Images of M31N 2008-12a were downloaded from the *Swift* archival data with ObsIDs 01–02 and 04–21 (ID no.:000109650**). The ObsID 14 is excluded as the exposure time was 35 s. The *uvw*2 filter archival data with a central wavelength of 1930 Å was used for analysis. The analysis of these data was on the cleaned level 2 files locally reprocessed at the Swift UK Data Centre with HEASOFT (v6.17) (High Energy Astrophysics SOFTware). For the analysis, HEASOFT (v6.25) with UVOTSOURCE was used. UVOTSOURCE task was used to extract the instrumental magnitude from an image. The source region of radius $\sim 3''.5$ and larger background region were chosen, and UVOTSOURCE with a curve-of-growth aperture correction was operated on these regions. The photometric calibration assumes the UVOT photometric (Vega) system (Poole et al., 2008) and was not corrected for extinction.

Swift XRT data were also downloaded from the *Swift* archive with ObsIDs as that of the UV. The analysis of these data was carried out on the cleaned level 2 files locally reprocessed at the Swift UK Data Centre with HEASOFT (v6.17). For the analysis, HEASOFT (v6.25) with XIMAGE (v4.5.1) and XSELECT (v2.4e) were used. The XRT count rates and upper limits were extracted using the SOSTA command in XIMAGE which corrects for vignetting, psf and dead-time losses.

2.4.4 AstroSat data

V3890 Sgr was observed with SXT configured as the prime instrument. It was observed throughout an orbit of the satellite. The data from individual orbits of the satellite that is Level-1 data were received at the SXT Payload Operation Centre (POC) from the ISSDC (Indian Space Science Data Center). It was in the photon counting mode and were initially processed with the $sxtpipeline$ task in the SXT software[12] (AS1SXTLevel2, V1.4b) at the SXT POC. The source events were calibrated using this pipeline, and the Level-2 cleaned event files were extracted for all the orbits. These files were merged into a single event file using the Julian based merger tool[13]. XSELECT (V2.4d) package in HEASOFT was used to extract the source spectra, and light curves from the processed Level-2 cleaned event files.

All the reduced data is then ready for scientific analysis as described in the next chapter.

[12] https://www.tifr.res.in/astrosatsxt/sxtpipeline.html
[13] https://www.tifr.res.in/astrosatsxt/dataanalysis.html

3

Modelling the ejecta of novae

The evolution of the emission line spectra in novae is sensitive to several physical conditions of the environment such as radiation field of the central continuum source, density, temperature and composition of the gas, and processes responsible for the gas to be ionized. Several numerical codes have played an essential role in understanding these objects.

A spectrum is formed in a cloud of gas which is exposed to radiative sources such as starlight or an accretion disc. The photons from this source ionize the gas and the residual kinetic energy of the photo-electrons heats up the gas. These electrons then collide with ions causing internal excitations which further decay to produce collisionally excited emission lines. At the same time, the recombination lines are formed by the combination of the ions and electrons. Hence, analysis of the emitted spectrum provides valuable information on the composition, density, pressure and temperature of the gas, revealing the history of the gas and the characteristic properties of the central ionizing source. To reproduce the spectrum of a gas cloud, the shape of the radiation field emitted by the central ionizing source, the density and its variation with depth, the photon flux striking the illuminated face of cloud and the chemical composition of the gas are required. This results in the prediction of the spectrum with continuum over a broad range of wavelengths and intensities of many emission lines. Though many forms of ionization parameters are defined, origins are

traced back to the ionization of hydrogen as it is the most abundant element. The ionization equilibrium equation (Osterbrock & Ferland, 2006) for a hydrogen cloud surrounding a hot central source is given by

$$n(\mathrm{H}^0)\int_{\nu_0}^{\infty}\frac{4\pi J_\nu}{h\nu}a_\nu(\mathrm{H}^0)d\nu = n(\mathrm{H}^0)\int_{\nu_0}^{\infty}\phi_\nu a_\nu(\mathrm{H}^0)d\nu = n(\mathrm{H}^0)\Gamma(\mathrm{H}^0)$$
$$= n_e n_p \alpha(\mathrm{H}^0, T)[cm^{-3}s^{-1}] \quad (3.1)$$

where J_ν is the mean intensity of radiation, ϕ_ν is the number of photons incident per unit area, per unit time, per unit frequency interval, $a_\nu(\mathrm{H}^0)$ is the ionization cross-section for hydrogen by photons with energy $h\nu$, $\Gamma(\mathrm{H}^0)$ represents number of photo-ionization per H atom per unit time. The $n(\mathrm{H}^0)$, n_e and n_p are neutral atom, electron and proton densities per unit volume respectively, $\alpha(\mathrm{H}^0, T)$ is the recombination coefficient. The physics governing such environment of the clouds is described in detail in Osterbrock & Ferland (2006).

The emission line strengths are estimated using electron number density, electron temperature, the state of ionization and the projection effects implying that it not just depends on density distribution but also illumination (Martin (1989) and references therein). The interpretation of relative line strengths in the integrated spectrum of novae is very complicated as different regions of the ejecta have different physical conditions at different times due to non-symmetric ejection followed by expanding photosphere, heated surface of secondary, and non-uniform illumination from the accretion disc. Hence, it is crucial to understand both the physics and geometry behind the formation of an emission line. A uniformly expanding shell gives rise to flat-topped emission line profiles which are symmetric with sharp boundaries or peaks could be rounded, and lines edges may not be sharp due to the presence of the range in velocities. The optical depth effects play a role in the formation of complex velocity profiles, for eg., in some cases, the line profiles of permitted lines are affected by self-absorption in the short wavelength wing and appear symmetric similar to that of forbidden lines. The width of the lines of different elements can be compared to understand the velocity systems contributing such as wind and shell.

The forbidden emission lines with saddle-shaped profiles often develop during the early decline phase of novae. The emission peaks are usually placed symmetrically at the principal velocity to the red and violet of rest wavelength. The ejecta is expanding, and optical depth decreases with time. As the systems evolve closer to the nebular phase, the permitted lines also show similar profiles as the effect of wind has diminished and optical depth effects on the line profile have subsided.

In some cases, emission line profiles of novae are known to be complex with multiple peaks or groves indicating the presence of regions in the outflows with favourable conditions for enhanced emissivity (Hutchings, 1972b). Also, some emission lines in novae have asymmetric profiles which could be as a consequence of line transfer effects or absorption due to dust. With the decreasing trend of the level of ionization with height in an envelope that is photo-ionized, one could interpret the regions of lines and dust formation from these asymmetries in the line profiles of different elements.

Many physical parameters can be obtained through spectral analysis, some of the parameters that are obtained for some novae are given below. Using the line fluxes of hydrogen and oxygen from the optical spectrum, the physical parameters like the optical depth of oxygen and electron temperature can be estimated. Using the formulae by Williams (1994),

$$\frac{F_{\lambda 6300}}{F_{\lambda 6364}} = \frac{(1 - e^{-\tau})}{(1 - e^{-\tau/3})} \tag{3.2}$$

Using the value of optical depth (τ), the electron temperature ($T_{\rm e}$) is given by

$$T_e = \frac{11200}{log[\frac{(43\tau)}{(1 - e^{-\tau})} \times \frac{F_{\lambda 6300}}{F_{\lambda 5577}}]} \tag{3.3}$$

where $F_{\lambda 5577}$, $F_{\lambda 6300}$ and $F_{\lambda 6364}$ are the line intensities of [O I] 5577, 6300 and 6364 Å lines respectively.

The hydrogen density is determined using the following relation,

$$n_{\rm H} = M_{\rm H}/V \tag{3.4}$$

$$M_{\rm H} = f m_{\rm H} d^2 / N_{\rm e} \epsilon_{\nu} \tag{3.5}$$

$$V = 4/3\pi r_{\rm s}^3 \phi, \tag{3.6}$$

where $M_{\rm H}$ is the mass of hydrogen ejected, f is the flux of hydrogen line, $m_{\rm H}$ is the mass of hydrogen atom, $N_{\rm e}$ is the electron density, ϵ_{ν} is the emission co-efficient (Osterbrock & Ferland, 2006), V is the line-emitting volume, $r_{\rm s}$ is the radius of the shell, and ϕ is the filling factor.

Shore (2008) provided an estimate of the ejected mass based on the SSS turn-on and expansion velocity as:

$$M_{\rm ejecta} \sim 6 \times 10^{-7} \phi N_{\rm H}(22)\ v_{\rm exp}(1000)^2\ t_{\rm on}^2\ M_{\odot} \tag{3.7}$$

Here, ϕ is the filling factor, $N_{\rm H}$ is column density in cm^{-2}, expansion velocity $v_{\rm exp}(1000)$ in the units of 1000 km s^{-1}, and $t_{\rm on}$ is the SSS turn-on time.

3.1 Methods

The ejecta of nova systems has been modelled for several years using spatially resolved nova shell observations combined with spectroscopy. This is carried out to understand the temporal evolution of the physical conditions in the nova ejecta. It also helps in understanding the nature of the binary system and its environment. Different methods have been adopted since then to carry out the modelling of the ejecta.

3.1.1 Numerical codes

Numerical methods were developed by Hutchings (1972a) to evaluate stellar line profiles and continuum for different geometries where the FORTRAN codes integrate

flux from the surface of a star for various rotation or distortion of the star. The code integrated the flux from each visible sector, with a limb-darkening factor depending on the angle between the normal to the surface and the line-of-sight of a sphere.

Another numerical code developed was by Gill & O'Brien (1999) where the optically thin emission line profiles of CN ejecta were evaluated. It was determined by producing a velocity cube with one dimension being the plane of the sky while other velocity along the line-of-sight. The one-dimensional spectral line profile was obtained by collapsing this cube in the spatial direction.

3.1.2 Radiative-transfer codes

A radiative-transfer code PHOENIX[1] was developed by Peter Hauschildt. It solves for the special relativistic equation of radiative transfer in the Lagrangian frame self-consistently with the multilevel, non-local thermodynamic equilibrium (NLTE) rate equations and the special relativistic radiative equilibrium equation in the Lagrangian frame. It generates atmospheric models for many astrophysical objects resulting in suitable atmospheres and spectra for objects.

The code RAINY 3D is used to obtain 3D models of nova ejecta. It utilizes 13.04 version of CLOUDY to solve matter–radiation interaction, including thermal and statistical equilibria, ionization and neutralization balances, heating and cooling processes and NLTE populations. At the same time, the code generates a 3D geometry of gas distribution and mass distribution in the shell.

The modelling of the nova ejecta is not a straightforward problem due to unavailability of extensive spatially resolved images of the shell. Hence, it is necessary to have codes that can be used to extract enough information from only the spectroscopic observational data (emission line profiles). This chapter will deal with the methodology used to model the ejecta of different novae. The spectral evolution of novae clearly shows that there is a change in ionization parameters with time due to the change in physical conditions of the environment. To understand the evolution of the physical conditions such as density and chemical abundances of the ejecta and

[1] https://www.physik.uni-hamburg.de/en/hs/group-hauschildt/research/phoenix.html

luminosity and temperature of the central source, plasma simulation code CLOUDY is adopted. The code pyCloudy generates pseudo-3D modelling of the ejecta that gives a better picture of the spatial distribution of the elemental lines present in the observed spectrum. Also, SHAPE is used to obtain the 3D morphology of the ejecta using line profiles. These particular codes were adopted because of the reasons such as the need for a necessary code to understand the physical nature of the systems, publicly accessibility of the code and less complexity in user programming.

3.2 Spectral synthesis and plasma simulation code

3.2.1 CLOUDY

CLOUDY is a spectral synthesis and plasma simulation code developed by Gary J. Ferland in 1978 to predict an astrophysical environment. It is designed to predict physical conditions within the region of interest right from inter-galactic medium to high-density regions. The versions C17.00, and C17.01 were used for this study and details of the code can be found in Ferland et al. (2017). It predicts the thermal, ionization and chemical structure given certain physical conditions, and also predicts its observed spectrum. Any environment is usually prone to different processes resulting in its dilute gas being heated and ionized by the radiation field striking the gas. Using this code, predicting the physical conditions across the region of interest will result in the synthetic spectrum that is consistent with the observed spectrum. The spectra are predicted mainly by the shape and intensity of the external radiation field encountering the cloud of gas; the chemical composition and grain content of the gas; and the geometry of the gas with its radial extent and radial dependence of density. The calculations in this simulation code take into account of several ionization processes such as photo, Auger, collisional-radiative and recombination ones.

Several parameters are used in CLOUDY to define the initial physical conditions of the source and the ejected shell. The parameters include the shape and intensity of the external radiation field striking a cloud of gas, the chemical composition of the gas, and the geometry of the gas with the defined radial extent and density

dependence on the radius. The code generates a predicted spectrum using these input parameters by solving the equations of thermal and statistical equilibrium from NLTE, illuminated gas clouds. The density, radii, geometry, distance, covering factor, filling factor, and elemental abundances define the physical conditions of the shell.

The geometry of the shell is assumed to be a spherically symmetric, expanding one illuminated by the central source.

Ionizing source

1. Early to the nebular phase of novae: A central ionizing source is defined by the brightness of the radiation field, luminosity, and a blackbody. The central source radiates the light onto 4π sr with a blackbody of certain effective temperature.

2. Quiescence phase of novae: A central ionizing source is defined by the brightness of the radiation field, luminosity, and multi-colour blackbody. A cylindrical accretion disk with a particular disk temperature along with a continuum being a blackbody with effective temperature are defined.

3. Special cases: In few systems, there is a presence of coronal emission lines that are due to the shock heated plasma. In such systems, an extra component is considered. The central ionizing source is defined by the brightness of the radiation field, luminosity, and a blackbody. The light is radiated by the central source into 4π sr with a blackbody of certain effective temperature. The other component is a cloud of gas that is heated by the shock of certain velocity (turbulent) leading to a collisionally ionized gas with certain kinetic temperature.

Nova shell

The density of a nova shell is defined by the hydrogen density obtained from the observed spectrum. The filling factor (fraction of the total volume occupied by

clumps) is set such that the hydrogen density is the density within regions containing gas, and the surrounding regions are assumed to be vacuum. The density and filling factor vary radially as

$$\begin{aligned} n(r) &= n(r_{\rm in})(\frac{r}{r_{\rm in}})^{\alpha} \\ f(r) &= f(r_{\rm in})(\frac{r}{r_{\rm in}})^{\beta}, \end{aligned} \tag{3.8}$$

where r_{in} is the inner radius, and α and β are exponents of power laws, here β=0 and $\alpha = -3$ for a shell undergoing ballistic expansion. The density profile is assumed to be dependent on the radius as r^{-3}. It is assumed that the nova atmosphere is undergoing steady mass-loss rate (Bath & Shaviv, 1976) and follows linear velocity law (Schwarz, 2002). The hydrogen density is estimated from the observed spectrum using Eqn. 3.4. The inner and outer radii define the extent of the shell. These values are determined using the minimum and maximum velocities obtained from the FWHM of the emission lines identified in the observed spectrum.

$$r_{\rm out} = v_{\rm max} \times t \tag{3.9}$$

$$r_{\rm in} = v_{\rm min} \times t \tag{3.10}$$

where, t is the time since discovery/outburst, $r_{\rm out}$ is the outer radius, $r_{\rm in}$ is the inner radius, $v_{\rm max}$ and $v_{\rm min}$ is the maximum and minimum velocity respectively. The covering factor (fraction of 4π sr covered by gas as viewed from central source) is defined for all the components such that the sum is always equal to one. The abundance values are defined approximately based on the elemental lines present in the observed spectrum.

Multi-component models are used to reproduce synthetic spectra of different novae. This is due to different ionization states and processes present in a single spectrum of a given nova. Hence, for all novae, more than one density region such as clump and diffuse are assumed to fit all the lines and continuum of the observed spectrum. The covering factor is defined in all the regions such that the sum is always equal to one. All the parameters are of the same values in both the regions

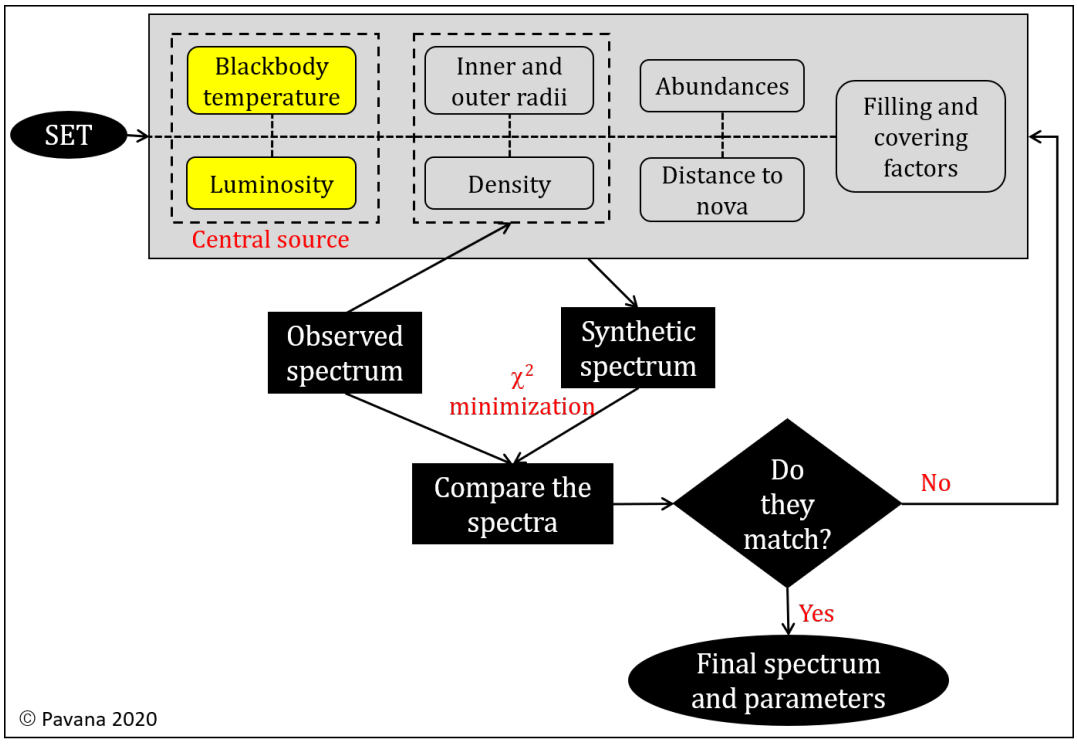

Figure 3.1: Flow of the steps involved in carrying out the modelling of the nova ejecta using the plasma simulation code, CLOUDY to obtain the synthetic spectrum.

except for hydrogen density and covering factor so that the number of free parameters is less in the model. Modelled line ratios were obtained by adding line ratios of each region after multiplying by its covering factor.

Several spectra are generated to obtain the best-fit one for each epoch by varying the free parameters like hydrogen density, effective blackbody temperature, and abundances of the elements simultaneously in all the components (Fig. 3.1). The best-fit model was obtained by calculating χ^2 and reduced χ^2:

$$\chi^2 = \sum_{i=1}^{n} \frac{(M_i - O_i)^2}{\sigma_i^2}$$
$$\chi^2_{\rm red} = \frac{\chi^2}{\nu,} \tag{3.11}$$

where $M_{\rm i}$ and $O_{\rm i}$ are the modelled and observed line ratios, σ_i is the error in observed flux ratio, n is the number of observed lines, $n_{\rm p}$ is the number of free parameters, and $\nu = n - n_{\rm p}$ are the degrees of freedom.

The ejected mass was determined using the relation (e.g. Schwarz et al. 2001;

Schwarz 2002; Schwarz et al. 2007a; Vanlandingham et al. 2005; Helton et al. 2010; Das & Mondal 2015; Mondal et al. 2018; Raj et al. 2018; Pavana et al. 2019a, and Pavana et al. 2020)

$$M_{\rm shell} = n(r_0) f(r_0) \int_{r_{\rm in}}^{r_{\rm out}} (\frac{r}{r_0})^{\alpha+\beta} 4\pi r^2 dr. \tag{3.12}$$

The ejected mass was calculated for all the regions, then multiplied by the corresponding covering factors and added to obtain the final value. The abundance values and other parameters are derived from the model. The abundance solutions are sensitive to changing opacity and physical conditions of the ejecta such as temperature.

3.2.2 pyCloudy

The code pyCloudy by Morisset (2013) consists of CLOUDY and a Python library which has routines for analyzing the models. The Python library consists of different routines to visualize the 1D models obtained from CLOUDY and integrating the emissivity of these models. This method is used to obtain pseudo-3D structure rather than full 3D as it is limited to modelling in axial- and point-symmetric objects. Also, CLOUDY is 1D, and the effect of the diffuse radiation field is not considered completely. The interpolation also introduces further uncertainties. However, computationally this is a faster code, and the current work explores the fitting of the data with these pseudo-3D models.

pyCloudy generates a series of 1D CLOUDY models which represent a structure of nova system at many different radial directions. Each 1D model is nothing but a spherically expanding symmetric nova shell which is composed of an inner region extending from the centre to specified inner radius followed by the shell at density varying as $1/r^3$ terminating at specified outer radius or the ionization boundary. From these, 1D grids of line emissivities and electron temperatures are produced. The 1D model is generated at a particular radial direction which is inclined to the equatorial plane at a specified angle with varying inner and outer radii. The angles

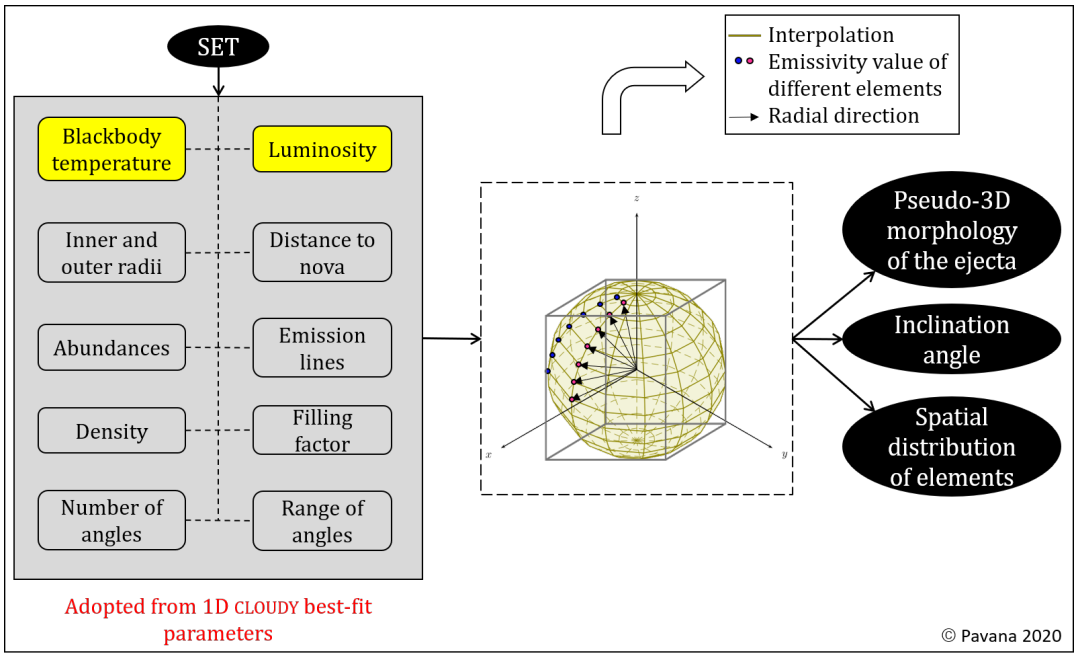

Figure 3.2: Flow of the steps followed to obtain 3D morphology of the nova ejecta using the pyCloudy code.

vary from 0° [equator] to 90° [symmetry axis] and are different for each model. Based on the computational time, six to eight different angles were used.

The 1D spatial distributions are re-connected in the XZ cross-section of the 3D cube. Only one quadrant of the plane is filled as the space between these 1D lines is filled in by standard linear interpolation of Python. The rest of the quadrants are filled by the symmetry conditions over the horizontal symmetry axis. Different routines are used to compute the full cube projection onto the sky plane. The sky plane is defined by the angle of inclination between the line-of-sight and the symmetry axis. The velocity field is established such that the velocity values are pointed radially with respect to the central source, and it depends on the radial distance from the centre. The velocity line profiles are obtained by integrating the particular line-of-sight through the cube, at any position within the projected image. By rotating the 3D cube of emissivities, a corresponding projected image is obtained at the sky plane. The line profile that is obtained corresponding to this image is verified to see if it is consistent with the observed profile. This gives the inclination angle of the system. Here, the inclination angle is the angle between the plane of the sky and the orbital plane.

The best-fit parameters from the 1D CLOUDY results were adopted as input parameters for this code (Fig. 3.2). The parameters such as density, inner and outer radii, luminosity, effective temperature and chemical abundances were adopted. An axisymmetric spheroid was assumed to be the initial structure of the cloud. Six to eight 1D CLOUDY runs along different radial directions were considered to build the 3D cube. Here, the parameters such as density, effective temperature, inner and outer radii of the cloud were varied across the six or eight directions. At the same time, the chemical abundance values, luminosity, distance to the nova were kept constant. The range of the effective blackbody temperature in these runs was within the error values obtained in 1D results unless another ionizing source (See Sec. 3.2.1) with different temperature was present. The emissivity values of every element were interpolated to obtain the 3D emissivity values for each element. The resulting image obtained was the 3D morphology of the ejecta at a particular epoch of the system.

3.3 Morphokinematic analysis

Morphokinematic application, SHAPE (Steffen et al., 2011) was used to analyze and understand the morphokinematic geometry of the nova ejecta using velocity profiles. SHAPE is a morphokinematic tool that can be used to construct 3D models and compared with the data available. These 3D structures result in position-position diagrams, position-velocity diagrams, and one-dimensional spectral lines. Analysis of the velocity profiles of the emission features using this method provides information about the inclination angle, position angle and geometrical structure of the nova ejecta. The interpretation of observational data, either the image of the astrophysical object or its spectrum, plays an essential role in this analysis. An ideal case for using this analysis would be to use observational data of an image of an object along with the spectrum of the object, however, in this study only the spectrum of the object was used.

The structure of the ejecta corresponding to a particular elemental line profile for a particular epoch was considered. It was initially assumed to be in the form of

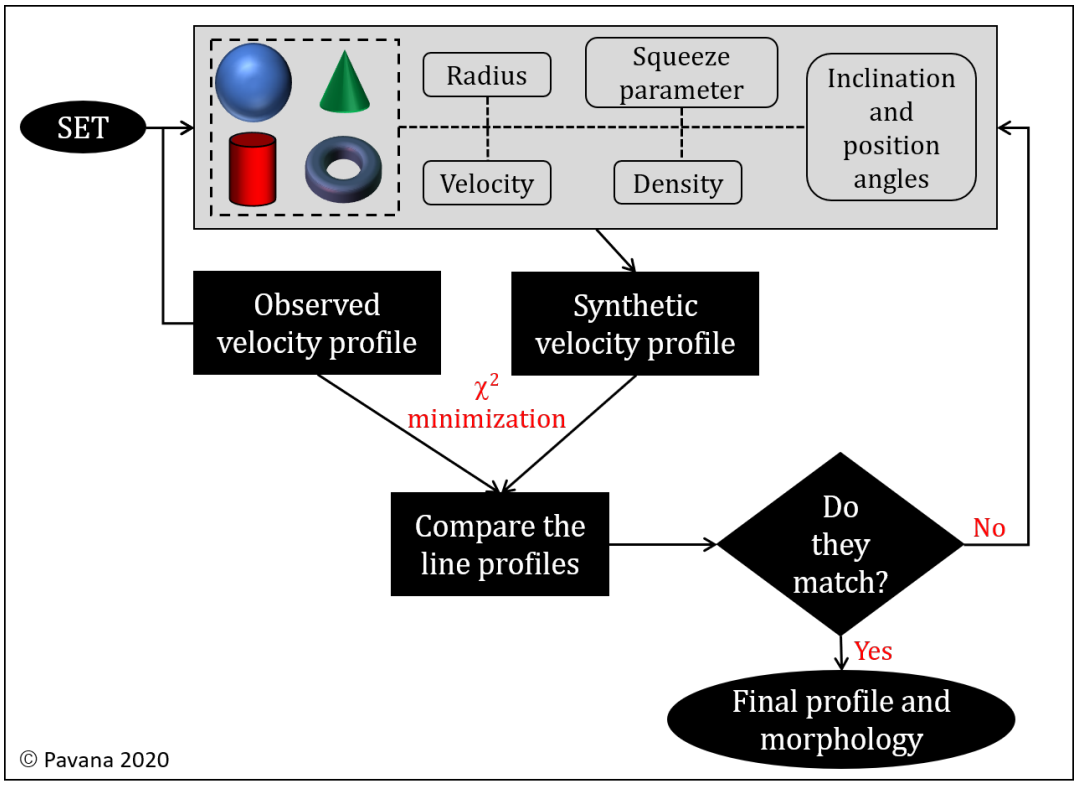

Figure 3.3: Flow of the steps involved in obtaining the 3D morphology of the nova ejecta using the morphokinematic application, SHAPE.

spheroidal (or cylindrical or conical) shell with (or without) equatorial rings (Fig. 3.3). The initial components of the nova shell were defined based on the studies of nova shell models in the literature, such as Hutchings (1972b) and Gill & O'Brien (1999), and also by trial and error basis with known complex line profiles. All the components were defined with necessary parameters such as temperature, density, radius and velocity. For some components, the squeeze parameter for the components such as a sphere or cone or cylinder was also defined when necessary. The squeeze parameter is nothing but the degree of shaping, and it refers to the ratio between the major and minor axis. The radius of all the components was defined using the FWHM of the observed emission line profiles and time since outburst. The initial density values were calculated using the observed fluxes of the emission lines and initial velocity using the FWHM of the emission line. The density was assumed to be varying with the radius as r^{-3} similar to that assumed in analysis using CLOUDY, and the ejecta follows the linear velocity law (See Sec. 3.2.1 for details). The temperature was kept constant throughout the shell. These parameters were defined for

the initial structure of the ejecta. The inclination angle for the system was varied from 0° (face-on) to 90° (edge-on). This structure resulted in the corresponding 1D line profile. The synthetic line profile was compared with the observed line profile visually in the initial stages. In the successive iterations, the values in the temperature, squeeze modifier, inclination and position angles were varied until the best-fit profile was obtained. This best-fit synthetic profile was derived using Eqn. 3.11. The 3D morphology obtained corresponding to that of the best-fit synthetic profile was the final 3D morphology of the ejecta at that particular epoch and for a particular elemental line.

The 3D morphology of the nova ejecta on that particular epoch can be obtained by modelling in a similar way for all the line profiles present. However, as hydrogen is the most abundant element in the system, in a few novae only Hα line profile was modelled.

3.4 Summary

To understand the physical characteristics and morphology of the ejecta, the aforementioned codes were used extensively in this work. It is important to note that many codes are available and utilized in the literature to understand the physical conditions of nova atmospheres and its shell geometry. In this study, the codes were chosen such that they are easily accessible, applicable to the study of nova ejecta and less complexity in programming for the user.

The spectral synthesis and plasma simulation code CLOUDY and the radiative-transfer code PHOENIX can both be used to generate 1D and 3D NLTE models of nova ejecta. However, CLOUDY is used in this work to reproduce emission line spectra of different novae. This code determines the physical conditions of the nova system such as effective blackbody temperature and luminosity of the central ionizing source, shell radius, density (clump and diffuse) and chemical abundances, which help in understanding the properties of the system. It was also used to understand the evolution of these physical conditions in few novae as the system evolves.

The 3D code pyCloudy was then used to obtain the pseudo-3D morphology of the nova ejecta and also the inclination of the systems. It was also used to understand the evolution in the morphology of the ejecta as the system evolves. This code involves the interpolation of the emissivity values of every element at given radial directions to form the 3D morphology. However, due to the limitation of this code that it is restricted to symmetric geometries, a morpho-kinematic application SHAPE is adopted to understand the asymmetry in the system, if any. This code also gives the 3D morphology of the nova ejecta; but, this focuses more on the density and velocity distribution of individual structures present in the morphology of a single emission line profile at a time.

4

"Fe II" class of novae

The gas ejected in the novae can happen via discrete shell ejection (He/N spectrum) and/or a continuous ejection (Fe II spectrum). These two components are regions of emission line formation with the WD remnant supplying energy for photoionization of the ejecta (Pottasch, 1959). The emission components that originate from these components can be distinguished based on the shape of the line profiles (Williams, 1992). The line profiles that are produced in the emission from gaseous shell during the optically thin and uniform expansion is rectangular with the flat top extending either side of line centre to the wavelengths corresponding to the ejecta velocity (Beals, 1931). The origin of these are suggested to be due to the high velocity of the gas and the episodic ejection (Williams, 2012). The line profiles due to the continuous ejection are narrow P-Cygni during the optical thick phase and round peaked, broader during the optical thin phase. The origin of these spectra is attributed to the envelope of gas with solar-like abundances coming from the secondary rather than WD because of the following reasons: a) strength of the heavy elements, b) narrow line widths equivalent to the escape velocities in late-type stars and c) P-Cygni profiles similar to that of a stellar wind (Williams, 2012).

Based on the prominent non-Balmer lines (Fe II or He and N) present in the spectra obtained during the decline immediately after the maximum phase of novae, they are classified into mainly into Fe II and He/N types (Williams, 2012). The

prominent non-Balmer lines in the early decline phase of the Fe II class of novae are Fe II lines. The spectra consist of several low excitations collisionally excited Fe II lines and CNO lines due to recombination and fluorescence scattering. These novae evolve slowly over a timescale of weeks with the early nebular spectra having dominant low ionization auroral lines. The dominant ejection in these novae based on the line profiles obtained is usually known to be wind ejection. In this chapter, the analysis of nine Fe II class of novae are discussed. The temporal evolution of spectra of two novae are presented in detail, and the morphology of the ejecta obtained for all the novae are presented.

Some novae were modelled using the spectral synthesis and plasma simulation code CLOUDY to understand the physical conditions of the system such as source luminosity, effective temperature, density and elemental abundances. To obtain the morphology of the ejecta of all the novae, pyCloudy and/or SHAPE was used.

4.1 V2362 Cyg

V2362 Cyg (Nova Cyg 2006) was discovered on 2006 April 2.807 UT by Nakano et al. (2006). It had a light curve similar to that of V1493 Aql ('C class' in Strope et al. (2010)). The nova went through a secondary brightening after an early decline. It was a fast nova with $t_2(V) = 10.5 \pm 0.5$ days before the rebrightening. This rebrightening started around 100 days and increased till 240 days, followed by a decline (Arai et al., 2010). The optical spectrum obtained by Yamaoka et al. (2006) on day 3 consist of Hα in P-Cygni, and other lines being absorption ones. On day 7, the spectrum obtained by Siviero et al. (2006) consist of prominent Fe II multiplets and lines such as hydrogen Balmer, Na I and [O I] lines were present, with FWZI of Hα and Hβ being 3750 and 1800 km s^{-1}. On day 73, the NIR spectrum obtained by Mazuk et al. (2006) showed low excitation emission lines such as Fe II, C I, N I and O I. The optical spectrum showed presence of forbidden lines like [O I], [O II] and [N II]. There was no evidence of dust in the ejecta on this day. The NIR spectrum obtained on day 242 by Rayner et al. (2006) around the peak of secondary maximum

showed the presence of strong emission lines of C, N, O and Fe without any higher excitation lines present previously with no sign of dust formation. On day 262, there was a drastic change in the NIR spectrum with the presence of narrow lines and increase in ionization level with the emergence of He II lines. The spectrum also showed the evidence for formation of hot dust. Also, the fast decline in the optical light curve from secondary maximum was attributed to the dust formation by Rayner et al. (2006). During the decline from the secondary maximum, the optical spectra underwent rapid changes (Kimeswenger et al., 2006). They were initially dominated by Hα, O I, N II and [N II] lines and later by hydrogen Balmer and [N II] lines. X-ray emission was detected from *Swift* by Ness et al. (2006a) on day 195 and the X-ray spectrum did not show any SSS emission and was found to harder than the supersoft source on day 233 (Ness et al., 2006b). The XMM-Newton X-ray spectrum on day 400 was fit by a two-temperature (at 0.2 keV and 2.3 keV) thermal plasma model by Hernanz et al. (2007). The photo-ionization analysis of the optical spectrum obtained on day 293 (Munari et al., 2008) showed overabundance of nitrogen and oxygen in the ejecta compared to solar abundance values with ejected mass of the order of 10^{-4} $M_{\odot}$. The evolution of the line profiles in the early phase to the nebular phase spectra indicate the presence of asymmetry in the eruption (Poggiani, 2009).

From the multi-wavelength analysis of this nova, Lynch et al. (2008) concluded that it went through secondary ejection that moved faster than the first one with line widths increasing three times as the optical light curve proceeded towards its maximum just before the dust formation. Coincident with the rebrightening, the spectrum changed from that of an early nebular phase to a post-maximum phase with low excitation lines. The peak in the *Swift* XRT light curve was observed about 100 days after the dust formation. SSS spectrum was not seen throughout the X-ray observations from day 194 to 484. Also, the X-ray flux remained unaffected by the formation of dust. Lynch et al. (2008) suggested that the dust formation was a consequence of the interaction of the expanding shell of the second ejection with the first one.

Low resolution spectroscopic observational log for V2362 Cyg is given in Table

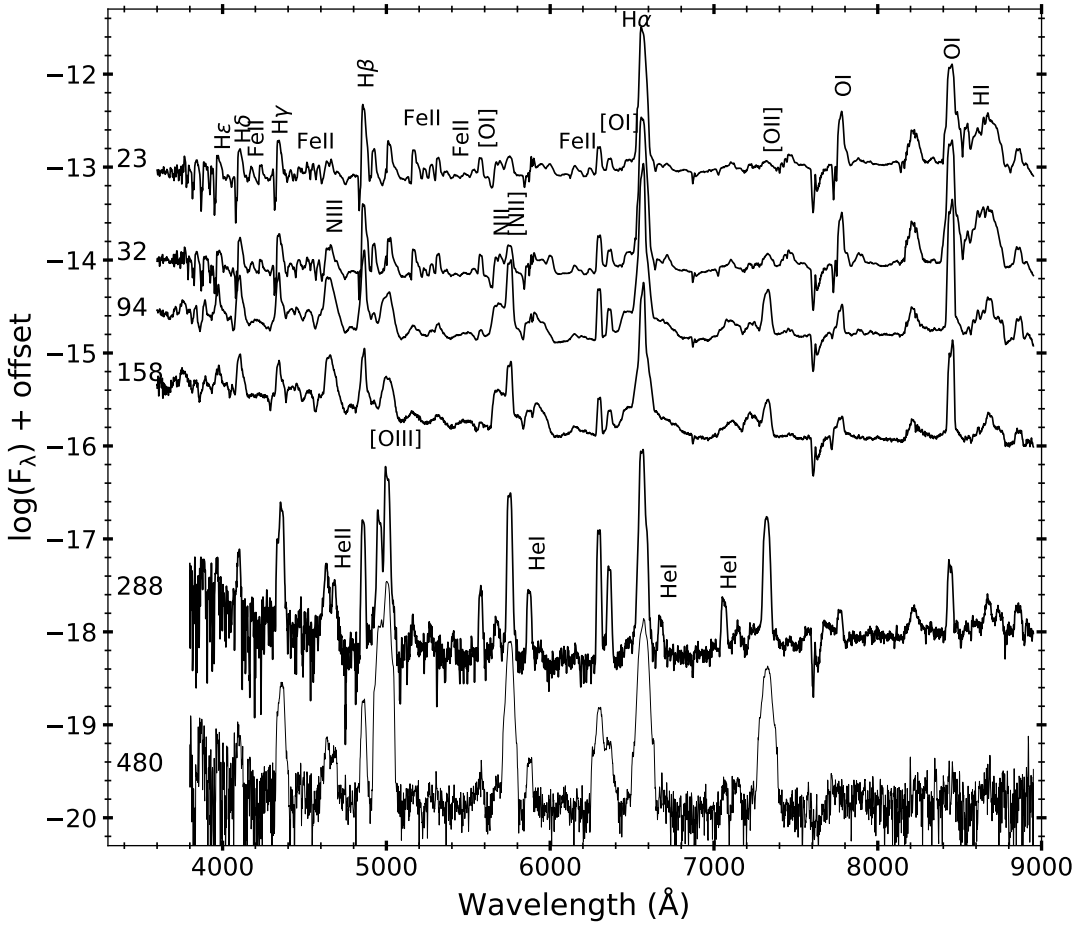

Figure 4.1: Evolution of the spectra from decline phase to nebular phase of V2362 Cyg from 24 Apr 2006 (day 23) to 25 Jul 2007 (day 480). The identified lines and time since discovery in days (numbers to the left) are marked.

4.1. The optical spectra obtained from day 23 to day 480 since discovery are as shown in Fig. 4.1. The spectrum consists of hydrogen Balmer, Fe II, [O I], O I and hydrogen Paschen lines till day 158. The N II (5679 Å) and [N II] lines are seen from day 32. The prominent non-Balmer emission is from the O I 8446 Å line. As the system evolves and the ejecta becomes optically thin, there is appearance of high ionization lines such as [O III], He I and He II. The prominent non-Balmer

Table 4.1: Spectroscopic observational log for V2362 Cyg

Date	**t (days)**	**Resolution**	**Coverage (Å)**	**Telescope**
24 Apr 2006	23	1300, 2200	3800–8800	HCT-HFOSC
03 May 2006	32	1300, 2200	3800–8800	HCT-HFOSC
04 Jul 2006	94	1300, 2200	3800–8800	HCT-HFOSC
06 Sep 2006	158	1300, 2200	3800–8800	HCT-HFOSC
14 Jan 2007	288	1300, 2200	3800–8800	HCT-HFOSC
25 Jul 2007	480	1300, 2200	3800–8800	HCT-HFOSC

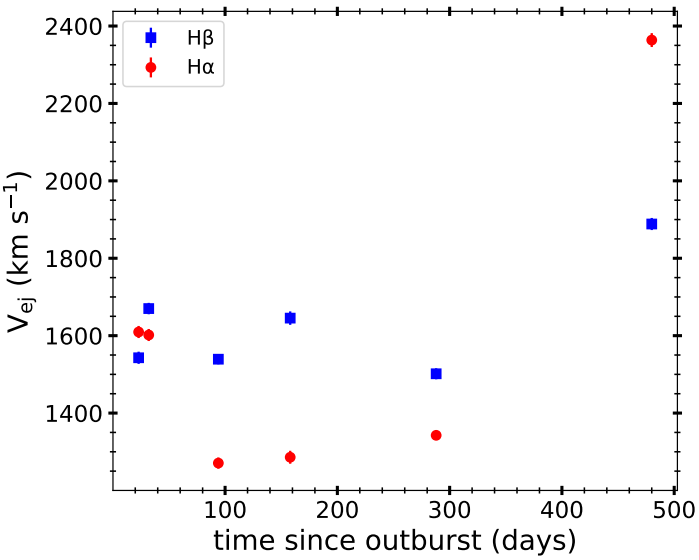

Figure 4.2: Evolution of Hα and Hβ FWHM velocities of V2362 Cyg from 24 Apr 2006 (day 23) to 25 Jul 2007 (day 480).

emission in the nebular phase is from the forbidden [O III] lines. The line profiles are initially P-Cygni with narrow sharp absorption component and round peaked emission component. They evolve slowly into broad round peaked and become more structured as the system evolves.

The evolution of observed FWHM velocities of Hα and Hβ lines are as shown in Fig. 4.2. The FWHM velocities of Hβ is around 1500–1600 km s^{-1} from day 23 to 288 and when the profiles become broader in the nebular phase, the velocity increases to around 1900 km s^{-1}. The FWHM velocities of Hα is initially around 1600 km s^{-1} and decreases to 1200 km s^{-1} on day 94 and slowly increase till day 288 upto 1400 km s^{-1}. On day 480, the velocity is of the order of 2400 km s^{-1}.

The optical depth τ of the ejecta for [O I] 6300 Å using the equation 3.2, and the electron temperature T_e using the equation 3.3 is as shown in Fig. 4.3. The temperature decreases initially by 2000 K and then slowly increases with time. The optical depth decreases with time.

Low resolution spectrum obtained on day 480 was used to carry out the analysis using CLOUDY to understand the physical conditions of the system. Day 480 was used as we expect the spectrum to contain signatures of both primary and secondary shell ejection. The central ionizing source was set to be at an effective temperature of 10^5 K and luminosity 10^{37} erg s^{-1}. To model the observed spectrum, the medium

was assumed to consist of a low-density diffuse component and a clump component. Most of the lines were fitted by the clump component, except a few lines like [N II] (5755 Å) and [O III]. To fit all the lines, a diffuse region (low-density) was used, covering 25% of the volume. The clump hydrogen density was 4.47 $\times$ 10^7 cm^{-3} and diffuse hydrogen density 1.78 $\times$ 10^7 cm^{-3}. The relative fluxes of the observed lines, the best-fit model predicted lines, and corresponding χ^2 values are given in Table 4.2. The values of best-fit parameters obtained from the model are given in Table 4.3. The estimated abundance values show that helium, nitrogen, oxygen, calcium and iron are over-abundant compared to solar, while other elements have the solar abundance values. The best-fit synthetic spectrum plotted over the observed spectrum is as shown in *right* panel of Fig. 4.4.

The morphology of the ejecta using pyCloudy was found to be bipolar frustum of prolate spheroid, conical with equatorial rings (*left* panel of Fig. 4.4). The hydrogen Balmer emission was coming from all the regions, the [O I] and [O III] emission from the equatorial rings. The bipolar frustum of prolate spheroid was formed due to [N II] emission. The He II (4686 Å) and He I lines are coming from the inner conical structures. The inclination angle of the system was estimated to be 48° $\pm$ 1.15°. The details on the extent of all the components and their distance from central

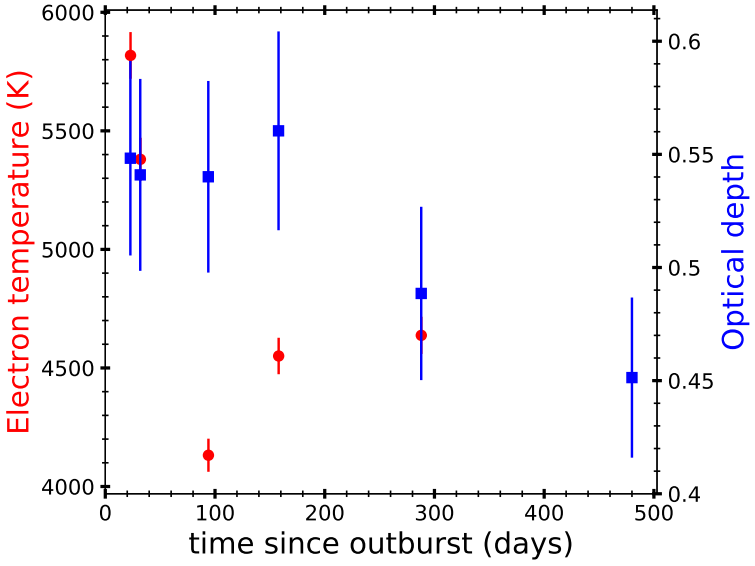

Figure 4.3: Evolution of optical depth for [O I] (6300) and electron temperature of the ejecta of V2362 Cyg from 24 Apr 2006 (day 23) to 25 Jul 2007 (day 480).

Table 4.2: Observed and best-fit CLOUDY model line flux ratios[a] for day 480 of V2362 Cyg

Line ID	λ (Å)	**Observed**	**Modelled**	χ^2
H I	3889	8.54E-01	7.18E-01	6.88E-01
H I	4102	7.32E-01	4.35E-01	1.65E+00
H I	4340	2.68E+00	2.93E+00	1.42E+00
He I	4471	9.22E-02	1.54E-01	6.90E-02
N III	4638	3.01E-01	1.54E-01	7.99E-01
He II	4686	5.52E-02	1.31E-01	3.09E-01
H I	4861	1.00E+00	1.00E+00	0.00E+00
[O III]	4959	7.59E+00	7.56E+00	3.62E-02
[O III]	5007	2.45E+01	2.43E+01	2.90E+00
[N II]	5755	4.36E+00	4.21E+00	1.28E+00
He I	5876	5.12E-02	1.35E-01	5.34E-01
[O I]	6300	6.34E-01	2.82E-01	2.91E+00
[O I]	6363	1.46E-01	4.44E-01	1.62E+00
H I	6563	7.70E+00	7.54E+00	7.03E-01
He I	6678	1.11E-01	6.81E-02	2.78E-02
He I	7065	1.05E-01	1.14E-01	3.41E-02
[O II]	7320	1.40E+00	1.44E+00	4.20E-02

[a] Relative to Hβ

Table 4.3: Best-fit 1D CLOUDY model parameters on day 480 for V2362 Cyg

Parameter	**Day 480**
T_{BB} ($\times 10^5$ K)	2.10 $\pm$ 0.08
Luminosity ($\times 10^{37}$ erg s^{-1})	1.00 $\pm$ 0.13
Clump Hydrogen density ($\times 10^7$ cm^{-3})	4.47
Diffuse Hydrogen density ($\times 10^7$ cm^{-3})	1.78
Covering factor (clump)	0.75
Covering factor (diffuse)	0.25
α	-3.00
Inner radius ($\times 10^{15}$ cm)	5.49
Outer radius ($\times 10^{16}$ cm)	1.86
Filling factor	0.10
N/N$_\odot$	2.78 $\pm$ 0.11 (2)[a]
O/O$_\odot$	4.03 $\pm$ 0.09 (5)
He/He$_\odot$	1.31 $\pm$ 0.14 (4)
Ejected mass ($\times 10^{-6}$ M$_\odot$)	8.08
Number of observed lines (n)	17
Number of free parameters (n_p)	6
Degrees of freedom (ν)	11
Total χ^2	15.02
χ^2_{red}	1.37

[a]The number in the parenthesis was the number of lines used to determine abundance estimate.

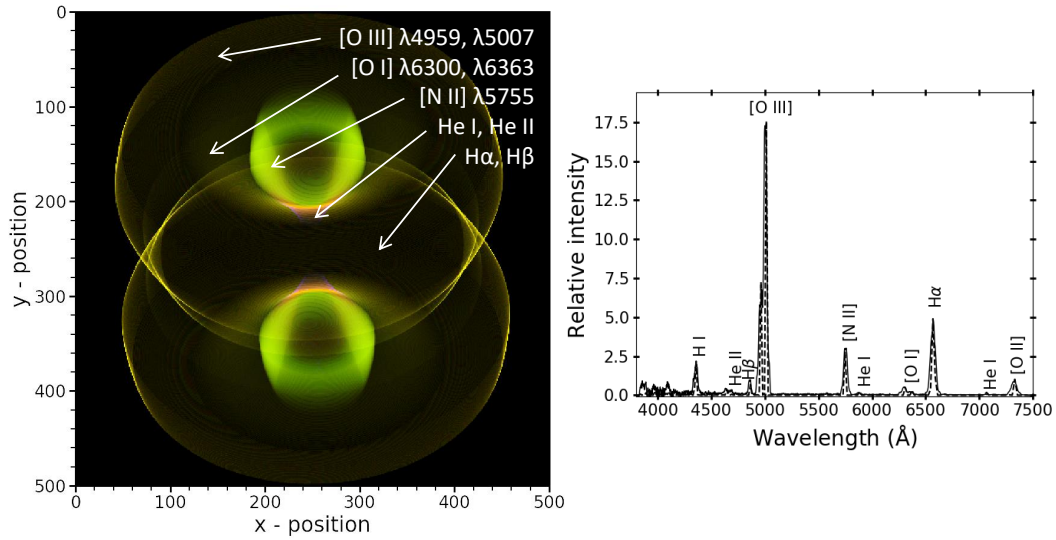

Figure 4.4: *Left:* Morphology of the ejecta of V2362 Cyg obtained on day 480 using the optical spectrum in the two-dimensional plane with X-axis being the line-of-sight direction and Y being the axis perpendicular to that of the plane of sky and line-of-sight. The lines corresponding to different colours are marked to show the spatial distribution of emission in the structure. Here, 1 unit of x and y correspond to 1.86×10^{13} cm. *Right:* Best-fit modelled spectrum (dash line) obtained using CLOUDY overplotted on the observed optical spectrum (continuous line).

source in the morphology of the ejecta are given in Table 4.4.

The origin of the forbidden lines such as [O III] and [N II] was found to be from the outer regions implying that they are coming from the optically thin expanding shell (Table 4.4). The distribution of the helium lines in the morphology suggests that they are coming from the inner regions (Table 4.4). The frictional interaction between the multiple ejecta might have resulted in the formation of a spheroidal frustum for the [N II] structure.

Table 4.4: Details of the morphology of the ejecta on day 480 for V2362 Cyg

Component	**Extent**[a] **($\times 10^{14}$ cm)**	**Radius ($\times 10^{14}$ cm)**	**Distance**[b] **($\times 10^{14}$ cm)**	**Angle**[c] **(°)**
Cone	5.21 ± 0.12	9.30 ± 0.19	1.49 ± 0.09	69 ± 1.12
Spheroidal frustum	23.8 ± 0.18	-	9.30 ± 0.15	-
Equatorial ring	-	28.3 ± 0.24	20.1 ± 0.21	-

[a]Extent of the component along the ejecta axis

[b]Distance from the central source to the component along the ejecta axis

[c]Outer opening angle of the cone

4.2 V5587 Sgr

V5587 Sgr (Nova Sgr 2011 No. 1) was discovered on 2011 Jan 25.86 UT by Nishimura (Nakano et al., 2011). It was classified as a classical nova based on the low resolution optical spectrum by Arai & Imamura (2011). The optical light curve of the system belongs to 'J class' of novae (Strope et al., 2010) with maximum at day 9 since discovery and $t_2(V) = 12$ days, $t_3(V) = 108$ days and reddening value, $E(B-V)$ = 0.85–1.26. The nova spectrum exhibited Hα, Hβ, He I, He II, N II, [N II], O I, [O I], [O II] and Fe II emission lines and in the nebular phase, the forbidden lines such as [O III] lines developed (Kajikawa et al., 2015).

Low resolution optical spectrum obtained from HCT-HFOSC on 06 Jun 2011 (day 132) consists of Hα, Hβ, He I, Fe II, [O I], [O II], N II and [N II] emission lines. The emission lines were found to round-peaked profiles with FWHM velocity of both Hα and Hβ as $\sim$1500 km s^{-1}. Using the Eqns. 3.2 and 3.3, the optical depth τ of the ejecta for [O I] 6300 Å was calculated and the electron temperature T_e was calculated using the estimated value of τ on day 132. The optical depth τ of the ejecta for [O I] 6300 Å was 0.38 $\pm$ 0.04. The electron temperature T_e calculated using the estimated value of τ was found to be 9185 $\pm$ 181 K. The mass of the WD using the relation by Livio (1992) was found to be 0.82 $\pm$ 0.05 M$_\odot$. The ejected

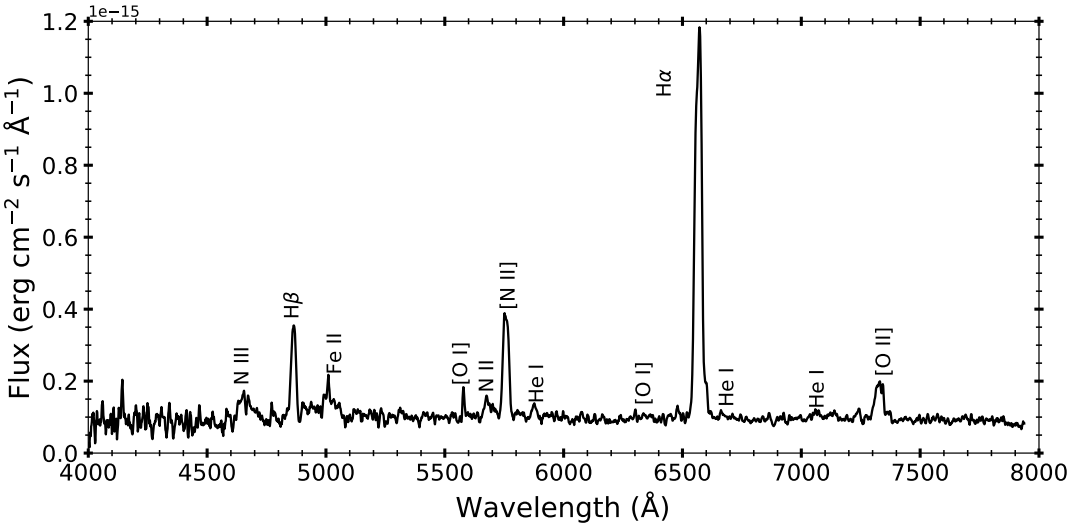

Figure 4.5: Low resolution optical spectrum of V5587 Sgr obtained on 06 June 2011 (day 132). The emission lines present are marked.

mass determined using equation 3.4 was found to be 2.97×10^{-4} $M_{\odot}$.

The morphokinematic analysis using SHAPE was carried out using the Hα observed velocity profile. The synthetic Hα velocity profile for V5587 Sgr was generated using the bipolar conical structures (*left* panel of Fig. 4.6). The base radius of both the conical frustum structures was found to be 2.5×10^{11} m with the opening angles of 39.3° and 49.08° for the top and bottom structures respectively. The tip radii of the top and bottom structures are 9.5×10^{10} m and 4.5×10^{11} m respectively. The bottom structure was found to be 75% less bright than that of the top one. The best-fit velocity profile corresponding to the observed profile is as shown in the *right* panel of Fig. 4.6. The best-fit inclination angle was found to be $54^{\circ} \pm 1.15^{\circ}$. The cones present are distinct shell-like layers with almost symmetric structure. The presence of these cones may be as a consequence of the wind interaction with the secondary (Gill & O'Brien, 1999; O'Brien et al., 1995).

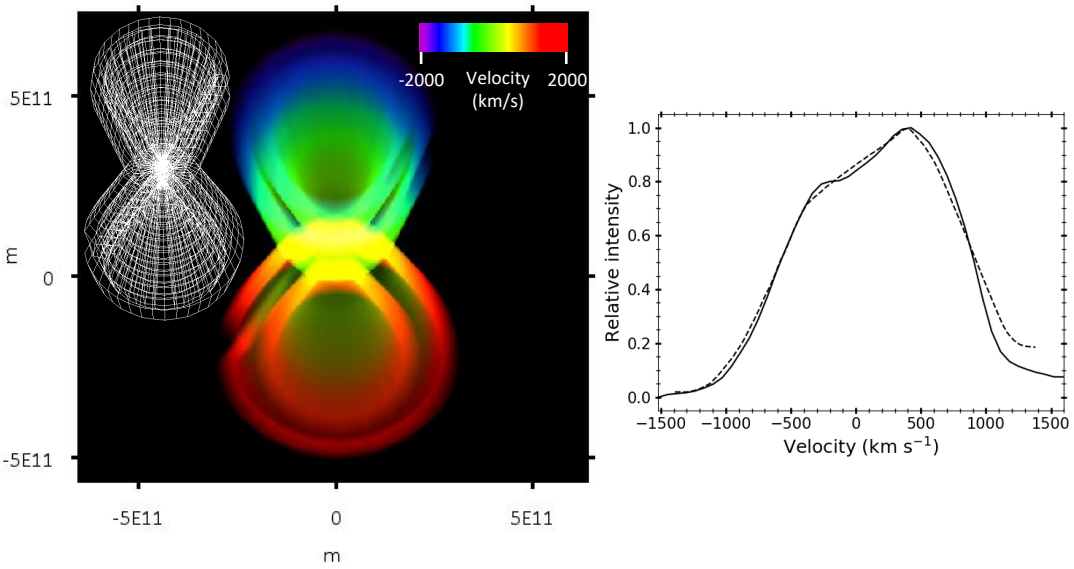

Figure 4.6: *Left:* Morphology of the ejecta of V5587 Sgr obtained on day 132 using Hα velocity profile. It is plotted in the two-dimensional plane with X-axis being the line-of-sight direction and Y being the axis perpendicular to that of the plane of sky and line-of-sight with X and Y axes in meters and Z is velocity (*top-right*) and grid structure (*left*) are shown. *Right:* Best-fit Hα velocity profile (dash line) overplotted on the observed profile (continuous line).

4.3 V2676 Oph

V2676 Oph was discovered on 2012 March 25.789 UT at $V = 12.1$ (Nishimura et al., 2012). The optical spectra indicated that the nova belonged to Fe II spectral class based on the numerous Fe II lines present. The distance to the nova was determined to be between 6.9 and 7.9 kpc by Raj et al. (2017). The nova showed molecule formation and also dust formation during the outburst (Kawakita et al. 2017 Kawakita et al. (2017) and references therein).

A nebular spectrum was obtained on 8 May 2015 (1138) with a resolution of about 3 Å using the COSMOS long-slit spectrograph at CTIO. The spectrum consists of hydrogen Balmer and Paschen, He I, He II and forbidden lines of Ar, S and O with FWHM velocity of Hα being $\sim$2500 km s^{-1}. The optical depth τ of the ejecta for [O I] 6300 Å using the Eq. 3.2 was found to be 0.60 $\pm$ 0.08.

The central ionizing source was set to be at an effective temperature 10^5 K and a total luminosity of 10^{38} erg s^{-1}. To model the observed spectrum, the medium was assumed to consist of a low-density diffuse component and a clump component. Most of the lines were fitted by the clump component, except some high ionization lines. To fit all the lines, a diffuse region (low-density) was used, covering 20% of the volume. The clump hydrogen density was 3.16 $\times$ 10^8 cm^{-3} and diffuse hydrogen density was 10^8 cm^{-3}. The relative fluxes of the observed lines, the best-fit model predicted lines, and corresponding χ^2 values are given in Table 4.5. The values of best-fit parameters obtained from the model are given in Table 4.6. The estimated abundance values show that helium, argon, oxygen and sulphur were over-abundant compared to solar, while other elements had the solar abundance values. The best-fit synthetic spectrum obtained is plotted over the observed spectrum as shown in *right* panel of Fig. 4.7. The optical depth τ of the ejecta for [O I] 6300 Å from CLOUDY was found to be 0.49 and the electron temperature varied from 11237 K in the first zone to 4000 K in the last zone. The ejected mass was found to be consistent with that of the values estimated by Raj et al. (2017).

The geometry of the ionized structure obtained using pyCloudy was found to be bipolar cones with very faint equatorial rings (*left* panel of Fig. 4.7). The hydrogen

Table 4.5: Observed and best-fit CLOUDY model line flux ratios[a] for day 1138 of V2676 Oph

Line ID	λ (μm)	**Observed**	**Modeled**	χ^2
[O I]	0.6300	2.70E-02	7.62E-02	2.51E+00
[O I]	0.6364	1.00E-02	4.13E-02	1.25E+00
H I	0.6563	1.00E+00	1.00E+00	0.00E+00
He I	0.6678	3.06E-03	2.07E-02	6.99E-02
[S II]	0.6716-0.6731	1.09E-02	1.20E-03	1.35E-02
O I	0.7002	5.46E-03	1.05E-02	2.06E-03
He I	0.7065	7.82E-03	1.50E-02	2.43E-02
[Ar III]	0.7134	9.28E-03	3.32E-02	1.07E-01
[Ar IV]	0.7237	6.94E-03	2.20E-02	1.12E-01
He I	0.7281	2.42E-03	7.01E-03	5.06E-03
[O II]	0.7320-0.7330	4.07E-02	1.51E-01	3.69E+00
[Ar III]	0.7751	1.18E-03	7.93E-03	1.24E-01
H I (P10)	0.9015	1.79E-03	1.93E-02	2.11E-01
[S III]	0.9069	1.09E-02	1.16E-02	1.32E-04
H I (P9)	0.9229	4.51E-03	2.42E-02	6.03E-02
[S III]	0.9531	2.96E-02	5.26E-02	1.45E+00
H I (P7)	1.0049	1.55E-03	5.87E-02	2.38E-01
He II	1.0124	1.01E-02	1.01E-03	1.44E-02

[a]Relative to Hα

Table 4.6: Best-fit CLOUDY model parameters on day 1138 for V2676 Oph

Parameter	**Day 1138**
T_{BB} ($\times$ 10^5 K)	1.00 $\pm$ 0.12
Source luminosity ($\times$ 10^{38} erg s^{-1})	1.00 $\pm$ 0.09
Clump Hydrogen density ($\times$ 10^8 cm^{-3})	3.16
Diffuse Hydrogen density ($\times$ 10^8 cm^{-3})	1.00
Covering factor (clump)	0.80
Covering factor (diffuse)	0.20
α	-3.00
Inner radius ($\times$ 10^{15} cm)	3.79
Outer radius ($\times$ 10^{16} cm)	2.34
Filling factor	0.05
$He/He_\odot$	2.14 $\pm$ 0.07 (4)[a]
$Ar/Ar_\odot$	2.37 $\pm$ 0.11 (3)
$O/O_\odot$	6.62 $\pm$ 0.08 (4)
$S/S_\odot$	3.25 $\pm$ 0.10 (3)
Ejected mass ($\times$ 10^{-5} $M_\odot$)	1.42
Number of observed lines (n)	18
Number of free parameters (n_p)	9
Degrees of freedom (ν)	9
Total χ^2	9.87
χ^2_{red}	1.10

[a]The number in the parenthesis refer to number of observed lines used to estimate abundance values

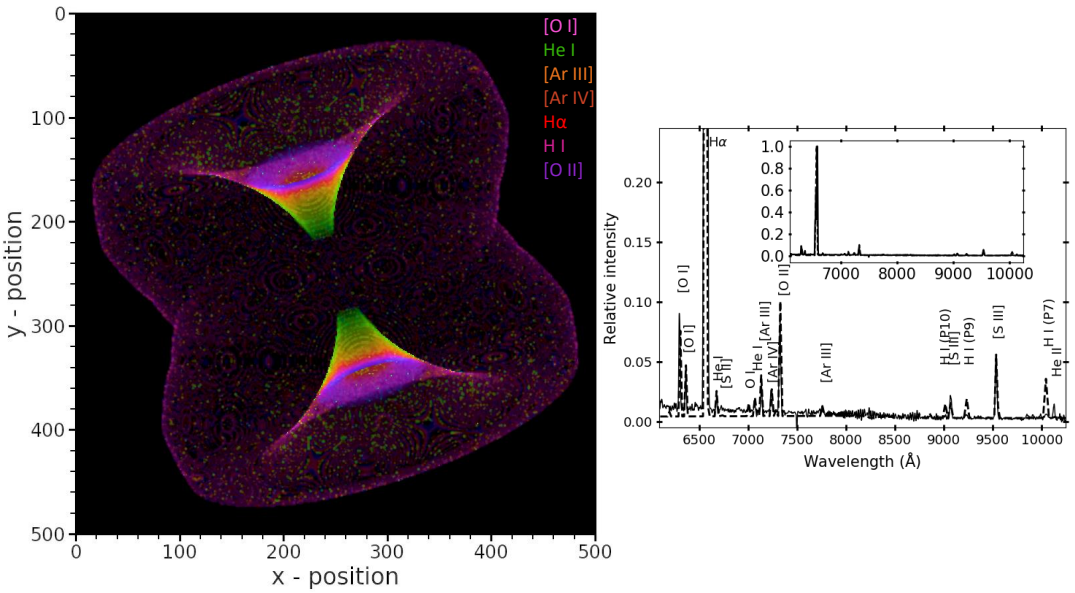

Figure 4.7: *Left:* Morphology of the ejecta of V2676 Oph obtained on day 1138 using the optical spectrum in the two-dimensional plane with X-axis being the line-of-sight direction and Y being the axis perpendicular to that of the plane of sky and line-of-sight. The lines corresponding to different colours are marked to show the spatial distribution of emission in the structure. Here, 1 unit of x and y correspond to 2.34×10^{14} cm. *Right:* Best-fit modelled spectrum (dash line) obtained using CLOUDY overplotted on the observed optical spectrum (continuous line) of V2676 Oph.

Balmer emission is coming from all the regions, the [O I] emission from the equatorial rings. The forbidden lines of Ar and S are coming from the outer regions of the cones. The He I lines are coming from the inner conical structures. The inclination angle of the system is estimated to be $65^\circ \pm 0.85^\circ$. The details on the extent of all the components and their distance from central source in the morphology of the ejecta are given in Table 4.7.

Most of the emission is arising from the cones. The high ionization lines are

Table 4.7: Details of the morphology of the ejecta on day 1138 for V2676 Oph

Component	**Extent**[a] **($\times 10^{16}$ cm)**	**Radius ($\times 10^{16}$ cm)**	**Distance**[b] **($\times 10^{16}$ cm)**	**Angle**[c] **($^\circ$)**
Cone	2.34 ± 0.08	2.53 ± 0.10	0.76 ± 0.01	52 ± 0.87
Equatorial ring	-	4.63 ± 0.16	1.52 ± 0.09	-

[a]Extent of the component along the ejecta axis

[b]Distance from the central source to the component along the ejecta axis

[c]Outer opening angle of the cone

coming from the outer regions (Table 4.7) implying that they are emerging from the optically thin expanding shell. The He lines are emerging from the inner cone regions suggesting that they are coming from the inner regions (Table 4.7). The He emission is also present in the form of clumps in the rings.

4.4 V339 Del

V339 Del (Nova Del 2013 or PNV J20233073+2056041) was discovered on 2013 August 14.58 UT at 6.8 visual magnitude by Koichi Itagaki (Waagen, 2013) before reaching its maximum during the rise phase. It reached its maximum at 4.3 mag on 2013 August 16.25 UT (Munari et al., 2015b). It was detected in higher energy such as gamma-rays (Ackermann et al., 2014) as well as in low energy radio range (Chomiuk et al., 2013; Roy et al., 2013). Many astronomers carried out detailed observations of this object as the object was very bright. It was confirmed as Fe II type nova by Darnley et al. (2013). Tajitsu et al. (2015) detected ^{7}Be in the NUV spectra obtained from day 38 to 48 using High Dispersion Spectrograph of Subaru telescope. This supports the theoretical production of lithium in novae.

The optical photometric light curve (BVR_cI_c) evolution of V339 Del from time since discovery (optical thick phase) till day 77 (optical thin phase) is discussed in detail by Munari et al. (2013). They estimated that the optical maximum reached in B and V at magnitudes 4.7 and 4.46 respectively implying that the outburst amplitude is 12.5 magnitude compared to 17.2 in B for USNO B-1 1107-0509795 progenitor (Denisenko & Masi, 2013). The characteristic times in B and V bands were estimated to be $t_2(B) = 12$, $t_3(B) = 30$, $t_2(V) = 10.5$ and $t_3(V) = 23.5$ days placing the nova in the marginal position between the fast and very fast novae based on classification scheme by Warner (1995).

Based on detailed early phase optical spectroscopic study of V339 Del from time since discovery to ∼day 40 by Skopal et al. (2014), it was determined that the stellar remnant is super-Eddington and its effective temperature is in the range of 6000–12000 K. The ejected mass was determined to be of the order of 10^{-4} $M_{\odot}$. The

optical spectral evolution was also studied extensively by many astronomers such as Shore et al. (2014); De Gennaro Aquino et al. (2015); Tarasova & Skopal (2016); Munari et al. (2015b) and references therein. The optical spectral evolution of this system is typical as that of a Fe II type novae with expansion velocities in the range of 610–2500 km s^{-1}. During the pre-maximum phase, the hydrogen Balmer and Fe II lines showed strong P-Cygni profiles while He I showed absorption profiles. During the maximum phase, all the line profiles showed deep absorption while Ca II and Hα show P-Cygni profiles with strong emission and deep absorption components. As the system underwent a decline phase, the P-Cygni profiles disappeared, and emission profiles emerged in the spectra. As the optical depth decreased, the high ionization lines such as He I and He II appeared followed by [O III] lines.

The interferometric observations were carried out by Schaefer et al. (2014) using the Center for High Angular Resolution Astronomy Array during the early phase (43 days). It was suggested that the system had prolate or bipolar structures based on ellipticity in the light distribution. A geometrical distance of 4.5 $\pm$ 0.6 kpc to the nova from Sun was estimated, combining the angular expansion rate with radial velocity measurements. Using the MMRD relation by Downes & Duerbeck (2000), they determined the distance to be in the range of 3.3–4.1 kpc.

X-ray observations were also carried out by *Swift*, Chandra and XMM by Kuulkers et al. (2013); Nelson et al. (2013b,a); Osborne et al. (2013); Page et al. (2013, 2014). V339 Del was first detected in X-rays on day 33 with weak emission consistent with shocked gas in an expanding shell. The super-soft emission emerged on day 58 with low flux values, and flux increased to about 1 count/s on day 69 in the energy range 0.3–1.0 keV. It reached a peak value of $\sim$100 counts/s on day 86. Also, observed was a quasi-periodic oscillation (QPO) of 54 s at the peak. This periodicity was also observed on day 97 by Newton-XMM observations. The super-soft phase ended on day 205.

Radio emission was undetected at 1.3 GHz on $\sim$day 14 by Roy et al. (2013). The radio thermal emission was detected at higher frequencies on $\sim$day 27 at 28.2, 36.5 and 95.7 GHz and undetected at frequencies lower than 7.5 GHz by Chomiuk

Table 4.8: Spectroscopic observational log for V339 Del

Date	t (days)	Resolution	Coverage (Å)	Telescope
28 Aug 2013	13	1300, 2200	3800–8800	HCT-HFOSC
04 Sep 2013	20	1300, 2200	3800–8800	HCT-HFOSC
05 Sep 2013	21	1300, 2200	3800–8800	HCT-HFOSC
10 Sep 2013	26	1300, 2200	3800–8800	HCT-HFOSC
22 Sep 2013	38	27000	4000-10000	VBT-Echelle
27 Sep 2013	43	27000	4000-10000	VBT-Echelle
30 Sep 2013	46	1300, 2200	3800–8800	HCT-HFOSC
07 Oct 2013	53	1300, 2200	3800–8800	HCT-HFOSC
14 Oct 2013	60	1300, 2200	3800–8800	HCT-HFOSC
30 Oct 2013	76	1300, 2200	3800–8800	HCT-HFOSC
06 Nov 2013	83	1300, 2200	3800–8800	HCT-HFOSC
13 Mar 2014	210	1300, 2200	3800–8800	HCT-HFOSC

et al. (2013). The object was also detected at ∼day 40 at 15 GHz by Anderson et al. (2013).

From the IR spectral evolution study by Evans et al. (2017), the IR emission lines were found to be symmetrical in the initial phase while distinct asymmetry was noticed from day 77 with a stronger blue wing. The onset of dust formation was on ∼day 34 at condensation temperature of 1480 K. This temperature is consistent with that of graphitic carbon. The dust formation peaked at ∼day 100, followed by a decline.

Polarimetric observations by Shakhovskoy et al. (2017) at $UBVRI$ bands of this system revealed variability in the degree of linear polarization. It was attributed to the non-spherical diffuse shell, with geometry more of bipolar rather than disc-shaped one.

The object was monitored from 28 Aug 2013 (day 13) to 13 Mar 2014 (day 210) and spectroscopic data was obtained from HCT and VBT. The log of optical spectroscopic observations obtained is as shown in Table 4.8. The time of discovery is considered as t=0 in this section. The optical light curve evolution in $BVRI$ bands is as shown in Fig. 4.8 generated using AAVSO data. The magnitude increases till ∼day 2 and reaches peak magnitude at $V \approx 4.4$. Then the light curve undergoes decline of 0.09 mag day^{-1} till day 43 followed by a rapid decline of 0.2 mag day^{-1} till day 71 and then a plateau till day ∼day 180 which is then followed by a slow decline. The mass of the WD using the relation by Livio (1992) was found to be

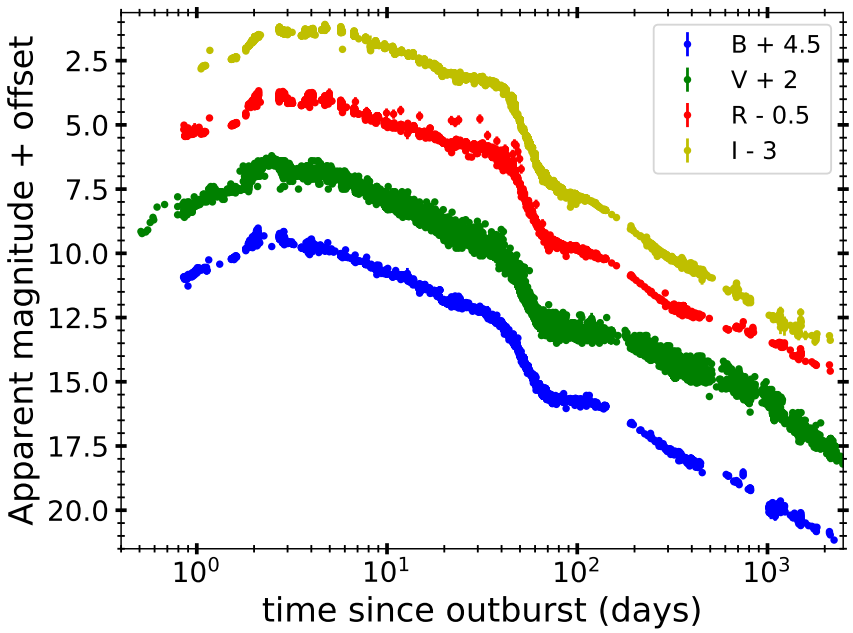

Figure 4.8: Apparent magnitude light curve generated using AAVSO optical data. Offset is introduced for clarity.

1.07 ± 0.09 $M_\odot$.

The optical spectra for V339 Del obtained from day 13 to day 210 since discovery is as shown in Fig. 4.9. The spectra consists of hydrogen Balmer, Fe II, [O I], O I, C II and hydrogen Paschen lines. As the system evolves, there is appearance of lines such as [O III], [N II], He I and N II. On day 210, the high ionization forbidden lines such as [Ne III], [Fe VI], [Fe VII], [Ar III] and [Ar VI] are seen in the spectrum. The line profiles are round peaked initially and are more structured as the system evolves.

The optical depth τ of the ejecta for [O I] 6300 Å using the equation 3.2, and the electron temperature T_e using the equation 3.3 is as shown in Fig. 4.10. The temperature does not decrease or increase with time consistently similar to other novae in the sample by Williams (1994).

High resolution data at R=27000 were also obtained for V339 Del on days 38 and 43. The prominent velocity line profiles are as shown in Fig. 4.11. The Hα and Hβ profiles are double-peaked structures on both the epochs. The He I profiles are similar. The O I profile obtained on day 38 is similar to that of the hydrogen Balmer profiles, however, the profile obtained on day 43 is noisy. The [O I] profiles

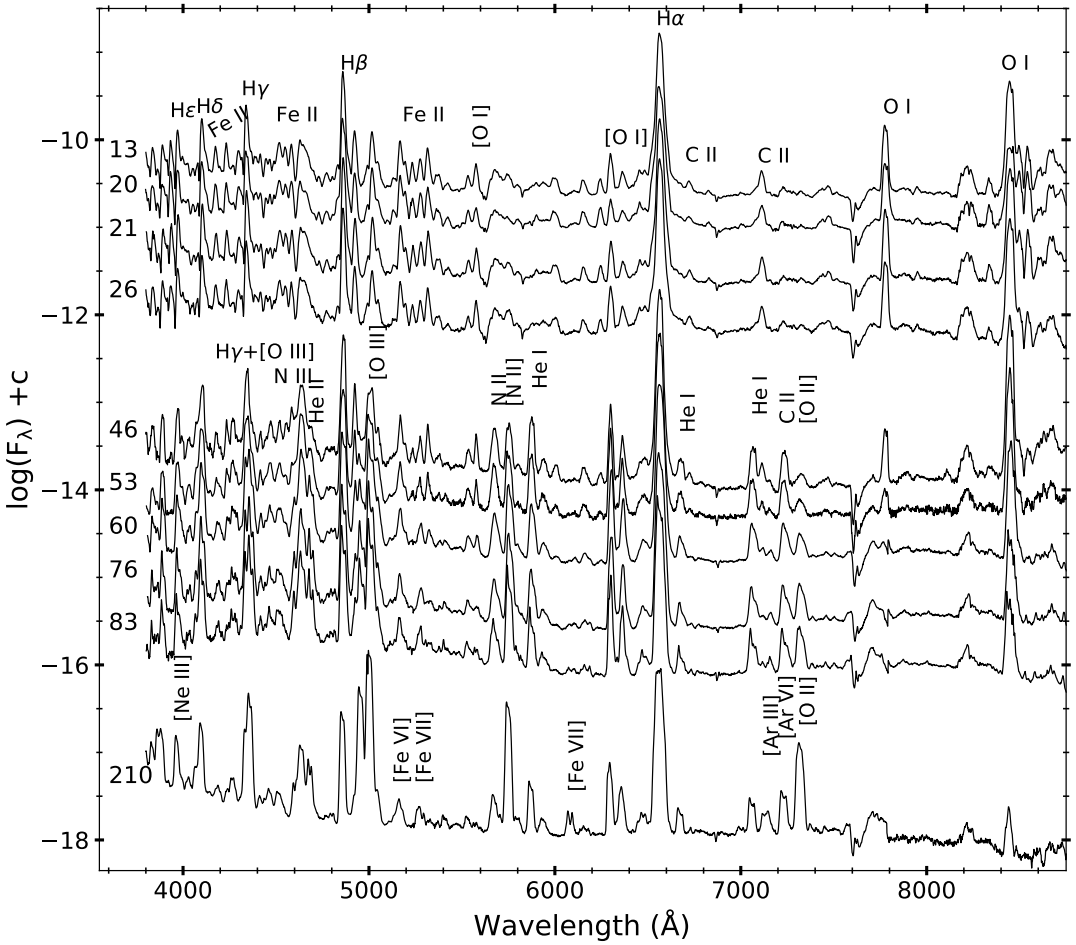

Figure 4.9: Evolution of the spectra from early phase to nebular phase of V339 Del from 28 Aug 2013 (day 13) to 13 Mar 2014 (day 210). The identified lines and time since discovery in days (numbers to the left) are marked.

are complex on both the epochs.

Low resolution optical spectrum obtained on epochs day 13, 20 and 53 using HCT-HFOSC were used to carry out the analysis using CLOUDY. The central ionizing source was set to be at an effective temperature 1.5–2 $\times$ 10^5 K and luminosity 3–6 $\times$ 10^{37} erg s^{-1}. To model the observed spectrum, the medium was assumed to consist of a low-density diffuse component and a clump component. During the days 13 and 20, most of the lines were fitted by the clump component, except a few lines like [O I] and N lines. In order to fit all the lines, a diffuse region (low density) was used, covering 15% of the volume. The clump hydrogen density was 4–6.5 $\times$ 10^{10} cm^{-3} and diffuse hydrogen density 1.5–3 $\times$ 10^{10} cm^{-3}. In the case of day 53, the

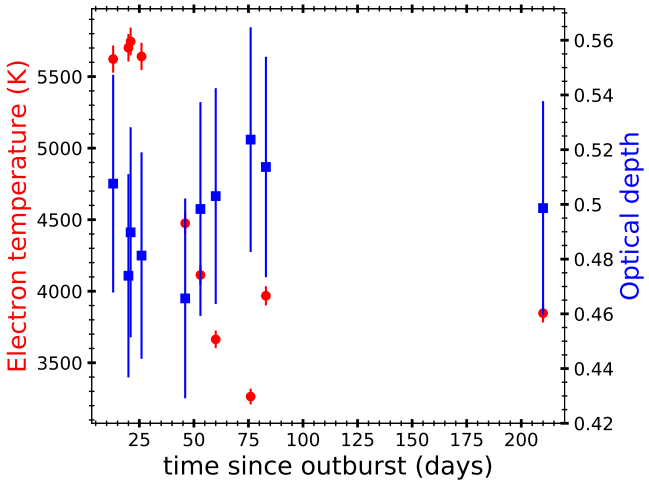

Figure 4.10: Evolution of optical depth for [O I] (6300) and electron temperature of the ejecta of V339 Del from 28 Aug 2013 (day 13) to 13 Mar 2014 (210).

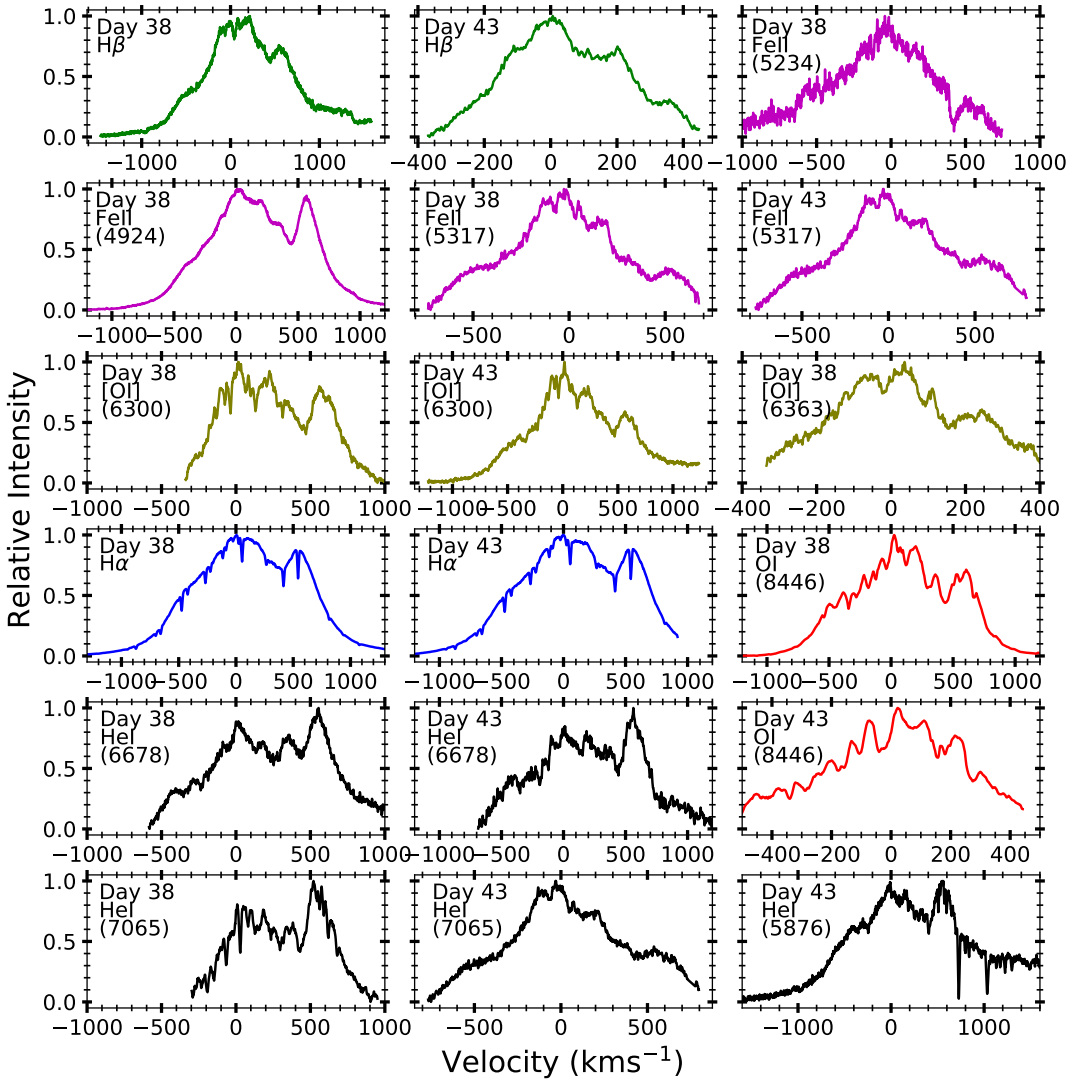

Figure 4.11: Evolution of high resolution velocity profiles of V339 Del obtained on day 38 and 43. The profiles are labelled against each panel.

central ionizing source was set to be at an effective temperature 2.5×10^5 K and luminosity of 7×10^{37} erg s^{-1}. Most of the lines were fitted by the clump component, except high ionization forbidden lines like [N II] (5755 Å) and [O III]. In order to fit all the lines, a diffuse region (low density) was used, covering 15% of the volume. The clump hydrogen density was 3.2×10^9 cm^{-3} and diffuse hydrogen density 10^{10} cm^{-3}. The relative fluxes of the observed lines, the best-fit model predicted lines, and corresponding χ^2 values are given in Table 4.9. The values of best-fit parameters

Table 4.9: Observed and best-fit CLOUDY model line flux ratios[a] for days 13, 20 and 53 of V339 Del

		Day 13			Day 20			Day 53		
Line ID	λ (Å)	**Observed**	**Modelled**	χ^2	**Observed**	**Modelled**	χ^2	**Observed**	**Modelled**	χ^2
H I	3835	9.77E-02	2.46E-01	2.32E-01	1.65E-01	1.02E-01	7.75E-02	2.41E-02	9.61E-02	5.39E-02
H I	3889	1.39E-01	2.74E-01	2.32E-01	1.35E-01	1.96E-01	7.50E-02	8.41E-02	2.30E-01	2.75E-01
Ca II	3934	9.38E-02	4.93E-01	2.89E+00	6.06E-02	2.83E-01	8.17E-01	-	-	-
Ca II + H I	3968	9.16E-02	1.70E-01	2.20E-01	1.13E-01	4.01E-01	1.54E+00	2.14E-01	2.90E-01	1.67E-01
H I	4102	1.12E-01	3.25E-01	8.61E-01	1.01E-01	2.41E-01	3.40E-01	1.53E-01	4.03E-01	8.79E-01
Fe II	4179	4.65E-02	1.75E-01	8.89E-01	3.86E-02	9.41E-02	1.94E-01	3.39E-02	6.90E-02	3.39E-02
Fe II	4233	1.79E-01	1.25E-01	3.59E-02	5.48E-02	4.74E-02	3.96E-03	4.58E-02	1.35E-01	1.29E-01
H I	4340	2.41E-01	5.39E-01	2.59E+00	1.73E-01	4.01E-01	1.93E+00	2.48E-01	8.55E-01	1.35E+01
Fe II	4417	-	-	-	-	-	-	9.55E-03	7.98E-02	6.05E-02
He I	4471	-	-	-	-	-	-	5.64E-02	1.12E-01	9.87E-02
Fe II	4517	6.94E-02	2.56E-01	1.17E+00	6.06E-02	6.91E-02	5.40E-03	2.23E-02	1.10E-01	1.72E-01
Fe II	4549	7.71E-02	2.25E-01	3.92E-01	6.17E-02	1.76E-01	1.89E-01	-	-	-
Fe II	4584	6.83E-02	2.53E-01	8.26E-01	8.24E-02	2.02E-01	3.88E-01	-	-	-
N III	4638	1.91E-01	4.52E-01	1.34E+00	1.49E-01	3.88E-01	8.90E-01	2.43E-01	9.33E-01	6.25E+00
H I	4861	1.00E+00	1.00E+00	1.59E-04	1.00E+00	1.00E+00	8.60E-04	1.00E+00	1.00E+00	0.00E+00
Fe II	4924	1.09E-01	5.96E-02	4.63E-02	1.16E-01	7.68E-02	3.94E-02	1.93E-01	1.46E-01	5.11E-02
[O III]	4959	-	-	-	-	-	-	1.04E-01	1.95E-01	2.21E-01
[O III]	5007	-	-	-	-	-	-	3.16E-01	6.78E-01	3.97E+00
Fe II	5018	8.95E-02	2.94E-01	7.36E-01	1.01E-01	3.44E-01	1.19E+00	-	-	-
Fe II + Mg I	5169	5.75E-02	2.56E-01	4.31E-01	6.91E-02	7.84E-01	2.30E+00	2.97E-02	2.40E-01	4.95E-01
Fe II	5235	3.83E-02	2.37E-01	4.56E-01	4.42E-02	2.94E-01	1.87E+00	-	-	-
Fe II	5276	4.33E-02	1.43E-01	2.99E-01	5.74E-02	5.19E-01	5.26E+00	1.51E-02	1.94E-01	3.04E-01
Fe II	5317	6.92E-02	1.78E-01	2.47E-01	5.85E-02	1.46E-01	3.30E-01	1.04E-02	2.37E-01	9.32E-01
Fe II	5363	4.36E-02	6.61E-02	7.97E-03	-	-	-	-	-	-
Fe II	5425	1.75E-02	8.17E-02	4.63E-02	-	-	-	-	-	-
Fe II + N II	5535	7.76E-02	7.72E-02	1.73E-06	1.73E-01	9.78E-02	1.20E-01	5.72E-02	2.78E-03	6.94E-02
[O I]	5577	1.06E-01	2.25E-01	3.55E-01	2.02E-01	1.59E-01	1.21E-01	1.21E-02	1.51E-01	5.38E-01
N II	5679	-	-	-	-	-	-	5.34E-02	1.74E-01	2.48E-01
[N II]	5755	-	-	-	-	-	-	8.30E-02	1.72E-01	8.79E-02
He I	5876	-	-	-	-	-	-	7.88E-02	2.23E-01	3.83E-01
Fe II	5991	3.70E-02	4.50E-02	1.19E-03	-	-	-	-	-	-
Fe II	6148	1.80E-02	1.10E-01	3.34E-01	1.39E-02	2.63E-01	1.07E+00	-	-	-
Fe II + N II	6248	2.07E-02	1.18E-01	4.09E-01	1.84E-02	7.44E-02	2.15E-01	-	-	-
[O I]	6300	3.29E-02	3.37E-02	2.83E-05	5.90E-02	7.75E-02	2.96E-02	1.04E-01	2.20E-01	9.29E-01
[O I]	6364	1.60E-02	5.37E-02	5.04E-02	2.59E-02	7.63E-02	1.92E-01	4.28E-02	5.64E-02	6.77E-03
Fe II	6456	9.48E-03	4.20E-02	2.30E-02	3.96E+00	4.06E+00	1.84E-01	-	-	-
H I	6563	3.13E+00	4.60E+00	2.18E+01	-	-	-	3.80E+00	3.72E+00	5.03E-02
He I	7065	-	-	-	-	-	-	3.47E-02	8.84E-02	4.48E-02
C II	7112	9.01E-02	1.19E-01	2.32E-02	2.69E-02	1.93E-02	4.41E-03	-	-	-
N I + O I	8227	2.94E-01	4.61E-02	1.06E+00	2.10E-01	6.24E-02	4.64E-01	3.83E-02	6.27E-03	1.59E-02
Ca II	8498	1.23E-01	1.80E-01	1.61E-01	4.02E-01	2.17E-01	5.08E-01	-	-	-
Ca II + H I	8545	1.12E-01	1.54E-01	3.71E-02	8.62E-02	1.21E-01	2.20E-02	-	-	-
Ca II + H I	8665	3.78E-01	1.40E-01	1.40E+00	1.00E-01	8.70E-02	2.79E-03	1.02E-01	8.45E-02	3.50E-03
H I	8863	2.01E-01	7.06E-02	5.14E-01	1.18E-01	4.37E-02	1.80E-01	1.69E-02	1.15E-01	1.22E-01

[a] Relative to Hβ

Table 4.10: Best-fit 1D CLOUDY model parameters on days 13, 20 and 53 for V339 Del

Parameter	**Day 13**	**Day 20**	**Day 53**
T_{BB} ($\times 10^5$ K)	1.5 ± 0.09	2 ± 0.11	2.5 ± 0.08
Luminosity ($\times 10^{37}$ erg s^{-1})	3.16 ± 0.13	5.62 ± 0.11	7.08 ± 0.09
Clump Hydrogen density ($\times 10^{10}$ cm^{-3})	6.31	4.47	0.32
Diffuse Hydrogen density ($\times 10^{10}$ cm^{-3})	3.16	1.58	1.00
Covering factor (clump)	0.85	0.85	0.85
Covering factor (diffuse)	0.15	0.15	0.15
α	-3.00	-3.00	-3.00
Inner radius ($\times 10^{14}$ cm)	0.88	1.40	2.47
Outer radius ($\times 10^{15}$ cm)	0.36	0.57	2.16
Filling factor	0.10	0.10	0.10
N/N$_\odot$	1.39 ± 0.11 (4)[a]	1.28 ± 0.09 (4)	4.17 ± 0.14 (6)
O/O$_\odot$	1.51 ± 0.10 (4)	2.21 ± 0.09 (4)	6.62 ± 0.12 (6)
He/He$_\odot$	–	–	1.13 ± 0.12 (3)
C/C$_\odot$	1.00 ± 0.09 (1)	1.10 ± 0.13 (1)	–
Ca/Ca$_\odot$	1.42 ± 0.10 (5)	1.13 ± 0.08 (5)	–
Fe/Fe$_\odot$	1.88 ± 0.14 (18)	3.00 ± 0.11 (16)	1.25 ± 0.15 (9)
Ejected mass ($\times 10^{-5}$ M$_\odot$)	3.25	6.43	10.89
Number of observed lines (n)	36	32	29
Number of free parameters (n_p)	10	11	11
Degrees of freedom (ν)	26	21	18
Total χ^2	40.12	28.49	30.24
χ^2_{red}	1.54	1.36	1.68

[a]The number in the parenthesis was the number of lines used to determine abundance estimate.

obtained from the model are given in Table 4.10. The estimated abundance values show that helium, nitrogen, oxygen, calcium and iron are over-abundant compared to solar, while other elements have the solar abundance values. The best-fit synthetic spectra plotted over the observed spectra are as shown in Fig. 4.12.

High resolution spectrum from VBT Echelle obtained on 2013 Sept 23 (39 days since discovery) was used to obtain the 3D morphokinematic model. The morphokinematic analysis using SHAPE was performed using the observed Hα velocity profile. The synthetic Hα velocity profile for V339 Del was generated using asymmetric bipolar conical structures (*left* panel of Fig. 4.13). The radii of the top and bottom cones are found to be 1.5×10^{11} and 2.5×10^{11} m with opening angles 41° and 71° respectively. The smaller cone was found to be 85% less bright than that of the bigger one. The best-fit velocity profile corresponding to the observed profile is as shown in the *right* panel of Fig. 4.13. The best-fit inclination angle was found to be $58^\circ \pm 2.25^\circ$. The morphology is asymmetric, and this can be attributed to the

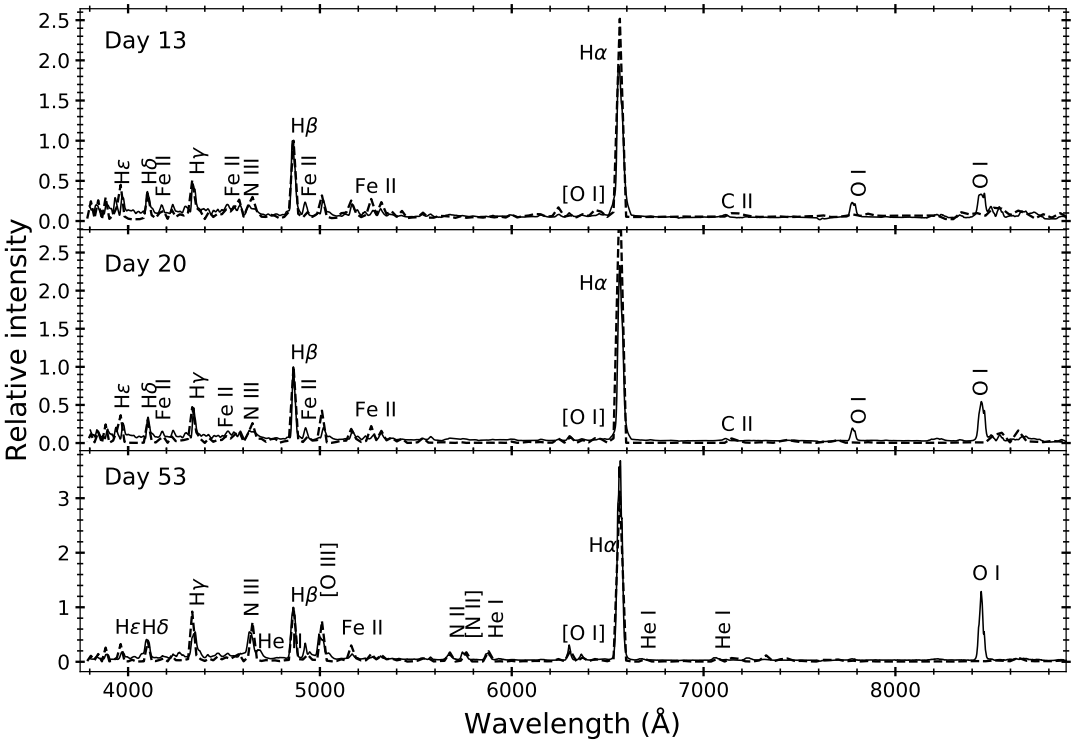

Figure 4.12: Best-fit modelled spectrum (dash line) obtained on days 13, 20 and 53 using CLOUDY over-plotted on the observed optical spectrum (continuous line) of V339 Del.

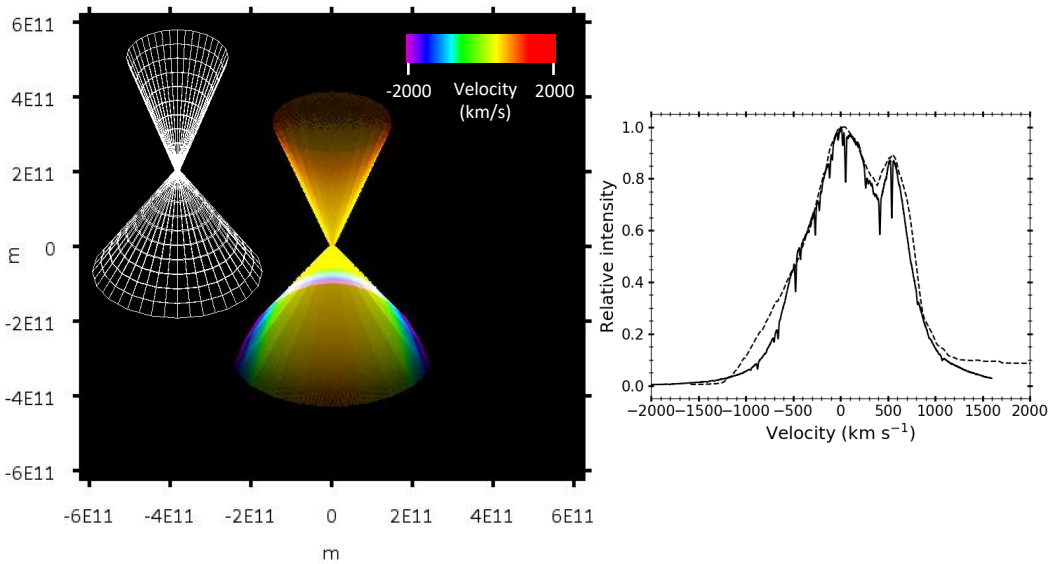

Figure 4.13: *Left:* Morphology of the ejecta of V339 Del obtained on day 39 using Hα velocity profile. It is plotted in the two-dimensional plane with X-axis being the line-of-sight direction and Y being the axis perpendicular to that of the plane of sky and line-of-sight with X and Y axes in meters and Z is the velocity (marked in *top-right*), and grid structure (*left*) are shown. *Right:* Best-fit Hα velocity profile (dash line) overplotted on the observed profile (continuous line).

optical depth effects (Ribeiro et al. 2011 and references therein) as the system is still in its early decline phase.

4.5 V1639 Cen

V1639 Cen (Nova Cen 2013) was discovered on 02 Dec 2013 by an amateur astronomer John Seach at a magnitude of 5.5. On 14 Dec 2013, it peaked at about magnitude of 3.3 (Combi et al., 2013). Similar to V339 Del, this nova was also observed to emit gamma-rays that were detected by the *Fermi* during 7–10 Dec 2013 (Cheung et al., 2013). Blue-shifted absorption feature of ^{7}Li I 6708 Å was detected in the early optical thick phase (Izzo et al., 2015). One among the two novae to have direct evidence of the presence of lithium (other being V5668 Sgr). Based on the AAVSO light curve, it was noticed by Cheung et al. (2013) that the object underwent similar multiple peaks in optical. The object rose to 3.6 mag in 3 days since discovery at the rate of 0.6 mag day^{-1} followed by a decline. The second peak ($V \sim 3.3$) was observed on day 12 since discovery with successive fainter peaks. The γ-ray emission was detected for a duration of 39 days peaking around the time when the system is on the rise to its second peak in the optical light curve.

High resolution spectra at R = 27000 were obtained from VBT-Echelle spectrograph on four epochs such as 15 Dec 2013 (day 13), 20 Dec 2013 (day 18), 21 Dec 2013 (day 19) and 22 Dec 2013 (day 20). The spectrum consists of Ca II, Fe II, O I, hydrogen Balmer and Paschen lines. The velocity line profiles of Hβ, Fe II, Hα and O I are plotted in the Fig. 4.14. On day 13, the absorption components are very prominent as the system is close to its peak during this epoch. The prominent components are present around -1000 km s^{-1} for the lines profiles and an absorption trough around -600 km s^{-1}. The absorption component weakened significantly as the system is on the rise to its second peak. All line profiles are more or less similar, indicating that they are originating from the same region.

High resolution spectrum from VBT-Echelle obtained on 22 Dec 2013 (20 days

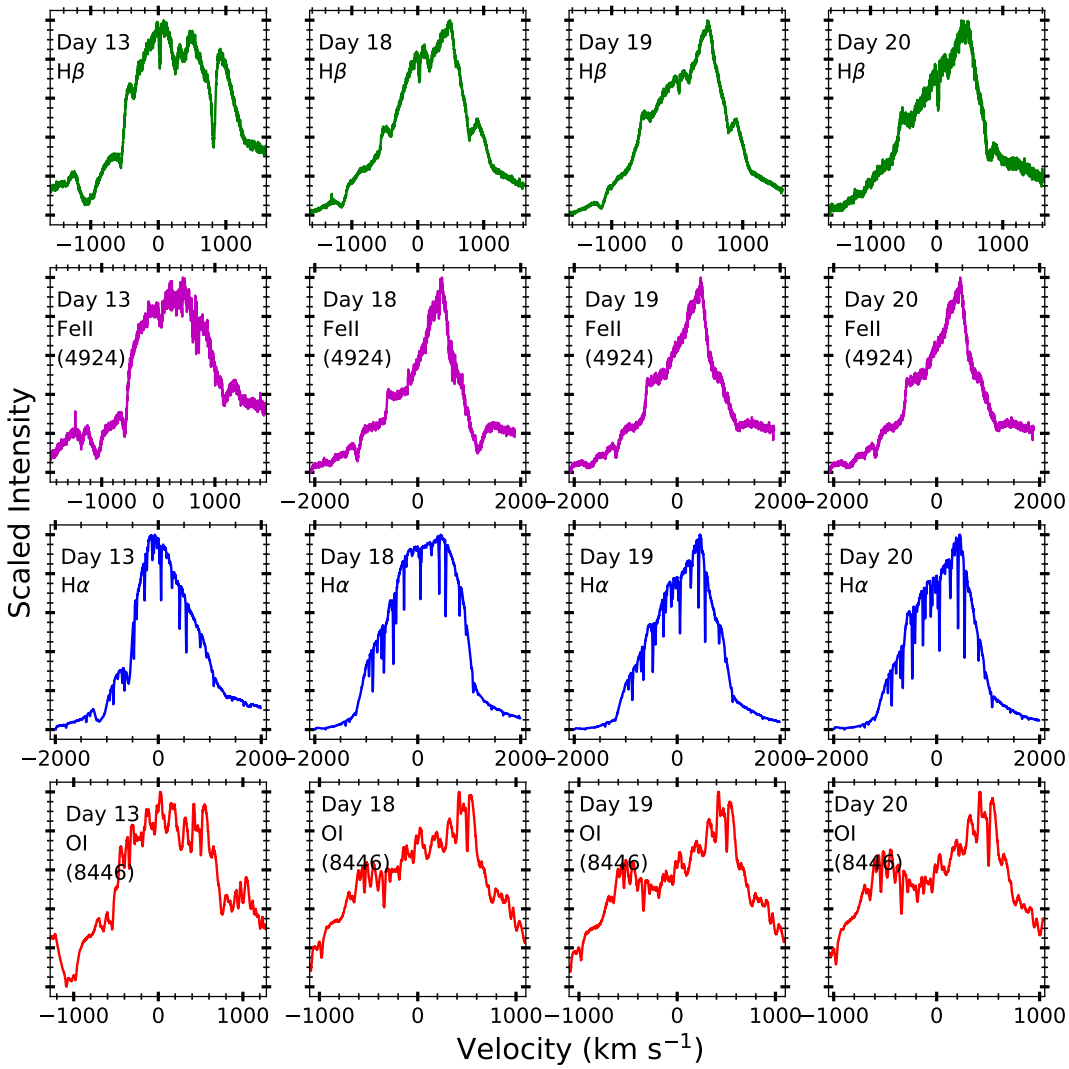

Figure 4.14: Evolution of high resolution velocity line profiles of V1369 Cen obtained on days 13, 18, 19 and 20. The profiles are labelled against each panel.

since discovery) was used to obtain the 3D morphokinematic model. The morphokinematic analysis using SHAPE was performed using the observed Hα velocity profile. The synthetic Hα velocity profile for V1369 Cen was generated using asymmetric bipolar conical structures (*left* panel of Fig. 4.15). The radius of the top cone is found to be 1.5 $\times$ 10^{11} m with an opening angle of 41° while the bottom structure is conical frustum with a base radius of 2.5 $\times$ 10^{11} m and tip radius of 9.5 $\times$ 10^{10} m with an opening angle of 30°. The smaller cone is found to be 74% less bright than that of the bigger one. The best-fit velocity profile corresponding to the observed profile is as shown in the *right* panel of Fig. 4.15. The best-fit inclination angle was found to be 50° $\pm$ 5°. There is significant asymmetry in the morphology

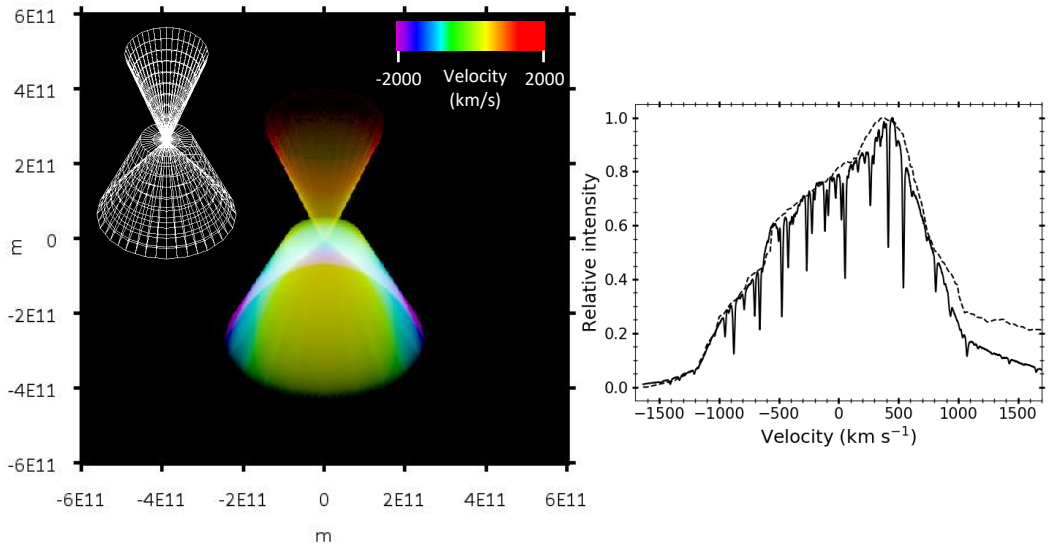

Figure 4.15: *Left:* Morphology of the ejecta of V1369 Cen obtained on day 20 using Hα velocity line profile. The structure is in the two-dimensional plane with X-axis being the line-of-sight direction and Y being the axis perpendicular to that of the plane of sky and line-of-sight with X and Y axes in meters and Z is velocity (marked in *top-right*) and grid structure (*left*) are shown. *Right:* Best-fit Hα velocity profile (dash line) over plotted on the observed profile (continuous line).

obtained. During this epoch, the system is still in its optically thick phase, and hence the asymmetry is attributed here to the optical depth effects (Ribeiro et al. 2011 and reference therein). The cones might have formed as a consequence of the interaction between the first and its subsequent ejecta.

4.6 V2944 Oph

V2944 Oph (Nova Oph 2015 or PNV J17291350-1846120) was discovered on 2015 March 29.766 UT by Nakano et al. (2015) at a magnitude of 12.2. It was classified as a He/N type of CN by Ayani & Fujii (2015a,b) based on the lines such as He I, N II and N III present in the low resolution optical spectrum on 2015 March 30.7 and 30.8 UT. Danilet et al. (2015) also classified it as He/N based on the spectrum obtained on 2015 April 1.459 UT. However, they also noticed the presence of sharp peaked line profiles and relatively lower velocities not consistent with that of line profiles seen usually in He/N class. Later when the system was closer to its optical

maximum, the spectrum obtained by Munari et al. (2015c) was similar to that of Fe II class of novae with reddened continuum and P-Cygni profiles of Hydrogen Balmer, Fe II, Ca II (H & K) and O I lines.

Munari & Walter (2016) indicated the presence of pre-existing CSM around the nova due to wind of an evolved companion probably from a sub-giant. It was suggested that ionization of winds from secondary by the initial UV flash of nova causes narrow component of FWHM 60 km s^{-1} which was detected in the first six days of the outburst. Another interesting phenomenon noticed was the presence of ^{7}Be in the high resolution UV spectrum obtained with Subaru telescope using the High Dispersion spectrograph by Tajitsu et al. (2016) during the post-outburst phase of the nova.

Low resolution optical spectrum was obtained from HCT on 24 Feb 2017 (day 699). The spectrum consists of He I, He II, [N II], [Fe VII], [O I], [O II], [O III] and hydrogen Balmer lines. The prominent non-Balmer emission lines in the spectrum are due to [O III]. The emission lines were found be round-peaked with FWHM velocities of Hα and Hβ lines measured as 2000 km s^{-1} and 1350 km s^{-1} respectively.

The spectrum was modelled using CLOUDY. The central ionizing source is set to be at an effective temperature 10^5 K and luminosity 10^{38} erg s^{-1}. To model the observed spectrum, the medium was assumed to consist of a low-density diffuse component and a clump component. Most of the lines are fitted by the clump component, except a few lines like [N II] (5755 Å), [Fe VII] and [O III]. To fit all the lines, a diffuse region (low density) is used, covering 20% of the volume. The clump hydrogen density was 2.52 $\times$ 10^8 cm^{-3} and diffuse hydrogen density 3.98 $\times$ 10^7 cm^{-3}. The relative fluxes of the observed lines, the best-fit model predicted lines, and corresponding χ^2 values are given in Table 4.11. The values of best-fit parameters obtained from the model are given in Table 4.12. The estimated abundance values show that helium, nitrogen, oxygen, calcium and iron are over-abundant compared to solar, while other elements have the solar abundance values. The best-fit modelled spectrum overplotted on the observed spectrum is as shown in *right* panel of Fig. 4.16.

Table 4.11: Observed and best-fit CLOUDY model line flux values[a] for day 699 of V2944 Oph

Line ID	λ (Å)	**Observed**	**Modelled**	χ^2
H I	3889	7.77E-01	8.94E-01	5.08E-01
H I	4102	4.14E-02	1.03E-01	2.18E-01
H I	4340	1.69E+00	1.83E+00	4.24E-01
He I	4471	2.56E-01	3.77E-01	2.61E-01
N III	4638	3.87E-01	5.12E-01	5.79E-01
He II	4686	6.31E-01	4.60E-01	1.56E+00
H I	4861	1.00E+00	1.00E+00	0.00E+00
[O III]	4959	1.03E+01	9.99E+00	4.48E+00
[O III]	5007	3.11E+01	3.12E+01	1.03E+00
[N II]	5755	2.79E+00	2.96E+00	1.78E+00
He I	5876	8.59E-02	1.91E-01	8.37E-01
[Fe VII]	6087	7.82E-01	9.67E-01	2.13E+00
[O I]	6300	3.08E-01	4.06E-01	2.23E-01
[O I]	6363	1.45E-01	1.91E-01	1.19E-01
H I	6563	7.92E+00	7.73E+00	1.06E+00
He I	6678	6.89E-02	1.33E-01	1.66E-01
He I	7065	8.42E-02	1.07E-01	1.93E-01
[O II]	7320	1.07E+00	1.37E+00	3.12E+00

[a] Relative to Hβ

Table 4.12: Best-fit 1D CLOUDY model parameters on day 699 for V2944 Oph

Parameter	**Day 699**
T_{BB} ($\times$ 10^5 K)	2.30 $\pm$ 0.06
Luminosity ($\times$ 10^{38} erg s^{-1})	3.16 $\pm$ 0.04
Clump Hydrogen density ($\times$ 10^8 cm^{-3})	2.52
Diffuse Hydrogen density ($\times$ 10^7 cm^{-3})	3.98
Covering factor (clump)	0.80
Covering factor (diffuse)	0.20
α	-3.00
Inner radius ($\times$ 10^{15} cm)	3.09
Outer radius ($\times$ 10^{16} cm)	1.26
Filling factor	0.10
N/N$_\odot$	1.82 $\pm$ 0.13 (2)[a]
O/O$_\odot$	2.65 $\pm$ 0.07 (6)
He/He$_\odot$	1.51 $\pm$ 0.11 (5)
Ejected mass ($\times$ 10^{-6} M$_\odot$)	9.13
Number of observed lines (n)	18
Number of free parameters (n_p)	6
Degrees of freedom (ν)	12
Total χ^2	18.68
χ^2_{red}	1.56

[a]The number in the parenthesis is the number of lines used to determine abundance estimate.

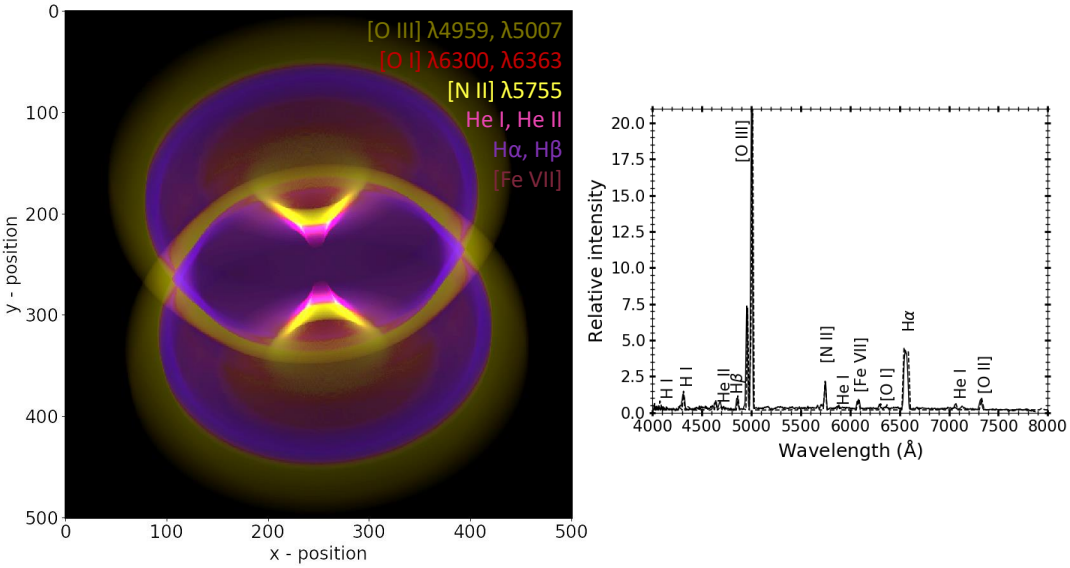

Figure 4.16: *Left:* Morphology of the ejecta of V2944 Oph obtained on day 699 using the optical spectrum. It is plotted in the two-dimensional plane with *X*-axis being the line-of-sight direction and *Y* being the axis perpendicular to that of the plane of sky and line-of-sight. The lines corresponding to different colours are marked to show the spatial distribution of emission in the structure. Here, 1 unit of x and y correspond to 1.26×10^{13} cm. *Right:* Best-fit modelled spectrum (dash line) over plotted on the observed profile (continuous line).

The geometry of the ionized structure obtained using pyCloudy is found to be bipolar cones with equatorial rings (*left* panel of Fig. 4.16). The hydrogen Balmer emission is coming from all the regions, while the [O III] and [O I] emission from the equatorial rings. The conical base is formed due to the [N II] emission. The He II (4686 Å) and He I lines are coming from the inner conical structures. [Fe VII] is coming from the polar blobs closely associated with conical bases. The inclination angle of the system is found to be $51^\circ \pm 1.73^\circ$. The observational evidence for the presence of pre-existing circumstellar medium (Munari & Walter, 2016) might suggest the presence of equatorial rings that is formed due to the interaction of the outflow with this CSM. The details on the extent of all the components and their distance from central source in the morphology of the ejecta are given in Table 4.13.

Table 4.13: Details of the morphology of the ejecta on day 699 for V2944 Oph

Component	**Extent**[a] **($\times 10^{14}$ cm)**	**Radius ($\times 10^{14}$ cm)**	**Distance**[b] **($\times 10^{14}$ cm)**	**Angle**[c] **(°)**
Cone	7.94 ± 0.17	7.06 ± 0.14	2.21 ± 0.11	72 ± 1.14
Equatorial ring	-	26.5 ± 0.21	11.0 ± 0.18	-

[a]Extent of the component along the ejecta axis

[b]Distance from the central source to the component along the ejecta axis

[c]Outer opening angle of the cone

4.7 V5856 Sgr

V5856 Sgr (ASASSN-16ma or PNV J18205200-2822100) was discovered on 2016 Oct 25.02 UT at V$\sim$13.7 by All Sky Automated Survey for SuperNovae (ASAS-SN) (Stanek et al., 2016). It was classified as a Fe II type nova by Luckas (2016) based on the optical spectrum obtained on 2016 Oct 27.5. After $\sim$28 days since discovery based on the optical and NIR spectrum, the Fe II spectral nature with low excitation environment was confirmed by Rudy et al. (2016). High energy γ-ray emission was detected in this object on day 14 by *Fermi*-LAT (Li et al., 2016). The object turned out to be a strong γ-ray source, and the emission was detected for nine days. The ratio between the γ-ray flux and optical flux is constant during the γ-ray emission period and was found to be 0.002. Based on this strong correlation, it was concluded by Li et al. (2017) that most of the optical light arises from the reprocessed emission from shocks than the WD.

The object was monitored from 05 Nov 2016 (day 11) to 14 Jul 2020 (day 1358) to obtain low (R=1300 and 2200) and high (R=30000 and 72000) resolution optical spectroscopic data using the spectrographs in HCT and VBT. The log of optical spectroscopic observations carried out is as shown in Table 4.14. The time of discovery that is, 2016 Oct 25 is considered as t=0 in this section.

Optical light curve was generated using the AAVSO optical database. The $BVRI$ bands are plotted; however, the BRI band data are sparse. The system undergoes initial rise phase till $\sim$day 9 followed by a small plateau for a couple of days and then reaches its maximum of $V \sim 5.4$ on day 14. It undergoes a dip in brightness to

Table 4.14: Spectroscopic observational log for V5856 Sgr

Date	t (days)	Coverage	Telescope	Instrument
05 Nov 2016	11	3800–8800	VBT	OMR
08 Nov 2016	14	3800–8800	VBT	OMR
09 Nov 2016	15	3800–8800	VBT	OMR
10 Nov 2016	16	3800–8800	VBT	OMR
11 Nov 2016	17	3800–7400	VBT	OMR
12 Nov 2016	18	3800–8800	VBT	OMR
14 Nov 2016	20	3800–8800	VBT	OMR
16 Nov 2016	22	3800–8800	VBT	OMR
17 Nov 2016	23	4200–8800	VBT	OMR
18 Nov 2016	24	4000–8800	VBT	OMR
19 Nov 2016	25	4000–8800	VBT	OMR
22 Nov 2016	28	4300–8800	VBT	OMR
23 Nov 2016	29	4300–8800	VBT	OMR
24 Nov 2016	30	4300–8800	VBT	OMR
25 Nov 2016	31	4300–8800	VBT	OMR
26 Nov 2016	32	4300–8800	VBT	OMR
27 Nov 2016	33	4300–8800	VBT	OMR
21 Feb 2017	119	3300–7700	VBT	OMR
23 Feb 2017	121	4200–8700	VBT	OMR
24 Feb 2017	122	4300–8800	VBT	OMR
25 Feb 2017	123	3700–8100	VBT	OMR
28 Feb 2017	126	3800–8700	VBT	OMR
27 Mar 2017	153	3800–9000	HCT	HFOSC
01 Apr 2017	158	3800–9000	HCT	HFOSC
09 Apr 2017	166	3800–9000	HCT	HFOSC
23 Apr 2017	180	4000–10000	HCT	HESP
24 Apr 2017	181	3800–9000	HCT	HFOSC
02 May 2017	189	4000–10000	VBT	Echelle
05 May 2017	192	3800–8500	HCT	HFOSC
10 May 2017	197	3800–8500	HCT	HFOSC
02 Jul 2017	250	4750–9000	VBT	OMR
04 Sept 2017	314	3800–9000	HCT	HFOSC
07 Oct 2017	347	3700–9000	HCT	HFOSC
16 Oct 2017	356	3800–9000	HCT	HFOSC
11 Apr 2018	533	3800–9000	HCT	HFOSC
01 Oct 2018	706	4000–10000	HCT	HESP
27 Mar 2019	869	3800–7500	HCT	HFOSC
13 Jun 2019	961	3800–9000	HCT	HFOSC
14 Jul 2020	1358	3800–9000	HCT	HFOSC

about 7 mag on day 19 followed by a rise to $V \sim 6$ in one day. Then, a rapid decline till ∼day 34.5 with a decline rate of 0.31 mag day^{-1} was observed. This is followed by the final decline post day 100. The t_2 and t_3 values were determined to be 11.12 $\pm$ 0.53 and 13.85 $\pm$ 0.68 days placing the object in the fast class of novae. Using

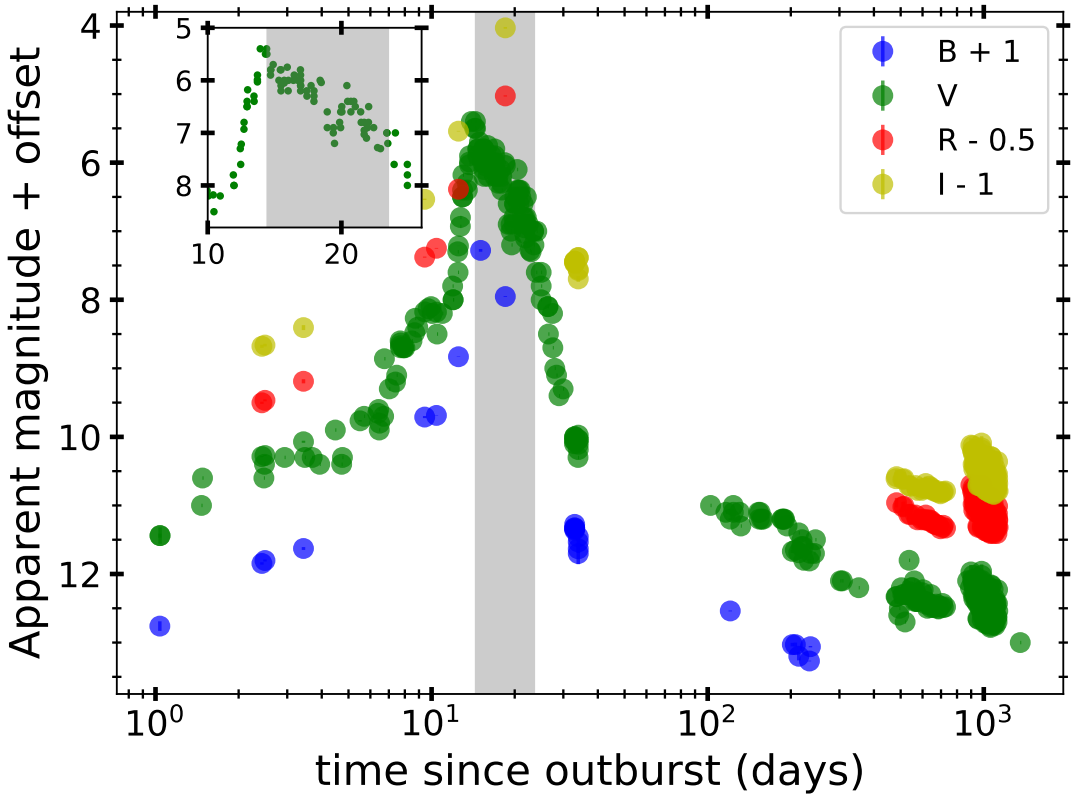

Figure 4.17: Apparent magnitude light curve of V5856 Sgr generated using the AAVSO data. Offset is given for clarity. The grey area represent the duration of γ-ray emission. On the *top-left*, the V magnitude light curve is zoomed-in for clarity during the optical maximum phase.

the MMRD relation by Downes & Duerbeck (2000), the absolute magnitude of the nova was estimated to be M_V = -8.78 $\pm$ 0.16. Using this absolute magnitude value in the relation by Livio (1992), the mass of WD was found to be 1.06 $\pm$ 0.18 $M_\odot$.

4.7.1 Pre-maximum, rise and early decline phase

The initial phase of the system from the spectroscopic data available here is t = 11 to 20. This phase is when the system goes through the initial rise and reaches the maximum (Fig. 4.17) in the optical regime. The spectrum (Fig. 4.18) is dominated by narrow absorption and P-Cygni profiles due to the optically thick shells. Initially, Fe II multiplets, Na I, O I (7774 Å), Ca II, Paschen and N I lines are seen only in absorption, while the hydrogen Balmer lines show a P-Cygni profile with weak emission. As the system evolves, the absorption lines evolve into P-Cygni profiles with stronger absorption components that are deeper and sharper. The FWHM of the

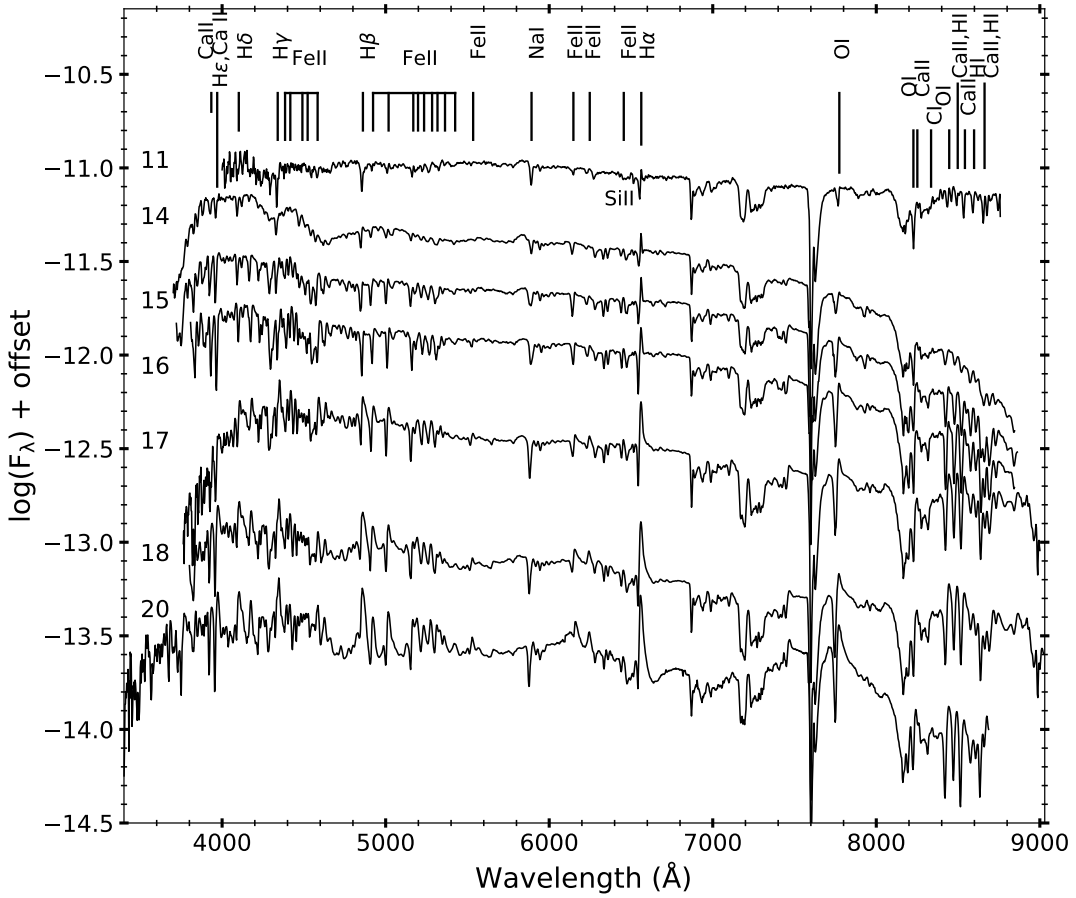

Figure 4.18: Low resolution optical spectroscopic evolution of V5856 Sgr from 05 Nov 2016 (day 11) to 14 Nov 2016 (day 20). The identified lines and time since outburst in days (numbers to the left) are marked.

lines increases with time. $E(B-V)$ was found to be 0.19 ± 0.013 using the Na I line present in the observed spectrum from the relation by Munari & Zwitter (1997). The reddening value is consistent with the value obtained by Munari et al. (2017a).

γ-ray emission was detected from day 14 to 23. A strong correlation between the γ-rays and optical emission based on the ratio between the γ-ray flux and optical flux (Li et al., 2017) was observed. During the γ-ray duration, the optical spectroscopic evolution also went through some significant changes. There was a rapid change in the line profiles from absorption profiles to that of P-Cygni and the narrow sharp-peaked emission components of P-Cygni profiles evolved into broad round-peaked emission line profiles. The onset of γ-ray emission was coincident with that of a blue bump observed in the optical spectrum extending from 3800–4600 Å. There was a significant drop in the blue edge in the optical spectrum on day 17 when both

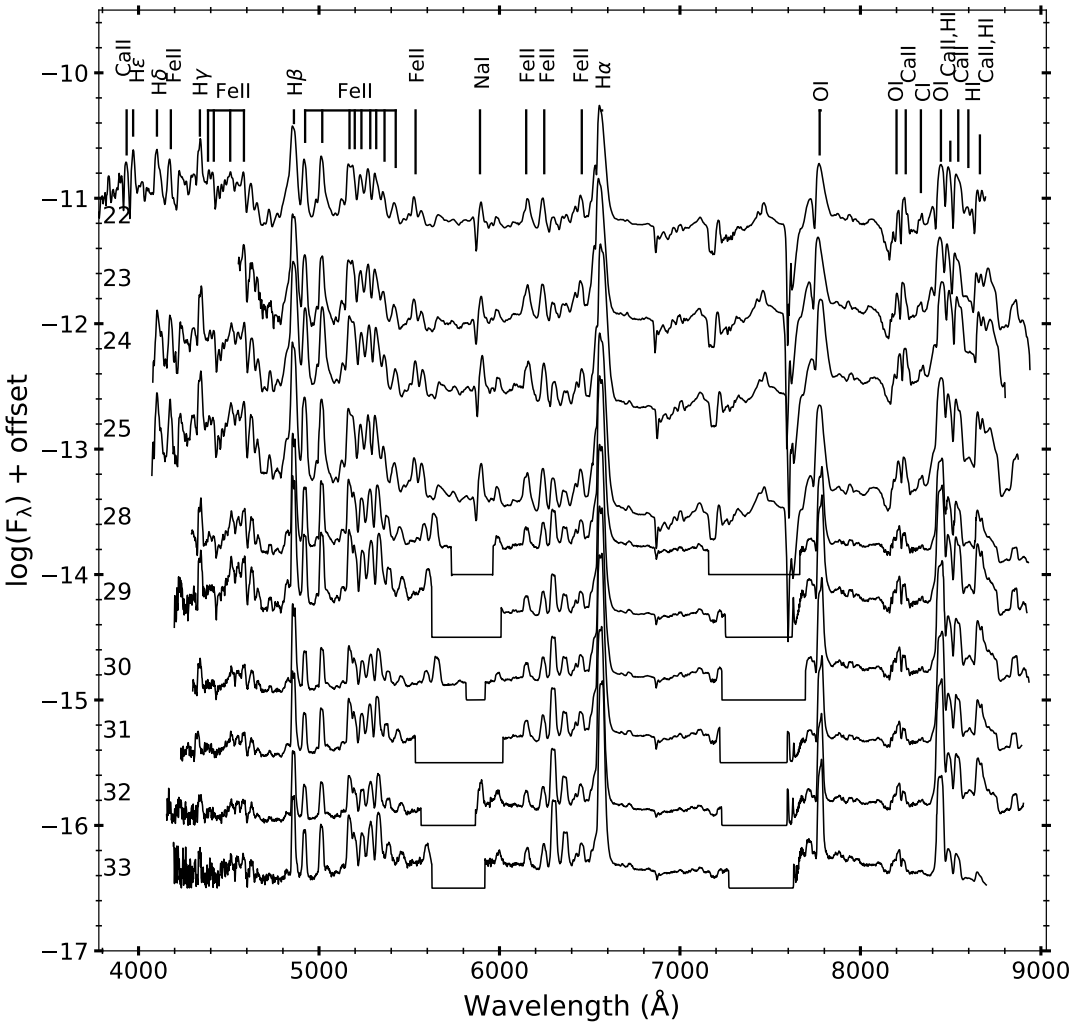

Figure 4.19: Low resolution optical spectroscopic evolution of V5856 Sgr from 16 Nov 2016 (day 22) to 27 Nov 2016 (day 33). The identified lines and time since outburst in days (numbers to the left) are marked.

the optical and γ-ray emission began to dip in brightness (Fig. 4.17). By day 23, all the lines have only emission profiles implying a decrease in the optical depth.

The phase covering t = 22 to 33 days is the post-maximum and early decline phase of the system in the optical regime. The P-Cygni profiles in the previous phase have manifested now into broader emission profiles as the ejecta thins out (Fig. 4.19). The lines present during this period are hydrogen Balmer, Fe II, Ca II, Paschen and O I lines. The Hα emission profile evolves from round peaked to a double-peaked structure. All the hydrogen Balmer lines show a double-peaked structure in this phase.

During this phase, day 25 was modelled to obtain the physical conditions using

Table 4.15: Observed and best-fit CLOUDY model line flux ratios[a] for day 25 of V5856 Sgr

Line ID	λ (Å)	**Observed**	**Modelled**	χ^2
H I	4102	9.47E-01	1.48E-01	1.06E+01
Fe II	4179	1.73E-01	1.06E-01	1.17E-01
Fe II	4233	4.20E-01	1.86E-01	1.36E+00
Fe II	4297	3.80E-01	2.12E-01	3.75E-01
Fe II	4352	5.20E-01	6.80E-01	2.59E-01
Fe II	4385	3.94E-01	9.07E-02	3.03E+00
Fe II	4417	4.74E-02	1.08E-01	5.17E-01
Fe II	4491	3.98E-01	8.22E-02	9.79E-01
Fe II	4515	1.91E-01	9.25E-02	1.10E-01
Fe II	4556	2.47E-01	7.45E-02	3.78E-01
Fe II	4584	1.63E-01	3.34E-01	1.27E+00
Fe II	4629	1.18E-01	4.11E-01	1.40E+00
H I	4861	1.00E+00	1.00E+00	0.00E+00
Fe II	4924	2.54E-01	4.37E-01	5.01E-01
Fe II	5018	2.50E-01	4.37E-01	1.28E-01
Fe II	5169	1.37E-01	4.94E-01	2.89E-03
Fe II	5198	1.93E-01	2.01E-01	9.61E-04
Fe II	5235	1.36E-01	4.63E-02	8.66E-02
Fe II	5265	1.71E-01	3.59E-01	4.97E-01
Fe II	5317	1.84E-01	2.32E-01	8.49E-02
Fe II	5363	6.43E-02	3.40E-02	2.04E-02
Fe II	5425	2.36E-02	1.17E-01	2.75E-01
Fe II	5535	6.18E-02	1.36E-01	8.18E-02
Na I	5890	2.40E-02	2.67E-02	3.86E-04
Fe II	5991	2.31E-02	4.29E-02	1.67E-02
Fe II	6148	6.25E-02	1.12E-01	4.02E-02
Fe II	6248	6.01E-02	1.37E-01	2.22E-01
Fe II	6456	6.85E-02	1.41E-01	5.24E-02
H I	6563	1.68E+00	1.83E+00	2.84E-01
Fe II	7462	7.92E-02	6.86E-02	1.28E-03
N I + O I	8212	4.82E-02	2.37E-01	5.70E-01
Ca II	8251	5.22E-02	4.03E-02	1.94E-03
C I	8335	2.56E-02	2.12E-02	7.51E-04
Ca II	8498	1.64E-01	2.59E-01	2.43E-01
Ca II	8542	2.99E-01	2.91E-01	1.10E-03
Ca II + H I	8662	8.81E-02	5.27E-01	6.02E+00

[a] Relative to Hβ

CLOUDY. The central ionizing source was set to be at an effective temperature 3.20 $\times$ 10^4 K and luminosity 9.2 $\times$ 10^{37} erg s^{-1}. To model the observed spectrum, the medium was assumed to consist of a low-density diffuse component and a clump component. Most of the lines were fitted by the clump component, except Ca II lines. In order to fit all the lines, a diffuse region (low density) was used, covering 15% of the volume. The clump hydrogen density was 10^{12} cm^{-3} and diffuse hydrogen

Table 4.16: Best-fit CLOUDY model parameters obtained on day 25 of V5856 Sgr

Parameter	**Day 25**
T_{BB} ($\times$ 10^4 K)	3.20 $\pm$ 0.12
Luminosity ($\times$ 10^{37} erg s^{-1})	9.20 $\pm$ 0.09
Clump Hydrogen density ($\times$ 10^{12} cm^{-3})	1.00
Diffuse Hydrogen density ($\times$ 10^{11} cm^{-3})	3.16
Covering factor (clump)	0.85
Covering factor (diffuse)	0.15
α	-3.00
Inner radius ($\times$ 10^{14} cm)	1.23
Outer radius ($\times$ 10^{14} cm)	3.31
Filling factor	0.1
$N/N_\odot$	1.00 $\pm$ 0.07 (1)[a]
$O/O_\odot$	1.00 $\pm$ 0.11 (1)
$Fe/Fe_\odot$	3.36 $\pm$ 0.14 (27)
$Ca/Ca_\odot$	1.13 $\pm$ 0.09 (4)
$C/C_\odot$	1.00 $\pm$ 0.08 (1)
Ejected mass ($\times$ 10^{-4} $M_\odot$)	8.43
Number of observed lines (n)	37
Number of free parameters (n_p)	10
Degrees of freedom (ν)	27
Total χ^2	33.54
χ^2_{red}	1.29

[a]The number in the parenthesis is the number of lines used to determine abundance estimate.

density, 3.16 $\times$ 10^{11} cm^{-3}. The relative fluxes of the observed lines, best-fit model predicted lines and corresponding χ^2 values are given in Table 4.15. The values of best-fit parameters obtained from model are given in Table 4.16. The estimated abundance values show that iron was over abundant compared to solar, while calcium and carbon have solar abundance values. The ejected mass was found to be of the order of 10^{-4} $M_\odot$. The best-fit synthetic spectrum corresponding to the observed spectrum is as shown in *top* panel of Fig. 4.20.

4.7.2 Transition phase

The transition phase from t = 119 to 250 (Fig. 4.21) marks the presence of forbidden lines like [O I] (5577, 6300 and 6363 Å), [N II] (5755 Å) and [O II] (7320 Å) lines. The lines other than previously present Fe II multiplets are He I lines (6678

Å and 7065 Å), N II λ5679 Å and N III. As the system evolves, the prominent non-Balmer lines are [O I] lines. The ejecta is optically thin and the system is entering its nebular phase.

During this phase, day 127 was modelled using CLOUDY to determine the physical conditions. The central ionizing source was set at an effective temperature 1.73 $\times$ 10^5 K and luminosity 9.83 $\times$ 10^{37} erg s^{-1}. To model the observed spectrum, the medium was assumed to consist of a low-density diffuse component and a clump component. Most of the lines were fitted by the clump component, except a few forbidden lines like [N II] (5755 Å), [O II] (7320 Å) and N II (5679 Å) line. In order to fit all the lines, a diffuse region (low density) is used, covering 15% of the volume. The clump hydrogen density was 10^{10} cm^{-3} and diffuse hydrogen density, 3.16 $\times$ 10^9 cm^{-3}. The relative fluxes of the observed lines, best-fit model predicted

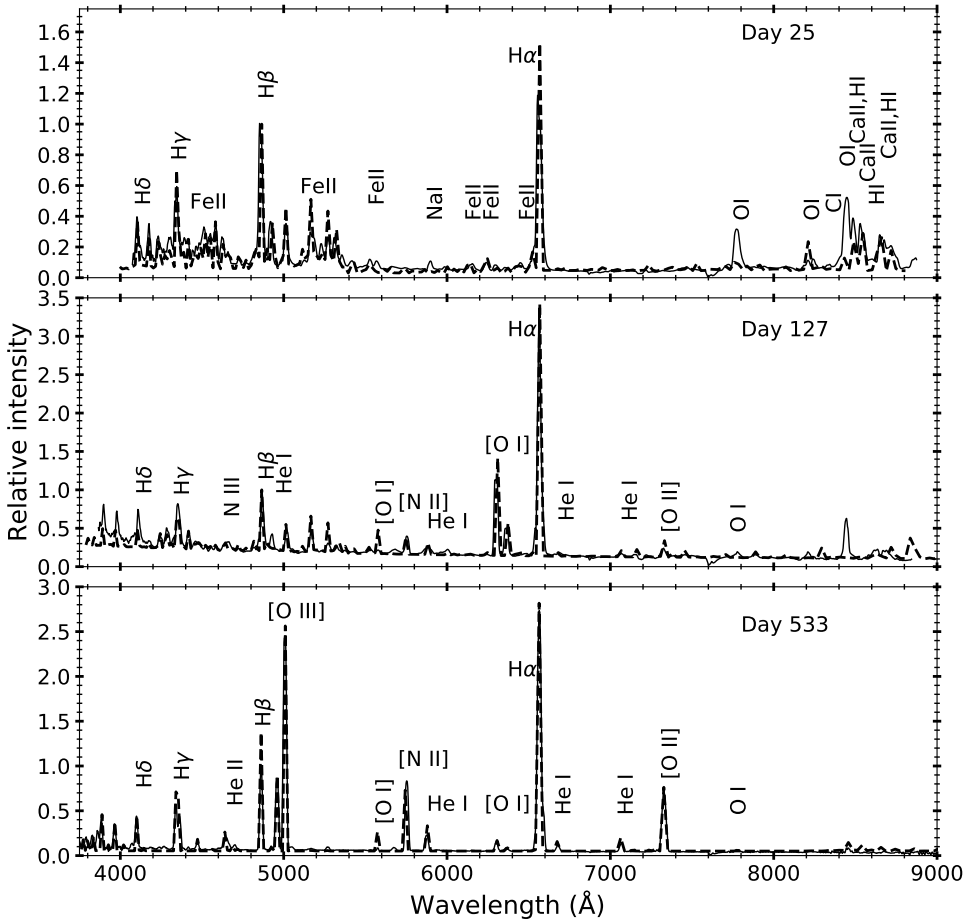

Figure 4.20: Best-fit CLOUDY modelled spectrum (dash line) plotted over the observed spectrum (continuous line) for days 25, 127 and 533 (*top* to *bottom*) for V5856 Sgr.

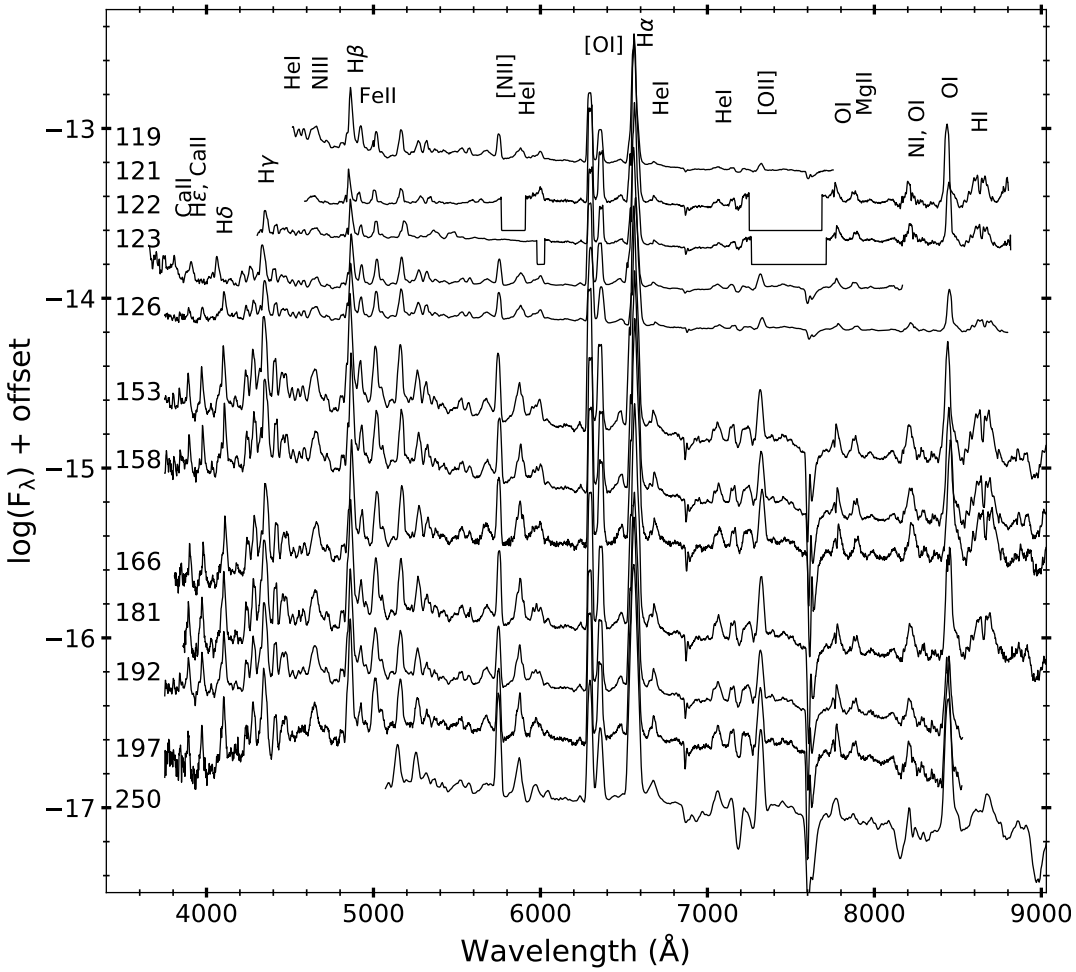

Figure 4.21: Low resolution optical spectroscopic evolution of V5856 Sgr from 21 Feb 2017 (day 119) to 02 Jul 2017 (day 250). The identified lines and time since outburst in days (numbers to the left) are marked.

lines and corresponding χ^2 values are given in Table 4.17. The values of best-fit parameters obtained from model are given in Table 4.18. The estimated abundance values show that nitrogen, oxygen and iron were over abundant compared to solar, while helium and carbon have solar abundance values. The ejected mass is found to be of the order of 10^{-4} $M_\odot$. The best-fit synthetic spectrum corresponding to the observed spectrum is as shown in *middle* panel of Fig. 4.20.

The geometry of the ionized structure obtained using pyCloudy was found to be bipolar conical structures with equatorial rings (*left* panel of Fig. 4.23). The hydrogen Balmer emission is coming from all the regions, while the Fe II and [O I] emission from the equatorial rings. The cones were formed due to the [N II] and N II emission. The inclination angle of the system was found to be $9^\circ \pm 0.85^\circ$.

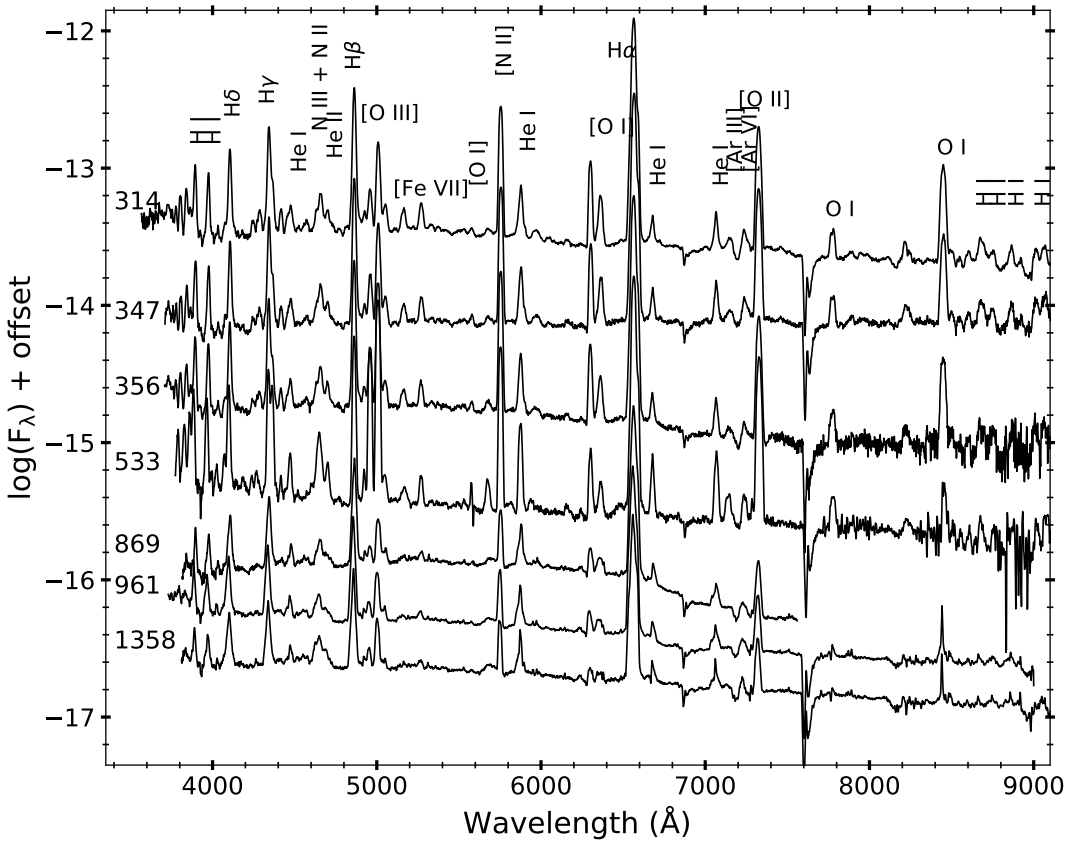

Figure 4.22: Low resolution optical spectroscopic evolution of V5856 Sgr from 04 Sept 2017 (day 314) to 14 Jul 2020 (day 1358). The identified lines and time since outburst in days (numbers to the left) are marked.

Morphokinematic analysis using SHAPE was performed using the observed Hα velocity profile of day 189. The synthetic Hα velocity profile for V5856 Sgr was generated using asymmetric bipolar conical structures with equatorial rings (*left* panel of Fig. 4.24). The radius of the bigger cone was found to be 1×10^{14} m with an opening angle of 31.89° while the smaller cone has a base radius of 7×10^{13} m and an opening angle of 15.94°. The blue component was found to be 70% less brighter than that of the red component. The best-fit velocity profile corresponding to the observed profile is as shown in the *left* panel of Fig. 4.25. The best-fit inclination angle was found to be $8.5° \pm 0.75°$.

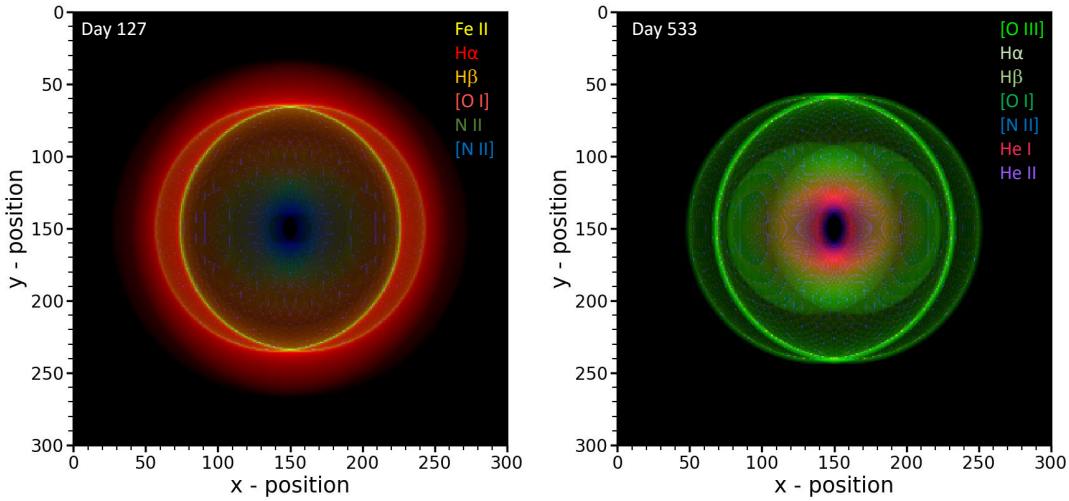

Figure 4.23: Morphology of the ejecta of V5856 Sgr obtained using the optical spectrum in the two-dimensional plane with X-axis being the line-of-sight direction and Y being the axis perpendicular to that of the plane of sky and line-of-sight. The lines corresponding to different colours are marked to show the spatial distribution of emission in the structure. Here, 1 unit of x and y correspond to 3.55×10^{13} cm for day 175 (*left* panel) and 8.71×10^{13} cm for day 692 (*right* panel).

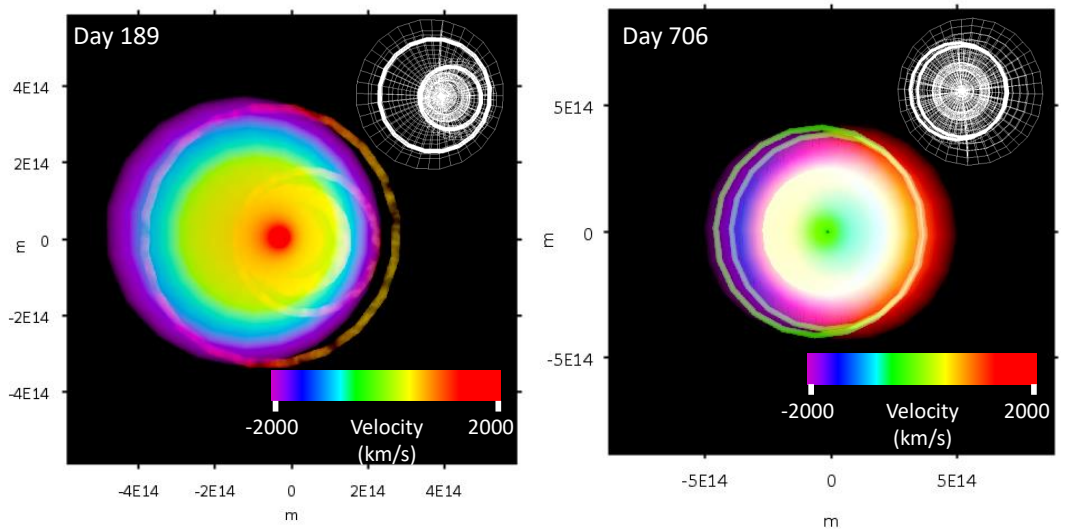

Figure 4.24: Asymmetric bipolar geometry of the ejecta of V5856 Sgr in the two-dimensional plane with X-axis being the line-of-sight direction and Y being axis perpendicular to that of the plane of sky and line-of-sight, and color gradient being the velocity values varying along the line-of-sight direction. The structure is obtained using the velocity profile of Hα obtained on day 189 (*left* panel) and day 706 (*right* panel). The grid structure is plotted in the *top-right* of each panel.

Table 4.17: Observed and best-fit CLOUDY model line flux ratios[a] for day 127 of V5856 Sgr

Line ID	λ (Å)	**Observed**	**Modelled**	χ^2
H I	3889	4.26E-01	1.49E-01	2.72E+00
H I	3970	3.70E-01	2.32E-01	4.68E-01
H I	4102	4.46E-01	2.18E-01	6.92E-01
Fe II	4179	6.04E-02	3.21E-02	8.09E-03
Fe II	4233	1.76E-01	2.08E-01	3.41E-02
Fe II	4297	4.02E-01	2.42E-01	3.58E+00
Fe II	4352	1.04E+00	3.19E-01	5.08E+00
Fe II	4417	2.19E-01	1.95E-01	6.76E-03
Fe II	4491	1.41E-01	5.68E-01	9.05E-02
Fe II	4549	5.15E-02	4.79E-02	5.34E-04
Fe II	4556	4.31E-02	7.64E-01	8.49E+00
Fe II	4584	7.45E-02	7.27E-02	6.28E-04
H I	4861	1.00E+00	1.00E+00	0.00E+00
Fe II	4924	3.02E-01	1.22E-01	7.35E-01
Fe II	5018	3.79E-01	4.82E-01	1.13E-01
Fe II	5169	4.15E-01	4.38E-01	7.23E-03
Fe II	5265	1.93E-01	3.49E-01	9.04E-01
Fe II	5317	1.43E-01	1.07E-01	2.81E-02
Fe II	5363	4.14E-02	9.03E-02	7.57E-02
Fe II	5425	1.46E-02	2.91E-02	3.11E-03
Fe II	5535	7.34E-02	5.12E-02	5.76E-03
[O I]	5577	4.95E-02	2.30E-01	6.24E-01
N II	5679	1.55E-01	1.84E-02	2.49E-01
[N II]	5755	3.22E-01	3.04E-01	5.97E-03
Na I	5890	2.68E-01	1.29E-01	8.28E-01
Fe II	5991	1.94E-01	2.22E-02	4.84E-01
Fe II	6148	5.36E-02	2.70E-02	2.65E-02
Fe II	6248	2.13E-02	1.64E-02	1.13E-03
[O I]	6300	1.48E+00	1.11E+00	2.01E+00
[O I]	6363	5.73E-01	3.28E-01	5.94E-01
H I	6563	2.02E+00	3.03E+00	1.27E+01
He I	6678	1.10E-02	4.81E-01	9.26E-02
He I	7065	1.17E-01	8.93E-02	1.77E-01
C II	7235	1.57E-01	1.13E-02	2.66E-01
[O II]	7320	1.77E-01	1.75E-01	1.93E-04
N II	7452	2.93E-02	1.29E-01	1.37E-01
N I + O I	8212	1.10E-01	2.19E-02	2.06E-01

[a] Relative to Hβ

4.7.3 Nebular phase

The evolution of the spectra in nebular phase (t = 314 to 1358) is given in Fig. 4.22. The high ionization forbidden lines are prominent in this phase. The spectra

Table 4.18: Best-fit CLOUDY model parameters obtained on day 127 of V5856 Sgr

Parameter	**Day 127**
T_{BB} ($\times 10^5$ K)	1.73 ± 0.11
Luminosity ($\times 10^{37}$ erg s^{-1})	9.83 ± 0.09
Clump Hydrogen density ($\times 10^{10}$ cm^{-3})	1.00
Diffuse Hydrogen density ($\times 10^{9}$ cm^{-3})	3.16
Covering factor (clump)	0.85
Covering factor (diffuse)	0.15
α	-3.00
Inner radius ($\times 10^{15}$ cm)	1.07
Outer radius ($\times 10^{15}$ cm)	3.55
Filling factor	0.1
He/He$_\odot$	1.00 ± 0.07 (2)[a]
N/N$_\odot$	1.57 ± 0.13 (4)
O/O$_\odot$	1.89 ± 0.10 (4)
C/C$_\odot$	1.00 ± 0.12 (1)
Fe/Fe$_\odot$	1.43 ± 0.09 (20)
Ejected mass ($\times 10^{-4}$ M$_\odot$)	3.43
Number of observed lines (n)	37
Number of free parameters (n_p)	10
Degrees of freedom (ν)	27
Total χ^2	41.49
χ^2_{red}	1.54

[a]The number in the parenthesis is the number of lines used to determine abundance estimate.

consist of [O III] (4959 and 5007 Å), [Fe VII], [O I], He I, [Ar III], [Ar VI], [O II], [N II], hydrogen Balmer and Paschen lines. In the beginning of this phase, [N II] and [O II] are the prominent non-Balmer lines. Around day 500, [O III] lines become the prominent non-Balmer lines and the intensity of these lines decreases as the system approaches day 1358. The intensity of [O I] lines decrease significantly with respect to the hydrogen Balmer lines. Towards the end of this phase, the profiles have sharp peaked structures.

During this phase, day 533 in the nebular phase was modelled to obtain the physical conditions using CLOUDY. The central ionizing source was set at an effective temperature 2.5×10^5 K and luminosity 1.26×10^{38} erg s^{-1}. To model the observed spectrum, the medium was assumed to consist of a low-density diffuse component and a clump component. Most of the lines were fitted by the clump component, except a few forbidden lines like [O III], [N II] and [O I]. In order to fit all the lines, a

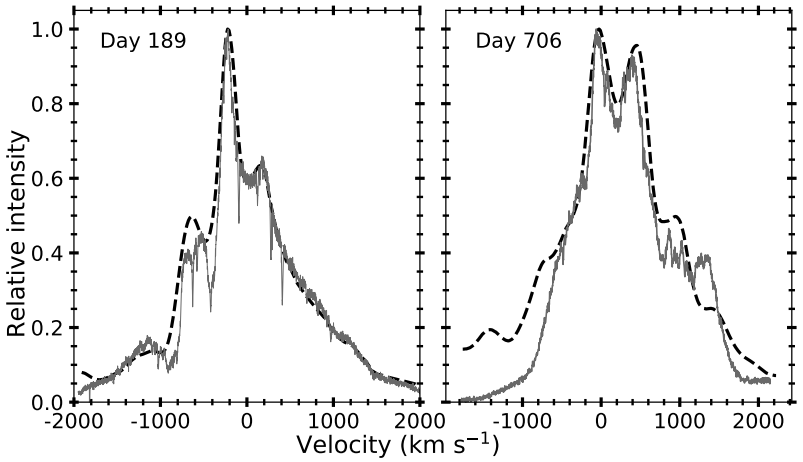

Figure 4.25: Best-fit velocity profiles (dash line) of Hα obtained using the morphokinematic analysis plotted over the observed profile (continuous line) on day 189 and 706 for V5856 Sgr.

diffuse region (low density) was used, covering 20% of the volume. The clump hydrogen density was 10^9 cm^{-3} and diffuse hydrogen density, 3.16×10^8 cm^{-3}. The relative fluxes of the observed lines, best-fit model predicted lines and corresponding χ^2 values are given in Table 4.19. The values of best-fit parameters obtained from model are given in Table 4.20. The estimated abundance values show that nitrogen, oxygen, iron and helium are more abundant compared to solar values. The ejected mass was found to be of the order of 10^{-4} M$_\odot$. The best-fit synthetic spectrum corresponding to the observed spectrum is as shown in *bottom* panel of Fig. 4.20.

The geometry of the ionized structure using pyCloudy was found to be bipolar conical structures with equatorial rings (*right* panel of Fig. 4.23). The hydrogen Balmer emission is coming from all the regions, while the [O III] and [O I] emission from the equatorial rings. The conical base is formed due to the [N II] emission and He I and He II are from inner cone regions. The inclination angle of the system was found to be $8.91^\circ \pm 0.53^\circ$. For days 127 and 533, the details on the extent of all the components and their distance from central source in the morphology of the ejecta are given in Table 4.21.

The morphokinematic analysis using SHAPE was performed using the observed Hα velocity profile of day 706. The synthetic Hα velocity profile for V5856 Sgr was generated using asymmetric bipolar conical structures with equatorial rings (*right* panel of Fig. 4.24). The radius of the bigger cone was found to be 5×10^{14} m with

Table 4.19: Observed and best-fit CLOUDY model line flux ratios[a] for day 533 of V5856 Sgr

Line ID	λ (Å)	**Observed**	**Modelled**	χ^2
H I	3798	1.03E-01	3.48E-02	7.22E-02
H I	3835	1.46E-01	2.56E-01	1.40E+00
H I	3889	2.71E-01	1.66E-01	7.39E-01
H I	3970	2.43E-01	2.77E-01	3.39E-02
H I	4102	3.56E-01	1.72E-01	9.24E-01
He II	4200	4.86E-03	4.68E-02	4.41E-02
C II	4267	2.69E-02	7.58E-02	5.35E-02
H I	4340	8.79E-01	9.51E-01	6.91E-01
He I	4471	7.22E-02	1.78E-01	1.80E-01
N III	4638	2.55E-01	4.96E-01	1.24E+00
He I	4713	7.39E-02	1.25E-01	4.61E-02
H I	4861	1.00E+00	1.00E+00	0.00E+00
[O III]	4959	1.00E+00	7.58E-01	1.98E+00
[O III]	5007	3.19E+00	3.52E+00	2.44E+00
[Fe II]	5159	5.44E-02	3.60E-02	1.04E-02
[Fe II]	5262	4.11E-02	1.67E-02	1.59E-02
[O I]	5577	6.57E-01	5.19E-01	2.49E+00
[N II]	5755	1.03E+00	1.31E+00	4.99E+00
He I	5876	2.34E-01	4.18E-01	2.53E+00
[O I]	6300	1.07E-01	3.09E-01	7.44E-01
[O I]	6363	4.10E-02	1.73E-01	9.64E-01
H I	6563	4.19E+00	4.61E+00	2.75E+00
He I	6678	7.83E-02	2.93E-01	9.57E-01
He I	7065	1.16E-01	4.16E-01	3.51E+00
[Fe II]	7155	3.59E-02	1.74E-01	8.34E-01
C II	7235	3.21E-02	1.71E-01	2.17E-01
[O II]	7320	1.14E+00	1.47E+00	4.54E+00
H I	8665	2.13E-02	1.70E-01	2.46E-01

[a] Relative to Hβ

an opening angle of 90° while the smaller cone has a base radius of 10^{14} m and an opening angle of 31.89°. The blue components were found to be 81% less bright than that of the red components. The best-fit velocity profile corresponding to the observed profile is as shown in the *right* panel of Fig. 4.25. The best-fit inclination angle was found to be $8.3° \pm 0.54°$.

Using Eqns. 3.2 and 3.3, the optical depth τ of the ejecta for [O I] 6300 Å and the electron temperature T_e calculated using the estimated value of τ is as shown in Fig. 4.26. It is seen that both the values increase post day 800 in this system.

High resolution data were also obtained for V5856 Sgr on days 180, 189 and 706. The prominent velocity line profiles are as shown in Fig. 4.27. The emission line profiles were found to be complex in nature, and most of them are asymmetrical.

Table 4.20: Best-fit CLOUDY model parameters obtained on day 533 of V5856 Sgr

Parameter	**Day 533**
T_{BB} ($\times 10^5$ K)	1.58 ± 0.11
Luminosity ($\times 10^{38}$ erg s^{-1})	1.00 ± 0.14
Clump Hydrogen density ($\times 10^9$ cm^{-3})	1.00
Diffuse Hydrogen density ($\times 10^8$ cm^{-3})	3.16
Covering factor (clump)	0.80
Covering factor (diffuse)	0.20
α	-3.00
Inner radius ($\times 10^{14}$ cm)	5.25
Outer radius ($\times 10^{15}$ cm)	8.71
Filling factor	0.1
He/He$_\odot$	1.65 ± 0.10 (5)[a]
N/N$_\odot$	3.34 ± 0.12 (2)
O/O$_\odot$	4.41 ± 0.09 (6)
Ejected mass ($\times 10^{-4}$ M$_\odot$)	3.40
Number of observed lines (n)	28
Number of free parameters (n_p)	10
Degrees of freedom (ν)	18
Total χ^2	34.65
χ^2_{red}	1.93

[a]The number in the parenthesis is the number of lines used to determine abundance estimate.

There are two absorption components present in the Hα and Hβ velocity profiles. On day 180, the two components are present at -150 km s^{-1} and -500 km s^{-1} for Hβ and at -250 km s^{-1} and -700 km s^{-1} for Hα implying that the absorption is limited to the low-velocity regions. On day 189, the same absorption components are present

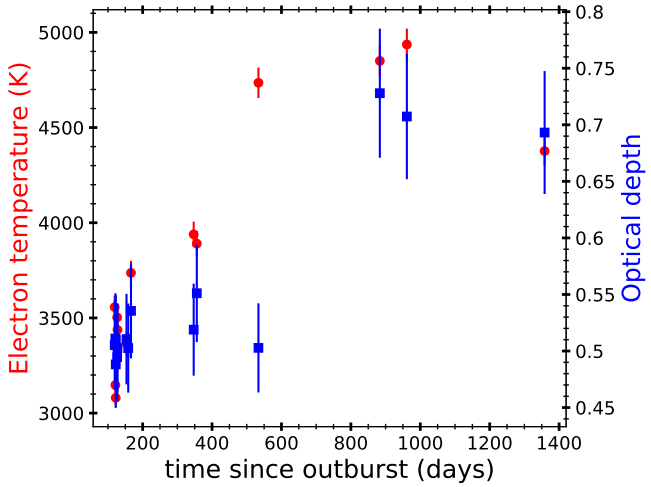

Figure 4.26: Evolution of optical depth for [O I] (6300) and electron temperature of the ejecta of V5856 Sgr from 21 Feb 2017 (day 119) to 14 Jul 2020 (1358).

Table 4.21: Details of the morphology of the ejecta on days 127 and 533 for V5856 Sgr

Epoch	**Component**	**Extent**[a] **($\times 10^{15}$ cm)**	**Radius ($\times 10^{15}$ cm)**	**Distance**[b] **($\times 10^{15}$ cm)**	**Angle**[c] **(°)**
Day 127	Cone	2.49 ± 0.10	1.78 ± 0.07	0.85 ± 0.03	63 ± 1.21
	Equatorial ring	-	3.02 ± 0.11	1.42 ± 0.08	-
Day 533	Cone	4.88 ± 0.13	6.10 ± 0.17	1.95 ± 0.09	68 ± 0.89
	Equatorial ring	-	9.76 ± 0.23	4.27 ± 0.11	-

[a]Extent of the component along the ejecta axis

[b]Distance from the central source to the component along the ejecta axis

[c]Outer opening angle of the cone

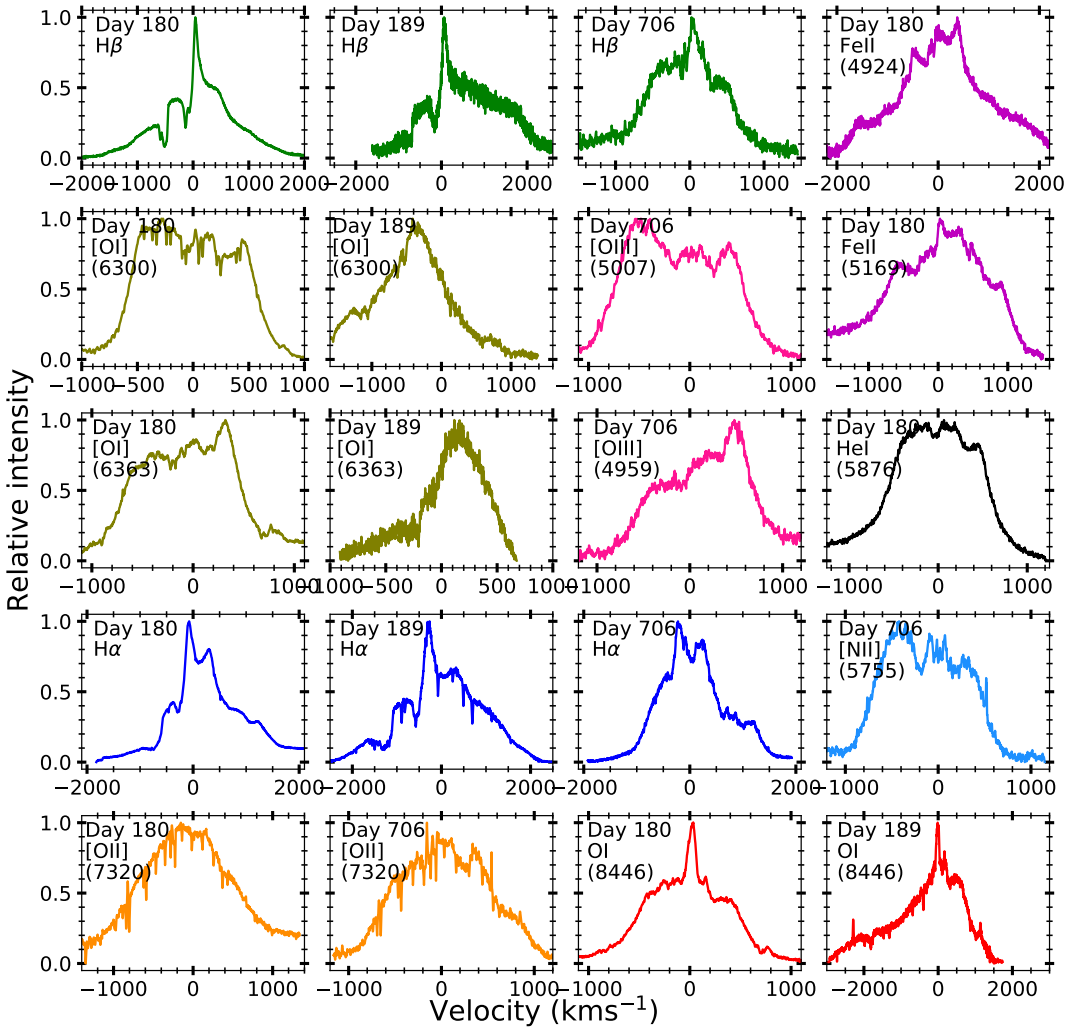

Figure 4.27: High resolution velocity profiles of V5856 Sgr obtained on days 180, 189 and 706 since outburst. The colour of the velocity profile represents a particular elemental line. The lines are labelled against each panel.

at -150 km s^{-1} and -750 km s^{-1} for Hβ and at -580 km s^{-1} and -1350 km s^{-1} for Hβ. There is a blue bump with 800 km s^{-1} on day 189 in Hα. A narrow emission

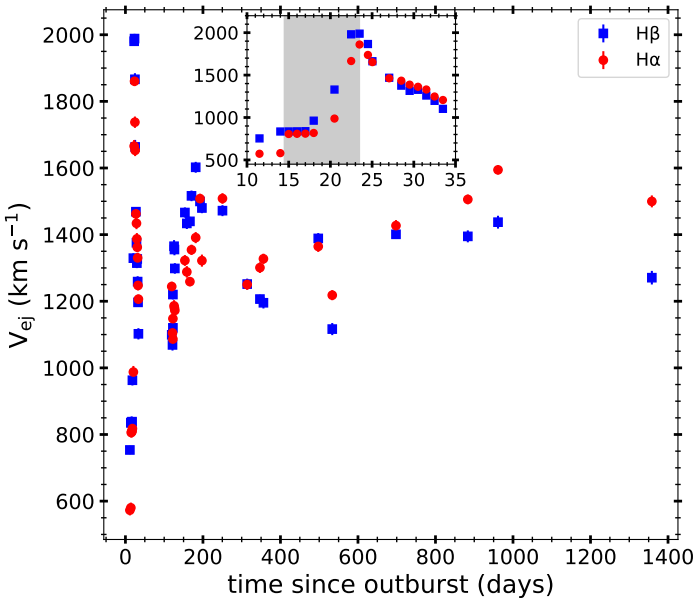

Figure 4.28: Evolution of Hα and Hβ FWHM velocities of V5856 Sgr from 05 Nov 2016 (day 11) to 14 Jul 2020 (day 1358). The zoomed-in region is from day 11 to day 35 and the grey region refers to γ-ray emission period.

peak is present in these epochs in the Hα, Hβ and O I profiles. On day 180, O I has bumps on either side of the peak, and the bump has evolved into wing-like on the left of the peak on day 189. The He I line has a three-peaked structure on day 180. On day 706, Hα and Hβ have bumps on either side, and Hα has a second peak around 250 km s^{-1} similar to day 180. It is interesting to note that the [O I] profiles of day 180 and [O III] of day 706 have remarkably similar structures with three peaks. The [N II] line also has three-peaked structure on day 706. The [O I] profiles of day 189 are very noisy, and only the brightest peak is visible clearly.

The evolution of observed FWHM velocities of Hα and Hβ lines are as shown in Fig. 4.28. There is sudden increase in the FWHM velocity of the both Hα and Hβ during the γ-ray emission period up to 2000 km s^{-1}. It is followed by a decline to about 1500 km s^{-1}. From $\sim$day 100, the FWHM velocities increases from 1000 to about 1400 km s^{-1} and remains around this value till $\sim$1400 days.

The morphology obtained on different epochs indicate that the system is bipolar and asymmetric with a very low inclination angle compared to other Fe II novae in the sample. The low inclination angle suggests that there is a strong connection

between the central system and the evolving geometry. The forbidden lines are distributed in the outer regions as rightly known that they do come from the optically thin ejecta (Table 4.21). The He lines are coming from the inner regions (Table 4.21). The [O III] and [O I] lines have similar profiles on different epochs, it is observed that they are coming from similar kind of regions (outer equatorial rings) at two different epochs (Fig. 4.23). The asymmetry observed in the line profiles is consistent with that seen in the morphokinematic morphology obtained (Fig. 4.24).

4.8 V3665 Oph

V3665 Oph (or Nova Oph 2018 No. 2 or TCP J17140253-2849233) was discovered on 2018 Mar 10 by Koichi Nishiyama and Fujio Kabashima at magnitude 9.5. The object was confirmed to be a Fe II type nova spectroscopically by Williams et al. (2018).

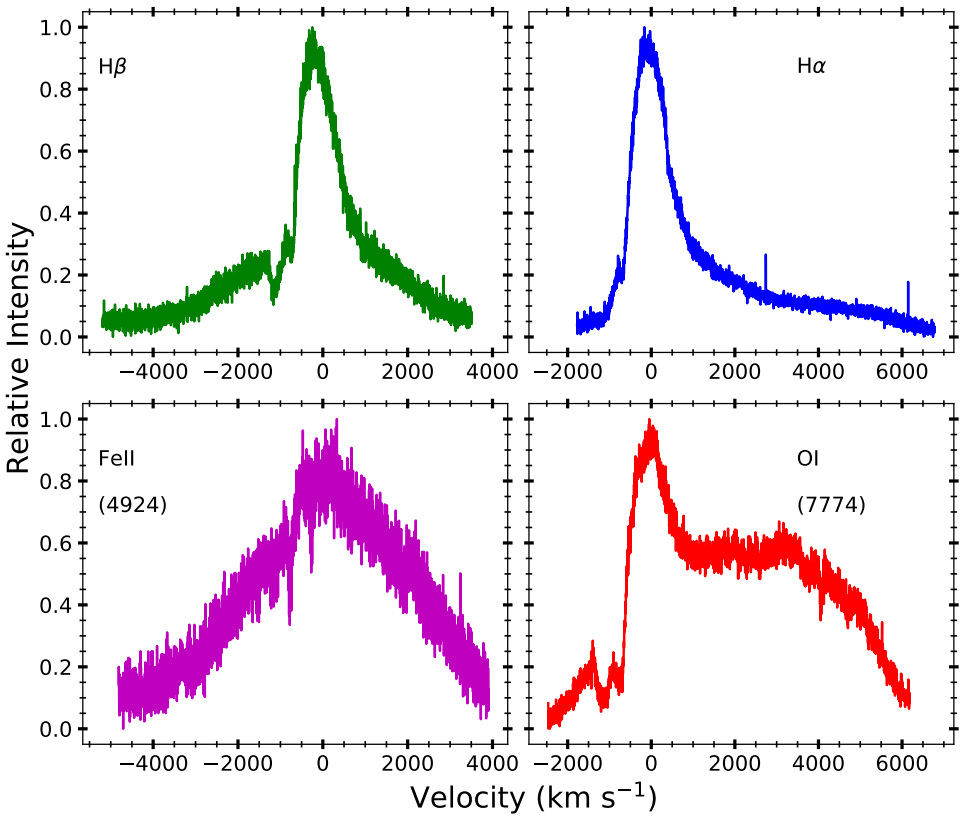

Figure 4.29: High resolution velocity profiles of V3665 Oph obtained on day 5. The profiles are labelled against each panel.

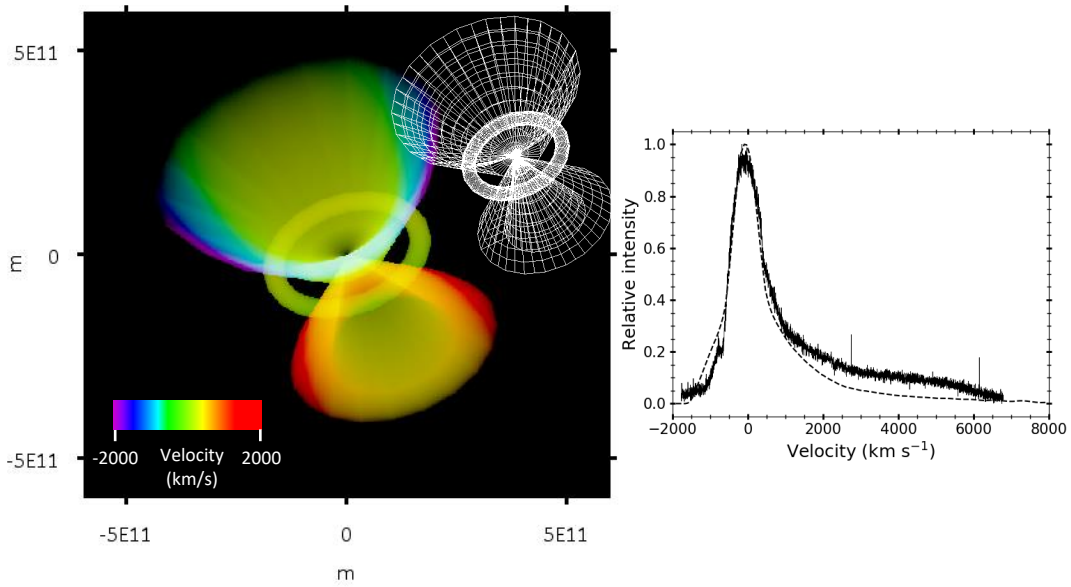

Figure 4.30: *Left:* Morphology of the ejecta of V3665 Oph obtained on day 5 using Hα velocity profile. It is plotted in the two-dimensional plane with X-axis being the line-of-sight direction and Y being the axis perpendicular to that of the plane of sky and line-of-sight with X and Y axes in meters and Z is velocity (marked in *bottom-left*) and grid structure (*top-right*) are shown. *Right:* Best-fit Hα velocity profile (dash line) over plotted on the observed profile (continuous line).

High resolution spectrum at R=60000 was obtained using HCT-HESP on 15 Mar 2018 (05 days since discovery). The spectrum consists of hydrogen Balmer, Fe II multiplets, N I and O I lines. The velocity profiles of Hβ, Fe II (4924), Hα and O I (8446) are plotted in Fig. 4.29. There are two absorption components present around -750 km s^{-1} and 1100 km s^{-1} in all the profiles. The O I profile has a broad bump-like structure towards red extending up to 4000 km s^{-1}. The Hα profile has a long tail towards the red extending up to 6000 km s^{-1}.

Morpho-kinematic analysis using SHAPE was performed using the observed Hα velocity profile. The synthetic Hα velocity profile for V3665 Oph was generated using asymmetric bipolar conical structures and an equatorial ring (Fig. 4.30). The base radius of the top conical frustum was found to be 3.5 $\times$ 10^{11} m with an opening angle of 30° and tip radius of 9.8 $\times$ 10^{10} m while the bottom cone is of 2.5 $\times$ 10^{11} m radius with an opening angle of 14°. The smaller cone was found to be 88% less bright than that of the bigger one. The equatorial ring was of 1.25 $\times$ 10^{11} m radius and 71% less bright than that of the bigger cone. The best-fit velocity

profile corresponding to the observed profile is as shown in Fig. 4.30. The best-fit inclination angle was found to be $45^\circ \pm 1.75^\circ$. During this epoch, the system is still in its optically thick phase, and hence the asymmetry is attributed here to the optical depth effects (Ribeiro et al. 2011 and references therein). The fast-moving material in the ejecta that is evident from the velocity profiles could give rise to equatorial ring.

4.9 V5857 Sgr

V5857 Sgr (Nova Sgr 2018 or PNV J18040967-1803581) was discovered on 2018 Apr 8 with a magnitude of 11.2 (Rupert et al., 2018). IR spectral observations revealed the presence of low excitation Na I lines implying the existence of cool zone by Joshi et al. (2018). Due to this, it was suggested to form dust in the system.

High resolution spectrum at R=30000 was obtained using HCT-HESP on 12 April 2018 (04 days since discovery). Spectrum obtained was noisy and consists

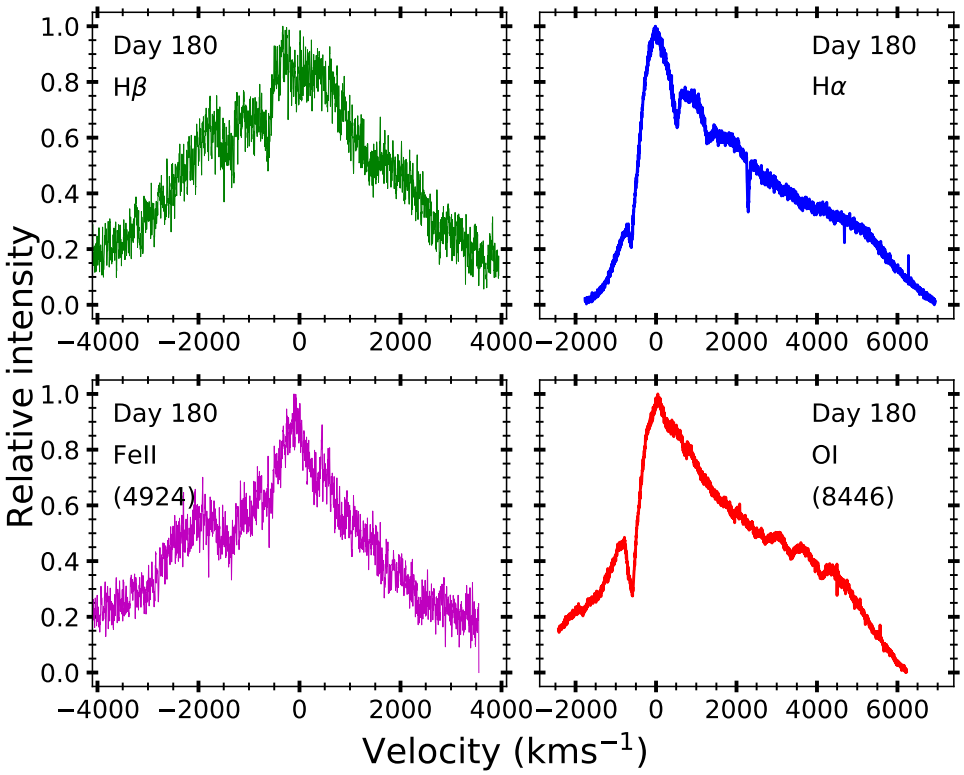

Figure 4.31: High resolution velocity profiles of V5857 Sgr obtained on day 4. The lines are marked against each panel.

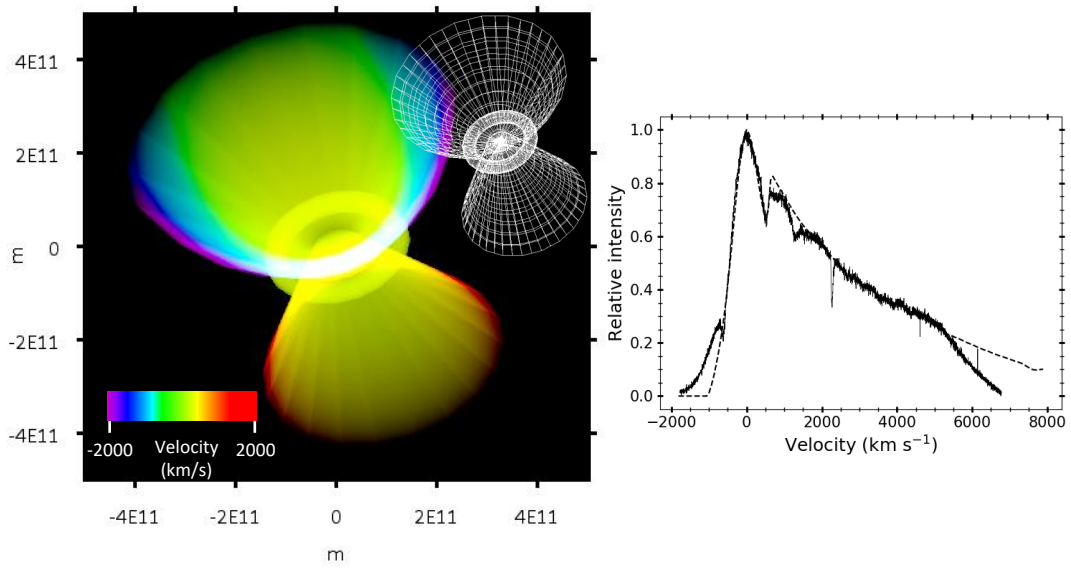

Figure 4.32: *Left:* Morphology of the ejecta of V5857 Sgr obtained on day 4 using Hα velocity profile. It is plotted in the two-dimensional plane with X-axis being the line-of-sight direction and Y being the axis perpendicular to that of the plane of sky and line-of-sight with X and Y axes in meters and Z is the velocity (marked in *bottom-left*), and grid structure (*top-right*) are shown. *Right:* Best-fit Hα velocity profile (dash line) overplotted on the observed profile (continuous line).

of hydrogen Balmer, Fe II multiplets and O I lines. The velocity profiles of Hβ, Fe II, Hα and O I are shown in Fig. 4.31. The line profiles of Fe II and Hβ are similar with absorption components at -600 km s^{-1} and -1400 km s^{-1}. There are several absorption components present in the line profiles of Hα and O I and a similar one at -600 km s^{-1}. The similarity in structure of the profiles indicates that they are originating from the same region.

Morpho-kinematic analysis using SHAPE was performed using the observed Hα velocity profile on day 4. The synthetic Hα velocity profile for V5857 Sgr was generated using asymmetric bipolar conical structures and an equatorial ring (left panel of Fig. 4.32). Both the top and bottom structures were conical frustums with base radii of 3.5 $\times$ 10^{11} and 2.5 $\times$ 10^{11} m with opening angles 30° and 14° respectively. The tip radii were found to be 9.5 $\times$ 10^{10} and 5 $\times$ 10^{10} m for the top and bottom cones respectively. The smaller cone was found to be 88% less bright than that of the bigger one. The equatorial ring is of 1.25 $\times$ 10^{11} m radius and 71% less bright than that of the bigger cone. The best-fit velocity profile corresponding to the observed

profile is as shown in the right panel of Fig. 4.32. The best-fit inclination angle is found to be $41^\circ \pm 3.35^\circ$. During this epoch, the system is still in its optically thick phase, and hence the asymmetry is attributed here to the optical depth effects (Ribeiro et al. 2011 and references therein). The fast-moving material in the ejecta that is evident from the velocity profiles could give rise to equatorial ring.

4.10 Summary

Analysis of nine Fe II class of novae are discussed. The temporal evolution of spectra of two novae are presented in detail. The morphology of the ejecta is obtained for all the novae.

During the outburst of V339 Del, the Fe II multiplets, O I, [O I] and hydrogen Balmer lines were present. As the optical depth decreases, many forbidden lines were present. The line profiles were round peaked initially followed by structured profiles. The optical depth τ of the ejecta for [O I] (6300) was about 0.5 throughout the evolution of the system. The mass of the WD was found to be 1.07 $M_\odot$.

During the outburst of classical nova V5856 Sgr, the $t_2(V)$ and $t_3(V)$ values were found to be 11.12 and 13.85 days respectively placing the system in the fast class of novae. The reddening $E(B-V)$ was found to be 0.19, and mass of the WD was found to be 1 $M_\odot$. The spectra were dominated by Fe II multiplets, Ca II, O I lines initially, followed by appearance of forbidden lines in the later phase. The line profiles were initially absorption ones which evolve into P-Cygni profiles and eventually emission line profiles. A sudden increase in the FWHM velocity of both Hα and Hβ during the γ-ray emission period up to 2000 km s^{-1} is observed.

The abundance values of five Fe II novae such as V2362 Cyg, V2676 Oph, V339 Del, V2944 Oph and V5856 Sgr were estimated using the spectral synthesis and plasma simulation code CLOUDY. During the optical thick phase, the elements like iron, oxygen and calcium abundance values were found be more than solar abundance values. As the novae evolved, the ejecta had nitrogen and helium abundance values more than that of solar values. In the case of V2676 Oph that was modelled

during the nebular phase, the ejecta had helium, oxygen, sulphur and argon values more than that of solar values.

All the Fe II class of novae in the sample have bipolar cone-like structures with or without equatorial rings with an inclination angle in the range of 40° – 65° except for V5856 Sgr which has an inclination angle of about 9°. The presence of cones and rings can be explained to be due to the wind interaction with the secondary or interaction of the ejecta with the pre-existing circumbinary material (Gill & O'Brien, 1999; O'Brien et al., 1995) or the interaction between the multiple ejecta. Origin of the forbidden lines like [O III] and [N II] are found to be from the outer regions implying that it is coming from the optically thin expanding shell. The helium lines are coming from the inner regions. The forbidden oxygen lines and Fe II present in the ejecta of any nova is predominantly contributed by the equatorial rings. The Fe II might be contributed mainly from the circumbinary material. [N II] lines when present, are coming either from the conical bases or the spheroidal frustum and are formed either due to the frictional interaction due to the presence of multiple ejecta or just from the optical thin outer regions.

5

"He/N" class of novae

The He/N class of novae are those events in which the most prominent non-Balmer lines in the early post-maximum phase are due to helium and nitrogen. The spectra, in general, consist of higher excitation lines compared to those of the Fe II class. The P-Cygni profiles are usually absent, and if present, are weak. The line profiles are broad and boxy/flat-top suggesting discrete shell ejection. These novae evolve faster over a timescales of days with the early nebular spectra, some showing dominant high ionization coronal lines while some show Ne III lines and some do not show any forbidden lines.

In this chapter, the analysis of two He/N novae V477 Sct and M31N 2008-12a are discussed. The multi-wavelength temporal evolution of M31N 2008-12a is presented in detail. Both novae were modelled using the spectral synthesis and plasma simulation code CLOUDY to understand the physical conditions of the system such as source luminosity, effective temperature, density and elemental abundances. To obtain the morphology of the ejecta of both the novae, pyCloudy and SHAPE were used.

5.1 V477 Sct

V477 Sct (Nova Scuti 2005 No. 2) was discovered on 2005 Oct 11.026 UT by Pojmanski et al. (2005) with a discovery magnitude of $V = 12$. The characteristic decline timescales for the system was found to be $t_2(V) = 3$ and $t_3(V) = 6$ days, placing the nova in the very fast nova category similar to novae V556 Ser and V838 Her. The NIR spectrum obtained on day 4 by Das et al. (2005) revealed prominent hydrogen Paschen and Brackett series along with O I lines with FWZI of Paβ being $\gtrsim$ 6000 km s^{-1}. On day 6, the optical spectrum by Fujii & Yamaoka (2005) consisted of broad emission lines of Hα, Hβ and O I lines with red continuum and FWHM velocity of Hα being 2900 km s^{-1}. Munari et al. (2006) identified at least five ripples in the high resolution emission line profiles at radial velocities ranging from -980 to +700 km s^{-1} obtained on day 16. The low resolution spectrum obtained on day 16 by Munari et al. (2006) consisted of hydrogen Balmer, He I, N II, N III, O I, [O I] and [O II] lines. The NIR spectrum obtained on day 35 by Mazuk et al. (2005) showed the presence of strong lines such as O I, H I, He I with weak emission from He II lines. The mass of the WD was found to be 1.3 M$_\odot$ by Hachisu & Kato (2007).

Low resolution optical spectrum from HCT was obtained on 23 Nov 2005 (43 days since discovery). The spectrum consists of hydrogen Balmer, He I, He II, N II, N III, O I, [O II] and [O III] lines, with FWHM velocities of Hα and Hβ being 2700 km s^{-1} and 3250 km s^{-1} respectively. The prominent non-Balmer emission is from O I λ8446 line. The presence of forbidden lines indicates that the ejecta is optically thin. The emission line profiles are multiple-peaked, broad and boxy indicating shell ejection in this system. The hydrogen Balmer and O I lines have similar profiles indicating that they are arising from same regions.

The observed spectrum was modelled using CLOUDY. The central ionizing source was set at an effective temperature of 2×10^5 K and luminosity 10^{37} erg s^{-1}. The medium was assumed to be of a low-density diffuse component and a clump component to obtain a modelled spectrum. Most of the lines were fitted by the clump component, except a few lines like [N II] (5755 Å), He I and He II. A diffuse region

Table 5.1: Observed and best-fit CLOUDY model line flux ratios[a] for day 43 of V477 Sct

Line ID	λ (Å)	**Observed**	**Modelled**	χ^2
H I	3970	8.70E-01	6.09E-01	8.76E-01
H I	4102	8.09E-01	7.41E-01	1.37E-01
H I	4340	7.89E-01	1.33E+00	5.11E+00
He I	4471	1.26E-01	4.30E-01	1.30E+00
N III	4638	5.69E-01	6.83E-01	2.12E-01
H I	4861	9.97E-01	1.00E+00	2.08E-04
[O III]	4959	6.54E-02	1.95E-01	6.19E-01
[O III]	5007	8.54E-01	3.16E-01	3.55E+00
N II	5679	1.52E-01	8.12E-02	1.12E-01
He I	5876	4.40E-01	9.57E-01	3.51E+00
Na I	6159	3.65E-02	6.68E-03	2.69E-02
H I	6563	6.45E+00	7.05E+00	3.46E+00
He I	6678	1.18E-01	2.79E-01	4.70E-01
He I	7065	3.93E-01	3.12E-01	1.55E-01
C II	7235	1.18E-01	3.58E-01	1.60E+00
[O II]	7320	8.05E-02	2.42E-01	2.91E-01
N I	8212	9.53E-02	1.62E-01	8.01E-02

[a] Relative to Hβ

(low-density) was used to fit all the lines, covering 20% of the volume. The clump hydrogen density was 1.59 $\times$ 10^{11} cm^{-3} and diffuse hydrogen density 5.62 $\times$ 10^{10} cm^{-3}. The relative fluxes of the observed lines, the best-fit model predicted lines, and corresponding χ^2 values are given in Table 5.1. The values of best-fit parameters obtained from the model are given in Table 5.2. The estimated abundance values show that helium, nitrogen and oxygen are over-abundant compared to solar, while other elements have solar abundance values. The ejected mass was found to be 1.67 $\times$ 10^{-5} M$_\odot$.

The geometry of the nova ejecta obtained using pyCloudy was found to be bipolar in nature and it had bipolar cones with equatorial rings (*top-left* panel of Fig. 5.1). The hydrogen emission is from all the regions while [O III] emission is from the bipolar structures. [N II] emission is predominantly from the equatorial rings. The He II (4686 Å) and He I lines are coming from the inner conical structures. The inclination angle of the system was found to be 82.30° $\pm$ 1.84°. The details on the extent of all the components and their distance from the central source in the

Table 5.2: Best-fit 1D CLOUDY model parameters on day 43 for V477 Sct

Parameter	**Day 43**
T_{BB} ($\times 10^5$ K)	2.0 ± 0.06
Luminosity ($\times 10^{37}$ erg s^{-1})	1.00 ± 0.14
Clump Hydrogen density ($\times 10^{11}$ cm^{-3})	1.59
Diffuse Hydrogen density ($\times 10^{10}$ cm^{-3})	5.62
Covering factor (clump)	0.8
Covering factor (diffuse)	0.2
α	-3.00
Inner radius ($\times 10^{14}$ cm)	4.57
Outer radius ($\times 10^{15}$ cm)	1.52
Filling factor	0.1
$N/N_\odot$	3.48 ± 0.12 (3)[a]
$O/O_\odot$	2.45 ± 0.08 (1)
$He/He_\odot$	2.14 ± 0.09 (6)
Ejected mass ($\times 10^{-5}$ M$_\odot$)	1.67
Number of observed lines (n)	17
Number of free parameters (n_p)	4
Degrees of freedom (ν)	13
Total χ^2	21.50
χ^2_{red}	1.65

[a]The number in the parenthesis is the number of lines used to determine abundance estimate.

morphology of the ejecta are given in Table 5.3.

As this system had an interesting emission line profile with multiple peaks and intriguing enhanced bipolar 3D pseudo structure of the ejecta, the low resolution Hα observed velocity profile was used to obtain morpho-kinematic structure for the ejecta using SHAPE. Morphology of the ejecta obtained was found to be similar to that obtained in pyCloudy. It had enhanced bipolar structure with cones and equatorial rings. However, the structure was slightly asymmetric in nature (*bottom-left*

Table 5.3: Details of the morphology of the ejecta on day 43 for V477 Sct

Component	**Extent**[a] **($\times 10^{14}$ cm)**	**Radius ($\times 10^{14}$ cm)**	**Distance**[b] **($\times 10^{14}$ cm)**	**Angle**[c] **(°)**
Cone	1.09 ± 0.08	0.79 ± 0.01	0.36 ± 0.01	46 ± 0.98
Equatorial ring	-	3.64 ± 0.13	0.97 ± 0.01	-
Bipolar (enhanced)	4.85 ± 0.16	-	1.70 ± 0.10	-

[a]Extent of the component along the ejecta axis

[b]Distance from the central source to the component along the ejecta axis

[c]Outer opening angle of the cone

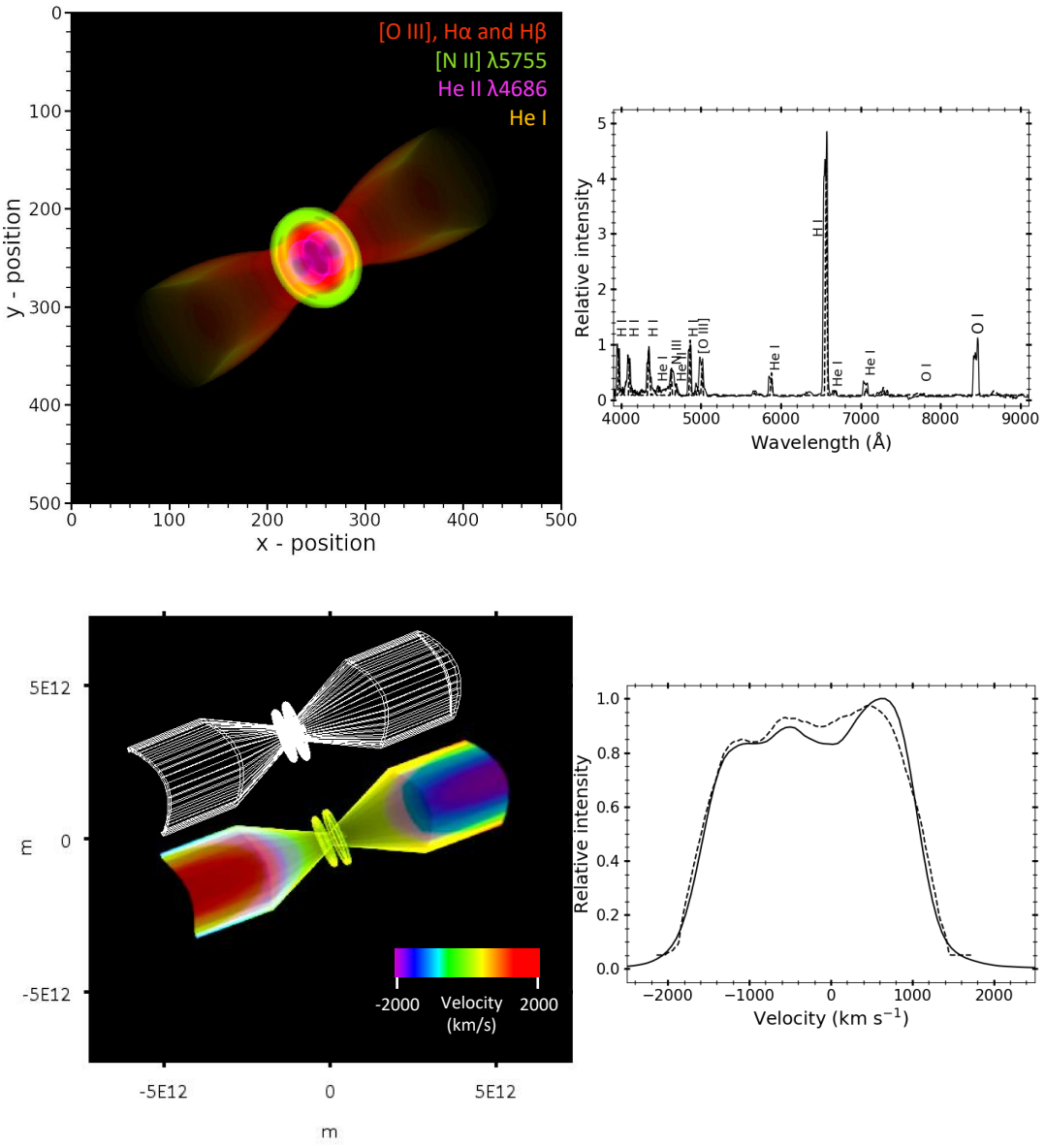

Figure 5.1: *Top-left:* Morphology of the ejecta of V477 Sct obtained on day 43 using the optical spectrum. It is plotted in the two-dimensional plane with X-axis being the line-of-sight direction and Y being the axis perpendicular to that of the plane of sky and line-of-sight. The lines corresponding to different colours are marked to show the spatial distribution of emission in the structure. Here, 1 unit of x and y correspond to 3.03×10^{12} cm. *Top-right:* Best-fit modelled spectrum (dash line) over plotted on the observed spectrum (continuous line). *Bottom-left:* Morphology of the ejecta of V477 Sct obtained using Hα velocity profile. It is plotted in the two-dimensional plane with X-axis being the line-of-sight direction and Y is the axis perpendicular to that of the plane of sky and line-of-sight with X and Y axes in meters and Z is velocity. The corresponding grid structure is shown in the *top*. *Bottom-right:* Best-fit Hα velocity profile (dash line) over plotted on the observed profile (continuous line).

panel of Fig. 5.1). The best-fit velocity profile corresponding to the observed profile is as shown in the *bottom-right* panel of Fig. 5.1. The best-fit inclination angle was

found to be $83^{\circ} \pm 3^{\circ}$. The multiple-peaks seen in the line profile can be attributed to the presence of enhanced bipolar nature and/or the projection effects of equatorial rings (Gill & O'Brien, 1999) present in the morphology.

5.2 M31N 2008-12a

M31N 2008-12a is an unusual RN, whose eruptions have been observed from 2008–2018 every year. It was first discovered during its 2008 eruption by Nishiyama & Kabashima (2008). From the 2014 eruption onwards, it has been monitored and studied in the multiwavelength regime to understand its short recurrence period and peculiar behaviour (Tang et al. 2014; Darnley et al. 2015; Henze et al. 2015; Darnley et al. 2016 and Henze et al. 2018). The optical spectral evolution was found to be similar during all the eruptions. The spectrum is dominated by Balmer, He and N lines. The optical light curve evolution from 2013 to 2015 outbursts were identical, the optical maximum is reached during day 0 to 1 since the eruption, then a linear decline in magnitude from day 1 to 4 followed by a plateau (approximately flat but jittery) from day 4 to 8, then the final decline. The plateau phase is consistent with the turn-on time of the supersoft X-ray source phase. A variation in the evolution was seen in the 2016 optical light curve in the form of a short-lived cuspy feature during the final rise phase. Henze et al. (2018) suggested this feature as photometric evidence of faster evolving polar ejecta. UV peak was observed before the optical peak. UV light curve for 2016 eruption had declined from its peak by day 3 since the eruption. From day 3, three plateaus were present from day 3–5, 6–8 and 9–12, followed by a short duration of rebrightening corresponding to the drop in X-ray flux, which disappeared on day 16. UV light curve is similar in all the eruptions except in 2016 when it faded faster. A peculiar dip in the X-ray light curve around day 11 was seen during the 2015 eruption. A shorter duration of SSS phase was noticed in the X-ray emission of 2016 eruption compared to previous eruptions. The peculiar behaviour of 2016 outburst was suggested to be due to a lower accretion rate seen prior to 2016 outburst (Henze et al., 2018). Based on the multiwavelength

Table 5.4: Observational log for optical photometric and spectroscopic data for the 2016 outburst of M31N 2008-12a.

Date (UT)	**Mode**	**Telescope**	**Filter**	**Magnitude**
2016-12-13.588	Spectroscopy	HCT-HFOSC	-	-
2016-12-14.534	Spectroscopy	HCT-HFOSC	-	-
2016-12-14.755	Photometry	HCT-HFOSC	*V*	20.03 $\pm$ 0.02
2016-12-14.722	Photometry	HCT-HFOSC	*R*	19.09 $\pm$ 0.03
2016-12-14.738	Photometry	HCT-HFOSC	*I*	18.80 $\pm$ 0.03
2016-12-15.679	Photometry	HCT-HFOSC	*B*	20.73 $\pm$ 0.09
2016-12-15.660	Photometry	HCT-HFOSC	*V*	20.98 $\pm$ 0.03
2016-12-15.638	Photometry	HCT-HFOSC	*R*	20.06 $\pm$ 0.03
2016-12-15.647	Photometry	HCT-HFOSC	*I*	19.42 $\pm$ 0.02

light curve modelling, Kato et al. (2015) concluded that the mass of the WD is 1.38 $M_{\odot}$.

Deep Hα imaging of the 2013 quiescence phase obtained using the Liverpool telescope revealed the presence of an elliptical shell with semi-major and semi-minor axes of $\sim 0''.3$ and $\sim 0''.2$ respectively (Darnley et al., 2015). Deep ground-based and HST observations by Darnley et al. (2019) further revealed a super remnant shell-like nebula around this nova with a projected size of 134 by 90 parsecs. Darnley et al. (2019) concluded that this kind of size and mass indicates that the system is undergoing eruption from millions of years. Also, this system was predicted to pass through Chandrashekar limit in less than 40 kyr by Darnley et al. (2017a).

In 2016, it was detected to be in outburst on Dec 12.48 UT with an unfiltered magnitude of 18.2 by Itagaki et al. (2016). The optical spectroscopic and photometric observations were obtained from 0.73 to 2.82 days since maximum during its 2016 outburst. In 2018, it was detected in outburst on Nov 06.80 UT at a magnitude of 19.15 $\pm$ 0.05 with the Liverpool telescope by Darnley et al. (2018). The optical photometric and spectroscopic observations during its 2018 outburst were obtained from 0.49 to 3.72 days since the maximum. UV and soft X-ray emission from day -0.14 to 18.03 days since maximum based on *Swift* archival data are used. The evolution of the system in the multiwavelength regime are discussed while comparing with the previous outbursts throughout this section. The time since maximum is considered as Δt for all the outbursts (2014–2016 and 2018).

Table 5.5: Observational log for optical photometric and spectroscopic data for the 2018 outburst of M31N 2008-12a.

JD	Date (UT)	Δt^a (days)	Filter	Exposure time (s)	Telescope
2458430.08	2018 Nov 07.58	0.49	B	1800	JCBT
2458430.06	2018 Nov 07.57	0.48	V	1200	JCBT
2458431.07	2018 Nov 08.57	1.48	V	300×3	HCT
2458431.05	2018 Nov 08.56	1.47	R	180×3	HCT
2458431.06	2018 Nov 08.55	1.46	I	150×3	HCT
2458431.25	2018 Nov 08.76	1.67	g	300×3	GIT
2458431.27	2018 Nov 08.77	1.68	r	300×3	GIT
2458431.21	2018 Nov 08.74	1.65	i	300×3	GIT
2458433.95	2018 Nov 10.78	3.69	g	900×3	GIT
2458433.96	2018 Nov 10.80	3.71	r	900×3	GIT
2458433.97	2018 Nov 10.81	3.72	i	900×3	GIT
Spectroscopic observations					
2458430.31	2018 Nov 07.81	0.72	...	2700	HCT
2458431.11	2018 Nov 08.61	1.52	...	3600	HCT

[a] time since maximum (t = 0 corresponds to 2018 Nov 7.09 UT)

5.2.1 Optical photometry and spectroscopy

$BVRI$ photometric values obtained during the 2016 outburst along with the observational log is as shown in Table 5.4. $BVRI$ photometric observations were carried out during the 2018 outburst from 0.49 to 1.46 days since maximum using JCBT and HCT, and gri observations were carried out from 1.67 to 3.72 days since maximum using GIT. The log of observations is given in Table 5.5. The photometric observations were combined with those of Kaur et al. (2018) and Tan & Gao (2018) for a detailed analysis. The photometric magnitudes obtained using JCBT, HCT and GIT are summarised in Table 5.6.

The 2018 light curve of the system is as shown in Fig. 5.2. A decrease in magnitude of about 0.4 is observed from Δt = 0 to 0.3 day in V band. This particular trend is also observed in BRI light curves (highlighted in grey in Fig. 5.2). This is followed by a slight increase in the magnitude of about 0.2 to 0.3 mag in $BVRI$ from Δt = 0.3 to 1 day. Then a linear decline in magnitude is observed from day 1 to 4 in all the filters with decline rates as given in Table 5.7. The evolution of the optical light curve of 2018 outburst of M31N 2008-12a is closer to the light curves of that

Table 5.6: Optical photometric observations of 2018 outburst of M31N 2008-12a.

Date (UT)	Telescope	Fliter	Magnitude
2018 Nov 07.58	JCBT	B	19.29 ± 0.28
2018 Nov 07.57	JCBT	V	18.78 ± 0.10
2018 Nov 08.57	HCT	V	19.27 ± 0.13
2018 Nov 08.56	HCT	R	19.11 ± 0.11
2018 Nov 08.55	HCT	I	18.83 ± 0.20
2018 Nov 08.76	GIT	g	19.60 ± 0.10
2018 Nov 08.77	GIT	r	19.15 ± 0.09
2018 Nov 08.74	GIT	i	19.28 ± 0.15
2018 Nov 10.78	GIT	g	21.08 ± 0.19
2018 Nov 10.80	GIT	r	20.82 ± 0.20
2018 Nov 10.81	GIT	i	20.27 ± 0.22

Table 5.7: Declining rate in Bessell $BVRI$ and SDSS gri bands obtained during 2018 outburst of M31N 2008-12a.

Filter	Decline rate (mag day^{-1})
B	0.75 ± 0.02
V	0.90 ± 0.04
R	0.85 ± 0.01
I	0.41 ± 0.02
g	0.82 ± 0.03
r	0.80 ± 0.04
i	0.61 ± 0.02

of 'S-class' novae (Strope et al., 2010). It is similar to the light curve of V4643 Sgr but with an early rebrightening. This kind of bump or rebrightening might be due to shock from a secondary ejection (Kato et al., 2009) or presence of two components namely central emission component due to an equatorial expansion of the ejecta and fast-evolving polar ejecta as suggested by Darnley et al. (2016, 2017b).

The apparent magnitude optical light curves for the outbursts 2014–2016 and 2018 are as shown in Fig. 5.3. The light curve post day 1 is similar in all the outbursts with a rapid linear decline in magnitude. The plateau phase post the decline was also found to be similar in all the outbursts where the data points are available. A short-lived cuspy feature was observed during the 2016 outburst by Henze et al. (2018). The magnitudes observed in 2016 continue to be higher than all the eruptions observed so far. During the 2018 outburst, there is a slight rebrightening of about 0.4 magnitude post-maximum which is not seen in the previous outbursts. The intrinsic

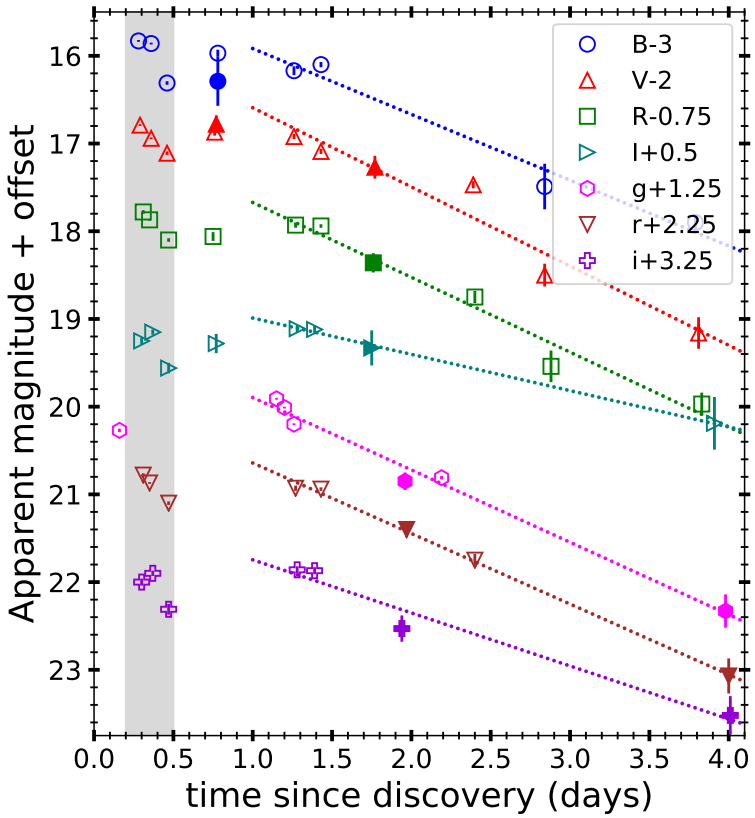

Figure 5.2: Apparent magnitude light curve of RN M31N 2008-12a in Bessell $BVRI$ and SDSS gri filters. The HCT, JCBT and GIT data (filled) are combined with other data (see Section 5.2.1 for details). Light curves are plotted with an offset.

colour evolution of 2014–2016 and 2018 outbursts are presented in Fig. 5.4. During all the outbursts, $(B-V)_0$ was found to decrease till day 3, followed by an increase to its initial value observed. The $(V-R)_0$ colour evolution shows that the emission is bluer corresponding to the slight dip in the light curve, and then the value of $(V-R)_0$ increases and decrease again followed by an increase till day 3.5. The $(V-R)_0$ colour evolution of 2018 outburst is different from other outbursts. The $(R-I)_0$ value increases in all the outbursts from 0 to 3.5 days.

Spectra obtained during 2016 and 2018 eruptions from HCT are as shown in the Fig. 5.5. The spectra are dereddened using $E(B-V) = 0.10$ (Darnley et al., 2017b). The optical spectra obtained during both the outbursts are dominated by the hydrogen Balmer lines. The spectra consists of hydrogen Balmer, He I (5018 Å, 5876 Å, 6678 Å, 7068 Å), He II (4686 Å) and N III (4638 Å) lines. The He II and N III lines are blended. The FWHM of the lines and the flux values for day 1.52 (2018

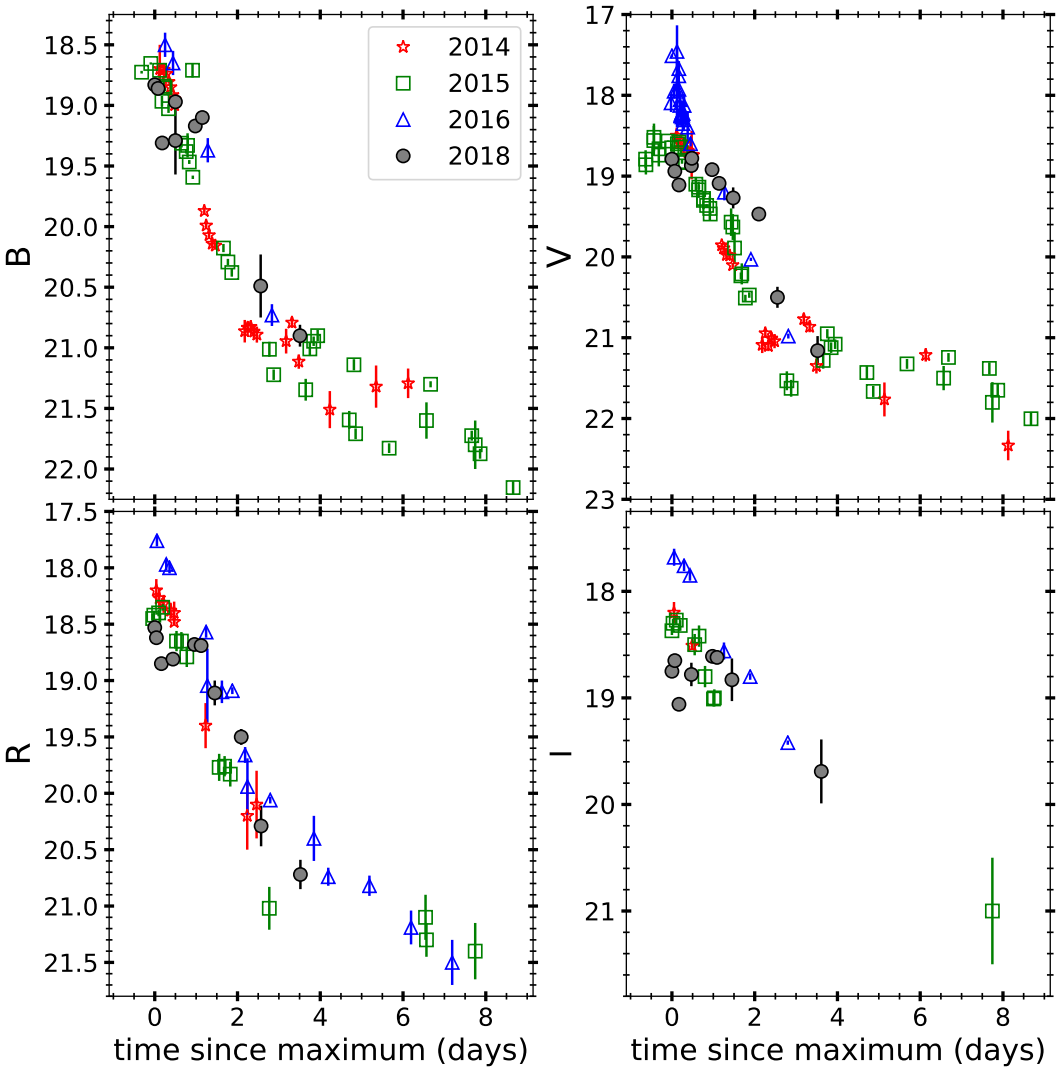

Figure 5.3: Apparent magnitude light curves for 2014, 2015, 2016 and 2018 outbursts of RN M31N 2008-12a. References– 2014: Darnley et al. (2015); 2015: Darnley et al. (2016); 2016: Henze et al. (2018).

Nov 8.61 UT) during the 2018 outburst are given in Table 5.8. The helium abundance of the ejecta for this system was estimated using intensity ratios of He I/Hβ and He II/Hβ. The line ratios and N(He)/N(H) values for both 2016 and 2018 outbursts are given in Table 5.9. The recombination coefficient values were obtained using the results from Hummer & Storey (1987) and Brocklehurst (1972), and Clegg (1987) was used for He I emissivity correction for collisional effects. N(He)/N(H) values obtained were found to be similar for 2016 and 2018 outbursts with a value of $\sim$0.50. This indicates that the ejecta was enriched in helium. The ejected mass using the hydrogen density values obtained from the spectrum was found to be (2.13$\pm$0.62)

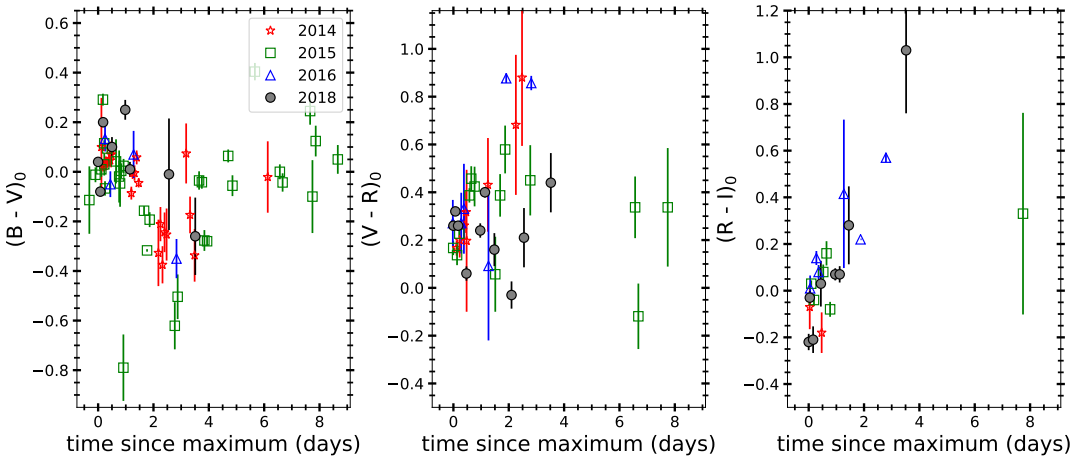

Figure 5.4: Evolution of intrinsic color terms of M31N 2008-12a during 2014, 2015, 2016 and 2018 outbursts.

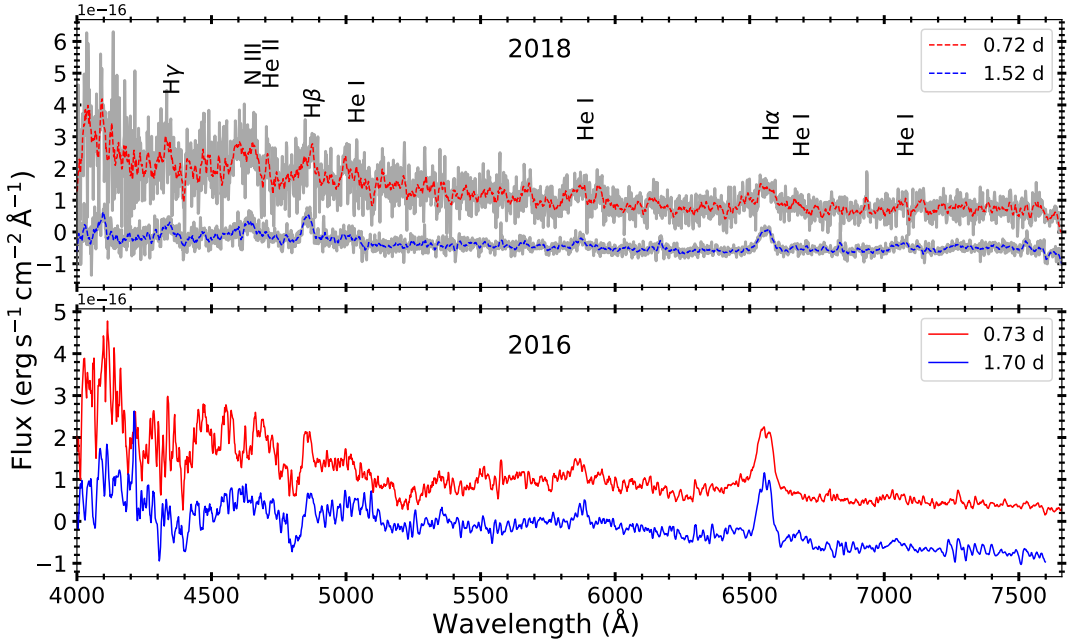

Figure 5.5: Optical spectra obtained from HCT during 2016 and 2018 outburst of M31N 2008-12a. Dashed line in the top panel refer to the smoothened spectra corresponding to continuous line (grey) for better visualization of emission lines.

$\times\ 10^{-8}\ M_{\odot}$.

The spectrum obtained on day 1.52 (2018 Nov 8.61) was used to model using CLOUDY. The central ionizing source was set at an effective temperature of 1.06×10^5 K and luminosity 10^{37} erg s^{-1}. The medium was assumed to be of a low-density diffuse component and a clump component to obtain a modelled spectrum. The clump hydrogen density was 10^{11} cm^{-3} and diffuse hydrogen density 10^{10} cm^{-3}.

Table 5.8: Line identifications and observed fluxes of 2018 outburst of RN M31N 2008-12a.

λ (Å)	**Identification**		**Flux** ($\times 10^{-15}$) (erg cm^{-2} s^{-1})	**FWHM** (km s^{-1})
4340	4335.18	H I	5.98 ± 0.33	2970 ± 90
4471	4469.38	He I	1.23 ± 0.13	1640 ± 28
4640	4638.04	N III	2.63 ± 0.39	2668 ± 46
4686	4676.82	He II	1.73 ± 0.23	608 ± 22
4861	4856.55	H I	10.8 ± 0.4	2257 ± 18
5876	5869.08	He I	5.82 ± 0.90	2507 ± 70
6563	6559.40	H I	18.4 ± 1.27	2554 ± 13
6678	6665.59	He I	2.37 ± 0.39	1341 ± 31
7068	7060.11	He I	3.39 ± 0.88	2003 ± 61

Table 5.9: Line ratios and helium abundance for 2016 and 2018 optical spectrum of M31N 2008-12a.

	2016	**2018**
Δt (days)	1.70[a]	1.52[b]
Flux ($\times 10^{-15}$ erg cm^{-2} s^{-1})		
Hα	10.06 ± 0.53	18.40 ± 1.52
Hβ	4.00 ± 0.71	10.8 ± 0.40
He I (5876 Å)	2.88 ± 0.10	5.82 ± 0.90
He I (6678 Å)	0.53 ± 0.12	2.37 ± 0.39
He I (7065 Å)	1.82 ± 0.18	3.39 ± 0.88
He II (4686 Å)	1.73 ± 0.23	1.17 ± 0.23
Line ratios		
Hα/Hβ	2.52	1.70
He I (5876)/Hβ	0.72	0.54
He I (6678)/Hβ	0.13	0.22
He I (7068)/Hβ	0.46	0.31
He II (4686)/Hβ	0.43	0.11
N(He^0)/N(H)		
Using He I (5876)	0.56	0.42
Using He I (6678)	0.36	0.61
N(He$^+$)/N(H)		
Using He II (4686)	0.04	0.01
N(He)/N(H)	0.46 ± 0.03	0.52 ± 0.02
Effective recombination coefficient ($\times 10^{-14}$ cm^2 s^{-1})		
Hβ	2.83	
He I (5876 Å)	3.64	
He I (6678 Å)	1.02	
He II (4686 Å)	30.78	

[a] time since maximum (t = 0 corresponds to 2016 Dec 12.58 UT)

[b] time since maximum (t = 0 corresponds to 2018 Nov 7.09 UT)

Table 5.10: Observed and best-fit CLOUDY model line flux ratios[a] for day 1.52 of 2018 outburst of M31N 2008-12a

Line ID	λ	**Observed**	**Modelled**	χ^2
H I	4340	5.54E-01	6.04E-01	9.45E-01
He I	4471	1.14E-01	1.99E-01	2.35E+00
He II	4686	1.60E-01	1.93E-01	1.14E+00
H I	4861	1.00E+00	1.00E+00	0.00E+00
He I	5876	5.40E-01	5.52E-01	1.59E-01
H I	6563	1.70E+00	1.50E+00	4.90E-01
He I	6678	2.19E-01	2.52E-01	4.52E-01
He I	7065	3.14E-01	4.03E-01	2.01E+00

[a]Relative to Hβ

The relative fluxes of the observed lines, the best-fit model predicted lines and corresponding χ^2 values are given in Table 5.10. The values of best-fit parameters obtained from the model are given in Table 5.11. The estimated abundance values show that nitrogen and helium were overabundant compared to solar abundance values. The ejected mass was found to be 7.21 $\times$ 10^{-8} $M_{\odot}$. The best-fit 1D spectrum obtained is shown in Fig. 5.6.

The morphology of the ejecta on day 1.52 during the 2018 outburst for the system using pyCloudy was found to be bipolar one with cones and an equatorial ring inclined at an angle of 81° $\pm$ 1.53°. The He I and He II lines are coming from the bipolar conical components (inner regions), and the hydrogen lines are coming from all the regions. The details on the extent and radii of all the components in the morphology of the ejecta are given in Table 5.12.

The morpho-kinematic analysis using SHAPE was also performed using the observed Hα and Hβ velocity profiles on day 1.52 during the 2018 outburst and He I, He II, Hα and Hβ velocity profiles on day 1.70 during the 2016 outburst. As the spectrum obtained during 2018 outburst was noisy, only Hα and Hβ were modelled. The He I 5876 Å line was modelled along with the Hα and Hβ lines during the 2016 outburst. The synthetic velocity profiles (Fig. 5.7) were generated using an asymmetric bipolar structure with bipolar cones and equatorial ring (Fig. 5.8). The radii of the red and blue cones of He I were found to be 8 $\times$ 10^9 m and 9 $\times$ 10^9 m with

Table 5.11: Best-fit CLOUDY model parameters obtained on day 1.52 for 2018 outburst of M31N 2008-12a

Parameter	**Day 1.52**
T_{BB} ($\times 10^5$ K)	1.06 ± 0.13
Luminosity ($\times 10^{37}$ erg s^{-1})	1.00 ± 0.09
Clump Hydrogen density ($\times 10^{11}$ cm^{-3})	1.00
Diffuse Hydrogen density ($\times 10^{10}$ cm^{-3})	1.00
Covering factor (clump)	0.80
Covering factor (diffuse)	0.20
α	-3.00
Inner radius ($\times 10^{13}$ cm)	1.11
Outer radius ($\times 10^{13}$ cm)	1.13
Filling factor	0.10
He/He$_\odot$	2.47 ± 0.11 (5)[a]
Ejected mass ($\times 10^{-8}$ M$_\odot$)	7.21
Number of observed lines (n)	8
Number of free parameters (n_p)	3
Degrees of freedom (ν)	5
Total χ^2	7.52
χ^2_{red}	1.51

[a]The number in the parenthesis is the number of lines used to determine abundance estimate.

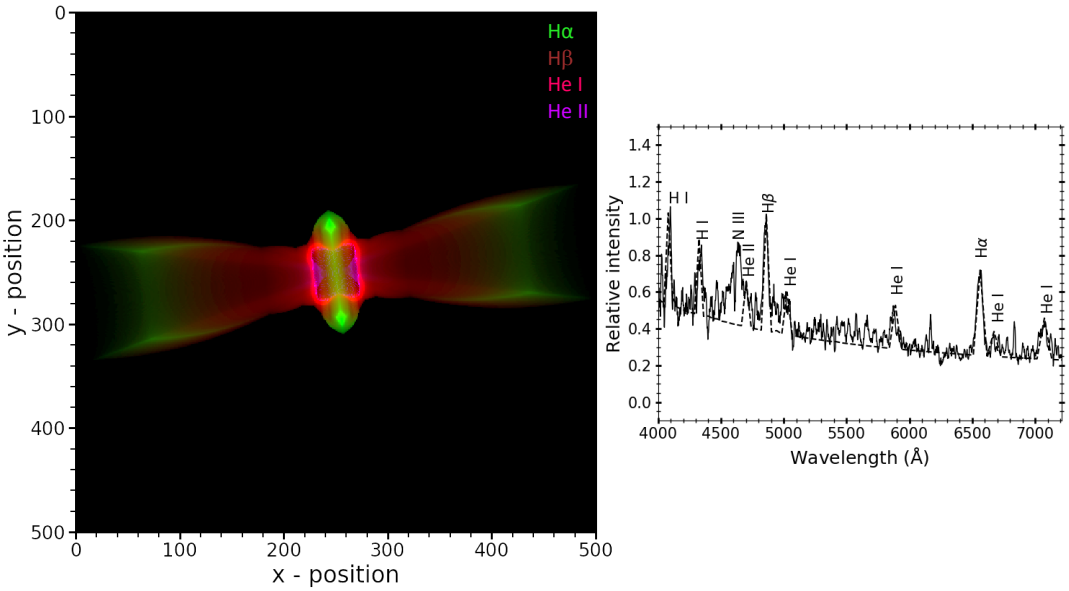

Figure 5.6: *Left:* Morphology of the ejecta of the 2018 outburst of M31N 2008-12a obtained on day 1.52 using the optical spectrum. It is plotted in the two-dimensional plane with *X*-axis being the line-of-sight direction and *Y* being the axis perpendicular to that of the plane of sky and line-of-sight. The lines corresponding to different colours are marked to show the spatial distribution of emission in the structure. Here, 1 unit of x and y correspond to 2.26×10^{10} cm. *Right:* Best-fit modelled spectrum (dash line) overplotted on the observed profile (continuous line).

Table 5.12: Details of the morphology of the ejecta on day 1.52 for M31N 2008-12a

Component	**Extent**[a] **($\times 10^{11}$ cm)**	**Radius ($\times 10^{11}$ cm)**	**Distance**[b] **($\times 10^{11}$ cm)**	**Angle**[c] **(°)**
Cone	3.62 ± 0.12	5.42 ± 0.14	2.71 ± 0.10	91 ± 1.10
Equatorial ring	-	1.27 ± 0.09	7.23 ± 0.19	-
Bipolar (enhanced)	45.2 ± 2.23	-	5.88 ± 0.16	-

[a]Extent of the component along the ejecta axis

[b]Distance from the centre to the component along the ejecta axis

[c]Outer opening angle of the cone

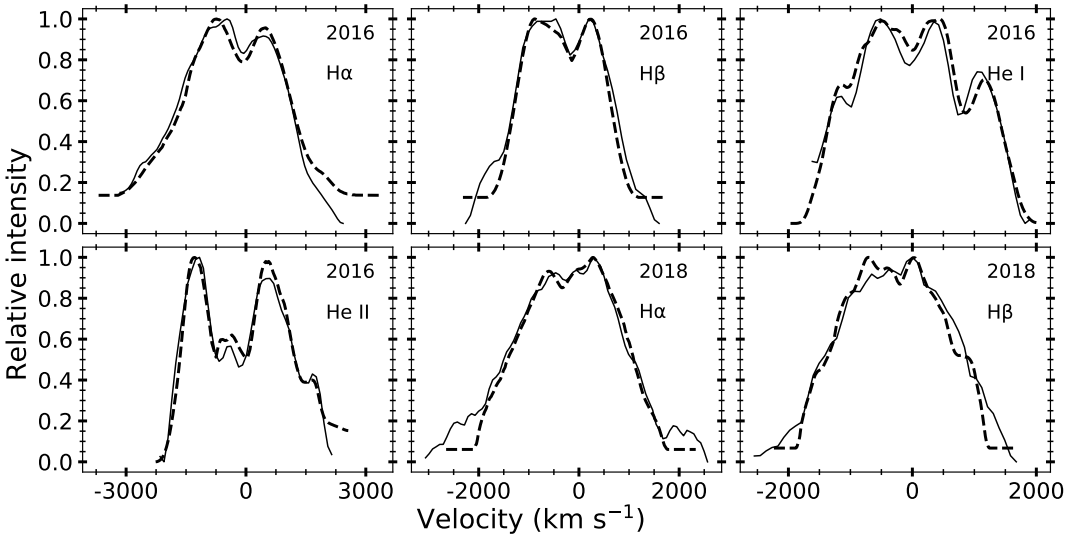

Figure 5.7: Best-fit velocity profiles obtained using morpho-kinematic analysis on the 2016 and 2018 outburst of M31N 2008-12a. The best-fit profile (dash line) is plotted over the observed velocity profile (continuous line).

opening angles 35.49° and 43.60° respectively. The radii of the red and blue cones of He II were found to be 8×10^9 and 9×10^9 m with opening angles 43° and 62° respectively. The best-fit model profiles over-plotted on the observed profiles are as shown in Fig. 5.7. The best-fit inclination of the system using this analysis was found to be $80.75° \pm 1.21°$. The enhanced bipolar nature suggest fast-moving polar ejecta along the ejecta axis as they are contributed more from the high-velocity hydrogen Balmer emission.

5.2.2 UV light curve

The estimated *Swift* UVOT *uvw*2 Vega magnitudes are summarised in Table 5.13. The evolution of UV magnitudes in 2014–2016 and 2018 outbursts are as

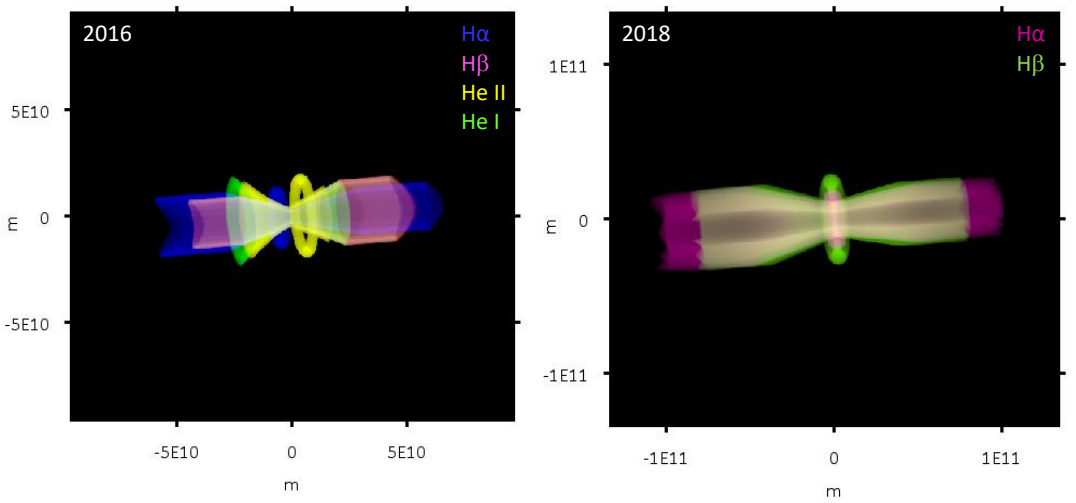

Figure 5.8: Morphology of the ejecta geometry of 2016 (*left*) and 2018 (*right*) outburst of the RN M31N 2008-12a obtained using the morpho-kinematic analysis on velocity profiles of day 0.72 and 1.52 since maximum. The structure is in the two-dimensional plane with X-axis being the line-of-sight direction and Y being the axis perpendicular to that of the plane of sky and line-of-sight with X and Y axes in meters and colors representing different emission lines as marked.

shown in Fig. 5.9. There was a linear decline in the 2018 *uvw*2 magnitudes from day 0 to 3 since the discovery, and this kind of decline was seen in other eruptions too. A plateau was seen from 4 days since discovery. The beginning of this plateau phase was consistent with the SSS turn-on time. The evolution in UV magnitudes in 2018 was closer to that of the 2016 magnitudes with regard to the presence of multiple plateaus. However, 2018 outburst appears to be brighter than that of the previous outbursts. When the X-ray flux starts dropping around day 11, there is a small duration of rebrightening in UV for about 3 days. The UV source disappeared by day 16.31.

5.2.3 X-ray light curve

The evolution in the soft X-ray emission during 2018 outburst is summarised in Table 5.13. The SSS phase observed for this system from 2013 to 2016, along with 2018 is depicted in Fig. 5.10. During the 2018 outburst, the system undergoes SSS phase from day 6.22 since discovery with a count rate of about 0.01 ct s^{-1}. The X-ray emission increases with time and then decrease around day 9.5 and then again increase. This was followed by a decline similar to the previous eruptions with the

Table 5.13: *Swift* UVOT and XRT observations of 2018 outburst of the RN M31N 2008-12a.

ObsID	**Date**	Δt^a	**Exp (ks)**	$uvw2^b$ **(mag)**	**Count rate**^{c} **(count s**$^{-1}$**)**
00010965001	2018-11-06.94	-0.14	0.98	17.15 ± 0.10	<1.16E-2
00010965002	2018-11-07.72	0.63	0.99	17.35 ± 0.08	<1.16E-2
00010965004	2018-11-08.17	1.08	1.85	17.79 ± 0.11	<6.16E-3
00010965005	2018-11-09.32	2.23	1.72	18.90 ± 0.11	<6.73E-3
00010965006	2018-11-10.03	2.94	6.11	19.41 ± 0.09	<2.09E-3
00010965007	2018-11-11.03	3.94	6.04	19.23 ± 0.10	6.16E-04 ± 4.90E-04
00010965008	2018-11-12.03	4.94	4.71	19.24 ± 0.09	1.61E-03 ± 8.30E-04
00010965009	2018-11-13.02	5.93	3.86	19.40 ± 0.10	1.06E-02 ± 2.40E-03
00010965010	2018-11-14.62	7.53	2.12	19.51 ± 0.13	2.55E-02 ± 4.60E-03
00010965011	2018-11-15.62	8.53	2.11	19.61 ± 0.14	5.69E-02 ± 7.60E-02
00010965012	2018-11-16.48	9.39	3.82	20.02 ± 0.13	3.27E-02 ± 3.90E-03
00010965013	2018-11-17.54	10.45	3.27	19.89 ± 0.13	5.30E-02 ± 5.30E-03
00010965015	2018-11-18.41	11.32	2.13	20.11 ± 0.19	4.06E-02 ± 5.80E-03
00010965016	2018-11-20.47	13.38	3.43	20.31 ± 0.17	5.05E-02 ± 5.10E-03
00010965017	2018-11-21.33	14.24	3.46	20.14 ± 0.14	3.09E-02 ± 4.00E-03
00010965018	2018-11-22.46	15.37	5.74	20.30 ± 0.13	1.16E-02 ± 1.90E-03
00010965019	2018-11-23.59	16.50	5.90	20.64 ± 0.16	1.11E-02 ± 1.80E-03
00010965020	2018-11-24.45	17.36	6.06	>20.5	2.92E-03 ± 9.40E-04
00010965021	2018-11-25.12	18.03	4.67	>20.3	5.72E-04 ± 6.10E-04

[a] time since maximum in days

[b] $uvw2$ filter has a central wavelength of 1930 Å and FWHM of 660 Å.

[c] Energy range: 0.3 to 1.5 keV.

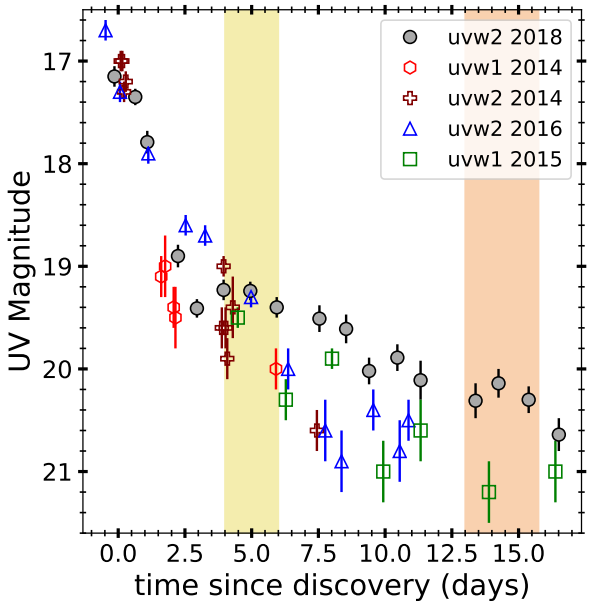

Figure 5.9: *Swift* UVOT light curve of M31N 2008-12a during its 2014, 2015, 2016 and 2018 outbursts. During 2018 outburst, a linear decline from the peak is seen, and then a plateau appears from the SSS turn-on time (highlighted in yellow). Period highlighted in orange: rebrightening corresponding to the drop in X-ray flux.

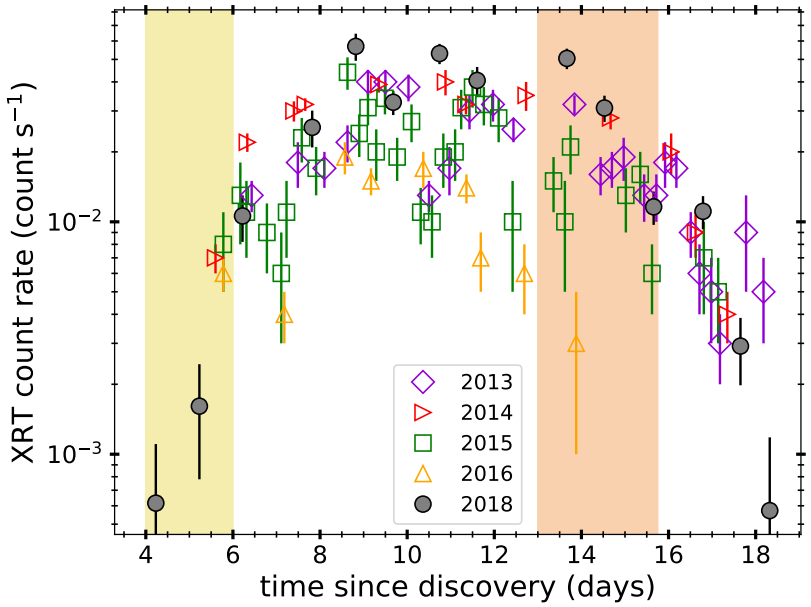

Figure 5.10: *Swift* XRT light curve of M31N 2008-12a during its 2013 to 2016 outbursts along with the 2018 outburst. SSS turn-on time is 5.23 days since discovery and turn-off is 17.65. SSS phase is similar in all the eruptions except that in the 2016 eruption, when it lasted for a shorter duration. Period highlighted in yellow: SSS turn-on and corresponding plateau in UV light curve. Period highlighted in orange: drop in X-ray flux and corresponding rebrightening in UV.

SSS turn-off time being 17.65 days since discovery. A dip in X-ray flux observed on day 9 since eruption is similar to that observed on day 11 during the 2015 outburst. However, the dip observed in 2018 was not as significant as that in 2015 one.

Henze et al. (2011) provide a relation for novae in M31 to calculate the ejected mass based on the SSS turn-on without using the optical spectrum. By using the column density value $N_{\rm H} = 0.7 \times 10^{21}$ cm^{-2} from Henze et al. (2018) in the relation and SSS turn-on during 2018 outburst, the value was determined to be (2.98$\pm$0.83) $\times$ 10^{-8} M$_{\odot}$.

5.3 Summary

Two He/N class of novae are discussed in this chapter. The spectral synthesis and plasma simulation code CLOUDY, pyCloudy and morphokinematic analysis using SHAPE were used for modelling both the novae.

Low resolution optical spectrum of V477 Sct reveals that the system is a typical He/N type nova with broad and boxy line profiles. The multiple-peaked line profiles seen in the optical spectrum can be attributed to the presence of enhanced bipolar nature and/or the projection effects of equatorial rings (Gill & O'Brien, 1999) present in the morphology.

During the 2016 outburst of M31N 2008-12a, the magnitudes were observed to be higher than all the eruptions observed so far. The spectra consist of hydrogen Balmer, He I and He II lines. The ejecta has N(He)/N(H) value of about 0.46, which indicates that the ejecta is enriched in helium.

The main results of multiwavelength analysis of 2018 outburst of RN M31N 2008-12a are summarised as follows.

1. An initial decline of 0.4 magnitude in the optical light curve from day 0 to 0.3 since maximum is observed.

2. A slight rebrightening is present from day 0.3 to 1 since maximum is seen in the optical light curve for the first time in 2018 outburst.

3. The optical decline time was measured as $t_2(V) = 3.15$ days, indicating that the system is evolving at a faster rate.

4. The linear decline post-maximum in the optical light curve was similar to that of the previous outbursts.

5. The optical spectra were dominated by Balmer, He and N lines, with an average FWHM velocity of Hα being around 3000 km s^{-1}.

6. The ejecta of M31N 2008-12a has N(He)/N(H) value of about 0.5, which indicates that the ejecta is enriched in helium.

7. The evolution of UV light curve was similar to that of the previous eruptions. A rapid decline since maximum is followed by a plateau phase coincident with the SSS turn-on time and rebrightening as the X-ray flux drops.

8. The SSS turn-on time during this outburst was 6.22 days since eruption and turn-off was 17.65 days since eruption.

9. The ejected mass from the optical spectrum was found to be consistent with that obtained from SSS turn-on time and is of the order of 10^{-8} $M_{\odot}$.

10. The morphology of the ejecta was found to be asymmetric bipolar one with cones and rings inclined at an angle of about 81°.

Both the He/N novae in the sample have enhanced bipolar structures along the ejecta axis with cones and equatorial rings at an inclination angle of about 80°. The [O III] lines are from the outer regions and [N II] lines are from the outer equatorial rings indicating that they are arising from the optical thin regions and He lines are coming from the cones in the inner regions of the bipolar structures.

6

“Hybrid” class of novae

The hybrid class of novae are those that show spectral properties similar to both the Fe II and He/N class. These novae have been observed to undergo transition from one type to another during the weeks post the outburst. The spectra of these objects may initially appear as He/N or Fe II and then transition to the other spectral class in a few weeks. They show emission due to both the components, wind and shell ejection. The transition is mainly due to the different physical conditions dominating at different epochs.

In this chapter, five hybrid novae are discussed. The multi-wavelength temporal evolution of V3890 Sgr is presented in detail, and detailed temporal spectral analysis of T Pyx, V612 Sct and V906 Car are discussed. The novae were modelled using the spectral synthesis and plasma simulation code CLOUDY to understand the physical conditions of the system such as source luminosity, effective temperature, density and elemental abundances. To obtain the morphology of the ejecta of all the novae, pyCloudy and/or SHAPE was used. In addition, evolution of the morphology of the ejecta was studied for T Pyx, V906 Car and V3890 Sgr.

6.1 V5588 Sgr

V5588 Sgr (Nova Sgr 2011 No. 2) was discovered on 2011 Mar 27 by Nishiyama et al. (2011) at a magnitude 11.7. The characteristic feature in this system is the presence of six repeated, nearly identical secondary maxima in the light curve, qualifying it to be a 'J type' nova (Strope et al., 2010). Munari et al. (2015a) suggested that they are a consequence of high velocity ejection of a limited amount of material. The spectrum obtained on day 0.8 by Arai et al. (2011) is a typical Fe II type spectrum with presence of hydrogen Balmer lines and Fe II multiplets. The spectrum obtained on day 25 by Munari et al. (2015a) before the rise to second maximum in the optical light curve, light curve showed the presence of helium lines along with Fe II lines. The nova morphed from a Fe II to that of both Fe II and He/N class. The coronal lines like [Fe VII] and [Fe X] lines were present the ejecta became optically thin (Munari et al., 2015a). Based on a detailed study of the optical and NIR photometric and spectral evolution of the system, Munari et al. (2015a) concluded the following: (a) the secondary rise corresponds to the initial expansion in the optically thick ejecta, (b) the maximum brightness corresponds to the maximum projected area gained by the expanding pseudo-photosphere and (c) the decline corresponds to the material becoming optically thin.

Low resolution spectrum from HCT-HFOSC obtained on 2011 May 09 (43 days since discovery) was used to determine physical conditions of the system and also obtain the 3D pseudo structure of the ejecta. The spectrum consists of hydrogen Balmer, Fe II, He I, He II, [N II] and Ca II lines.

The central ionizing source was set to be at an effective temperature 10^5 K and luminosity 10^{38} erg s^{-1}. The medium was assumed to be of a low-density diffuse component and a clump component to obtain a modelled spectrum. Most of the lines are fitted by the clump component, except a few lines like [N II] (5755 Å), He I and He II. To fit all the lines, a diffuse region (low density) was used, covering 20% of the volume. The clump hydrogen density was 5.62×10^{10} cm^{-3} and diffuse hydrogen density 1.12×10^{10} cm^{-3}. The relative fluxes of the observed lines, the best-fit model predicted lines, and corresponding χ^2 values are given in Table 6.1. Some of

Table 6.1: Observed and best-fit CLOUDY model line flux ratios[a] for day 43 of V5588 Sgr

Line ID	λ (Å)	**Observed**	**Modelled**	χ^2
H I	3835	1.19E-01	2.81E-01	3.50E-01
He II	3858	4.33E-02	3.61E-03	1.59E-02
H I	3889	1.51E-01	1.48E-01	1.06E-03
Ca II	3934	5.78E-02	1.04E-01	2.09E-02
Ca II	3968	2.05E-01	1.73E-01	1.16E-02
He I	4026	8.00E-02	7.36E-02	5.14E-04
H I	4102	1.43E-01	2.27E-01	2.92E-01
Fe II	4179	5.14E-02	1.40E-01	1.28E-01
Fe II	4233	7.42E-02	2.47E-01	1.01E+00
Fe II	4303	5.60E-02	4.12E-01	1.90E+00
H I	4340	2.83E-01	8.74E-01	6.08E+00
Fe II	4385	2.80E-02	7.32E-02	2.19E-02
Fe II	4417	3.48E-02	8.66E-02	3.76E-02
He I	4471	1.74E-02	3.38E-01	3.81E+00
Fe II	4508	5.77E-02	1.28E-01	1.11E-01
Fe II	4556	6.18E-02	1.18E-01	1.01E-01
Fe II	4584	6.55E-02	1.61E-01	1.35E-01
N III	4638	7.54E-02	3.28E-01	7.41E-01
He II	4686	1.15E-01	1.43E-01	1.49E-02
H I	4861	1.00E+00	1.00E+00	0.00E+00
He I	4922	8.69E-02	9.78E-02	2.14E-03
He I	5016	1.50E-01	5.64E-01	7.32E+00
Fe II	5169	6.31E-02	7.28E-01	7.23E+00
Fe II	5235	2.90E-02	3.75E-02	3.43E-03
Fe II	5276	4.01E-02	5.69E-01	4.08E+00
Fe II	5317	7.01E-02	2.54E-01	3.33E-01
Fe II	5363	1.49E-02	8.13E-02	5.48E-02
He II	5412	2.47E-02	1.63E-01	4.54E-01
Fe II	5535	1.70E-02	2.00E-01	1.21E+00
[N II]	5755	1.33E-02	8.02E-02	5.63E-02
He I	5876	8.84E-02	5.65E-01	4.61E+00
Fe II	5991	1.48E-02	5.63E-02	2.39E-02
Fe II	6084	5.49E-03	6.57E-02	9.66E-02
Fe II	6148	6.38E-03	1.03E-01	3.31E-01
Fe II	6248	1.32E-02	1.22E-01	2.89E-01
Fe II	6456	7.06E-03	1.97E-01	1.19E+00
H I	6563	4.91E+00	4.46E+00	5.90E+00
He I	6678	1.61E-02	1.52E-01	1.81E-01
He I	7065	4.22E-02	2.47E-01	4.80E-01
Fe II	7712	1.07E-02	1.49E-01	7.85E-01
Mg II	7896	1.93E-02	3.61E-02	4.63E-03
O I	8227	2.75E-02	4.66E-02	1.23E-02
Ca II	8498	3.77E-02	5.54E-01	6.06E+00
Ca II + H I	8545	1.81E-02	1.15E-01	1.01E-01
Ca II + H I	8665	3.00E-02	3.29E-01	3.32E+00
H I	8750	3.29E-02	1.15E-01	1.48E-01
H I	8863	5.19E-02	6.72E-01	1.22E+01
H I	9015	6.47E-02	2.37E-01	4.38E-01
N I	9060	2.59E-02	6.20E-02	1.51E-02

[a] Relative to Hβ

Table 6.2: Best-fit 1D CLOUDY model parameters on day 43 for V5588 Sgr

Parameter	**Day 43**
T_{BB} ($\times 10^5$ K)	1.00 ± 0.12
Luminosity ($\times 10^{38}$ erg s^{-1})	1.00 ± 0.09
Clump Hydrogen density ($\times 10^{10}$ cm^{-3})	5.62
Diffuse Hydrogen density ($\times 10^{10}$ cm^{-3})	1.12
Covering factor (clump)	0.80
Covering factor (diffuse)	0.20
α	-3.00
Inner radius ($\times 10^{14}$ cm)	2.69
Outer radius ($\times 10^{14}$ cm)	8.51
Filling factor	0.10
$N/N_\odot$	2.08 ± 0.13 (3)[a]
$O/O_\odot$	2.21 ± 0.10 (1)
$He/He_\odot$	1.53 ± 0.06 (11)
$Ca/Ca_\odot$	1.13 ± 0.09 (5)
$Fe/Fe_\odot$	1.47 ± 0.14 (21)
Ejected mass ($\times 10^{-6}$ $M_\odot$)	1.12
Number of observed lines (n)	49
Number of free parameters (n_p)	10
Degrees of freedom (ν)	39
Total χ^2	71.73
χ^2_{red}	1.84

[a]The number in the parenthesis is the number of lines used to determine abundance estimate.

the Fe II and H I lines are overestimated and have high χ^2 values. The He I (5016 Å) and Ca II + H I lines also have high χ^2 values. Though the reduced χ^2 values suggest that the generated spectrum matches the observed spectrum, the above contributions from different lines might hinder the calculated abundance values. The higher χ^2 values are as a consequence of blending of the lines in some cases. The values of best-fit parameters obtained from the model are given in Table 6.2. The estimated abundance values show that helium, nitrogen, oxygen, calcium and iron are over-abundant compared to solar, while other elements have the solar abundance values. The best-fit synthetic spectrum obtained is plotted over the observed spectrum as shown in *right* panel of Fig. 6.1. The ejected mass was found to be 1.12×10^{-6} $M_\odot$.

The geometry of the ionized structure obtained using pyCloudy was found to be bipolar cones with equatorial rings and bipolar frustum of prolate spheroid (*left* panel of Fig. 6.1). The hydrogen Balmer emission is coming from all the regions, and Fe II

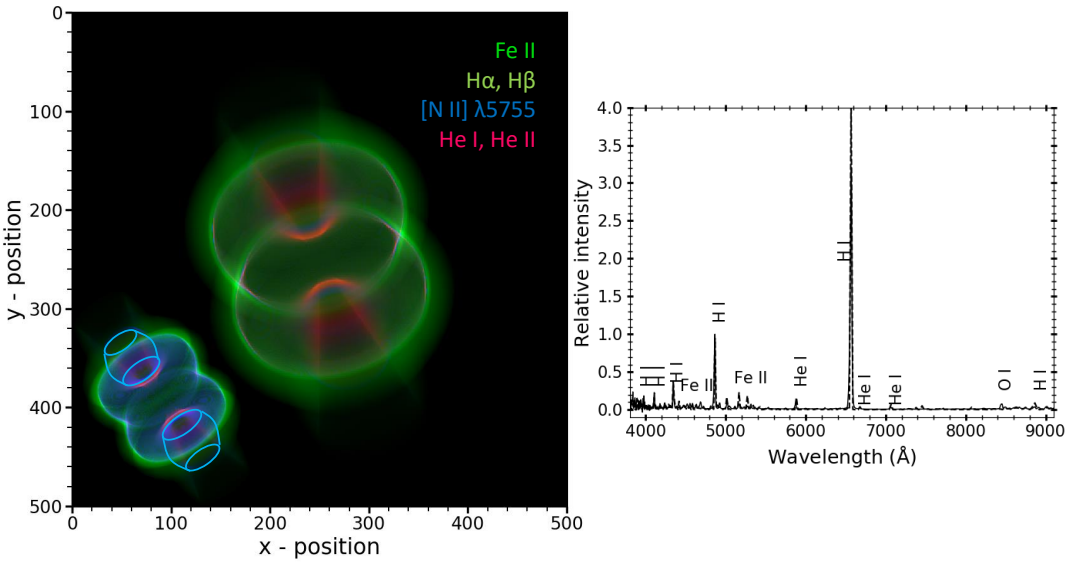

Figure 6.1: *Left:* Morphology of the ejecta of V5588 Sgr obtained on day 43 using the optical spectrum. It is plotted in the two-dimensional plane with X-axis being the line-of-sight direction and Y being the axis perpendicular to that of the plane of sky and line-of-sight. The lines corresponding to different colours are marked to show the spatial distribution of emission in the structure. The colour blue is increased in the *bottom-left* to have better clarity on the [N II] structure. Here, 1 unit of x and y correspond to 1.7×10^{12} cm. *Right:* Best-fit modelled spectrum (dash line) obtained using CLOUDY over plotted on the observed optical spectrum (continuous line).

emission from the equatorial rings. The bipolar frustum of prolate spheroid is formed due to the [N II] emission. The He II (4686 Å) and He I lines are coming from the inner conical structures. The inclination angle of the system was estimated to be 63° ± 1.35°. The details on the extent of all the components and their distance from the central source in the morphology of the ejecta are given in Table 6.3. The frictional interaction between the multiple ejecta might have resulted in the formation of a spheroidal frustum for [N II] structure. The equatorial ring may be present due to the low expansion ejecta velocity of Fe II lines (Lloyd et al., 1997).

6.2 The 2011 outburst of T Pyxidis

The well-known RN T Pyxidis was observed in eruptions multiple times in 1890, 1902, 1920, 1945, 1966, and 2011. On the plates of Harvard Map during 1902 outburst, it was first discovered by H. Leavitt as a nova (Duerbeck, 1987). It was

Table 6.3: Details of the morphology of the ejecta on day 43 for V5588 Sgr

Component	**Extent**[a] **($\times 10^{14}$ cm)**	**Radius ($\times 10^{14}$ cm)**	**Distance**[b] **($\times 10^{14}$ cm)**	**Angle**[c] **(°)**
Cone	0.75 ± 0.02	0.95 ± 0.03	0.37 ± 0.01	55 ± 0.87
Equatorial ring	-	2.99 ± 0.12	1.26 ± 0.09	-
Spheroidal frustum	1.50 ± 0.08	-	1.22 ± 0.10	-

[a]Extent of the component along the ejecta axis
[b]Distance from the central source to the component along the ejecta axis
[c]Outer opening angle of the cone

observed that the accretion disc spectrum dominates the quiescence spectrum of T Pyx (Anupama 2008 and Selvelli et al. 2008). The 2011 outburst was discovered by M. Linnolt at 13.0 V magnitude (Schaefer et al., 2013), on 2011 April 14.29 UT, and was studied in detail in the multi-wavelength regime.

The photometric and spectroscopic properties of the 2011 outburst have been reported by Chesneau et al. (2011); Shore et al. (2013); Sokoloski et al. (2013); De Gennaro Aquino et al. (2014); Surina et al. (2014), and Joshi et al. (2014). Sokoloski et al. (2013) estimated the distance to T Pyx as 4.8 kpc using the light echoes method, while Schaefer (2018) estimated the distance to be $\sim$3.1 kpc using the parallax data from Gaia. Optical and IR spectra indicate that the object morphed from a He/N to Fe II spectral class within the first few days, on its rise to the maximum, and transitioned to He/N class during its post-maximum decline. Izzo et al. (2012) suggested that the multiple absorptions seen in the P-Cygni profiles during the early phase are due to the presence of a clumpy wind surrounding the WD. Broadband interferometric observations and medium spectral resolution Brγ line by Chesneau et al. (2011) indicated a bipolar event with an inclination angle i = 15°, and a position angle, PA = 110°. An axisymmetric conical bipolar geometry was used to model the ejecta using high resolution optical spectroscopic observations by Shore et al. (2013) at an inclination angle of i = 15 $\pm$ 5°, and estimated the ejected mass to be $M_{\rm ej} = 2 \times 10^{-6}\,{\rm M}_{\odot}$. The ejected mass was determined as $3 \times 10^{-5}\,{\rm M}_{\odot}$ or more by Patterson et al. (2017) using period change during the 2011 outburst, while Nelson et al. (2014) estimated the ejected mass as $(1-30) \times 10^{-5}\,{\rm M}_{\odot}$ using the high peak flux densities in the radio emission. Based on the slow turn-on time observed for the

SSS phase, a large ejecta mass $\gtrapprox 10^{-5}\,M_{\odot}$ was suggested by Chomiuk et al. (2014). Evans et al. (2012) found a weak, cool IR excess that was attributed to the heating of pre-outburst dust in the swept-up interstellar environment of the nova from an IR photometric properties. The object was detected as a SSS from day 105 to 349. *Swift* satellite detected the X-ray emission peak that was coincident with the development of high ionization lines such as [Ne III], [C III], and N III (4640 Å) around day 144 in the optical spectrum. The appearance of coronal lines like [Fe VII] and [Fe X] was found to be coincident with the peak of radio emission around day 155, and the plateau phase in X-ray (Surina et al., 2014).

T Pyx is the only RN with a discernible shell that was first detected by Duerbeck & Seitter (1979). Subsequent observations using the Hubble Space Telescope (Shara et al. 1989, 1997, and Schaefer et al. 2010) revealed the shell to be expanding very slowly and to consist of several knots. Based on 3D gas dynamical simulations of the evolution of the ejecta of T Pyx, Toraskar et al. (2013) predicted the observed expansion of the shell and its morphology. Their simulations demonstrated that the knots are formed due to Richtmyer-Meshkov instabilities that set in when the ejecta from later outbursts that collide with the older, swept-up, cold, dense shell.

The optical spectral evolution of 2011 outburst of T Pyx from t = 1.28 (pre-maximum phase) to 2415.62 days (late post-outburst phase) since discovery are presented. The physical conditions of the system at different epochs and also the evolution of morphology of the ejecta are discussed in detail. The date of outburst discovery, 2011 April 14.29 UT (JD 2455665.79), is considered as t=0.

6.2.1 Light curve

The optical light curve for T Pyx generated using AAVSO magnitudes is given in Fig. 6.2. There was an initial rise in the magnitude till day 3 followed by a pre-maximum halt phase in all the bands. This phase continues till around day 13 followed by the final rise. Multiple small rebrightenings were observed from day 12 to 66 in all the bands. The maximum visual magnitude was reached around day 28 with 6.3 V mag. Post the maximum, the light curve underwent an early decline phase

Table 6.4: Spectroscopic observational log for the 2011 outburst of T Pyx

Date	**t (days)**	**Coverage (Å)**	**Telescope**
15 Apr 2011	1.28	3800–9200	HCT, IGO
16 Apr 2011	2.28	3800–9200	HCT
18 Apr 2011	4.43	3900–8250	IGO
19 Apr 2011	5.46	3900–8250	IGO
20 Apr 2011	6.34	3800–9200	HCT
21 Apr 2011	7.57	3900–8250	IGO
22 Apr 2011	8.49	3900–8250	IGO
28 Apr 2011	14.31	3800–9200	HCT
29 Apr 2011	15.29	3800–9200	HCT
30 Apr 2011	16.29	3800–9200	HCT
06 May 2011	22.29	3800–8500	VBT
10 May 2011	26.27	3800–8800	VBT
12 May 2011	28.27	3800–8500	VBT, IGO
26 May 2011	42.30	3800–8500	VBT
07 Jun 2011	54.29	3800–8500	VBT
21 Jun 2011	68.28	3800–8500	VBT
23 Nov 2011	223.66	3800–6800	HCT
24 Nov 2011	224.65	3800–6800	HCT
30 Nov 2011	230.62	3800–9000	HCT
22 Dec 2011	252.63	3800–9000	HCT
05 Jan 2012	266.58	3800–8600	HCT
19 Jan 2012	280.50	4000–8600	VBT
20 Jan 2012	281.56	4000–8600	HCT
27 Feb 2012	319.43	4000–8600	HCT
15 Mar 2012	336.40	4000–8300	HCT
17 Mar 2012	339.40	4200–8300	VBT
13 Apr 2012	365.28	4000–9000	HCT
21 Jan 2013	648.80	4000–8600	HCT
13 Mar 2014	1064.39	4000–7500	HCT
30 Dec 2015	1721.54	4000–7500	HCT
31 Jan 2016	1753.44	4000–7500	HCT
24 Feb 2017	2143.37	4200–7500	HCT
23 Nov 2017	2415.62	4100–7500	HCT

till ∼day 250 which was followed by the final decline at about 12 visual magnitude. The characteristic timescales $t_2(V)$ and $t_3(V)$ was found to be ∼48 and ∼87 days respectively.

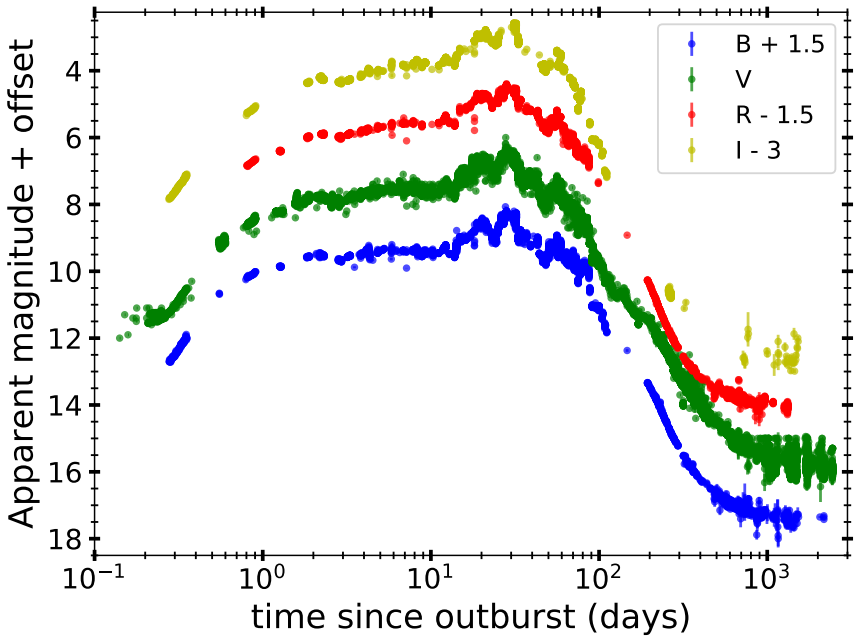

Figure 6.2: Apparent magnitude light curve evolution of T Pyx generated using optical data from AAVSO. Offset applied for all the magnitudes except V for clarity.

6.2.2 Spectral evolution

Optical spectral evolution from the pre-maximum to the post-outburst phase is described here.

Pre-maximum phase

The spectral evolution during the initial optically thick phase before optical maximum from days 1.28 to 8.49 is as shown in Fig. 6.3. The spectra consist of strong hydrogen Balmer, oxygen, helium, neon, carbon, calcium, nitrogen, and a few iron lines. The strength of hydrogen Balmer, Fe II, O I, and N I lines increase with time, while high excitation lines like He I, Ne I, Ne II, O II + N III, and C III drop in intensity and at the end of this phase some lines eventually disappear at the end of this phase. Fe lines become prominent towards the end of this phase. A decrease in the ejecta velocity, from $\sim$2500 km s^{-1} to $\sim$1000 km s^{-1}, was observed until day 12.32 (Fig. 6.4). On day 1.28, hydrogen Balmer, O I (7774 Å) and N II lines have P-Cygni profile with blue-shifted absorption components. These lines develop deeper and sharper P-Cygni absorption components and narrow emission components. The

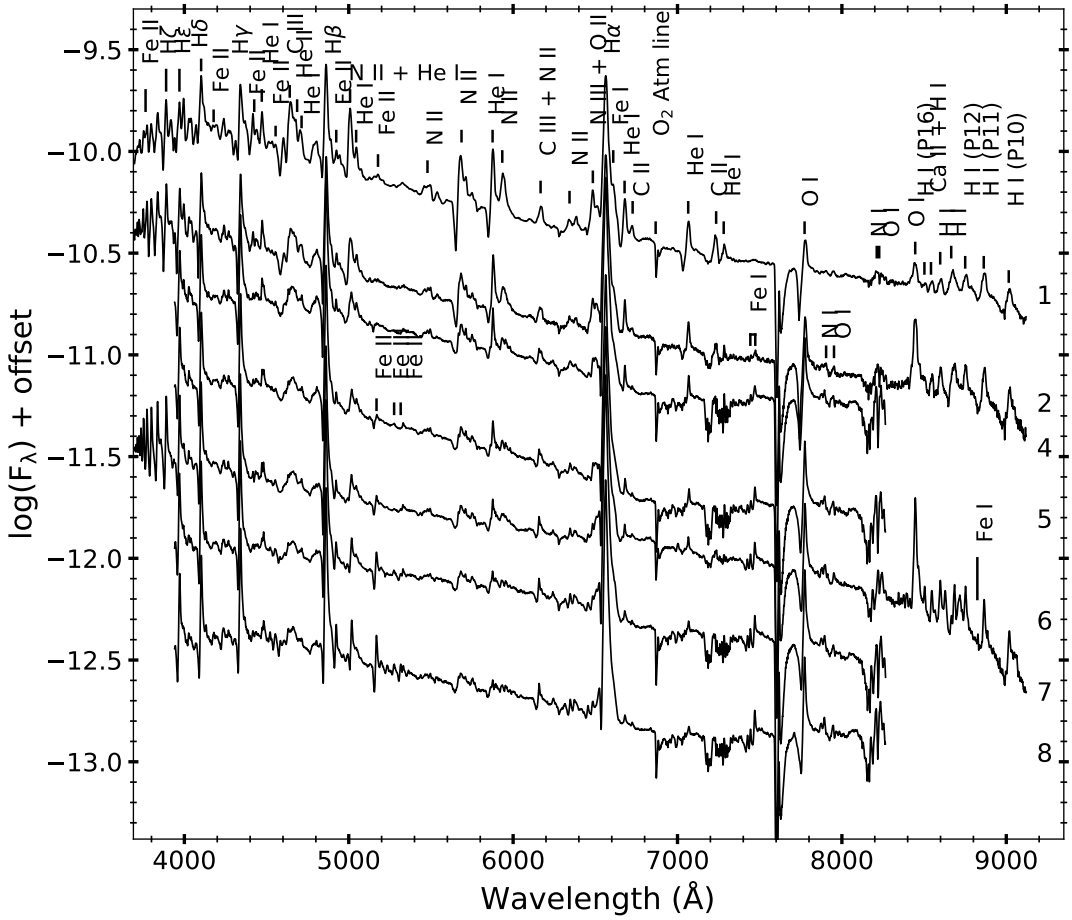

Figure 6.3: Low resolution optical spectral evolution of optical thick phase of T Pyx from 15 April 2011 (day 1) to 22 April 2011 (day 8). The line identification and time since discovery in days (numbers to the right) are marked.

other elements that have P-Cygni profiles are Fe II and He I. This phase marks the end of the fireball stage (pseudo-photospheric expansion).

Maximum and early decline phase

Fe II multiplets (Fig. 6.5) are the most prominent non-Balmer lines as the system evolves to its optical maximum and during the early decline (days 14.31 to 68.28). The O I (8446 Å) line, which was an emission line until the previous phase, develops a P-Cygni profile from day 22.29 to 28.27 (around the optical maximum). The Fe II multiplets, Balmer, and O I lines that have P-Cygni profiles slowly evolve into emission lines towards the end of this phase. The Hα line becomes broader with a velocity up to $\sim$2000 km s^{-1} with a rounded peak profile near the optical maximum.

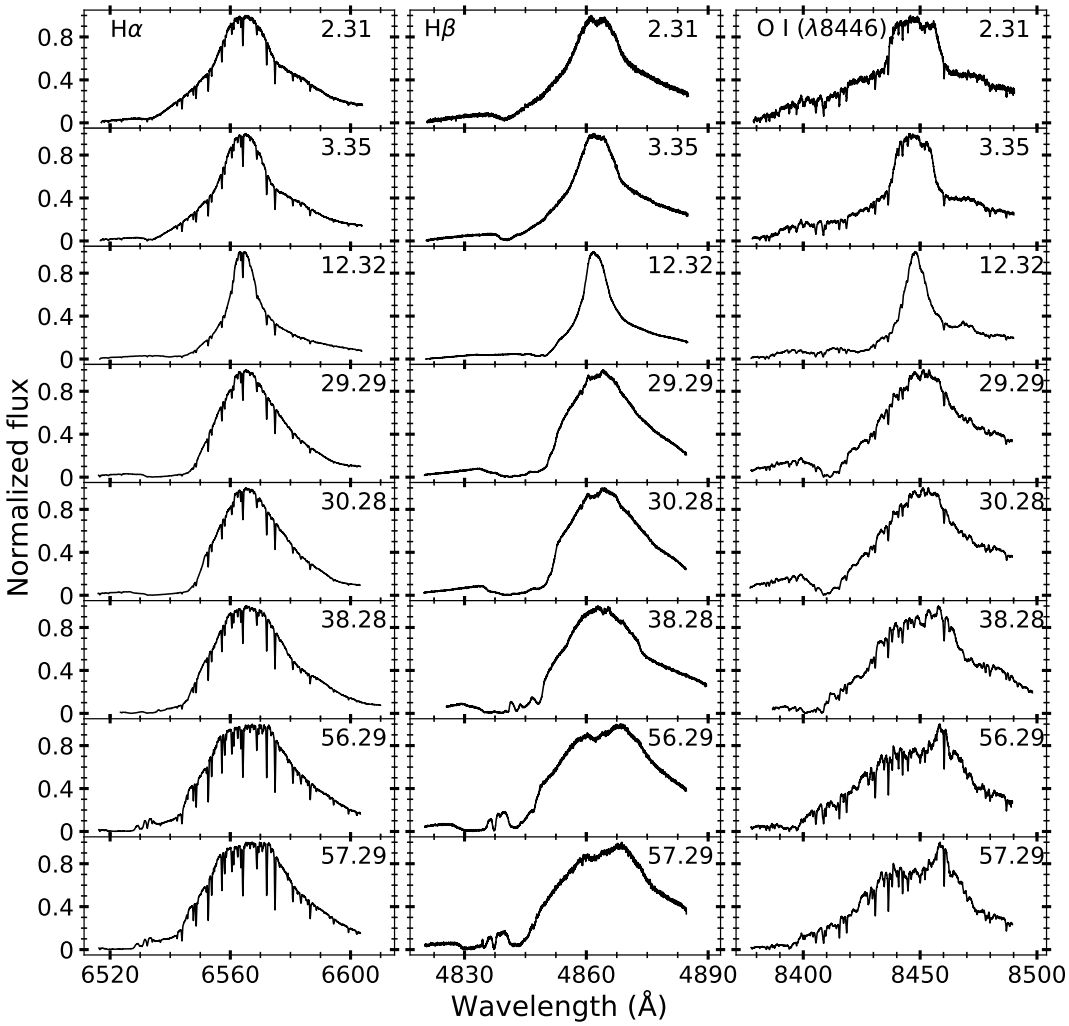

Figure 6.4: High resolution spectral (R = 27000) evolution of T Pyx from 16 April 2011 (day 2) to 10 June 2011 (day 57). Evolution of Hα, Hβ, and O I (8446 Å) line profiles are shown. We note the variation in the velocity of the lines as the system evolves. There is a decrease in velocity from day 2.31 to 12.32 and then an increase up to $\sim$2000 km s^{-1} until day 57.29.

The FWHM of the lines increases from $\sim$1000 to $\sim$2000 km s^{-1} during day 14.31 to 68.28. From day 42.30 to 68.28, the presence of [N II] (5755 Å) and N II lines was clearly seen. The emission component of N II (5679 Å) P-Cygni profile, which is weak on $\sim$day 14, becomes stronger by $\sim$day 42.

During this phase, the spectrum of day 68 was modelled to obtain the physical conditions using the plasma simulation code CLOUDY. The central ionizing source was set to be at an effective temperature 10^5 K and luminosity 10^{37} erg s^{-1}. To obtain the synthetic spectrum, three regions were used: a diffused region with density 4.46 $\times$ 10^8 cm^{-3} to fit most of the lines like helium, C III, and [N II]; Fe II lines were

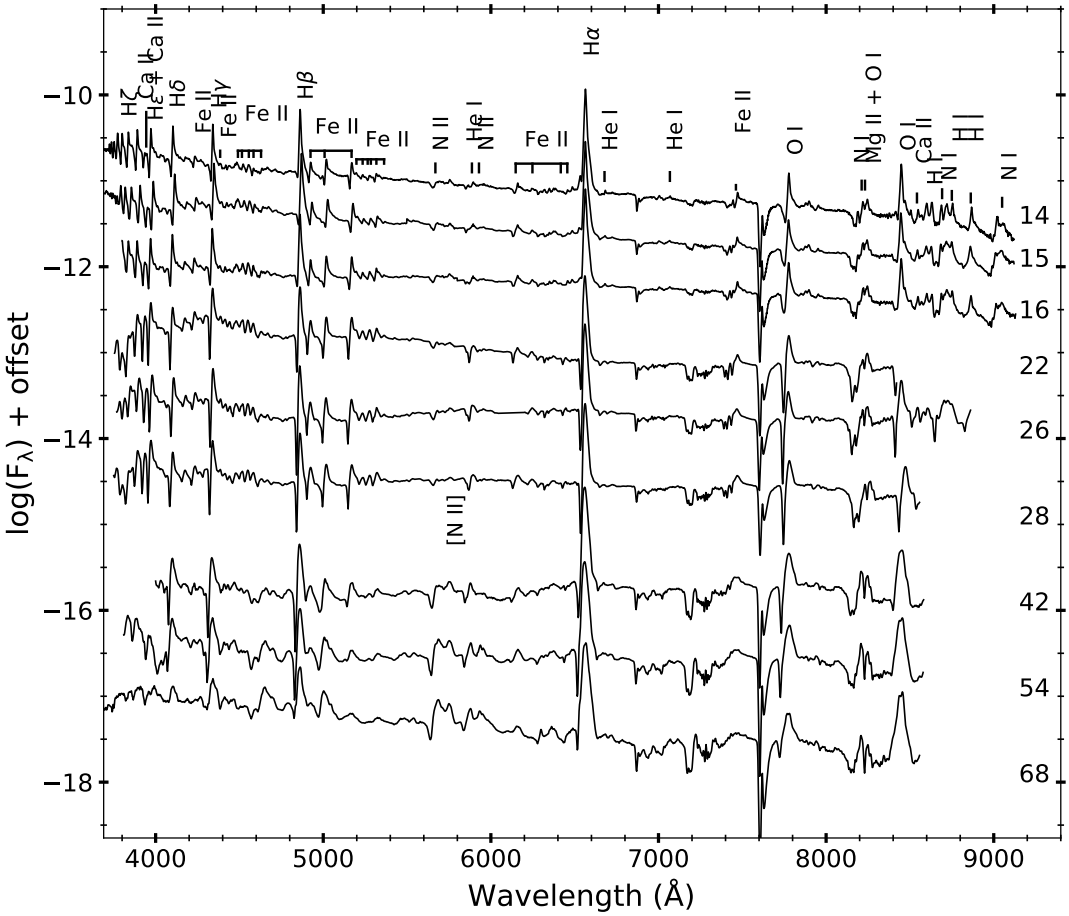

Figure 6.5: Spectral evolution of T Pyx as it passes through optical maximum and early decline phase from 28 April 2011 (day 14) to 21 June 2011 (day 68). The lines identified and time since discovery in days (numbers to the right) are marked.

fit dominantly by a clumpy region with a higher density, 5.62 $\times$ 10^8 cm^{-3}; and N II recombination lines were fit using a region with lower temperature, 3 $\times$ 10^4 K, and a higher density, 5.62 $\times$ 10^8 cm^{-3}. The relative fluxes of the observed lines, best-fit modelled lines, and corresponding χ^2 values are given in Table 6.5, and the values of best-fit parameters are given in Table 6.6. The estimated abundance values show that nitrogen and helium abundances are more than solar, while iron, calcium, and carbon abundance values are solar. The best-fit modelled spectrum (dashed line) with the corresponding observed optical spectrum (continuous line) are as shown in Fig. 6.6. Absorption components of the P-Cygni profiles are not modelled here because of the limitations of the code. The best-fit parameters obtained for this epoch are accurate to 65-70% only.

Table 6.5: Observed and best-fit CLOUDY model line flux ratios[a] for day 68 of the 2011 outburst of T Pyxidis.

Line ID	λ (Å)	**Observed**	**modelled**	χ^2
H I	3889	2.30E-01	4.26E-01	9.45E-01
Ca II (K)	3934	1.18E-01	2.28E-01	1.60E-01
H I, Ca II (H)	3970	1.26E-01	2.40E-01	1.30E-01
H I	4102	4.11E-01	3.09E-01	3.43E-01
Fe II	4178	2.82E-02	6.22E-02	1.64E-01
Fe II	4233	2.42E-02	4.85E-02	5.83E-03
H I	4340	1.11E+00	9.07E-01	4.71E-01
Fe II	4491	1.59E-01	3.96E-02	1.82E-01
C III	4650	4.48E-01	3.18E-01	6.98E-01
He II	4686	2.76E-01	1.86E-01	1.34E-01
H I	4861	1.00E+00	1.00E+00	0.00E+00
Fe II	4924	1.29E-01	6.58E-02	2.8E-01
Fe II	5018	7.32E-01	5.91E-01	2.98E-01
Fe II	5168	1.97E-01	1.33E-01	1.52E-01
Fe II	5235	5.40E-02	1.51E-01	1.41E-01
Fe II	5317	9.60E-02	3.78E-02	6.07E-02
Fe II + N II	5535	3.51E-02	9.27E-02	1.42E-01
N II	5679	8.02E-01	1.79E-01	8.81E+00
[N II]	5755	1.73E+00	2.90E-01	1.46E-01
He I	5876	1.76E+00	2.86E-01	1.68E-01
N II	5938	1.37E-01	4.89E-02	2.87E-01
Fe II	6148	1.02E-01	5.36E-02	5.11E-02
Fe II + N II	6248	3.42E-02	3.95E-02	8.93E-04
Fe II	6417	1.58E-01	5.50E-02	1.58E-01
H I	6563	3.54E+00	2.65E+00	9.03E+00
He I	6678	2.92E-02	5.19E-02	9.80E-03
He I	7065	2.99E-02	1.21E-01	1.10E-01

[a] Relative to Hβ

Nebular phase

Nebular phase (day 223.66 to 648.80) is marked by dominant, broad [O III] 4959 and 5007 Å lines (Fig. 6.7). The [N II] line develops a double-peaked profile with wing-like structures on either side, which is similar to the [O III] and the Balmer lines. Other forbidden lines seen are the [Fe VII] (5158, 5276 and 6087 Å), [Fe X] (6375 Å), [O II] (7330 Å), [C III]+[O III] (Blend 4364 Å with H I), and [Ne III] (3869 and 3968 Å) lines. The intensity of the [N II] and [Fe VII] lines slowly decreases and [N II] disappears by day 1064. All the nebular lines disappear by day 1064, except for the [O III] 4959, 5007 Å lines.

Table 6.6: Best-fit CLOUDY model parameters for day 68 of the 2011 outburst of T Pyxidis

Parameter	**Day 68**
T_{BB} ($\times 10^5$ K)	1.00 ± 0.14
Luminosity ($\times 10^{37}$ erg/s)	1.00 ± 0.07
Clump Hydrogen density ($\times 10^8$ cm^{-3})	5.62
Diffuse Hydrogen density ($\times 10^8$ cm^{-3})	4.46
Covering factor (clump)	0.40, 0.40[a]
Covering factor (diffuse)	0.20
α	-3.00
Inner radius ($\times 10^{14}$ cm)	3.63
Outer radius ($\times 10^{15}$ cm)	1.00
Filling factor	0.1
Fe/Fe$_\odot$	1.41 ± 0.13 (12)[b]
N/N$_\odot$	5.76 ± 0.11 (5)
Ca/Ca$_\odot$	1.13 ± 0.09 (2)
C/C$_\odot$	1.00 ± 0.10 (1)
He/He$_\odot$	2.00 ± 0.07 (4)
Ejected mass ($\times 10^{-5}$ M$_\odot$)	2.74
Number of observed lines (n)	27
Number of free parameters (n_p)	12
Degrees of freedom (ν)	15
Total χ^2	23.08
χ^2_{red}	1.54

[a]The covering factor used for the third region to fit N II lines.

[b]The number in the parentheses is the number of lines used to determine the abundance estimate.

Three epochs, day 224, 252, and 336, were modelled to understand the evolution during the nebular phase using CLOUDY. The central ionizing source was set to be at an effective temperature $\sim 10^5$ K and luminosity $\sim 10^{37}$ erg s^{-1}. The medium was assumed to be of a low-density diffuse component and a clump component to obtain a modelled spectrum. Most of the lines were fitted by the clump component, except a few forbidden lines like [N II] (5755 Å), [O III] (4959 & 5007 Å), and [Ne III] (3869 & 3968 Å). To fit all the lines, a diffuse region (low density) was used, covering 20% of the volume. The clump hydrogen density was in the range of (5.6–7.9) $\times$ 10^7 cm^{-3} and diffuse hydrogen density (1.8–3.2) $\times$ 10^7 cm^{-3}. The relative fluxes of the observed lines, the best-fit model predicted lines, and corresponding χ^2 values are given in Table 6.7. The values of best-fit parameters obtained from the model are given in Table 6.8. The estimated abundance values show that helium, nitrogen, oxygen, and neon are over-abundant compared to solar, while iron and carbon have solar abundance values. On day 252, nitrogen and helium abundance values are more than that of day 224 and 336. Oxygen abundance values continue to

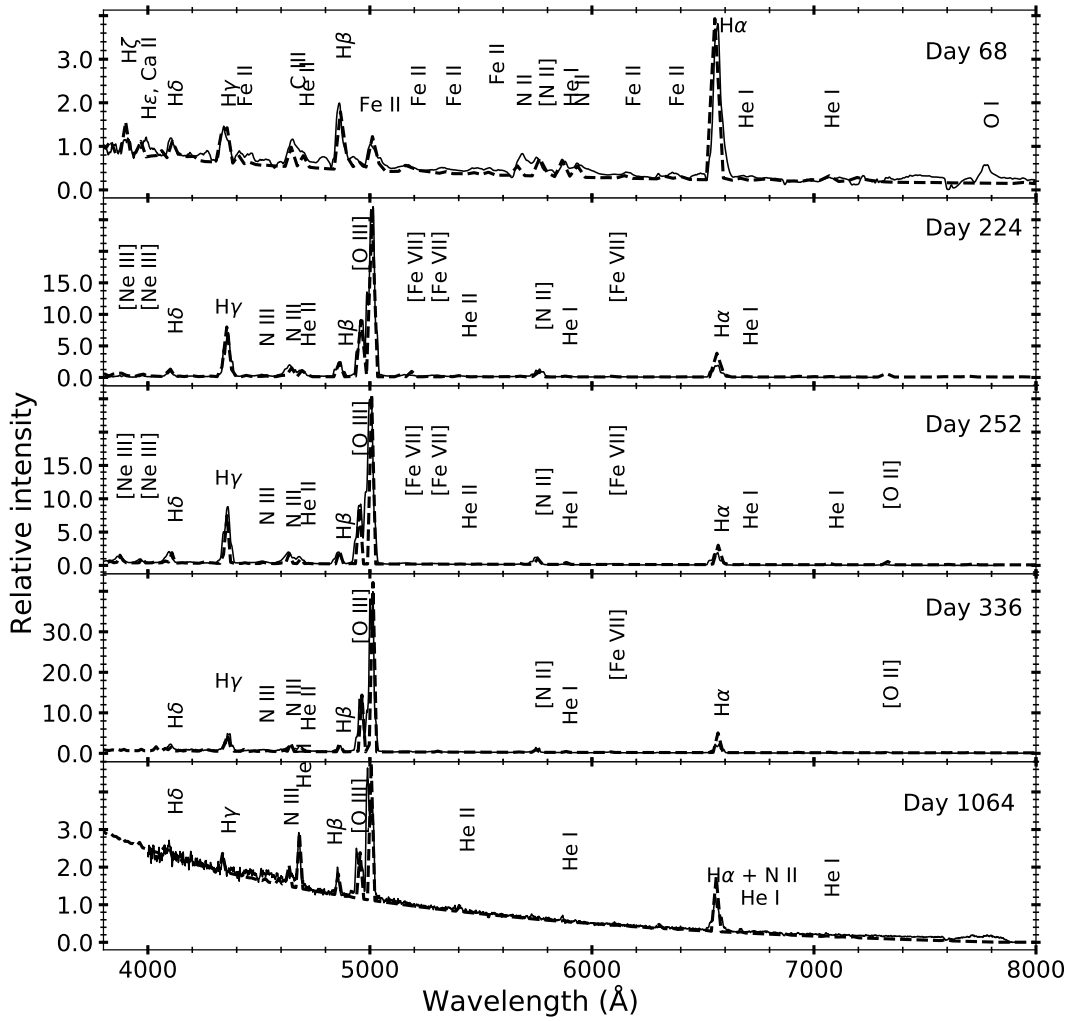

Figure 6.6: Best-fit CLOUDY model spectra (dashed line) plotted over the observed spectra (continuous line) of T Pyxidis obtained on days 68, 224, 252, 336, and 1064. The spectra are normalized to Hβ. The identified lines and time since discovery in days (numbers to the right) are marked.

be above the solar values in all the epochs. The best-fit modelled spectra for all the epochs are shown in Fig. 6.6, together with the corresponding observed spectra.

The geometry of the ionized structure obtained using pyCloudy during the nebular phase was found to be a bipolar conical one with equatorial rings (Fig. 6.9). [O III] emission is dominant in the outermost regions of the cones and equatorial rings. The emissivity increases with time while the structure remains the same. The nitrogen lines are present in the innermost regions of the equatorial rings and cones. The He II (4686 Å) line is present in the innermost regions of the cones, while hydrogen lines are present in the innermost regions of the equatorial rings. No significant

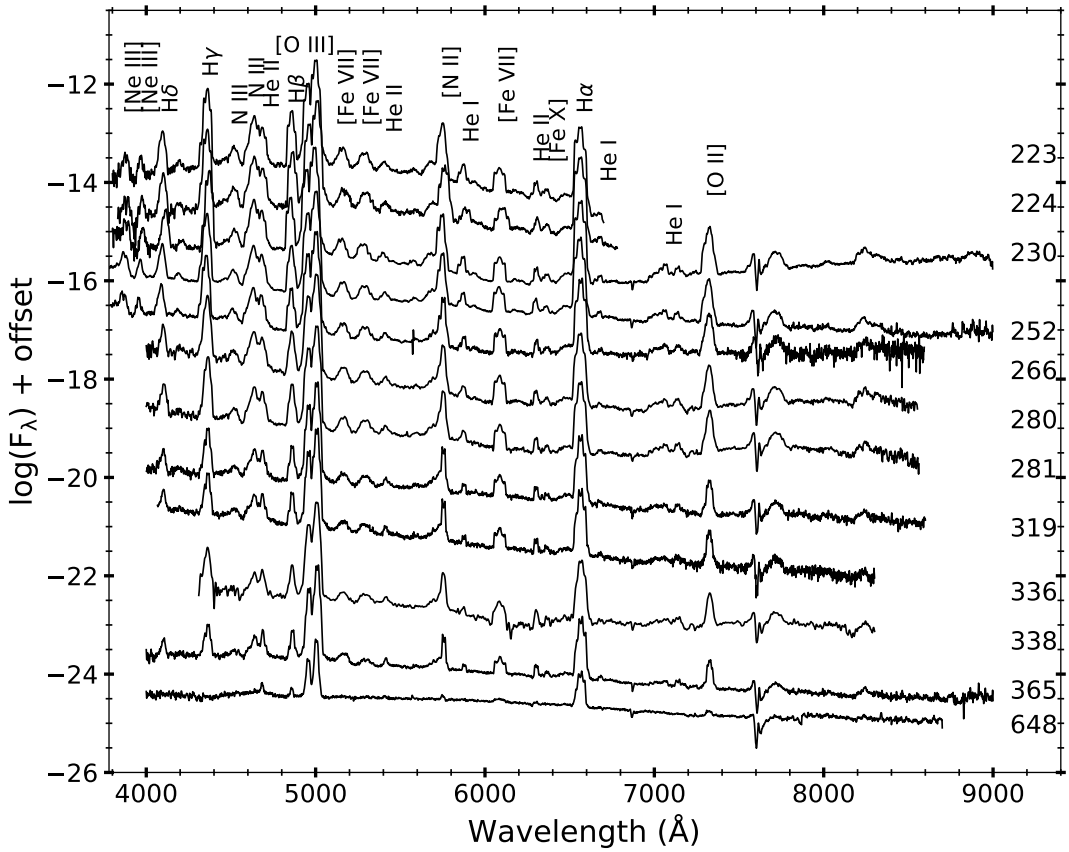

Figure 6.7: Spectral evolution during the nebular phase of T Pyx from 23 Nov 2011 (day 223) to 21 Jan 2013 (day 648). The lines identified and time since discovery in days (numbers to the right) are marked.

change is seen in the emissivity of these lines.

Late post outburst phase

The intensity of [O III] lines reduced during the nova's decline to late post-outburst phase during days 1064.39 to 2415.62 (Fig. 6.8). Strong helium emission lines are seen during this phase. The [O III] lines show a blue-shift by $\sim$780 km s^{-1} beyond day 1721, which is not seen in the hydrogen and helium emission lines. This could be due to the fact that while the [O III] lines arise in the fading nova ejecta, the hydrogen and helium lines arise in the accretion disc.

During the late post outburst phase, the spectrum obtained on day 1064 was modelled using CLOUDY. The observed spectrum is dominated by hydrogen, helium, and [O III] lines. The medium was assumed to be of a low-density diffuse component and a clump component to obtain a modelled spectrum. One component had an

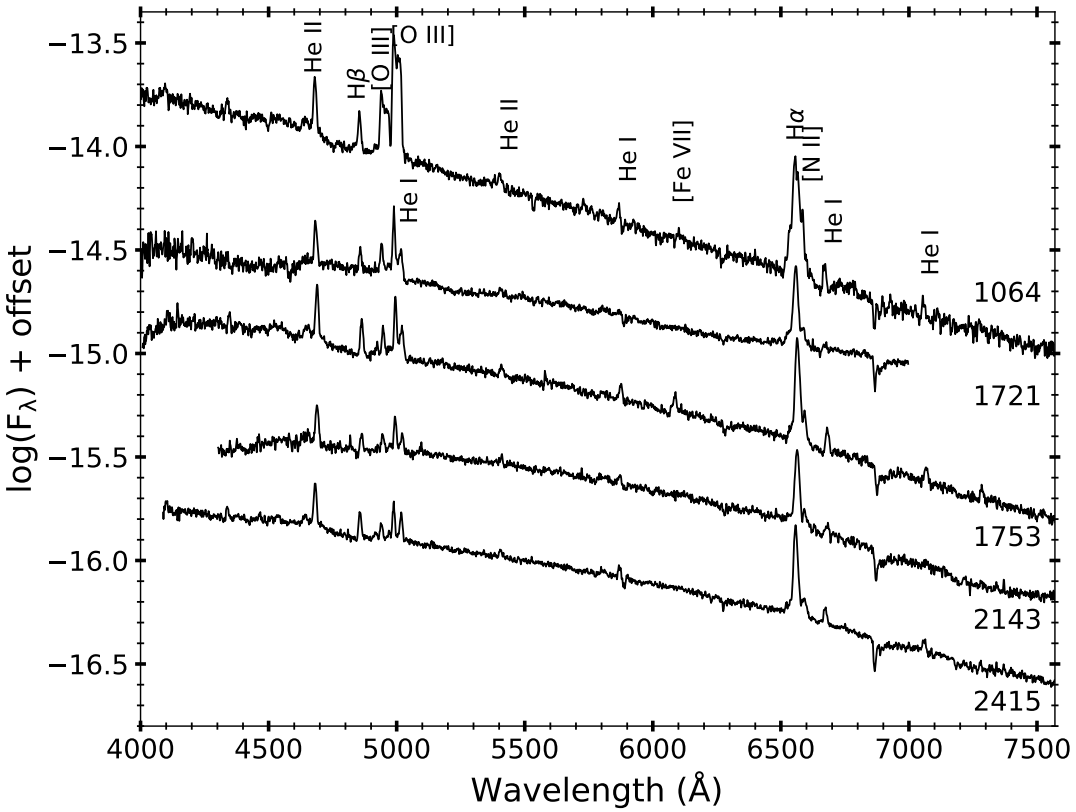

Figure 6.8: Spectral evolution during the late post-outburst phase of T Pyx from 13 Mar 2014 (day 1064) to 23 Nov 2017 (day 2415). The lines identified and time since discovery in days (numbers to the right) are marked.

ionizing source of luminosity 10^{35} erg s^{-1}, and disc with density 2×10^9 cm^{-3} at T = 7.5×10^4 K and cylindrical semi height, 10^4 cm. The helium and hydrogen lines were dominantly fit by this component. The other component had a similar ionizing source luminosity and lesser density region, 10^6 cm^{-3} at T = 9.5×10^4 K. The [O III] and nitrogen lines were fit using this component. The radius, luminosity, and density were calculated by adopting the values of the mass of the WD, accretion rate, period, and binary separation from Patterson et al. (2017) and Selvelli et al. (2008). The modelled spectrum was obtained by adding the values generated by the above components (Fig. 6.6). Best-fit parameters were obtained for these values (Table 6.9). The estimated abundance values of helium, nitrogen, and oxygen were found to be more than those of the solar abundance values. The details on the extent and distance from the central source of all the components in the morphology of the ejecta for all the epochs are given in Table 6.10.

Table 6.7: Observed and best-fit CLOUDY model line flux ratios[a] for epochs of nebular and late post-outburst phase of 2011 outburst of T Pyxidis

Line ID	λ (Å)	**Observed**	**modelled** Day 224	χ^2	**Observed**	**modelled** Day 252	χ^2	**Observed**	**modelled** Day 336	χ^2	**Observed**	**modelled** Day 1064	χ^2
[Ne III]	3869	5.51E-01	4.73E-01	1.00E-01	8.96E-01	6.33E-01	7.24E-01	...	...	...	...	...	...
[Ne III]	3968	7.65E-02	1.08E-01	3.67E-02	3.09E-01	3.83E-01	2.18E-01	...	...	...	...	...	...
H I	4102	3.58E-01	3.51E-01	2.17E-03	1.16E+00	9.19E-01	7.31E-01	8.12E-01	6.97E-01	4.02E-01	4.94E-01	4.39E-01	2.61E-02
H I, [C III], [O III]	4364	3.54E+00	3.52E+00	6.45E-02	6.23E+00	5.90E+00	1.22E+00	3.47E+00	3.19E+00	1.46E+00	1.19E+00	8.95E-01	1.22E+00
N III	4517	2.23E-01	6.14E-02	2.58E-01	3.02E-01	3.12E-02	4.59E-01	3.47E-01	1.68E-01	4.98E-01	...	...	...
N III + C III	4640	1.07E+00	7.84E-02	1.04E+00	1.50E+00	1.32E+00	5.79E-01	5.57E-01	4.55E-01	1.83E-01	5.64E-01	7.58E-01	8.16E-01
He II	4686	5.42E-01	2.78E-01	1.66E+00	8.59E-01	6.32E-01	7.04E-01	4.45E-01	5.76E-01	1.15E+00	1.79E+00	2.06E+00	0.80E-01
H I	4861	1.00E+00	1.00E+00	0.00E+00	1.00E+00	1.00E+00	0.00E+00	1.00E+00	1.00E+00	0.00E+00	1.00E+00	1.00E+00	0.00E+00
[O III]	4959	3.69E+00	3.96E+00	7.95E-01	3.17E+00	3.33E+00	3.14E-01	6.87E+00	7.31E+00	2.17E+00	2.84E+00	2.53E+00	1.41E+00
[O III]	5007	9.27E+00	9.36E+00	1.01E-01	1.39E+01	1.36E+01	1.09E+00	2.42E+01	2.41E+01	9.41E-02	7.08E+00	6.74E+00	9.65E-01
[Fe VII]	5158	3.75E-01	6.33E-01	4.48E+00	2.68E-01	4.63E-03	3.46E+01	...	...	...	...	...	...
[Fe VII]	5276	2.66E-01	1.97E-02	6.56E-01	2.57E-01	7.53E-03	9.95E-01	...	...	...	...	...	...
He II	5411	1.17E-01	2.38E-02	1.19E-01	3.64E-01	1.79E-02	1.83E-03	...	...	...	2.75E-01	2.52E-01	5.78E-03
N II	5679	...	...	...	3.53E-02	1.12E-02	1.05E-01	...	...	...	...	...	...
[N II]	5755	8.28E-01	9.87E-01	1.01E+00	7.47E-01	4.71E-01	1.00E+00	6.78E-01	4.07E-01	1.46E+00	...	...	...
He I	5876	2.20E-01	1.05E-01	2.37E-01	5.32E-02	2.14E-01	8.06E-01	1.19E-01	1.85E-01	5.69E-01	4.53E-01	1.71E-01	8.74E-01
[Fe VII]	6087	9.91E-02	2.16E-03	2.50E-01	3.23E-01	1.84E-02	1.51E+00	5.51E-01	4.34E-01	2.34E-01	...	...	...
H I + [N II]	6563	1.34E+00	1.06E+00	1.18E+00	1.62E+00	1.93E+00	1.18E+00	2.41E+00	2.66E+00	1.06E+00	3.50E+00	3.14E+00	1.36E+00
He I	6678	1.45E-02	4.52E-02	1.47E-02	1.70E-02	5.80E-02	1.29E-02	...	...	...	2.66E-01	2.89E-01	2.77E-02
He I	7065	...	...	...	...	...	...	...	...	...	3.88E-01	9.05E-02	1.17E+00
[O II]	7330	...	...	...	9.51E-02	1.18E-01	6.02E-02	2.19E-01	4.32E-02	4.59E-01	...	...	...

[a] Relative to Hβ

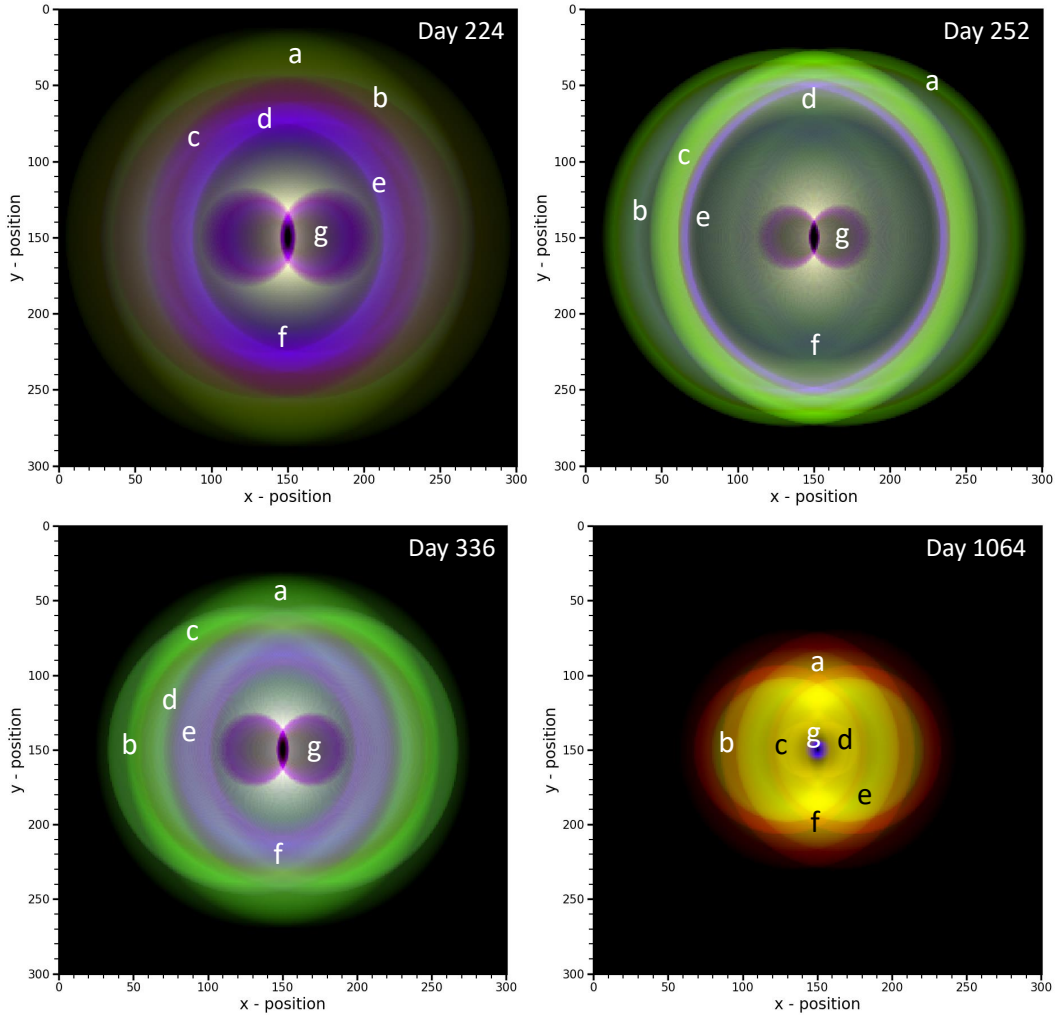

Figure 6.9: Evolution of the geometry of ejecta on day 224 (*top left*), 252 (*top right*), 336 (*bottom left*), and 1064 (*bottom right*) in the two-dimensional plane with X-axis being the line-of-sight direction and Y being the axis perpendicular to that of the plane of sky and line-of-sight. The lines corresponding to different colours are marked to show the spatial distribution of emission in the structure. There is formation of multiple equatorial rings and also the spatial distribution of the ionized lines as the system evolves. Here, a: [O III] λ5007, b: [O III] λ4959, c: Hα, d: Hβ, e: N III λ4638, f: [N II] λ5755, g: He II λ4686. Only dominant lines are marked. Here, 1 unit of x and y position correspond to $x_{224} = 6.3 \times 10^{12}$ cm, $x_{252} = 1.41 \times 10^{13}$ cm, $x_{336} = 2.09 \times 10^{13}$ cm, and $x_{1064} = 1.66 \times 10^{12}$ cm.

The ionized structures of different emission lines obtained in this phase have distinct spatial locations, unlike previous epochs. The overall geometry of the ejecta is prominently divided into a nitrogen zone, an oxygen zone, and a helium-hydrogen zone (from outer to inner regions) as shown in Fig. 6.9. The conical structures appear more evolved compared to the previous epochs. The outermost regions and the cones are of nitrogen lines, and the next inner regions are of [O III] lines indicating that

Table 6.8: Best-fit CLOUDY model parameters during the nebular phase of the 2011 outburst of T Pyxidis

Parameter	**Day 224**	**Day 252**	**Day 336**
T_{BB} ($\times 10^5$ K)	1.50 ± 0.14	2.5 ± 0.12	3 ± 0.08
Luminosity ($\times 10^{37}$ erg/s)	3.16 ± 0.11	3.98 ± 0.09	5.01 ± 0.10
Clump Hydrogen density ($\times 10^6$ cm^{-3})	79.43	63.09	56.23
Diffuse Hydrogen density ($\times 10^6$ cm^{-3})	31.62	25.12	17.78
Covering factor (clump)	0.80	0.80	0.80
Covering factor (diffuse)	0.20	0.20	0.20
α	-3.00	-3.00	-3.00
Inner radius ($\times 10^{15}$ cm)	2.34	2.88	3.09
Outer radius ($\times 10^{16}$ cm)	0.38	0.85	1.26
Filling factor	0.10	0.10	0.10
He/He$_\odot$	1.43 ± 0.11 (4)[a]	1.65 ± 0.09 (4)	1.16 ± 0.13 (2)
N/N$_\odot$	3.02 ± 0.07 (4)	3.63 ± 0.05 (5)	2.96 ± 0.10 (4)
O/O$_\odot$	3.01 ± 0.11 (3)	2.65 ± 0.08 (3)	2.63 ± 0.09 (4)
Ne/Ne$_\odot$	3.25 ± 0.12 (2)	1.36 ± 0.10 (2)	...
C/C$_\odot$	1.00 ± 0.05 (1)	1.02 ± 0.07 (1)	1.09 ± 0.05 (1)
Fe/Fe$_\odot$	1.09 ± 0.13 (3)	1.00 ± 0.11 (3)	1.00 ± 0.11 (1)
Ejected mass ($\times 10^{-6}$ $M_\odot$)	0.46	1.52	2.13
Number of observed lines (n)	18	20	13
Number of free parameters ($n_{\rm p}$)	10	10	7
Degrees of freedom (ν)	8	10	6
Total χ^2	12.74	15.18	9.22
$\chi^2_{\rm red}$	1.59	1.52	1.54

[a]The number in the parentheses is the number of lines used to determine the abundance estimate.

Table 6.9: Best-fit CLOUDY model parameters for the late post-outburst phase spectrum of the 2011 outburst of T Pyxidis.

Parameter	**Component 1/Component 2**
T_{BB} ($\times 10^4$ K)	$7.5 \pm 0.15/9.5 \pm 0.13$
Luminosity (log(L in erg/s))	$35 \pm 0.11/35 \pm 0.09$
Hydrogen density	9.3/6
α	-3.00
Inner radius (log(r in cm))	9/12
Outer radius (log(r in cm))	12/15
Covering factor	0.65/0.35
Filling factor	0.1
He/He$_\odot$	5.35 ± 0.11 (5)[a]
N/N$_\odot$	2.78 ± 0.08 (2)
O/O$_\odot$	2.21 ± 0.04 (2)
Shell mass ($\times 10^{-6}$ M$_\odot$)	3.64
Number of observed lines (n)	12
Number of free parameters ($n_{\rm p}$)	7
Degrees of freedom (ν)	5
Total χ^2	8.69
$\chi^2_{\rm red}$	1.74

[a]The number in the parentheses is the number of lines used to determine the abundance estimate.

Table 6.10: Details of the morphology of the ejecta on days 224, 252, 336 and 1064 for T Pyxidis

Epoch	Component	Extent[a] (cm)	Radius (cm)	Distance[b] (cm)	Angle[c] (°)
Day 224	Cone	$(3.32 \pm 0.11) \times 10^{14}$	$(4.49 \pm 0.14) \times 10^{14}$	$(1.27 \pm 0.09) \times 10^{14}$	87.75 ± 1.09
	Equatorial ring	-	$(1.13 \pm 0.10) \times 10^{15}$	$(3.78 \pm 0.11) \times 10^{14}$	-
Day 252	Cone	$(8.46 \pm 0.23) \times 10^{14}$	$(7.19 \pm 0.17) \times 10^{14}$	$(2.96 \pm 0.11) \times 10^{14}$	77.23 ± 0.99
	Equatorial ring	-	$(1.65 \pm 0.13) \times 10^{15}$	$(5.50 \pm 0.18) \times 10^{14}$	-
Day 336	Cone	$(1.61 \pm 0.10) \times 10^{15}$	$(1.85 \pm 0.13) \times 10^{15}$	$(3.01 \pm 0.11) \times 10^{14}$	61 ± 1.11
	Equatorial ring	-	$(2.61 \pm 0.13) \times 10^{15}$	$(1.07 \pm 0.07) \times 10^{14}$	-
Day 1064	Cone	$(1.93 \pm 0.10) \times 10^{13}$	$(9.63 \pm 0.24) \times 10^{12}$	$(4.81 \pm 0.15) \times 10^{9}$	49.89 ± 1.17
	Equatorial ring	-	$(2.31 \pm 0.14) \times 10^{14}$	$(5.30 \pm 0.21) \times 10^{12}$	-

[a]Extent of the component along the ejecta axis

[b]Distance from the central source to the component along the ejecta axis

[c]Outer opening angle of the cone

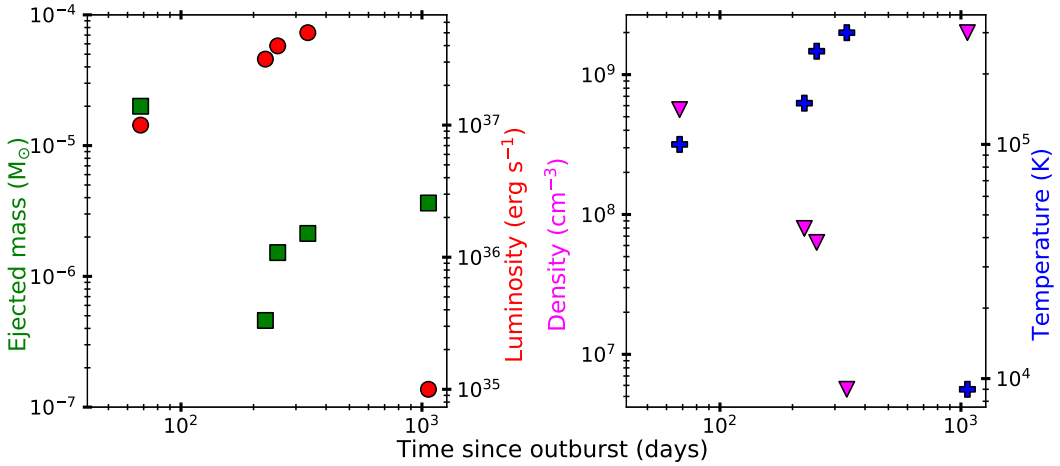

Figure 6.10: Variation of best-fit parameters obtained from CLOUDY such as luminosity, effective temperature, density, and ejected shell mass for the 2011 outburst of T Pyxidis are shown.

they are coming from a shell ejected by the system. The helium lines are coming from the region of a radius of about 7.4×10^9 cm. If the accretion rate suggested by Godon et al. (2018) is considered, then this radius value would correspond to that of the outermost regions of the accretion disc. This suggests that helium lines predominantly come from the accretion disc.

The best-fit model obtained for day 68 was used to fit only the emission components. The P-Cygni profiles and O I (7774 Å) line were not modelled due to the limitations of the code. The N II (5679 Å) line has a high χ^2 value, a broad emission component, and a narrow absorption component. The He II (4686 Å) line has higher χ^2 values and hence contributes more to the total χ^2. In the late post-outburst phase,

the [O III] and He I (7065 Å) lines have higher χ^2 values. Though the reduced χ^2 values suggest that the generated spectrum matches the observed spectrum well, the above contributions from different lines might hinder the calculated abundance values. The higher χ^2 values are as a consequence of blending of the lines. The [Fe VII] (6087 Å) line has a higher χ^2 value on a few days. It is a coronal line possibly excited by shock interaction, hence resulting in a higher χ^2 value. The variation of the best-fit parameters during the system's evolution is given in Table 6.10.

The estimate of the ejected mass, averaged over all epochs, is $7.03 \times 10^{-6}\,M_{\odot}$. This value is similar to that obtained by Shore et al. (2013). Best-fit model parameters suggest the presence of a hot WD source with a roughly constant luminosity of 10^{37} erg s^{-1}. Helium and nitrogen abundance values are above solar values in all the phases, whereas neon is more only during the nebular phase. Oxygen abundance is also found to be more than solar, while the iron and calcium abundances are nearly solar. Though the distance to T Pyxidis used for analysis is 4.8 kpc, the results were also verified for the distance given by Gaia of $\sim$3 kpc. The 1D CLOUDY results do not vary as relative intensity is considered for the calculations.

The modelled structure of the ionized ejecta shows that the evolution of the ejecta is consistent with the line profiles observed. The variation in the spatial distribution of the elements as the physical conditions change from one epoch to another is consistent with the observed spectra. The inner and outer cone angles found using this method are consistent with that estimated by Shore et al. (2013). The inner conical angles lie in the range of 21.08° to 77.86° while the outer conical angles varied from 49.89° to 87.75°. The value of the inclination angle of the ejecta axis to the line of sight was found to be $14.75° \pm 0.65°$. This value is consistent with that of the values reported by Patterson et al. (1998); Chesneau et al. (2011), and Shore et al. (2013).

Typically, the ejected mass estimates for other RNe are $\sim 10^{-7} - 10^{-6}\,M_{\odot}$, while the estimates for CNe are in general higher, at $\sim 10^{-5} - 10^{-4}\,M_{\odot}$. The ejected mass obtained for the T Pyx system in the early phase (day 68) is similar to CNe, while for the nebular phase the ejected mass values are similar to RNe.

Using accretion disc models, Godon et al. (2018) estimate a mass accretion rate of $10^{-6}\,M_{\odot}\,yr^{-1}$ for a distance of 4.8 kpc, or a rate of $10^{-7}\,M_{\odot}\,yr^{-1}$ for the Gaia distance estimate of $\sim$ 3.3 kpc, for a WD mass of $1.35\,M_{\odot}$. This indicates the mass accumulated between the 1967 and 2011 outbursts is lower than the ejected mass, for an ejecta mass of $\gtrsim 10^{-5}\,M_{\odot}$.

The morphology of the ejecta is a bipolar conical one with equatorial rings. The [O III] and nitrogen lines mainly originate from the outer regions, and hydrogen lines predominantly are from the inner regions (Table 6.10). As the shell evolves, expansion of equatorial rings can be seen in the nebular phase. In the late post-outburst phase, a complex structure of [O III] and nitrogen is formed with inner helium and hydrogen structure, most likely from the accretion disc. From the study of Chesneau et al. (2011), it is known that the system is oriented nearly face-on, and it is bipolar. Hence, the outer regions (especially [O III]) are moving away from the central system towards us (nearly face-on) resulting in the blue-shifted [O III] lines from day 1721.

6.3 V612 Sct

V612 Sct (or ASASSN-17hx or Nova Sct 2017) was discovered on 2017 June 19.41 UT by ASASSN (Stanek et al., 2017). Though it was spectroscopically confirmed as He/N nova by Kurtenkov et al. (2017b), the object was still in the rise phase. However, later the intensity of He I lines reduced and there was appearance of Fe II lines as reported by Munari et al. (2017b). The optical spectroscopic observations was reported by many other astronomers such as Williams & Darnley (2017); Berardi et al. (2017); Munari et al. (2017c,d); Pavana et al. (2017); Guarro et al. (2017); Poggiani (2017). A rapid re-brightening was reported in the optical light curve $\sim$40 days after maximum by Kurtenkov et al. (2017a). Also, reported was *Swift* UVOT observations by Kuin et al. (2017) on day 10.86 on wards. The UV spectrum consisted of N III] (1750), N II] (2143), Mg II (2800), Mg I (2850), C

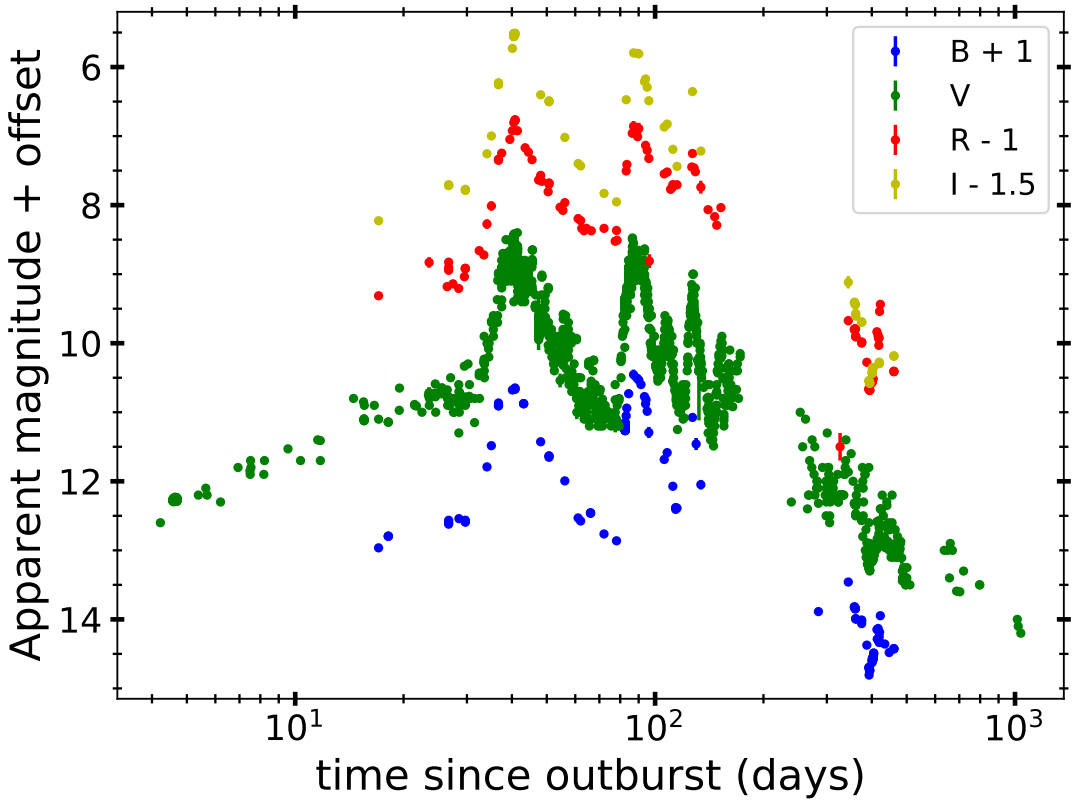

Figure 6.11: Apparent magnitude light curve of V612 Sct generated using the AAVSO data. Offset is given for clarity.

III (1909), O II (2471) and C II (2323). A large Fe-curtain absorption was seen at 1800-3800 Å with minimum depletion at 2600 Å on day 51.

A detailed study on this peculiar nova system with observational data for two years since discovery was presented by Mason et al. (2020). They found that the ejecta is undergoing free ballistic expansion with a typical CN structure with an ejected mass of the order of 10^{-3} $M_{\odot}$. The nebular spectrum was found to consist of coronal lines suggesting the ionizing source energy to be of the order of 20–250 eV. It was concluded that this nova belongs to a distinct subgroup of slow novae occurring on a very low mass WD or an impostor for a different class of transient.

In this section, the time of discovery 2017 June 19.41 is considered as t=0. The optical light curve was generated using the available AAVSO optical database (Fig. 6.11). The light curve shows many rebrightenings consisting of five maxima. The first maximum in V is on ∼day 40 at 8.4 mag. The decline rate from maximum was 0.1 mag day^{-1}, and it was followed by a rise phase starting on ∼day 77. The

Table 6.11: Optical spectroscopic observational log for V612 Sct.

Date	t (days)	Resolution	Coverage (Å)	Telescope
03 Jul 2017	14	1300, 2200	3800–9000	HCT-HFOSC
05 Jul 2017	16	1300, 2200	3800–9000	HCT-HFOSC
27 Jul 2017	38	1400	3800–9000	VBT-OMR
18 Aug 2017	60	60000	4000-10000	HCT-HESP
04 Sep 2017	77	1300, 2200	4200–8900	HCT-HFOSC
08 Sep 2017	81	1300, 2200	3800–9000	HCT-HFOSC
12 Sep 2017	85	1300, 2200	3800–9000	HCT-HFOSC
07 Oct 2017	110	1300, 2200	3800–9000	HCT-HFOSC
11 Oct 2017	114	1300, 2200	3800–9000	HCT-HFOSC
16 Oct 2017	119	1300, 2200	3800–9000	HCT-HFOSC
16 Oct 2017	119	60000	4000–10000	HCT-HESP
25 Oct 2017	128	1300, 2200	3800–9000	HCT-HFOSC
06 Mar 2018	260	1300	4000–7500	CZT-UAGS
10 Mar 2018	264	1300, 2200	3800–9000	HCT-HFOSC
11 Apr 2018	296	1300, 2200	3800–9000	HCT-HFOSC
11 May 2018	326	1300, 2200	3800–8800	HCT-HFOSC
27 Mar 2019	646	1300, 2200	3800–9000	HCT-HFOSC
25 Apr 2019	675	1300, 2200	3800–9000	HCT-HFOSC
16 May 2020	1062	1300, 2200	3800–9000	HCT-HFOSC

rise happened at a rate of 0.27 mag day^{-1} and reached the second maximum at 8.5 V mag on $\sim$day 87. The decline rate since second maximum was 0.16 mag day^{-1} faster than that of the first decline. The rise to third maximum started around day 103 with a rate of 0.18 mag day^{-1}. The maximum was reached around day 107 at V 9.5 mag. This was followed by a decline at the rate of 0.14 mag day^{-1}. The rise to the fourth maximum started on day 117 with a rate 0.18 mag day^{-1} reaching the maximum at 9 mag on $\sim$day 127. This was followed by a decline 0.13 mag day^{-1} and then the onset of the rise to the fifth maximum on $\sim$day 145 with a rate of 0.20 mag day^{-1}. The fifth maximum was reached at $V \sim 9.9$ mag on day 153. It was then followed by a decline with few variations in the sparse data available till day 1000. Similar rebrightenings are also seen in BRI bands. The $t_2(V)$ is found to be 18 days and $t_3(V)$ is found to be 105 days. Using the MMRD relation by Downes & Duerbeck (2000), the absolute magnitude of the nova was determined to be M_V = -6.71 $\pm$ 0.14. Using this absolute magnitude value in the relation by Livio (1992), the mass of WD was estimated to be 0.66 $\pm$ 0.06 $M_\odot$.

Log of the optical spectroscopic observations obtained for V612 Sct is given in

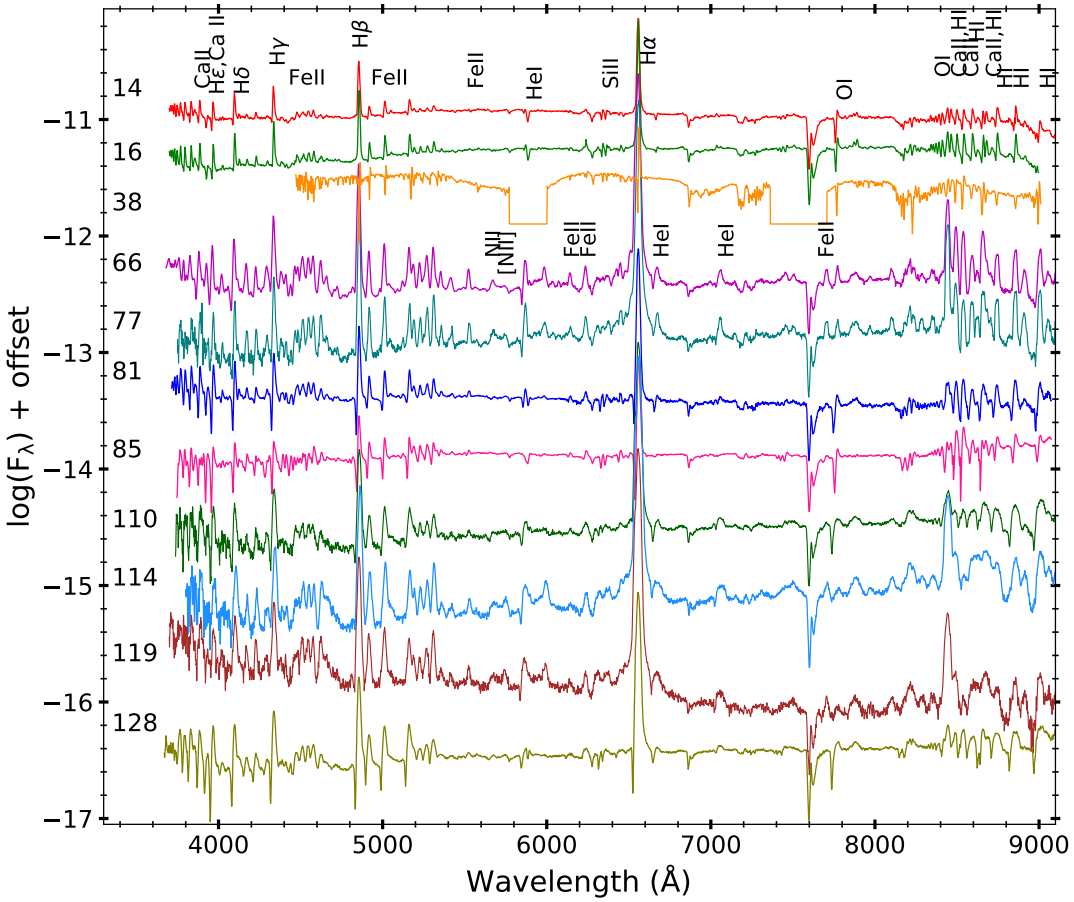

Figure 6.12: Low resolution spectral evolution of V612 Sct from 03 Jul 2017 (day 14) to 25 Oct 2017 (day 128). The identified lines are marked and the days since outburst are marked on the left. The line profiles evolving from P-Cygni to emission ones and back to P-Cygni are noted here.

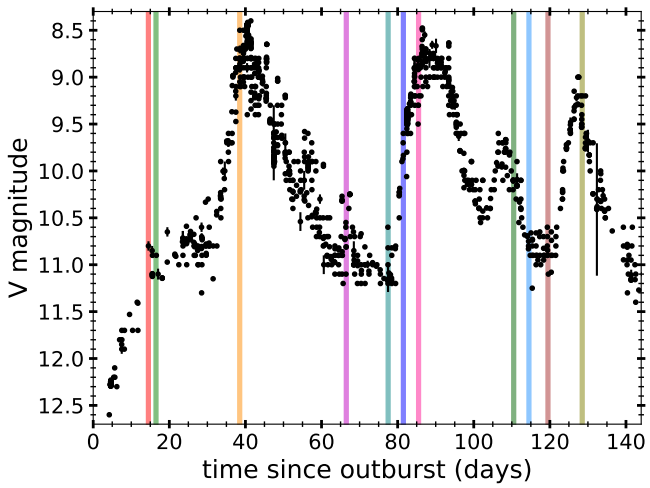

Figure 6.13: Apparent V magnitude light curve of V612 Sct with verticals lines marked in different colors corresponding to that of the spectral epoch in Fig. 6.12.

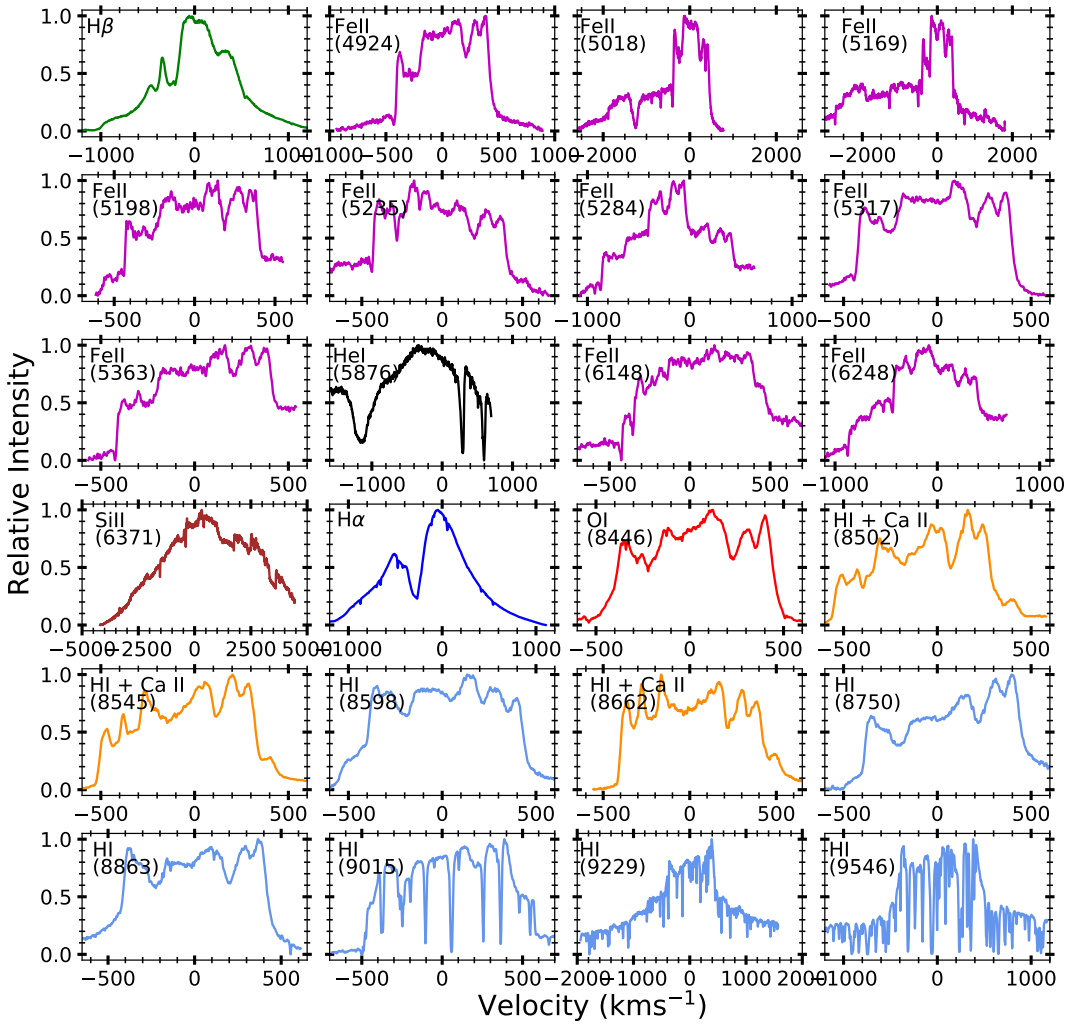

Figure 6.14: High resolution velocity profiles of V612 Sct obtained on day 60 since outburst. The color of the velocity profile represent particular elemental line. The lines are labelled against each panel.

Table 6.11. The optical spectral evolution from day 14 to 128 is as shown in Fig. 6.12. The epochs corresponding to rise, peak and decline of different maxima are depicted in Fig. 6.13 for clarity. The spectra consist of Fe II multiplets, Ca II, Si II, O I, He I and hydrogen Balmer and Paschen lines till the first maximum. The absorption components of the P-Cygni profiles become stronger as the system rises towards its first optical peak. Along with the lines present previously, the N II, [N II], He I and other Fe II lines are present. The P-Cygni absorption component is absent in most of the lines during the first decline phase. Once the system undergoes its second rise phase, the same lines evolve into P-Cygni profiles from day 81. On day 110 during the third decline phase, the lines again evolve into an emission only

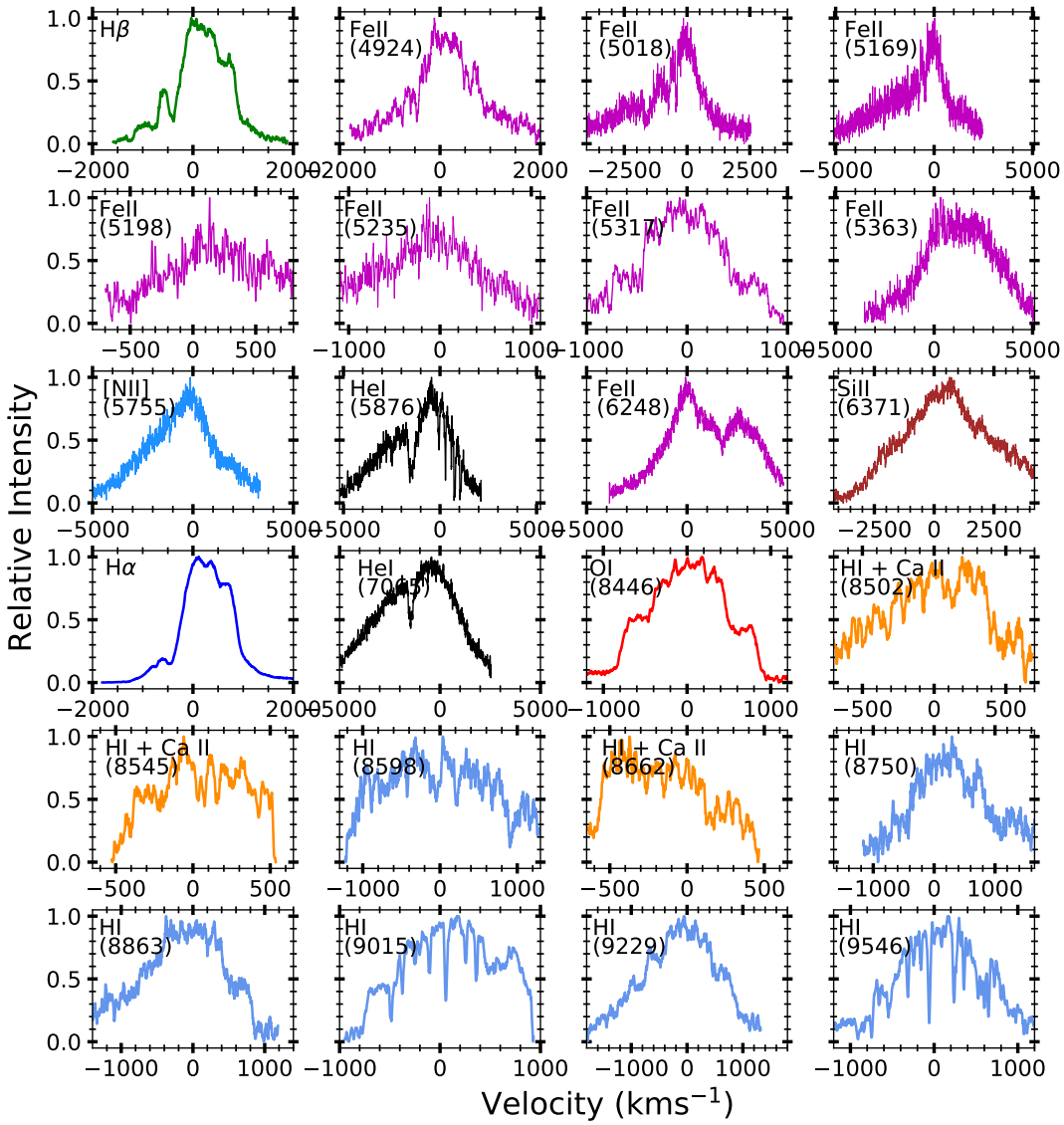

Figure 6.15: High resolution velocity profiles of V612 Sct obtained on day 119 since outburst. The color of the velocity profile represent particular elemental line. The lines are labelled against each panel.

profiles, followed by P-Cygni profiles on day 128 around the fourth peak. This indicates an increase in the optical depth during each rise. During every decline, the prominent non-Balmer line is O I (8446). The ionization states of the cloud of gas changes corresponding to the the rebrightenings seen in the photometric data. It is high at the minima than at every maximum.

High resolution spectroscopic data obtained on day 60, that is, the epoch during the decline phase since its first maximum is as shown in Fig. 6.14. Most of the profiles are rectangular/boxy in nature with several components. The hydrogen

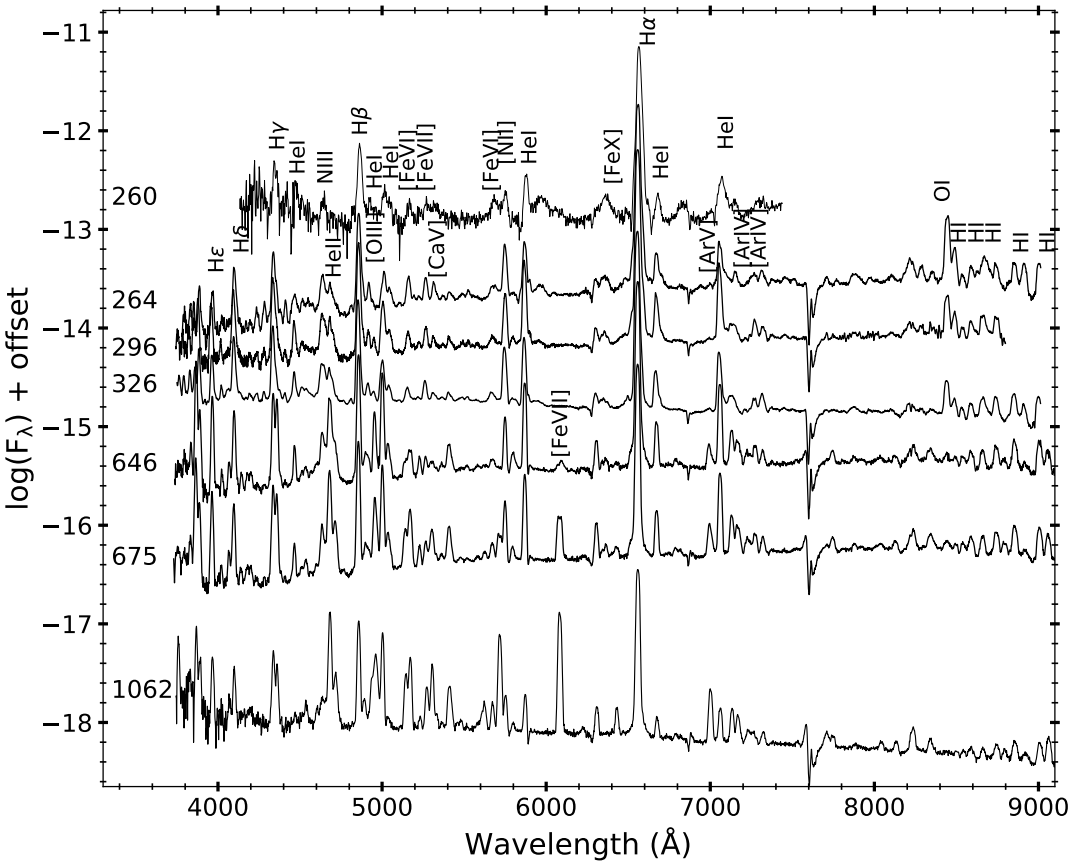

Figure 6.16: Low resolution spectral evolution of V612 Sct from 06 Mar 2018 (day 260) to 16 May 2020 (day 1062). The identified lines are marked and time since outburst is marked in days on the left.

Balmer line profiles have an absorption trough on the blue side. The He I has a P-Cygni profile with deeper absorption component and broader emission component. The high resolution spectroscopic data obtained on day 119 (fourth rise) is as shown in Fig. 6.15. The profiles are smoother compared to that of day 60. However, the hydrogen Balmer profiles are rectangular with an absorption trough on the blue side. The O I and hydrogen Paschen are less rectangular/boxy kind compared to that of the previous epoch.

Optical spectroscopic evolution in the optically thin phase from day 260 to 1062 is as shown in Fig. 6.16. There is appearance of high ionization forbidden and coronal lines in this phase. The emission lines present are N III, He I, [N II], He II, [Fe VI], [Fe VII], [Fe X], [Ar IV], [O III], O I and hydrogen Balmer and Paschen. The intensity of the forbidden lines and He I increases from day 264 to day 675 relative to hydrogen Balmer lines and then decreases. On day 1062, N III and [Fe VII] are

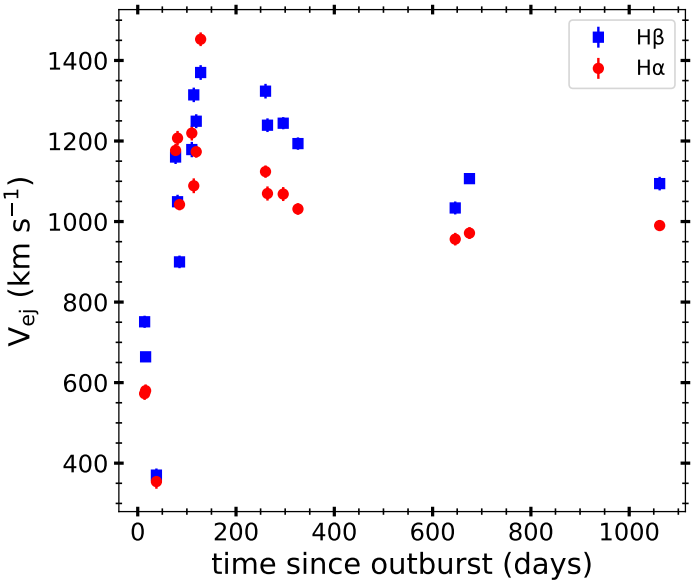

Figure 6.17: Evolution of Hα and Hβ FWHM velocities of V612 Sct from 03 Jul 2017 (day 14) to 16 May 2020 (day 1062).

the strongest non-Balmer lines.

The evolution of observed FWHM velocities of Hα and Hβ lines are as shown in Fig. 6.17. There is increase in the FWHM velocities of both Hα and Hβ from day 14 to 128 reaching up to 1400 km s^{-1} from $\sim$400 km s^{-1}. It is followed by a decline to about 1200 km s^{-1}. From $\sim$day 250, the FWHM velocities decrease very slowly from $\sim$1200 to about 1000 km s^{-1} and remains around this value till $\sim$1060 days.

Many novae are known to have re-brightenings during the early phase of their outbursts like V5113 Sgr (Kiyota et al., 2004), V2540 Oph (Ak et al., 2005), V4745 Sgr (Csák et al., 2005), V1186 Sco (Schwarz et al., 2007b), V458 Vul (Poggiani, 2008), V5558 Sgr (Tanaka et al., 2011b) and V2676 Oph (Raj et al., 2017). Following the rebrightening phases in these novae, the optical spectrum is seen to undergo some changes such as the re-appearance of the P-Cygni profiles (Tanaka et al., 2011a) as seen in V612 Sct. The absorption component that generally disappears during the post maximum decline reappears post the rebrightening. Tanaka et al. (2011a) suggest the appearance of the P-Cygni profiles to be due to a re-expansion of the photosphere after it has shifted sufficiently inside.

6.4 V906 Car

V906 Car (ASASSN-18fv or Nova Car 2018) was discovered on 2018 March 16.32 UT by Stanek et al. (2018) at magnitude of $V = 10.4$. A pre-discovery image obtained on 2018 March 16.227 UT indicated a magnitude of V = 10.21 $\pm$ 0.05 (Corbett et al., 2018). Strader et al. (2018) reported early optical spectroscopic observations of 21 March 2018 showing Hα, Ca II triplet, O I, Mg I, and several Fe II lines with P-Cygni profiles. The spectrum showed hydrogen Balmer and Paschen lines in absorption as well as a bump-like feature between 8300–9300 Å, with no obvious broad molecular features. It was suggested that this object is a young stellar object (YSO) or nova in the early phase. The optical spectrum obtained at a similar epoch by Luckas (2018) showed several Fe II features, Si II 6347, 6371 Å and absence of O I and He I lines suggesting the object to be a CN of Fe II class. They also reported very large optical depth for all the lines. Izzo et al. (2018) reported high resolution optical spectroscopic observations obtained on 22 March 2018. The continuum indicated an A-type main sequence star peaking around 5300 Å. The Hα line showed P-Cygni profile having blue-shifted heliocentric velocity, v $\sim$ -340 km s^{-1}, and a narrow emission line characterized by a measured FWZI = 670 km s^{-1} and FWHM = 325 km s^{-1}. O I 7773 Å line was found to be the strongest non-Balmer emission in the spectrum. Izzo et al. (2018) also reported the presence of several Fe II multiplets with P-Cygni absorption centered at a heliocentric velocity of v $\sim$ -250 km s^{-1} as well as weak blue continuum and low expansion velocities suggesting a different nature for V906 Car than a typical CN. The presence of narrow absorption features resembling peculiar explosions like the 'helium-flash' explosion observed in the Sakurai object (Duerbeck & Benetti, 1996), V4332 Sgr (Martini et al., 1999), V838 Mon or V1309 Sco (Mason et al., 2010; Tylenda et al., 2011) were reported by Izzo et al. (2018). However, Rabus & Prieto (2018) based on a NIR spectrum suggested that the system belongs to an *hybrid* class of novae. The spectrum (range 0.8–1.7 μm, R$\sim$3500) obtained on 2018 April 1.23 UT showed a large number of emission lines of H I, He I, Ca II, N I, O I and C I with relatively flat continuum.

The FWHM velocities ranged from few 100 km s^{-1} to 2000 km s^{-1}. The strong absorption lines or P-Cygni profiles which were present in the optical spectra 10 days earlier were almost absent. This clearly suggests that this nova is notably different from that of other peculiar explosions and rather it belongs to the hybrid class of novae. V906 Car showed γ-ray emission (Jean et al., 2018; Piano et al., 2018) and also shock detection (Nelson et al., 2018) during its evolution. No radio emission was reported at the nova position (Ryder et al., 2018).

Photometric and spectroscopic evolution of the ejecta of V906 Car based on the AAVSO and spectral data obtained are presented. In this section, t=0 corresponds to 2018 Mar 16.

6.4.1 Optical and near-Infrared light curve, reddening and distance

Optical and NIR light curves based on the data from AAVSO and Small and Moderate Aperture Research Telescope System (SMARTS[1]) (Walter et al., 2012) are presented in Fig. 6.18. The nova rose to a maximum in about 8 days after discovery, reaching a peak brightness of $V_{\rm max}$ = 5.8. Rebrightenings were seen in the optical light curve from day 24–34 followed by a decline. NIR light curve followed a similar trend as optical with small fluctuations primarily in the H and K bands. From the least-squares regression fit to the post-maximum light curve, $t_2(V)$ and $t_3(V)$ were determined to be 50 $\pm$ 5 days and 70 $\pm$ 5 days respectively. However, the t_3 value obtained using the relation t_3 = 2.75 $(t_2)^{0.88}$ by Warner (1995) was determined to be 85 days. This suggests that the system belongs to moderately fast nova category. The source was not detected on 15.34 Mar 2018 with limiting magnitude of about 17.0 by Stanek et al. (2018), hence the amplitude of the nova was estimated as ΔV $\sim$ 11 mag. In the amplitude versus decline rate plot for CNe (Fig. 2.3 of Warner (2008)), t_2 for this system and the amplitude places the system closer to the centre of the observed spread. Using the MMRD relation by Downes & Duerbeck (2000), the absolute magnitude of the nova was determined to be M_V = -7.0 $\pm$ 0.1. Using

[1]http://www.astro.sunysb.edu/fwalter/SMARTS/NovaAtlas/

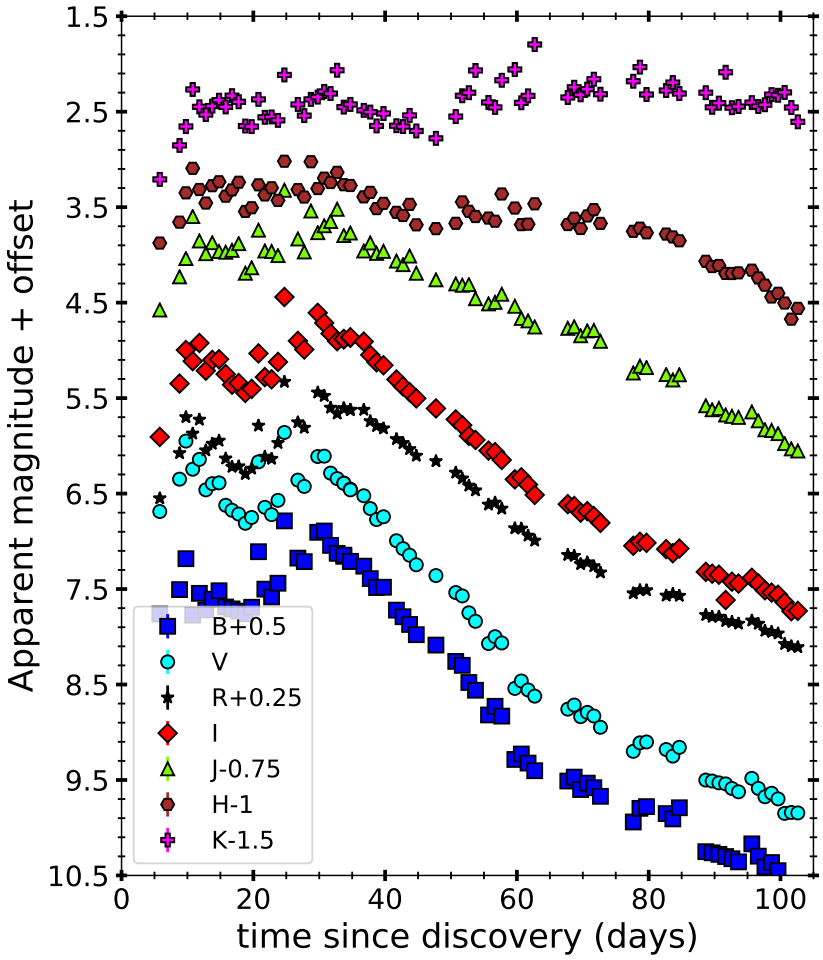

Figure 6.18: Apparent magnitude light curves of V906 Car generated using optical and NIR data from AAVSO and SMARTS. Offset applied for all the magnitudes except V for clarity.

the absolute magnitude value in the relation by Livio (1992), the mass of WD was determined to be 0.74 $M_{\odot}$. Reddening was estimated using the observed spectrum, and optical photometry data from SMARTS and AAVSO and the values obtained by both the methods were consistent. $E(B-V)$ was found to be 0.76 ± 0.02 using the Na I line present in the observed optical spectrum and determined using the relation given by Munari & Zwitter (1997). $E(B-V) = 0.75 \pm 0.07$ and $A_V = 2.3 \pm 0.2$ for R = 3.1 using the intrinsic colors of novae at peak brightness (van den Bergh & Younger, 1987). The extinction map by Neckel & Klare (1980) shows A_V value in the range of 1–2 in the direction of V906 Car, around 1–2 kpc. In a dust map given by Schlafly & Finkbeiner (2011), it was reported that the extinction value was $A_V \sim 3.6$ towards the direction of V906 Car, and a large error was suggested close to the Galactic centre (l, b: 286, -1.1). The moderate value of A_V estimated here appears to

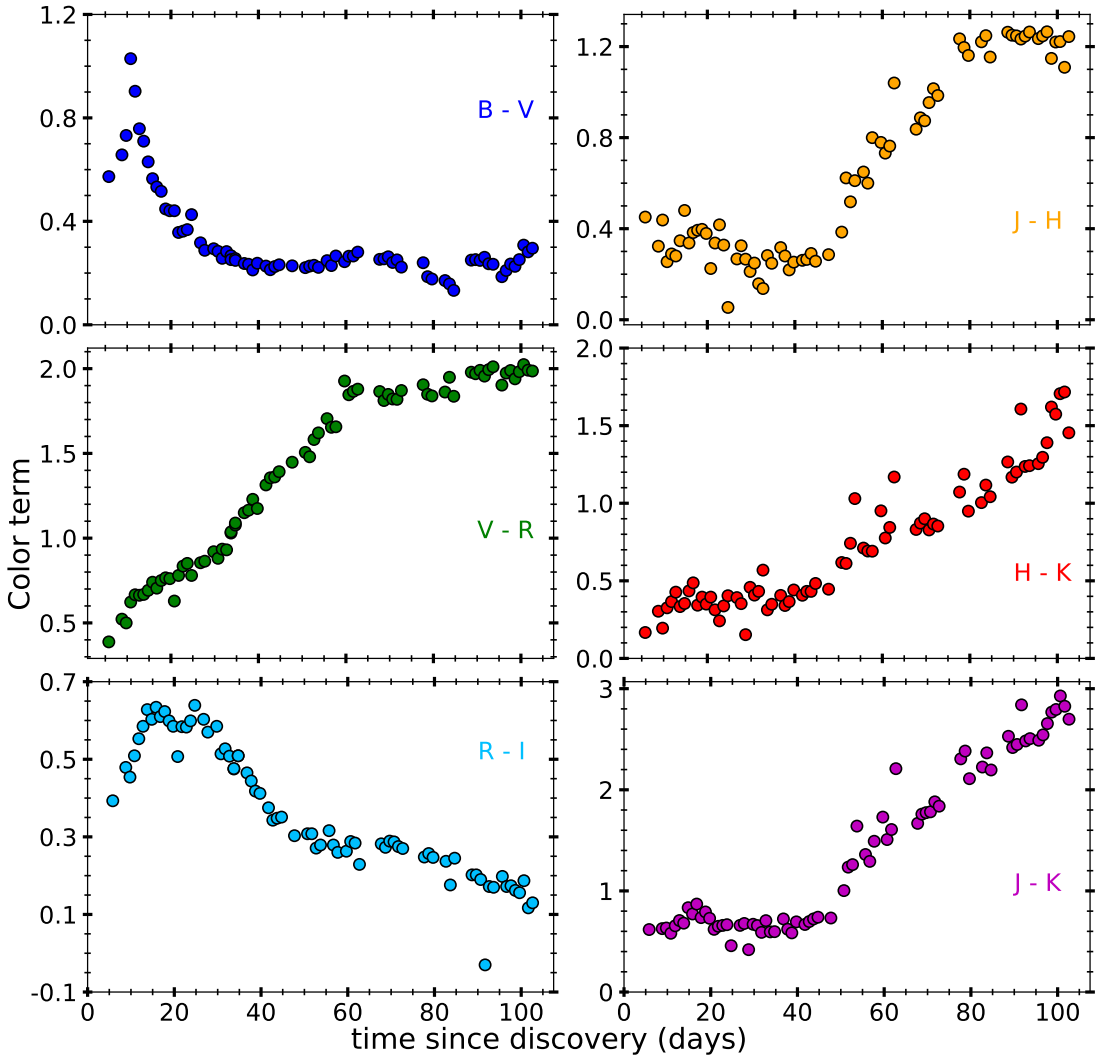

Figure 6.19: Evolution of optical and NIR color terms of nova V906 Car from day 0 (pre-maximum phase) to 100 (decline phase) since discovery.

be reasonable even though the nova is situated close to the direction of the Galactic centre. The distance to the nova was determined to be d = 1.3 $\pm$ 0.2 kpc using the above values.

A prolonged gamma-ray emission was reported during days 28-33 (Jean et al., 2018; Piano et al., 2018) coincident with the re-brightenings in the optical light curve. V906 Car was detected in hard X-rays by NuSTAR during day 35–37, but not detected in soft X-rays by *Swift* XRT (Nelson et al., 2018). Both observations indicate the presence of shock, as a result of the interaction of WD wind with the initial ejection, or due to the interaction of the ejecta with a pre-existing material such as wind from the secondary, or thick circumbinary material. NuSTAR observations

suggest the presence of a deeply embedded internal shock in the nova ejecta (Nelson et al., 2018), while the presence of a shock heated circumbinary material is indicated by McLoughlin et al. (2020) based on time-lapsed spectroscopic observations during the early phases. Based on γ-ray, X-ray, optical and radio observations, Aydi et al. (2020) suggest an initial ejection of a slow-moving torus followed by the ejection of a faster wind that shock interacts with the earlier ejected material.

Optical and NIR colour evolution for the nova is as shown in Fig. 6.19. The B-V and R-I colour evolution showed a rise for the first 10 days, reaching a peak of 0.8 and 0.64 respectively. This was followed by a steep decline and flattening for B-V and a slow decline for R-I colour. J-H, H-K, J-K and V-R colour evolution showed an increasing trend throughout the observations with small fluctuations. The shape of the optical light curves of this nova (Fig. 6.18) has characteristics similar to that of a 'J class' nova as it shows small fluctuations during its evolution. It can be classified as J(70) type as the estimated value of $t_3(V)$ is 70 days (see Strope et al. (2010) for more details).

6.4.2 Spectral evolution

Log of spectroscopic observations is given in Table 6.12. Low resolution spectral evolution of V906 Car during the pre-maximum and early decline phase is shown in Fig. 6.20. The spectra show presence of hydrogen Balmer and Fe II multiplets along with Ca II (H and K) and He I lines at 4922, 5876 Å. Rabus & Prieto (2018) reported the NIR spectrum taken on day 16 and suggested that the spectrum is consistent with a normal Fe II initially and then transition (Fe II + He/N) class novae after peak.

The spectra obtained after a month from day 50 during the decline phase (Fig. 6.21) consists of several emission lines like Fe II lines at 4179, 4297, 4549, 4629, 5018, 5169, 5284 Å etc. along with [N II] 5755, [O I] 5577, 6300 and 6364, [S II] 6724, O I 7002, 7477 Å. The other emission lines present were He I 4471, 5048 Å and broad He II 8237 Å and C II 4267 Å and N II 6482 Å. The spectrum obtained on day 96 consists of few Fe II lines along with some high excitation lines like He I 4922, 5876, 6678, 7065 and 7281 Å, Fe II lines at 5007 and 5018 Å, C IV 5805 Å,

Table 6.12: Observational log for spectroscopic data obtained for V906 Car.

Date	Time since discovery (days)	Resolution	Wavelength range (Å)	Instrument
2018 Mar 22	6	15000	6500–6670	LHIRES
2018 Mar 24	8	15000	6500–6670	LHIRES
2018 Mar 25	9	15000	6500–6670	LHIRES
2018 Mar 26	10	15000	6500–6670	LHIRES
2018 Mar 28	12	15000	6500–6670	LHIRES
2018 Mar 29	13	15000	6500–6670	LHIRES
2018 Mar 30	14	1500	3800–7250	LISA
2018 Mar 30	14	15000	6500–6670	LHIRES
2018 Mar 31	15	1500	3800–7250	LISA
2018 Apr 01	16	1500	3800–7250	LISA
2018 Apr 01	16	15000	6500–6670	LHIRES
2018 Apr 03	18	15000	6500–6670	LHIRES
2018 Apr 04	18	72000	4000-10000	VBT Echelle
2018 Apr 04	19	1400	4250–7600	OMR
2018 Apr 05	20	1300	4250–7600	UAGS
2018 Apr 06	21	27000	4000-10000	VBT Echelle
2018 Apr 06	21	1300	4250–7600	UAGS
2018 Apr 07	22	1300	4250–7600	UAGS
2018 Apr 08	23	1500	3800–7250	LISA
2018 Apr 09	24	15000	6500–6670	LHIRES
2018 Apr 09	24	1300	4250–7600	UAGS
2018 Apr 10	25	1300	4250–7600	UAGS
2018 Apr 11	26	15000	6500–6670	LHIRES
2018 Apr 30	45	15000	6500–6670	LHIRES
2018 May 05	50	1500	3800–8200	LISA
2018 May 06	51	1500	3800–8200	LISA
2018 May 09	54	15000	6500–6670	LHIRES
2018 May 10	55	1500	3800–8400	LISA
2018 May 19	64	15000	6500–6670	LHIRES
2018 May 27	72	1500	3800–7400	LISA
2018 Jun 21	96	1500	3800–7400	LISA
2019 Jan 26	316	66700	3800–8900	SALT

LISA and LHIRES are low and medium resolution spectrographs through a 0.28 m Celestron C11 telescope at Mirranook observatory, Australia. These data were obtained and reduced by T. Bohlsen.

N II 5938, 6482 Å. Hybrid nature of this system was suggested by Rabus & Prieto (2018) from the NIR spectrum (0.8–1.7 μ) and the lines like H I, He I, Ca II, N I, O I, C I were identified. The optical spectra of V906 Car also showed the presence of C II 4267 Å and N II 6482 Å lines and flat top profiles in May and June 2018 . The presence of He, N and C II spectral lines at such early epochs and also the flat top profiles (Williams, 1992) indicate that V906 Car belongs to the hybrid class of nova.

High resolution optical spectrum was obtained on day 316 using SALT-HRS

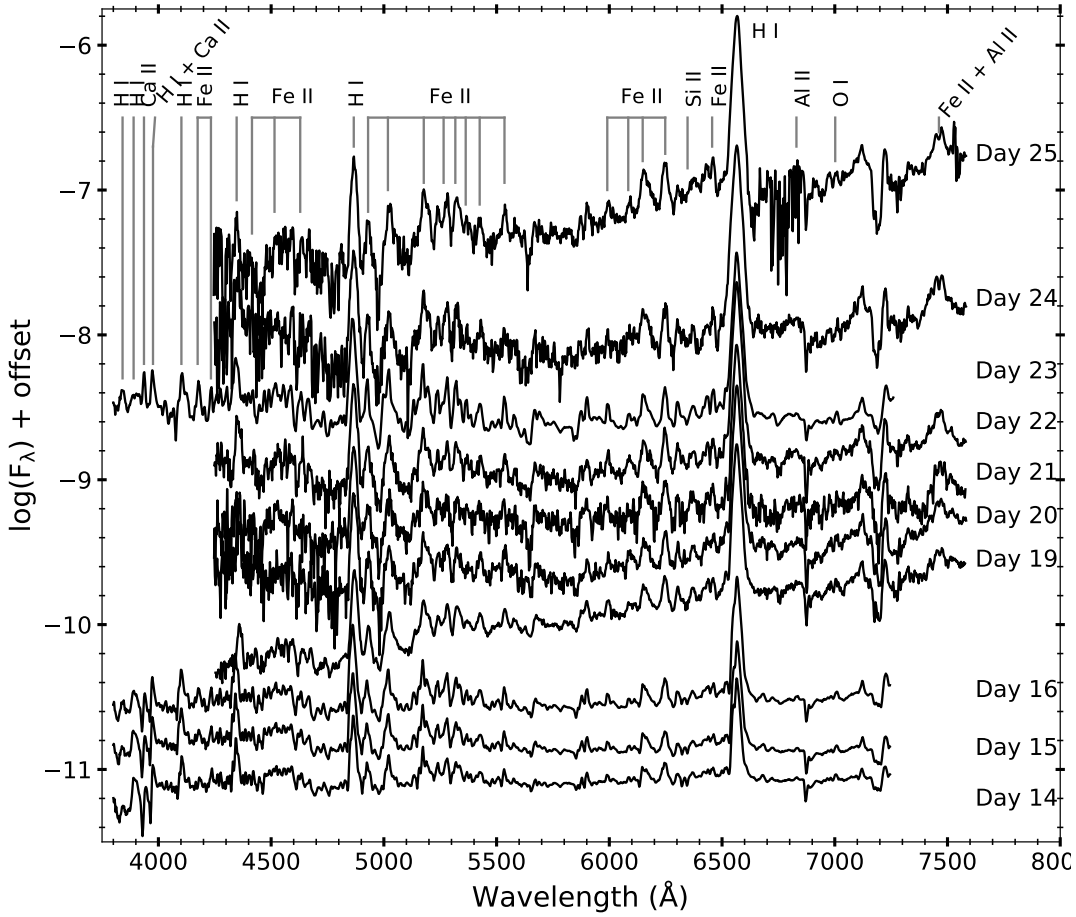

Figure 6.20: Low-resolution optical spectral evolution of V906 Car obtained from 2018 March 30 (day 14) to 2018 April 10 (day 25). Spectra are dominated by Fe II multiplets and hydrogen Balmer lines. The lines identified are marked on the top, and time since discovery in days are marked to the right.

spectrograph. The prominent lines present in the spectrum are hydrogen Balmer, N III 4638 Å, He II 4686 Å, He I 5876, 6678 and 7068 Å and [N II] 5755 Å. The emission line profiles are boxy and structured with multiple peaks. The He I lines are boxy with multiple peaks. The Hβ line profile appears to have boxy profile with three peaks.

The Hα velocity profile evolution is as shown in Fig. 6.22. The P-Cygni profile of Hα line has a blue-shifted component at $\sim$ -250 km s^{-1}. The P-Cygni profile was present until day 14. The observed FWHM velocities of Hα and Hβ lines are plotted in Fig. 6.23. During the early decline phase, the velocities range from 1500–2000 km s^{-1}. In the decline phase, FWHM velocities range from 800–1100 km s^{-1} followed by an increase in the velocities to 1400 km s^{-1} on day 316.

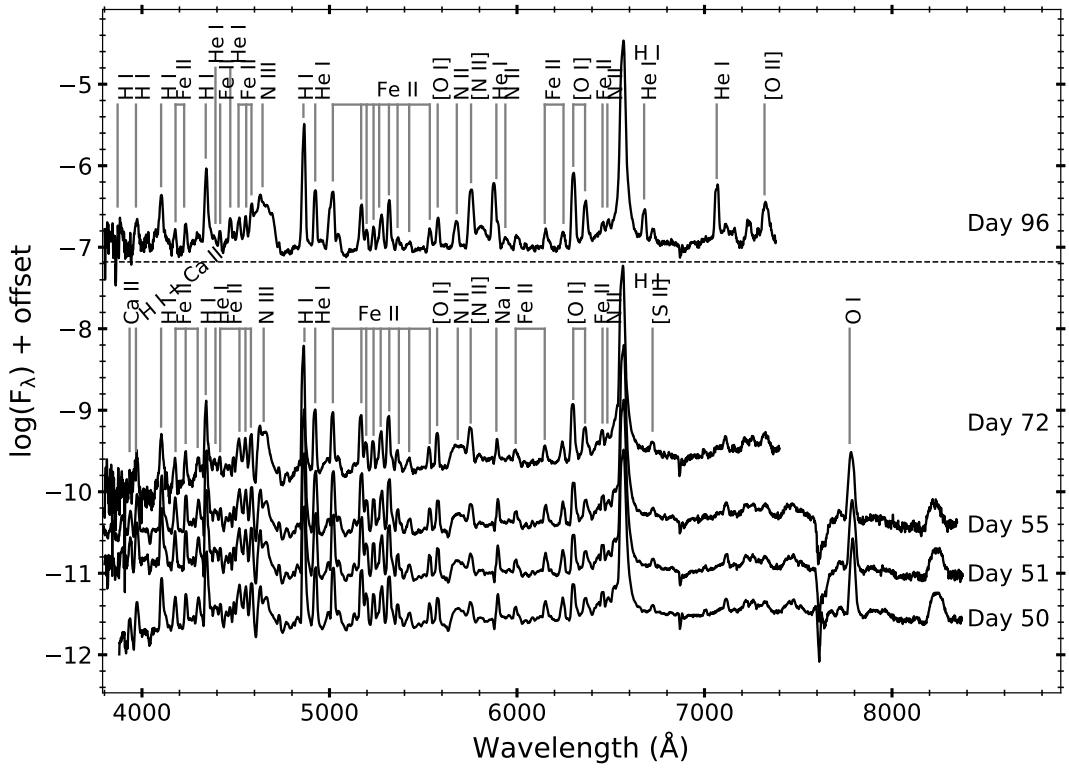

Figure 6.21: Low-resolution optical spectral evolution of V906 Car obtained from 05 May 2018 (day 50) to 21 June 2018 (day 96). From day 50 to 72, He, [O I], [N II] and N III lines appear and on 21 June 2018 (day 96), He I lines become very prominent. The lines identified are marked on the top, and time since discovery in days are marked to the right.

6.4.3 Physical parameters

Day 96 was chosen for analysis the spectrum during the transition phase as it shows both Fe II and the He/N features. The optical depth τ of the ejecta for [O I] 6300 Å using Eq. 3.2 was 0.50 ± 0.13. The electron temperature T_e calculated using the estimated value of τ in Eq. 3.3 was found to be 7026 ± 74 K. The hydrogen mass was estimated using the Eq. 3.4 as $(2.16 \pm 0.17) \times 10^{-4}$ M$_\odot$.

CLOUDY was used to model the system on day 96. The effective temperature and luminosity for the central ionizing source were set at 1.38×10^5 K and 10^{38} erg s^{-1} respectively. The medium was assumed to be of a low-density diffuse component and two clump components to obtain the modelled spectrum. Fe II and He lines were generated by two different clump components, and [N II] (5755 Å), [O I] (5577, 6300, 6364 Å), [O II] (7320 Å) and N II (5679 Å) lines were generated by a diffuse component (low density) covering 15% of the volume. The clump hydrogen density

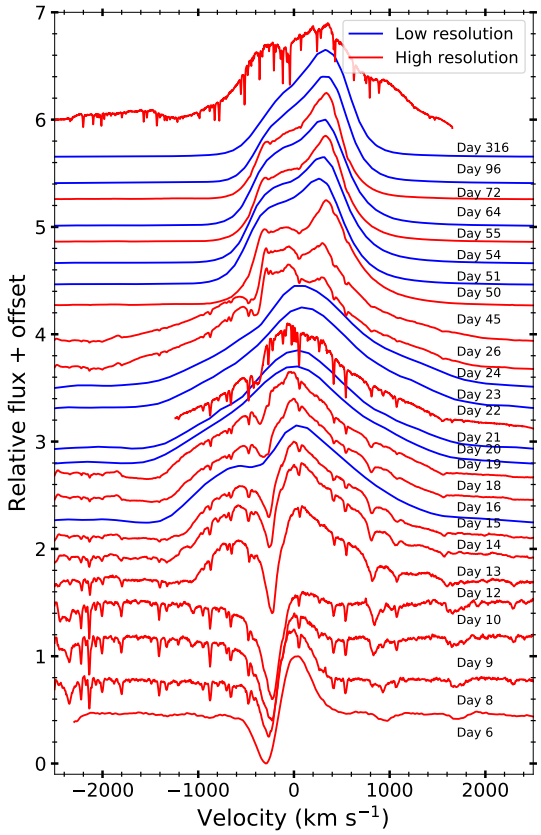

Figure 6.22: Evolution of Hα velocity profile of V906 Car from 22 Mar 2018 (day 6) to 26 Jan 2019 (day 316) obtained using the low, medium and high resolution optical spectroscopic data.

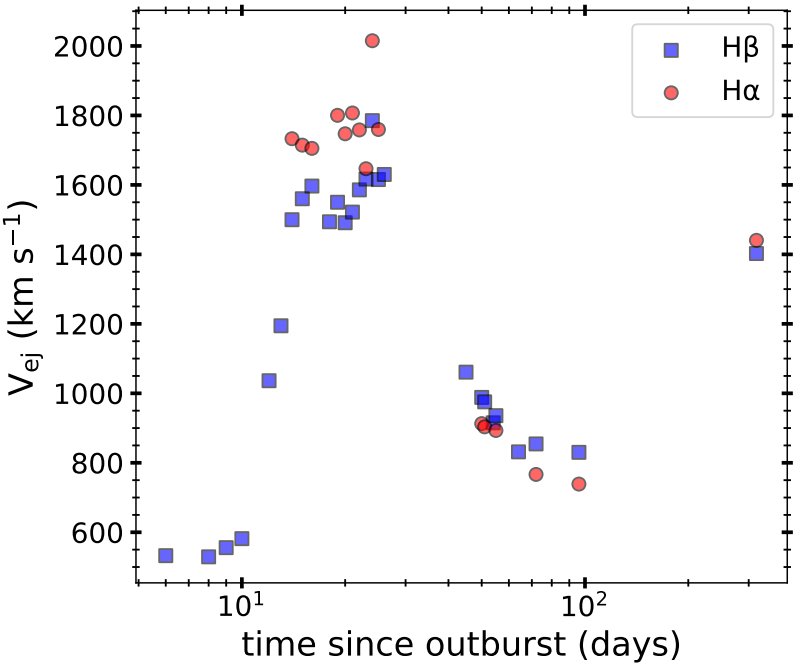

Figure 6.23: Evolution of Hα and Hβ FWHM velocities of V906 Car from 30 Mar 2018 (day 14) to 21 Jun 2018 (day 96).

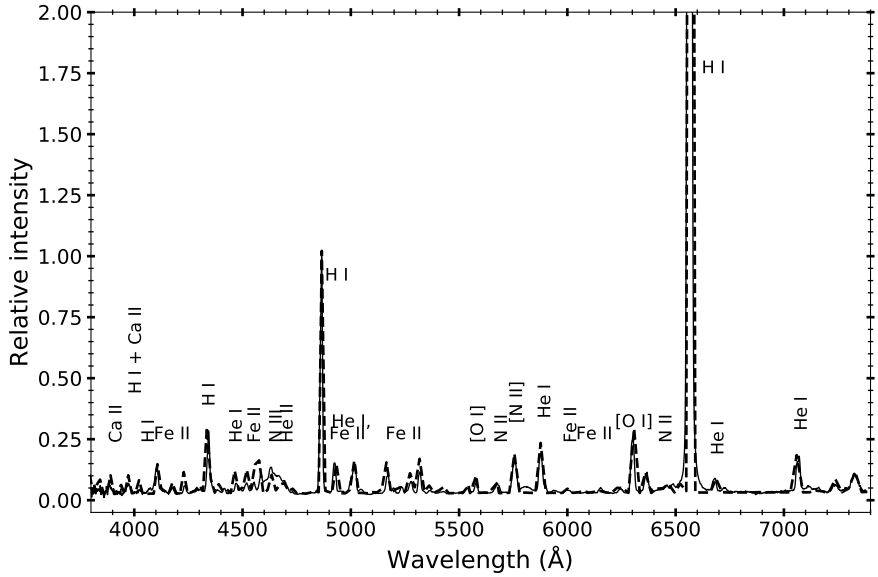

Figure 6.24: Best-fit CLOUDY synthetic spectrum (dash line) plotted over the observed spectrum (continuous line) of V906 Car obtained on 21 June 2018 (day 96).

was 10^{10} cm^{-3} and diffuse hydrogen density, 3.16×10^{9} cm^{-3}. The relative fluxes of the observed and modelled lines, and their corresponding χ^2 values are given in Table 6.13. The best-fit parameters obtained from the model are given in Table 6.14. The estimated abundance values show that helium, iron, oxygen and nitrogen are overabundant compared to solar values, while carbon abundance is solar. The ejected mass was found to be 6.07×10^{-4} M$_{\odot}$. The best-fit 1D spectrum obtained is as shown in Fig. 6.24. The optical depth τ of the ejecta for [O I] 6300 Å was 0.57 and the electron temperature $T_{\rm e}$ was $\sim$6000 K from the 1D model and the values were consistent with that obtained from spectral analysis.

6.4.4 Morpho-kinematic analysis

The morpho-kinematic analysis was carried out for the system using SHAPE. Hydrogen velocity profiles at epochs days 18, 21, 64, 96 and 316 were used to obtain the model profiles as hydrogen is the most abundant element in these systems. Few other line profiles like He I, He II, O I, N III, and [N II] were also modelled to study the behaviour of the ejecta geometry. The best-fit modelled profiles overplotted on the observed profiles are as shown in Fig. 6.25. The used and obtained best-fit parameters are provided in Table 6.15.

Table 6.13: Observed and best-fit CLOUDY model line flux ratios[a] for day 96 of V906 Car

Line ID	λ (Å)	**Observed**	**Modelled**	χ^2
H I	3889	1.57E-01	5.02E-01	2.94E+00
H I	3970	2.31E-01	5.09E-01	1.03E+00
He I	4026	4.92E-02	3.52E-01	9.23E-01
H I	4102	6.89E-01	8.94E-01	1.39E+00
Fe II	4179	7.55E-02	2.21E-01	3.01E+00
Fe II	4233	1.21E-01	4.47E-01	1.04E+00
H I	4340	1.01E+00	1.34E+00	1.21E+00
Fe II	4352	2.28E-01	6.76E-01	2.56E+00
He I	4471	2.77E-01	3.75E-01	4.00E-01
Fe II + N III	4517	4.85E-01	8.29E-01	1.94E+00
Fe II	4556	1.41E+00	1.54E+00	3.14E+00
Fe II	4584	1.03E+00	9.37E-01	5.60E-01
N III	4638	4.01E+00	4.06E+00	3.87E-02
He II	4686	7.02E-01	8.39E-01	6.94E-01
H I	4861	1.00E+00	1.00E+00	0.00E+00
He I + Fe II	4924	4.28E-01	6.49E-01	1.10E+00
He I + Fe II	5016	1.11E-01	9.91E-02	1.53E-03
He I	5048	2.82E-01	5.59E-01	1.08E+00
Fe II	5169	4.65E-01	6.64E-01	1.47E+00
Fe II	5198	4.43E-02	1.93E-01	4.92E-01
Fe II	5235	4.53E-05	1.64E-01	8.50E-01
Fe II	5276	1.15E-01	1.91E-01	8.64E-02
Fe II	5317	2.22E-01	6.06E-01	1.72E+00
Fe II	5363	2.82E-01	1.46E-01	3.50E-01
He II	5412	1.09E+00	1.18E+00	9.59E-02
Fe II	5535	1.02E+00	1.37E+00	2.20E+00
[O I]	5577	9.72E-02	1.06E-01	3.61E-03
N II	5679	2.66E-03	2.87E-02	2.52E-02
[N II]	5755	1.39E-01	3.27E-02	5.40E-01
C IV	5805	9.45E-02	1.39E-01	5.26E-01
He I	5876	1.39E+00	1.94E+00	3.00E+00
[O I]	6300	1.43E+00	1.15E+00	1.01E+00
[O I]	6364	5.53E-01	2.39E-01	2.36E+00
H I	6563	3.06E-01	3.91E-01	1.67E+00
He I	6678	1.11E+00	1.20E+00	1.00E-01
He I	7065	2.03E-01	1.09E-01	1.11E-01
C II	7235	3.57E-01	4.34E-01	4.00E-01
[O II]	7320-30	1.00E+00	6.64E-01	1.85E+00

[a]Relative to Hβ

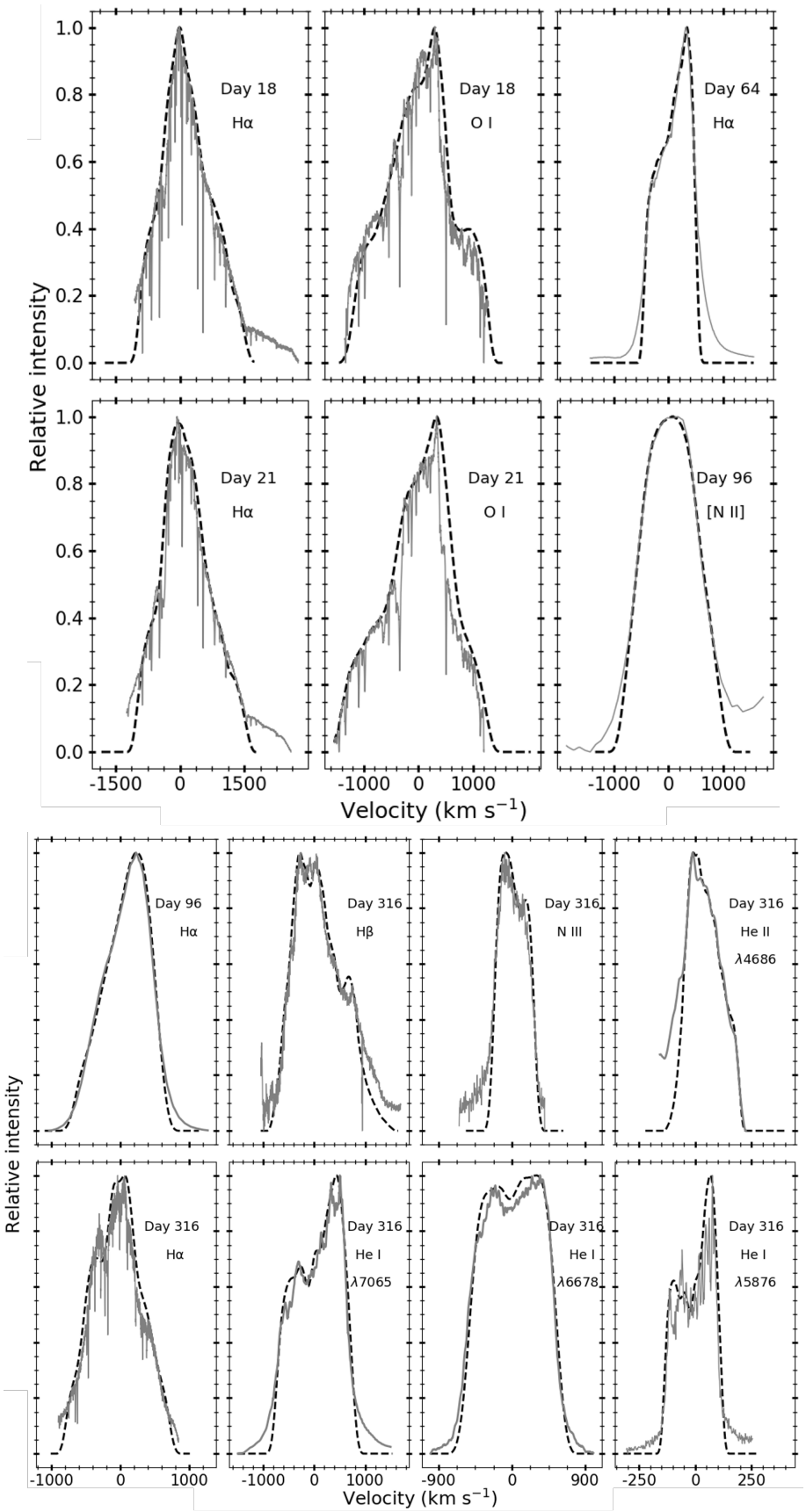

Figure 6.25: Best-fit modelled velocity profiles (dash black line) plotted over the observed Hα profile (continuous grey line) of V906 Car obtained on days 18, 21, 64, 96 and 316 since discovery. The day since discovery and identified lines are marked against each profile.

Table 6.14: Best-fit CLOUDY model parameters obtained on day 96 for the system V906 Car

Parameter	**Day 96**
T_{BB} ($\times$ 10^5 K)	1.38 $\pm$ 0.10
Luminosity ($\times$ 10^{38} erg s^{-1})	1.00 $\pm$ 0.08
Clump Hydrogen density ($\times$ 10^{11} cm^{-3})	1.58
Diffuse Hydrogen density ($\times$ 10^9 cm^{-3})	3.16
Covering factor (clump)	0.80
Covering factor (diffuse)	0.20
α	-3.00
Inner radius ($\times$ 10^{14} cm)	1.45
Outer radius ($\times$ 10^{14} cm)	6.76
Filling factor	0.10
$N/N_\odot$	3.48 $\pm$ 0.14 (4)[a]
$O/O_\odot$	2.88 $\pm$ 0.11 (4)
$Fe/Fe_\odot$	2.20 $\pm$ 0.10 (15)
$He/He_\odot$	2.14 $\pm$ 0.04 (9)
$C/C_\odot$	1.00 $\pm$ 0.03 (2)
Ejected mass ($\times$ 10^{-4} $M_\odot$)	6.07
Number of observed lines (n)	38
Number of free parameters (n_p)	12
Degrees of freedom (ν)	26
Total χ^2	41.92
χ^2_{red}	1.61

[a]The number of lines availed to obtain abundance estimate is as shown in the parenthesis.

Days 18 and 21

The ejecta geometry of O I 8446 Å obtained on days 18 and 21 (03 and 06 April 2018) was found to be asymmetric bipolar structures (dumbbell shape) with an inclination angle of about 60°. The best-fit O I 8446 Å geometrical structures corresponding to their best-fit velocity profiles are as shown in Fig. 6.26.

The ejecta geometry of Hα (Fig. 6.27) on days 18 and 21 were also found to be asymmetric bipolar with an inclination angle of about 53°. On days 18 and 21, the extent of red component was 1.7 and 2.2 times larger than that of the blue component respectively. Also, the red component was 1.3 and 1.2 times brighter than that of the blue component (*bottom* panel in Fig. 6.27) on days 18 and 21 respectively.

The ejecta geometry of Hα and O I have an extent ratio along the polar axis of 1.11:1 for both the epochs. These ejecta morphology and similarity in the velocity profiles indicated that they are coming from the same region. It also suggests that the O I line could be excited by Hα. This is possible when there is optically thick

gas in the medium (Strittmatter et al., 1977).

Day 64

The ejecta geometry of Hα on day 64 post the rebrightenings continues to be an asymmetric bipolar structure with an inclination angle of about 53°. The red component was 1.25 times bigger than that of the blue component along the polar axis (Fig. 6.27). The highest peak intensity component was located around the centre, which was ∼1.6 times higher than that of blue and red components (*bottom* panel in Fig. 6.27).

Day 96

The ejecta geometry of Hα (Fig. 6.27) on this epoch continues to be an asymmetric bipolar structure one with an inclination angle of about 82°. The red component

Table 6.15: Details of the morpho-kinematic analysis of the nova shell of V906 Car at different epochs.

Epoch	Line profile	Size ratio[a]	i[b] (°)	P.A.[c] (°)	χ^2_{red}[d]
Day 18	Hα	3.71 ± 0.12	55 ± 1.65	83 ± 1.85	1.39
	O I 8446 Å	4.21 ± 0.10	60 ± 1.80	83 ± 1.70	1.76
Day 21	Hα	3.79 ± 0.11	53 ± 1.55	83 ± 1.60	1.46
	O I 8446 Å	4.79 ± 0.12	60 ± 1.75	83 ± 1.45	1.82
Day 64	Hα	1.68 ± 0.04	53 ± 1.70	82 ± 1.85	1.24
Day 96	[N II] 5755 Å	1.90 ± 0.02	50 ± 1.25	82 ± 1.70	1.22
	Hα	1.45 ± 0.03	53 ± 1.65	82 ± 1.55	1.11
Day 316	N III 4638 Å	3.06 ± 0.07	50 ± 1.10	85 ± 1.35	1.73
	He II 4686 Å	3.13 ± 0.04	40 ± 1.30	85 ± 1.00	1.81
	Hβ	1.73 ± 0.06	50 ± 1.50	85 ± 1.15	1.62
	He I 5876 Å	2.65 ± 0.11	35 ± 1.65	85 ± 1.60	1.77
	Hα	3.18 ± 0.05	50 ± 1.95	85 ± 1.25	1.86
	He I 6678 Å	2.09 ± 0.04	40 ± 1.35	85 ± 1.00	1.41
	He I 7065 Å	2.64 ± 0.04	35 ± 1.40	85 ± 1.80	1.58

[a] Ratio of polar to the equatorial size.

[b] Inclination angle of the ejecta axis.

[c] Position angle of the ejecta axis.

[d] Reduced χ^2 calculated using the observed and modelled profiles and the degrees of freedom in the model.

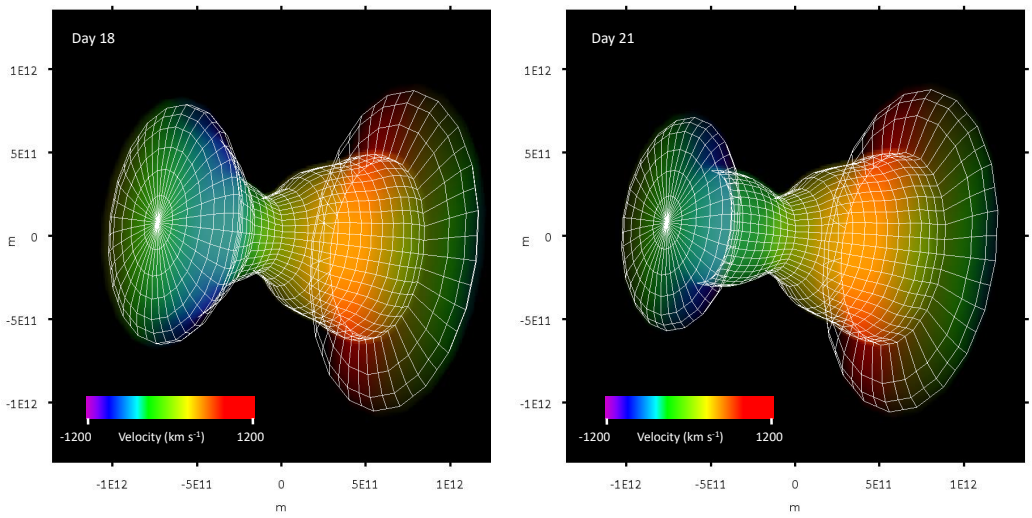

Figure 6.26: The asymmetric dumbbell-like O I 8446 Å structure of the ejecta of V906 Car on days 18 and 21 in the two-dimensional plane with X-axis being the line-of-sight direction and Y being the axis perpendicular to that of the plane of sky and line-of-sight. The colour gradient represents the velocity values varying along the line-of-sight.

was 1.5 times bigger than that of the blue component. However, the highest peak intensity component was located around the centre, similar to that of day 64 (*bottom* panel in Fig. 6.27).

The ejecta geometry of [N II] 5755 Å was asymmetric bipolar ellipsoidal-like structure with an inclination angle of about 82°. The best-fit [N II] 5755 Å geometrical structure corresponding to its best-fit velocity profile is as shown in Fig. 6.28. The blue component is 1.3 times bigger than that of the red component.

The ejecta geometry of Hα and [N II] have the extent ratio along the polar axis of 1.88:1. The dissimilarity in the ejecta structures of these two lines and their extents along the polar axis suggest that they are coming from different regions.

Day 316

The velocity line profiles of N III 4638 Å, He II 4686 Å, Hβ, He I 5876 Å, Hα, He I 6678 Å and He I 7065 Å were modelled during this epoch to obtain the ejecta structure. The ejecta geometries obtained corresponding to the above-mentioned velocity profiles are as follows:

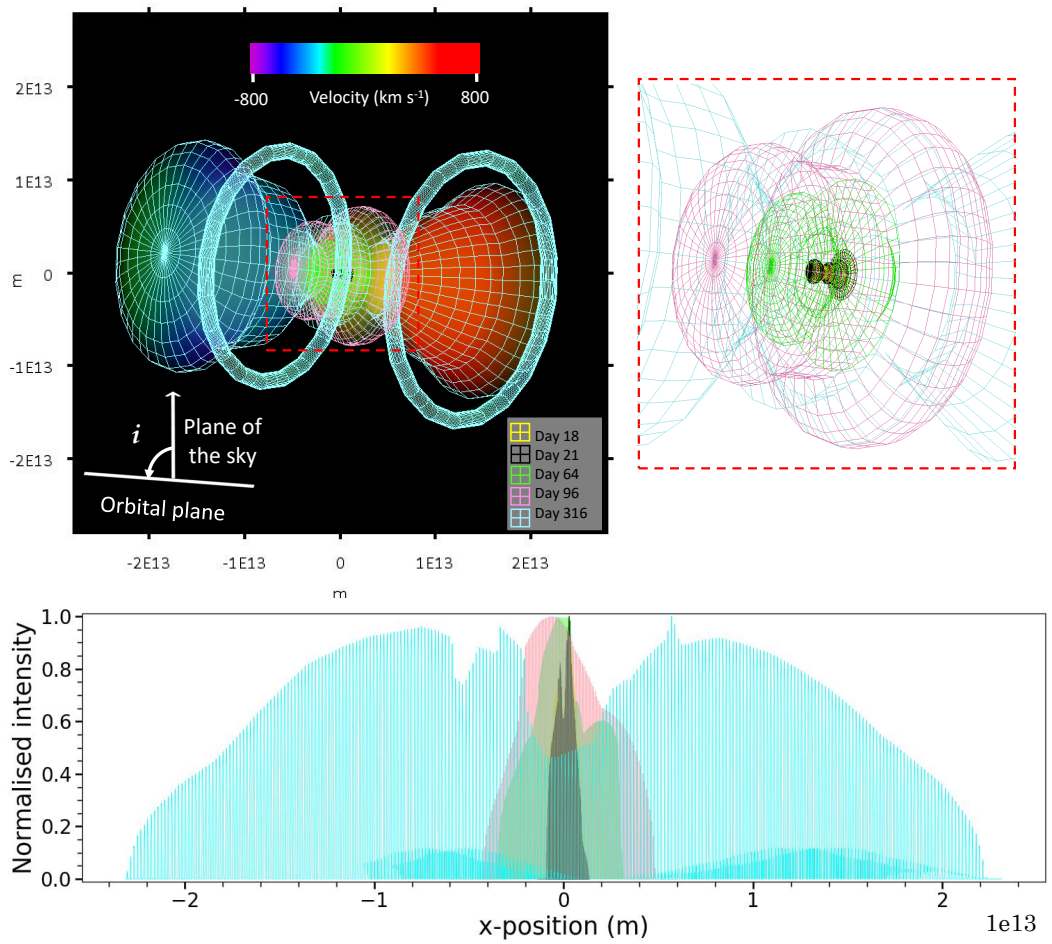

Figure 6.27: *Top-left:* The dumbbell-like Hα geometry obtained on days 18, 21, 64, 96 and 316 using the Hα velocity profiles of V906 Car. The ejecta structure is represented in the two-dimensional plane with X-axis being the line-of-sight direction and Y being axis perpendicular to the plane of sky and line-of-sight. The colour gradient represents the velocity values varying along the line-of-sight. The ejecta structure in the form of a grid is over-plotted to show different epochs. A zoomed view of the region highlighted in red in the centre is shown in the *top-right* panel. The inclination angle of the system is the angle between the plane of the sky and the orbital plane. *Bottom:* Histogram of the normalised intensity variation along the line-of-sight. The colours represent different epochs. This shows that the asymmetry in the ejecta structure decreases as the system evolves. The intensity distribution along the line-of-sight becomes uniform on to the red and blue components as the system approaches day 316.

* N III 4638 Å: Asymmetric bipolar structure with an inclination angle of about 50°. The blue component is slightly (∼1.1 times) bigger than that of the red component.

* He II 4686 Å: Asymmetric bipolar structure with an inclination angle of about 40°. The blue component is twice as big and twice the peak intensity value as

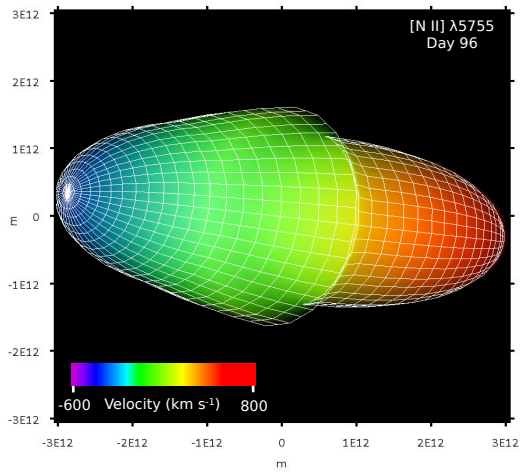

Figure 6.28: The asymmetric ellipsoidal-like [N II] geometry of the ejecta of V906 Car in the two-dimensional plane with X-axis being the line-of-sight direction and Y being axis perpendicular to that of the plane of sky and line-of-sight, and color gradient being the velocity values varying along the line-of-sight direction. The structure is obtained using the velocity profile of [N II] 5755 Å obtained on 21 June 2018 (day 96).

that of the red component. The polar end of the red component is triangular.

* Hβ: Asymmetric bipolar one with an inclination angle of about 50°. The blue component is 1.5 times bigger than that of the red component.

* He I 5876 Å: Asymmetric bipolar one with an inclination angle of about 35°. The red component is 1.5 times bigger than that of the blue component. The polar end of the blue component is triangular.

* Hα: The asymmetry in the Hα ejecta geometries seen in the previous epochs shows a decreasing trend as the system evolves. On day 316, the Hα geometry is found to be bipolar with equatorial rings with almost symmetric structures with an inclination angle of about 50°. The blue component is found to be 1.1 times that of the red component with similar peak intensity values (*bottom* panel in Fig. 6.27).

* He I 6678 Å: Asymmetric bipolar with similar size and intensity values of the blue and red components, with an inclination angle of about 40°. The polar end of the blue component is triangular while the red component has a more circular polar end.

∗ He I 7065 Å: Asymmetric bipolar structure with an inclination angle of about 35°. The red component is 1.5 times bigger than that of the blue component. The polar end of the blue component is triangular similar to 6678 Å line.

The best-fit geometrical structure of day 316 corresponding to their best-fit velocity profiles are as shown in Fig. 6.29. It is interesting to note that the extent of He II structure along the polar axis is eight times smaller than that of Hα extent suggesting that it is coming from the inner regions of the system. The extent of He I and N

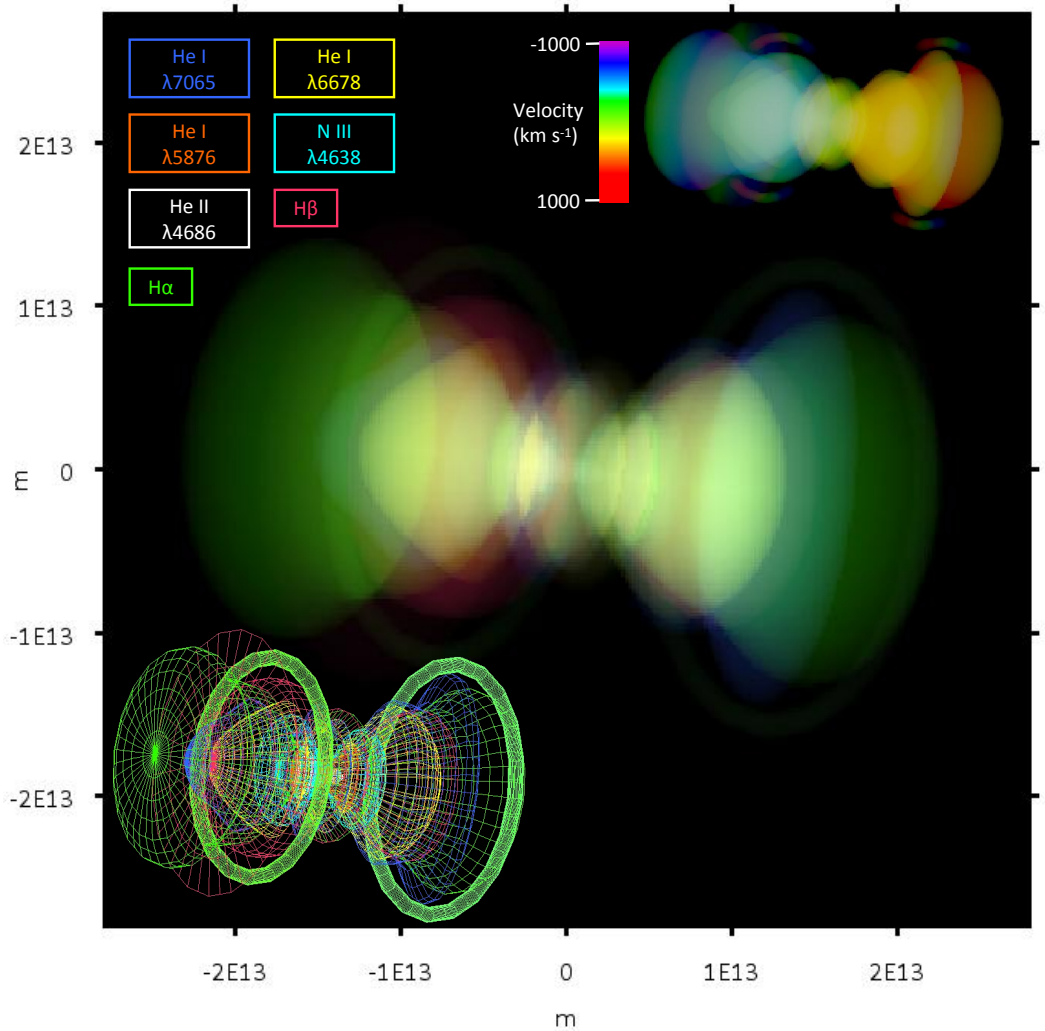

Figure 6.29: The geometry of the ejecta of V906 Car obtained on day 316 using H I, He I, He II and N III velocity profiles. The ejecta structure is represented in the two-dimensional plane with the line-of-sight direction along the X-axis and Y axis perpendicular to that of the plane of sky and line-of-sight. The colours representing different line profiles are as indicated. In the *top-right* panel, color gradient represent the velocity values varying along the line-of-sight. H I and N III regions have a more dumbbell-like structure, while the He region is bipolar with triangular polar ends.

III structures are also 2 to 6 times smaller than that of the Hα extent. Further, the structures of helium are different from that of N III. This suggests that they are coming from different regions.

The best-fit Hα geometrical structure of all the epochs corresponding to their best-fit velocity profiles are as shown in Fig. 6.27. An evolution of the ejecta geometry is seen along the polar axis. Significant asymmetry of the ejecta is seen in the initial epochs, (zoomed-in region in *top-right* panel of Fig. 6.27), as also indicated by the emission line profiles. As the system evolves, there is a clear indication of expansion in both polar and equatorial direction. The intensity and velocity variation along the line-of-sight also significant. The geometry of the Hα emitting region changes from an asymmetric one to a more symmetric one as the nova evolves to the nebular phase (*bottom* panel of Fig. 6.27).

Hα geometry of the ejecta obtained on days 18 and 21 have an asymmetric dumbbell-like structure with a brighter high-velocity component along the line-of-sight. On days 64 and 96, the Hα geometry is more like an intersection of spheres of different radii with the high-velocity component being bigger and brighter along the line-of-sight. The change in the geometry post day 21 could be due to the internal shocks present in the ejecta as suggested by Nelson et al. (2018) based on the absorbed thermal plasma model which fit the NuSTAR X-ray spectrum or evidence of internal shocks based on γ-ray emission by Aydi et al. (2020), or the presence of He/N class spectral lines. On day 316, the geometry is back to its dumbbell-like structures; however, it is closer to a symmetric morphology. As the shell expands, its interaction is probable with the secondary or with any CSM present. This could lead to the formation of ring-like structures in the ejecta. The geometrical evolution of the system is significant from day 18 to 316 in terms of symmetry. The asymmetry observed in the system gradually decreases with time, and the system is almost symmetric on day 316. The decreasing asymmetry is consistent with the behaviour of an expanding shell. The asymmetric ellipsoidal structure of [N II] obtained on day 96 is completely different when compared to that of the structures of O I 8446 Å, Hα and He. This suggests that [N II] is originating from a different region. O I

8446 Å region has a geometry and size very similar to that of Hα that is, asymmetric dumbbell-like structure suggesting that they could be originating from the same region. The extent of He structures along the polar axis suggests that they are coming from the inner regions of the shell. They have more triangular-like polar ends rather than circular ends seen in other structures.

6.5 The 2019 outburst of V3890 Sgr

The RN V3890 Sgr had two previous recorded outbursts in 1962 (Duerbeck, 1987) and 1990 Jones & Pearce (1990); Liller & Vina del Mar. (1990). The object was discovered to be in outburst for the third time on 2019 August 27.87 UT, when it was found to be at a visual magnitude of 6.7 as against its quiescence magnitude of $>$15.0 (Pereira 2019, VSNET-Alert 23505). V3890 Sgr belongs to the class of RNe with RG secondaries, such as RS Oph and V745 Sco (Anupama & Mikołajewska, 1999). These RNe are known to exhibit a shock interaction of the nova ejecta with the red giant wind, giving rise to strong hard X-ray and radio emission from the shock heated plasma.

Similar to RS Oph (Bode et al., 2006) and V745 Sco (Page et al., 2015), X-ray emission has been detected from V3890 Sgr by *Swift* XRT on 2019 Aug 28.44 UT with a net count rate of 1.85 $\pm$ 0.03 ct/s and unabsorbed 0.3–10 keV flux was estimated to be 1.8 $\times$ 10^{-10} ergs cm^{-2} s^{-1} (Sokolovsky et al., 2019). An optical spectrum of V3890 Sgr obtained with the 2 m HCT on August 29 (Pavana et al., 2019b) indicates the presence of weak coronal lines arising from the shocked plasma.

Novae are known to produce radio emission from freely expanding ionized gas at late times once the ejecta has become optically thin to free-free absorption (Seaquist & Palimaka, 1977; Hjellming et al., 1979; Seaquist et al., 1980; Kwok, 1983). However, there is a growing evidence for an early radio peak in several novae with brightness temperatures 10^5 – 10^6 K higher than that of the photo-ionized gas Taylor et al. (1987); Krauss et al. (2011); Chomiuk et al. (2014). RN RS Oph had an early radio

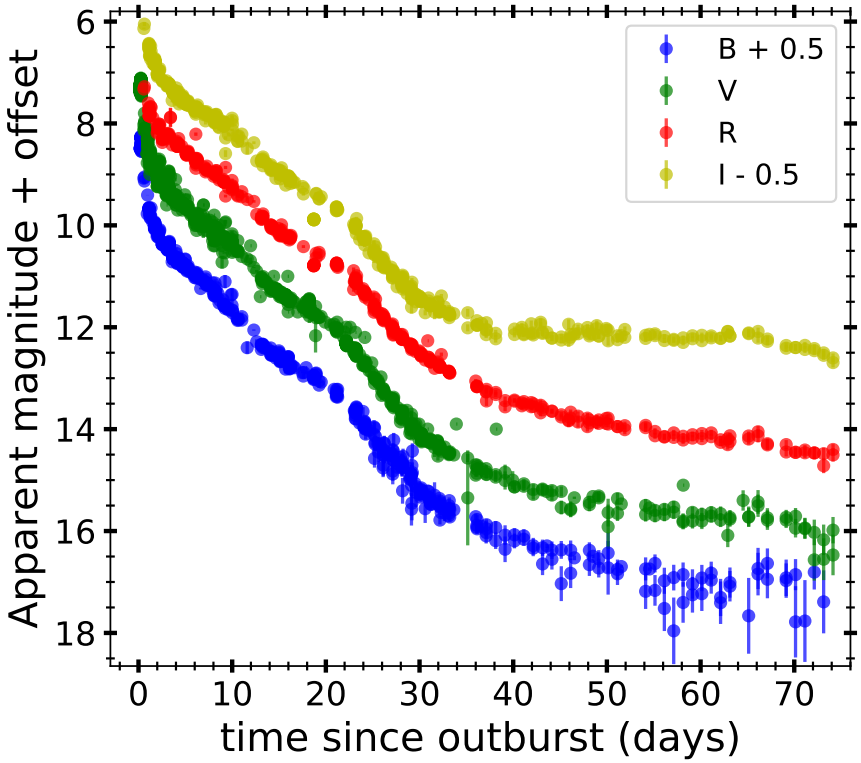

Figure 6.30: Apparent magnitude light curve of V3890 Sgr during its 2019 outburst generated using the AAVSO optical database. Offset is given for clarity.

peak before 13 days since outburst (Sokoloski et al., 2008; Eyres et al., 2009) during its 2006 outburst. Both thermal and non-thermal radio emission was detected. The GMRT observations of RS Oph (Kantharia et al., 2007) showed an early (< 20 days since outburst) non-thermal emission at the lower frequencies. Likewise, non-thermal emission was detected in V745 Sco using the GMRT (Kantharia et al., 2016) as early as day 12 from outburst. The non-thermal radio emission during the 2019 eruption of V3890 Sgr was first detected from MeerKAT on day 6.7 at 1.28 GHz (Nyamai et al., 2019). γ-ray emission was also detected by the *Fermi*-LAT during 2019 Aug 26–29 (Buson et al., 2019).

Optical and radio data observational log for the 2019 outburst of V3890 Sgr is as shown in Table 6.16.

6.5.1 Optical photometric and spectral evolution

The apparent magnitude light curve generated using the AAVSO optical database is as shown in Fig. 6.30. There is a sudden increase of 3.5 mag day^{-1} in V magnitude

Table 6.16: Observational log of optical and radio data for the 2019 outburst of V3890 Sgr

Optical spectroscopic observations			
Date	**t (days)**	**Coverage (Å)**	**Telescope**
30 Aug 2019	2	3800–9000	HCT-HFOSC
31 Aug 2019	3	3800–9000	HCT-HFOSC
04 Sep 2019	7	3800–9000	HCT-HFOSC
05 Sep 2019	8	3800–9000	HCT-HFOSC
09 Sep 2019	12	3800–9000	HCT-HFOSC
11 Sep 2019	14	3800–9000	HCT-HFOSC
13 Sep 2019	16	3800–9000	HCT-HFOSC
14 Sep 2019	17	3800–9000	HCT-HFOSC
15 Sep 2019	18	3800–9000	HCT-HFOSC
16 Sep 2019	19	3800–9000	HCT-HFOSC
23 Sep 2019	25	4000–9000	HCT-HFOSC
11 Oct 2019	43	4000–7500	HCT-HFOSC
22 Apr 2020	237	3800–9000	HCT-HFOSC
16 May 2020	262	3800–9000	HCT-HFOSC
Radio continuum imaging observations			
Date	**t (days)**	**Frequency (MHz)**	**Telescope**
06 Sep 2019	10	1420	GMRT
07 Sep 2019	11	610	GMRT
13 Sep 2019	17	610	GMRT
14 Sep 2019	18	1420	GMRT
17 Sep 2019	21	610	GMRT
19 Sep 2019	23	610	GMRT
21 Sep 2019	25	610	GMRT
22 Sep 2019	26	1420	GMRT
31 Oct 2019	65	1420	GMRT
16 Nov 2019	81	1420	GMRT
03 Dec 2019	98	1420	GMRT
21 Dec 2019	116	610	GMRT
23 Dec 2019	118	1420	GMRT
03 Jan 2020	129	610	GMRT
04 Jan 2020	130	1420	GMRT
31 Jan 2020	157	1420	GMRT
01 Feb 2020	158	610	GMRT
17 Feb 2020	174	610	GMRT

from 0 to 0.25 days with the system reaching its optical maximum at $V \sim 7.5$ and then rapid decline till day 2 of about 0.8 mag day^{-1}. This was followed by a decline of 0.16 mag day^{-1} from day 2 to 21. Then the decline rate increased to about 0.22 mag day^{-1} till day 31. Post day 31, the decline is very slow with a rate of 0.033 mag

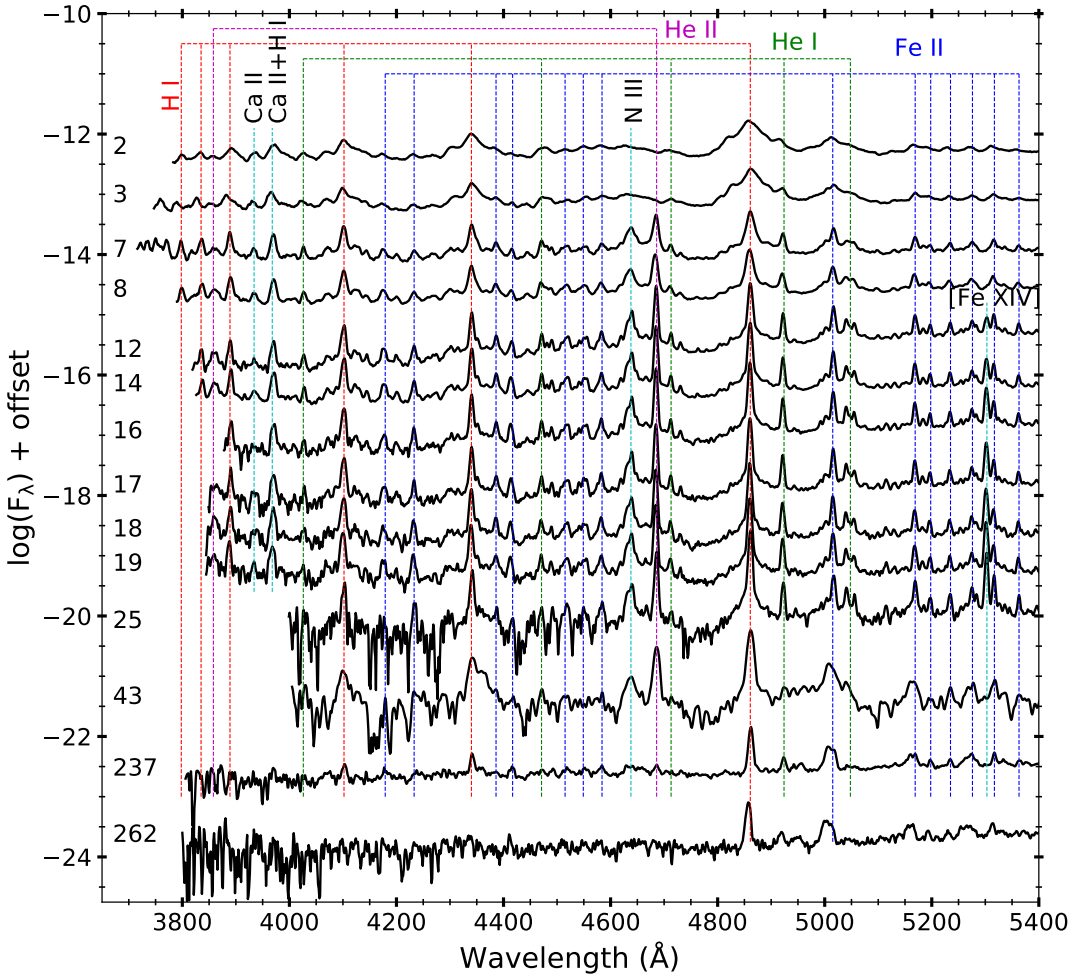

Figure 6.31: Low resolution optical spectral evolution of V3890 Sgr from 30 Aug 2019 (day 2) to 16 May 2020 (day 262) in the range of 3800–5400 Å.

day^{-1}. A linear regression fit to the light curve post maximum resulted in $t_2(V)$ = 2.89 $\pm$ 0.24 days and $t_3(V)$ = 8.6 $\pm$ 0.13 days. This light curve is similar to that of 'S class' as suggested by Strope et al. (2010). Using the MMRD relation by Downes & Duerbeck (2000), the absolute magnitude of the nova was determined to be M$_V$ = -9.90 $\pm$ 0.09. Using this absolute magnitude value in the relation by Livio (1992), mass of WD was estimated to be 1.37 M$_\odot$.

Optical spectrum obtained by Strader et al. (2019) on day 0.11 consisted of H I and He I lines with broad P-Cygni profiles and also presence of He II, N III and Na lines. They also reported a broad absorption trough of Hα extending up to 4200 km s^{-1} from the emission component center. The optical spectral evolution obtained

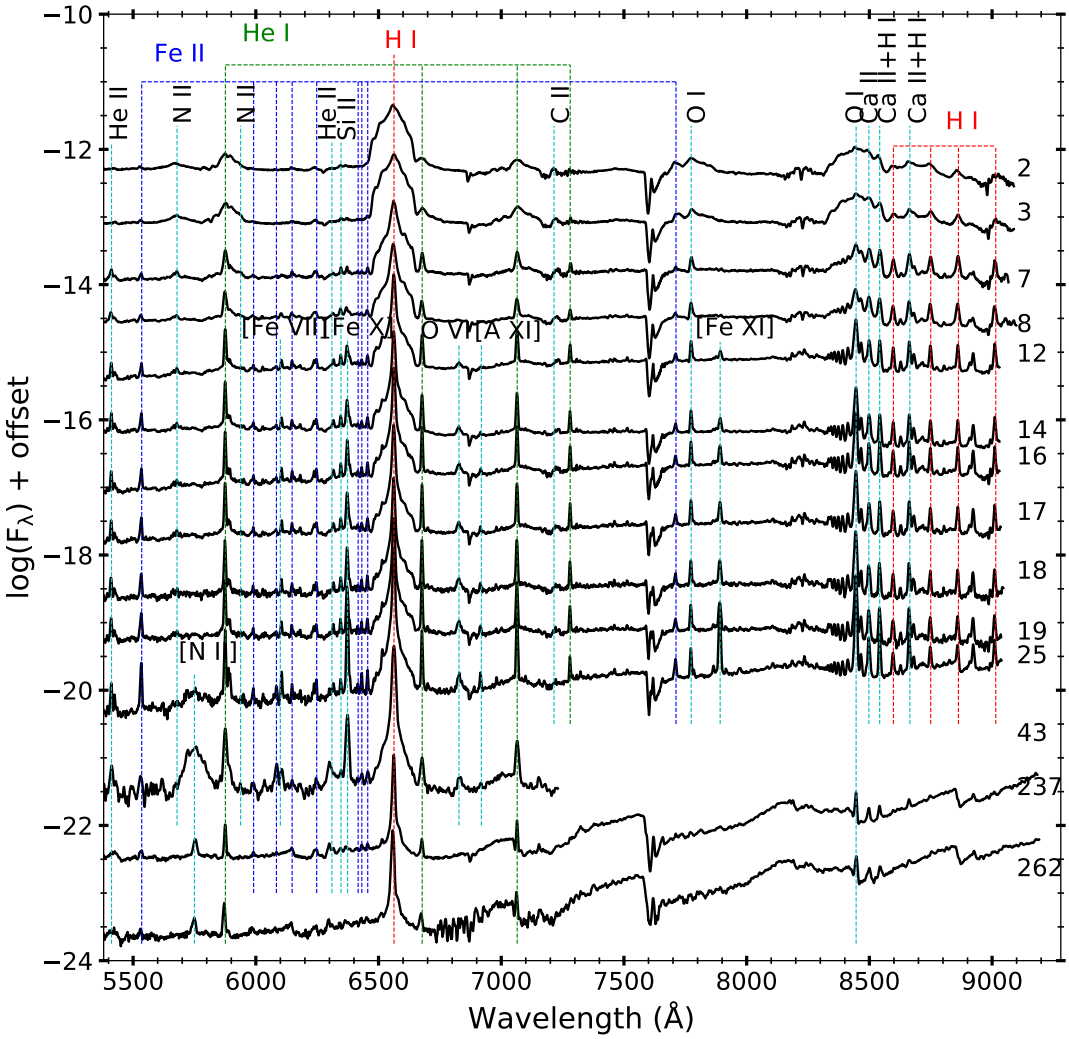

Figure 6.32: Low resolution optical spectral evolution of V3890 Sgr from 30 Aug 2019 (day 2) to 16 May 2020 (day 262) in the range of 5400–9000 Å.

from HCT during day 2 to 262 is as shown in Figs. 6.31 and 6.32. The broad absorption component seen on day 0.11 is no longer present and a weak Fe II emission is present on day 2 spectrum. The spectrum consists of Ca II, N III, He I, He II, O I, C II, Si II and Fe II lines. The prominent non-Balmer emission was from O I on days 2 and 3 while from day 7, dominant emission was from He II lines and it remained so till day 25. The broad emission lines slowly evolve into emission lines that show narrower core with sharper peaks along with the presence of coronal lines since day 12 such as [Fe VII], [Fe X], [Fe XI] and [Fe XIV] implying the presence of shocked plasma. The forbidden [N II] line appears on day 25 and it is broader when compared to that of other emission lines in the spectrum. On day 237 and 262, the

contribution from the secondary is evident with the presence of TiO and VO bands. The diagnostics for K-M stars using TiO and VO bands by Kenyon & Fernandez-Castro (1987) was used. The TiO bands indicated the secondary to be a M8E type, and VO bands indicate that the secondary is M8E III or M6.6 III spectral type on day 262. During the post-1990 outburst, the spectral type of secondary was found to be M8 III by Williams et al. (1991). The spectral type of the secondary during the quiescence phase of 1990 outburst was found to be M5 III type by Anupama & Mikołajewska (1999), and the IR colours using photometry of the system in 1991 by Harrison et al. (1993) indicated the spectral type of secondary as M5 III. The evolution of observed FWHM velocities of Hα and Hβ lines are as shown in Fig. 6.33. There is rapid decrease in the FWHM velocity of the both Hα and Hβ as the system evolves. It declines from very high velocity of 4500 km s^{-1} to about 500–1000 km s^{-1} values. The presence of narrow emission lines with time and appearance of coronal lines suggest the shock interaction of the ejecta with the surrounding medium as also observed during the 1990 outburst of the system by Anupama & Sethi (1994).

CLOUDY was used to model the system at seven different epochs at different phases of the system.

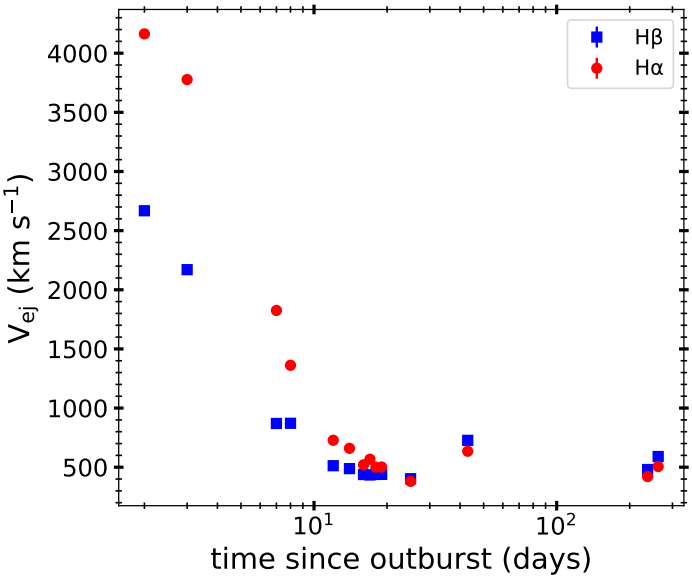

Figure 6.33: Evolution of Hα and Hβ FWHM velocities of the 2019 outburst of V3890 Sgr from 30 Aug 2019 (day 2) to 16 May 2020 (day 262).

Days 2 and 7

The central ionizing source was set to be at effective temperature 10^5 K and luminosity 10^{37} erg s^{-1}. The medium was assumed to be of a low-density diffuse component and a clump component to obtain the modelled spectrum. The optically thick (dense) clump component was used to fit most of the lines in the spectrum. The high ionization lines were fit using the diffuse component. The diffuse component has a lower density and covers 20% of the volume. The relative fluxes of the observed lines, the best-fit model predicted lines and the corresponding χ^2 values are given in Table 6.17. The values of best-fit parameters obtained from the model are given in Table 6.18. The estimated abundance values show that nitrogen, iron and helium were overabundant compared to solar abundance values. The ejected mass was found to be 1.95×10^{-6} $M_\odot$. The best-fit 1D spectrum obtained is as shown in Fig. 6.35.

The morphology of the ejecta was obtained using pyCloudy on day 7. It was found to be bipolar structures with equatorial rings (Fig. 6.34). Hα and Hβ are present in all the regions. The He I and He II lines are from the inner regions and Fe II from the equatorial rings.

Day 12–43

The epochs day 12, 16, 19, 25 and 43 were modelled to obtain the synthetic spectrum during this phase. The central ionizing source was set to be at effective temperature (1.5–3.3) $\times$ 10^5 K and luminosity (1.58–5.01) $\times$ 10^{37} erg s^{-1}. The medium consists of one clumpy and two diffuse regions to obtain the modelled spectrum. The optically thick (dense) clump component was used to model most of the lines in the spectrum. Few high ionization lines were fit using non-collisionally excited diffuse region covering 10% of volume. The collisionally excited diffuse component covering 10% of the volume was used to fit the coronal lines in the spectrum. This component was of temperature (4–5) $\times$ 10^6 K and density in the range of (3–6) $\times$ 10^7 cm^{-3}. The relative fluxes of the observed lines, best-fit modelled lines, and corresponding χ^2 values of all the epochs are given in Tables 6.17, 6.19 and 6.20, and

Table 6.17: Observed and best-fit CLOUDY model line flux ratios[a] of the 2019 outburst of V3890 Sgr

		Day 2			Day 7			Day 12		
Line ID	λ (Å)	**O**	**M**	χ^2	**O**	**M**	χ^2	**O**	**M**	χ^2
H I	3734	–	–	–	1.47E-01	1.70E-01	1.79E-02	–	–	–
H I	3798	2.05E-01	5.74E-03	6.52E-01	1.94E-01	2.49E-01	4.57E-02	9.15E-02	7.54E-03	8.79E-02
H I	3835	2.46E-01	8.78E-02	9.35E-01				1.01E-01	1.12E-01	1.63E-02
He II	3858	2.10E-02	4.18E-02	2.07E-02	7.40E-02	3.41E-01	9.96E+00	2.20E-01	1.45E-02	7.88E-01
H I	3889	2.61E-01	2.19E-01	4.79E-01	1.68E-01	4.54E-01	1.15E+00	8.19E-02	2.47E-01	1.70E+00
Ca II	3934	5.18E-02	2.60E-02	6.60E-03	1.29E-01	6.58E-02	6.83E-02	1.96E-01	3.52E-01	4.70E-01
Ca II + H I	3970	2.91E-01	1.80E-01	1.52E-01	3.12E-01	6.76E-01	4.57E+00	1.08E-01	2.45E-01	2.08E+00
He I	4026	1.40E-01	5.58E-02	1.67E-01	9.97E-02	1.54E-01	5.81E-02	3.12E-02	1.51E-03	1.06E-02
H I	4102	4.00E-01	2.88E-01	2.85E+00	4.42E-01	4.45E-01	2.51E-04	2.06E-01	2.49E-01	2.49E-02
Fe II	4179	1.51E-01	7.86E-02	6.08E-02	8.50E-02	3.77E-02	3.75E-02	7.93E-02	1.73E-02	5.46E-02
Fe II	4233	9.69E-02	4.09E-02	3.95E-02	7.06E-02	9.87E-02	2.41E-02	5.43E-02	3.91E-02	3.01E-03
H I	4340	4.87E-01	5.16E-01	5.88E-02	3.52E-01	8.72E-01	4.42E+00	2.14E-01	2.58E-01	2.82E-01
Fe II	4352	5.59E-02	3.77E-02	5.31E-03	8.98E-02	1.77E-01	2.24E-01	2.39E-01	5.18E-02	1.49E+00
He I	4471	1.57E-01	1.12E-01	2.88E-02	1.16E-01	3.99E-01	1.12E+00	5.85E-02	1.80E-01	6.29E-01
Fe II	4517	5.23E-02	3.01E-02	1.95E-02	1.14E-01	3.69E-02	8.98E-02	1.30E-01	3.48E-02	1.48E-01
Fe II	4556	1.22E-01	1.02E-01	7.52E-03	7.40E-02	1.11E-01	3.63E-02	8.88E-02	4.30E-02	2.14E-01
Fe II	4584	9.43E-02	4.34E-02	6.90E-02	1.12E-01	1.93E-01	2.06E-01	8.56E-02	1.33E-02	4.96E-01
He II	4686	5.28E-02	3.49E-02	4.89E-03	4.76E-01	9.98E-01	2.29E+01	7.45E-01	3.76E-01	3.43E+00
H I	4861	1.00E+00	1.00E+00	0.00E+00	1.00E+00	1.00E+00	0.00E+00	1.00E+00	1.00E+00	0.00E+00
He I + Fe II	4924	2.14E-01	1.46E-01	1.14E-01	2.04E-01	3.16E-01	1.75E-01	3.24E-01	1.68E-01	2.92E-01
He I + Fe II	5016	6.68E-01	3.18E-01	1.64E+00	3.09E-01	6.28E-01	3.14E+00	1.78E-01	2.82E-01	4.36E-01
He I	5048	1.01E-02	2.34E-02	1.80E-03	1.38E-01	9.07E-02	4.30E-02	2.92E-01	2.38E-02	1.47E+00
Fe II	5169	4.33E-01	3.12E-01	1.53E+00	2.75E-01	3.77E-02	3.80E+00	3.79E-01	1.36E-01	1.19E+00
Fe II	5198	4.03E-01	1.77E-01	1.69E+00	1.62E-01	3.21E-03	6.44E-01	2.49E-01	1.54E-01	1.26E+00
Fe II	5235	1.10E-01	7.67E-02	1.55E-01	1.98E-01	1.81E-01	6.55E-03	2.65E-01	6.79E-02	2.68E+00
Fe II	5276	2.51E-01	8.98E-02	2.56E-01	2.19E-01	1.05E-01	1.50E-01	2.30E-01	3.81E-02	8.18E-01
[Fe XIV]	5303	–	–	–	–	–	–	3.76E-01	7.66E-02	1.44E+00
Fe II	5317	8.42E-02	5.58E-02	9.16E-03	2.57E-01	1.69E-01	1.01E-01	2.31E-01	3.71E-02	4.46E-01
Fe II	5363	1.01E-01	3.74E-02	5.13E-02	3.10E-02	7.54E-02	2.37E-02	2.30E-01	3.32E-02	9.61E-01
He II	5412	7.46E-02	1.63E-02	1.40E-01	6.99E-02	1.85E-01	2.50E-01	1.96E-01	2.82E-02	9.58E-01
Fe II	5535	1.43E-01	7.17E-02	8.43E-02	5.16E-02	7.62E-02	7.46E-03	1.15E-01	7.15E-03	4.33E-01
N II	5679	2.92E-01	1.11E-01	6.22E+00	1.31E-01	1.12E-01	8.47E-03	1.33E-01	8.93E-03	1.84E-01
He I	5876	6.92E-01	5.41E-01	1.64E+00	3.98E-01	6.80E-01	2.19E+00	6.44E-01	6.80E-01	4.44E-02
Fe II	5991	6.36E-02	1.31E-02	3.81E-02	5.79E-02	1.44E-02	6.90E-02	3.42E-02	2.78E-03	7.20E-02
[Fe VII]	6087	–	–	–	–	–	–	8.19E-02	5.44E-03	6.05E-01
He II	6310	8.93E-01	3.36E-01	4.64E+00	7.43E-02	2.17E-02	6.78E-06	5.64E-02	5.42E-03	3.66E-02
Si II	6347	7.40E-01	3.11E-01	3.19E+00	3.87E-02	1.02E-01	2.40E-05	1.07E-01	8.95E-03	1.24E-01
[Fe X]	6374	–	–	–	–	–	–	4.12E-01	3.93E-03	4.25E+00
H I	6563	6.53E+00	5.99E+00	4.12E+00	7.64E+00	6.05E+00	6.73E-03	1.08E+01	1.10E+01	9.26E-01
He I	6678	2.63E-01	1.95E-01	1.74E-01	2.63E-01	5.12E-01	2.09E-04	5.53E-01	3.00E-01	2.07E+00
O VI	6828	–	–	–	–	–	–	1.22E-01	1.97E-03	1.37E+00
[A XI]	6919	–	–	–	–	–	–	1.73E-02	2.69E-02	4.22E-03
He I	7065	3.45E-01	2.37E-01	3.69E-01	3.20E-01	7.06E-01	7.01E-04	1.49E+00	1.09E+00	4.77E+00
C II	7235	7.42E-01	2.80E-01	3.14E+00	3.70E-01	9.71E-02	1.85E-04	1.37E-01	1.53E-01	4.39E-03
He I	7281	8.09E-02	6.33E-02	3.60E-02	1.02E-01	4.26E-01	1.27E-03	2.03E-01	9.78E-03	2.67E+00
Fe II	7712	6.52E-02	4.12E-02	6.41E-02	7.14E-02	5.14E-02	5.96E-06	1.06E-01	2.30E-02	1.95E-01
[Fe XI]	7892	–	–	–	–	–	–	2.46E-01	3.77E-02	2.99E+00
Ca II	8498	1.57E+00	1.04E+00	4.87E+00	3.82E-01	3.45E-02	5.05E-04	5.06E-01	2.62E-01	1.24E+00
Ca II + H I	8542	7.83E-01	5.13E-01	3.11E+00	3.84E-01	1.07E+00	1.23E-03	3.93E-01	3.97E-01	8.57E-04
H I	8598	1.07E+00	5.13E-01	2.59E+00	2.29E-01	4.98E-01	2.52E-04	2.28E-01	1.69E-02	1.16E+00
Ca II + H I	8665	1.69E+00	1.25E+00	3.07E+00	2.75E-01	9.13E-01	5.93E-04	4.37E-01	3.16E-01	3.69E-01
H I	8750	1.01E+00	5.41E-01	4.85E+00	2.42E-01	3.97E-01	4.38E-05	3.52E-01	3.85E-02	1.21E+01
H I	8863	1.10E+00	9.11E-01	1.98E+00	3.05E-01	2.59E-01	7.97E-06	4.15E-01	1.04E-01	1.21E+00
H I	9015	1.08E+00	9.31E-01	1.33E+00	2.07E-01	5.30E-02	8.20E-05	3.47E-01	1.36E-01	4.71E+00

[a]Relative to Hβ

the values of best-fit parameters are given in 6.18. The estimated abundance values show that iron, nitrogen, calcium, silicon and helium abundances were more than solar, while other abundance values were solar. The ejected mass was found to be in

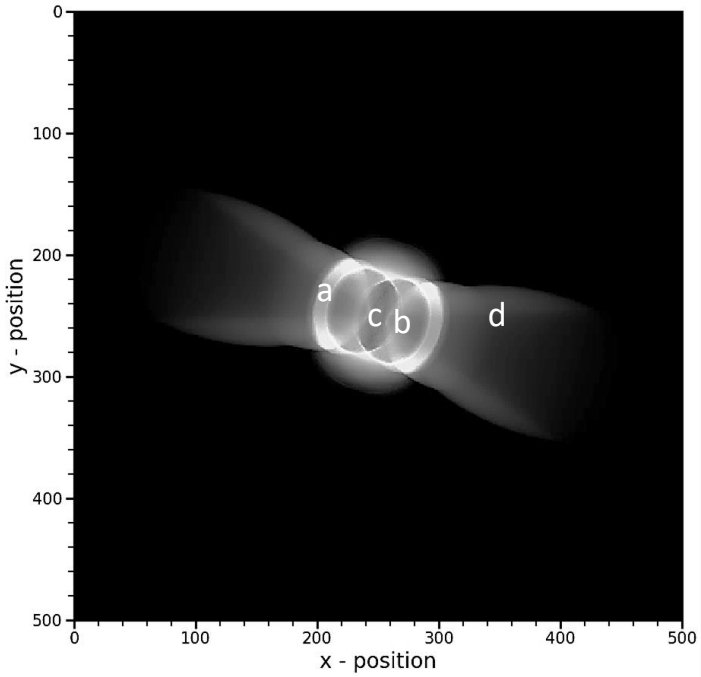

Figure 6.34: Morphology of the ejecta of V3890 Sgr during its 2019 outburst obtained using the optical spectrum in the two-dimensional plane with X-axis being the line-of-sight direction and Y being the axis perpendicular to that of the plane of sky and line-of-sight on day 7. Here, 1 unit of x and y correspond to 4.27×10^{11} cm. The labels marked represent a: Fe II, b: He I, c: He II, d: H I.

the order of 10^{-6} $M_{\odot}$. The best-fit modelled spectrum (dashed line) with the corresponding observed optical spectrum (continuous line) are as shown in Fig. 6.35. The evolution of few parameters like luminosity, effective temperature, density, temperature and density in collisionally ionized region, ejected mass is given in Fig. 6.36. O I (7774 Å, 8446 Å) lines were not modelled due to the limitations of the code. In the early phase, the N II (5679 Å), He II (4686 Å) and some of the very less prominent Fe II lines have higher χ^2 values and hence contributes more to the total χ^2. From day 12, few He I, He II, Fe II and coronal lines have higher χ^2 values. Though the reduced χ^2 values suggest that the generated spectrum matches the observed spectrum well, the above contributions from different lines might hinder the calculated abundance values. The higher χ^2 values are as a consequence of blending of the lines. Also, coronal lines excited by shock interaction results in higher χ^2 value.

Table 6.18: Best-fit CLOUDY model parameters at different epochs for the 2019 outburst of V3890 Sgr

Parameter	**Day 2**	**Day 7**	**Day 12**	**Day 16**	**Day 19**	**Day 25**	**Day 43**
T_{BB} ($\times 10^5$ K)	1 ± 0.09	1.25 ± 0.11	1.5 ± 0.10	2 ± 0.12	2.2 ± 0.07	3 ± 0.10	3.3 ± 0.11
Luminosity ($\times 10^{37}$ erg s^{-1})	1 ± 0.12	1 ± 0.11	1.58 ± 0.09	2 ± 0.10	2.52 ± 0.07	3.55 ± 0.11	5.01 ± 0.13
Clump Hydrogen density (in log [cm^{-3}])	12.00	11.75	11.25	11.00	10.69	10.00	9.50
Diffuse Hydrogen density (in log [cm^{-3}])	11.00	9.25	9.00	9.00	8.65	8.75	8.75
T_{coll} ($\times 10^6$ K)	–	–	4	4	4.25	5.15	5
ρ_{coll} ($\times 10^7$ cm^{-3})	–	–	3.16	3.16	3.98	5.62	6.3
Covering factor (clump)	0.8	0.8	0.8	0.8	0.8	0.8	0.8
Covering factor (diffuse)	0.2	0.2	0.1/0.1	0.1/0.1	0.1/0.1	0.1/0.1	0.1/0.1
α	-3	-3	-3	-3	-3	-3	-3
Inner radius ($\times 10^{13}$ cm)	1.15	4.27	5.25	5.62	8.13	8.71	18.60
Outer radius ($\times 10^{14}$ cm)	0.79	1.26	1.41	1.58	1.64	1.74	14.50
Filling factor	0.1	0.1	0.1	0.1	0.1	0.1	0.1
$N/N_\odot$	1.39 ± 0.12 (1)[a]	1.43 ± 0.09 (1)	1.28 ± 0.11 (1)	1.21 ± 0.10 (1)	1.23 ± 0.08 (1)	1.67 ± 0.12 (2)	2.09 ± 0.13 (2)
$Si/Si_\odot$	1.00 ± 0.08 (1)	1.28 ± 0.11 (1)	1.31 ± 0.11 (1)	1.25 ± 0.09 (1)	1.25 ± 0.10 (1)	1.22 ± 0.08 (1)	1.21 ± 0.11 (1)
$Fe/Fe_\odot$	2.05 ± 0.09 (17)	1.64 ± 0.12 (17)	1.71 ± 0.10 (20)	1.44 ± 0.09 (21)	1.48 ± 0.08 (21)	1.34 ± 0.11 (21)	1.29 ± 0.10 (15)
$He/He_\odot$	1.34 ± 0.12 (13)	2.14 ± 0.12 (13)	3.57 ± 0.09 (13)	4.28 ± 0.11 (11)	4.65 ± 0.08 (12)	4.86 ± 0.09 (11)	6.11 ± 0.12 (10)
$Ca/Ca_\odot$	1.13 ± 0.09 (5)	1.13 ± 0.10 (5)	2.26 ± 0.11 (5)	2.26 ± 0.10 (5)	1.13 ± 0.10 (5)	1.13 ± 0.08 (5)	–
Ejected mass ($\times 10^{-6}$ $M_\odot$)	1.95	15.70	6.71	7.70	5.76	2.71	4.94
Number of observed lines (n)	48	50	53	51	51	46	32
Number of free parameters (n_p)	11	11	14	14	14	14	14
Degrees of freedom (ν)	39	41	39	37	37	32	18
Total χ^2	60.28	55.57	65.44	44.74	42.37	38.49	30.42
χ^2_{red}	1.55	1.36	1.68	1.21	1.15	1.20	1.69

[a]The number of lines availed to obtain abundance estimate is as shown in the parenthesis.

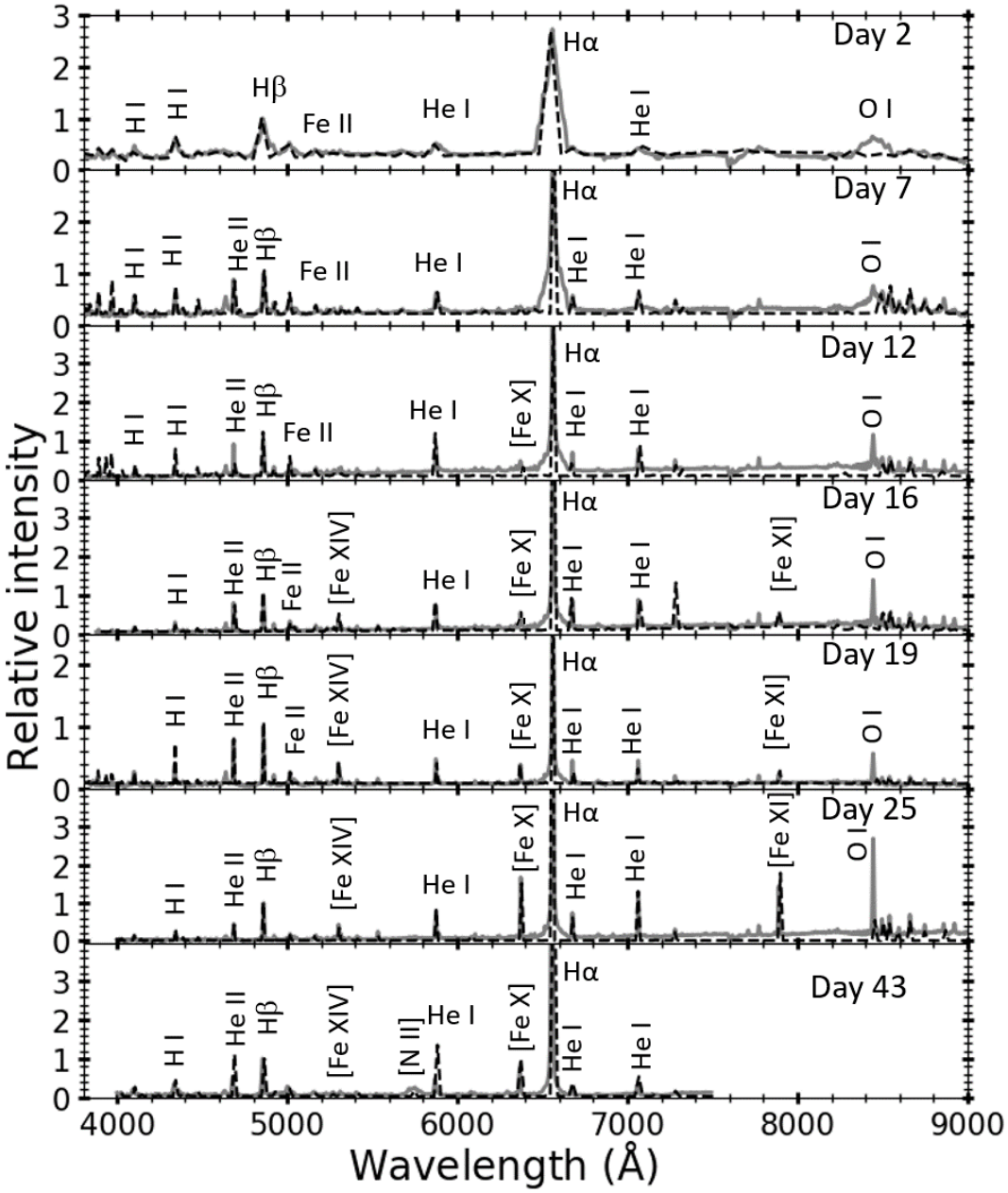

Figure 6.35: Best-fit CLOUDY synthetic spectrum (dash line) plotted over the observed spectrum (continuous line) for each epoch for the 2019 outburst of V3890 Sgr.

The ejected mass was found to be of the order of 10^{-6} $M_{\odot}$ except for day 12 which is around the t_3 epoch. This is consistent with the suggestion by Shara (1981) based on the numerical calculations that during t_3 most of the mass is ejected. The very high temperature of the order of 10^6 K of the component producing coronal lines suggest shock excitation for their formation rather than photoionization of the shell.

The morphology of the ejecta was obtained using pyCloudy on day 16, 19, 25 and

Table 6.19: Observed and best-fit CLOUDY model line flux ratios[a] for different epochs for the 2019 outburst of V3890 Sgr

		Day 16			Day 19			Day 25		
Line ID	λ (Å)	**O**	**M**	χ^2	**O**	**M**	χ^2	**O**	**M**	χ^2
He II	3858	–	–	–	2.59E-02	8.83E-02	7.28E-02	–	–	–
H I	3889	3.77E-01	8.05E-02	2.59E+00	3.75E-02	1.94E-01	1.70E+00	–	–	–
Ca II	3934	3.39E-01	9.88E-02	2.89E+00	9.30E-03	1.46E-02	3.79E-04	–	–	–
Ca II + H I	3970	1.88E-01	3.48E-03	6.23E-01	4.27E-02	3.91E-02	3.98E-04	–	–	–
He I	4026	2.73E-01	9.27E-02	2.93E+00	3.28E-02	7.67E-03	2.41E-02	3.25E-02	1.23E-02	9.20E-03
H I	4102	5.30E-01	2.91E-01	1.07E+00	7.40E-02	1.60E-01	1.20E-01	1.31E-01	7.77E-02	2.79E-01
Fe II	4179	2.78E-01	1.44E-01	2.72E-01	1.97E-02	7.52E-02	4.10E-02	2.20E-02	1.23E-02	5.18E-03
Fe II	4233	2.32E-01	6.83E-02	4.65E-01	2.19E-02	1.07E-02	1.45E-03	4.42E-02	2.59E-02	5.71E-03
H I	4340	1.17E-01	4.09E-02	9.44E-01	1.05E-01	1.46E-02	5.40E-01	2.13E-01	2.07E-01	5.99E-03
Fe II	4352	4.02E-01	1.73E-01	1.31E+00	1.77E-02	3.91E-02	1.70E-02	7.44E-03	4.69E-02	3.87E-02
He I	4471	1.75E-01	3.29E-02	1.42E+00	1.81E-02	7.52E-02	9.47E-02	4.85E-02	3.82E-02	2.07E-03
Fe II	4517	3.82E-01	2.82E-01	1.13E+00	2.60E-02	8.44E-03	7.25E-03	7.55E-02	4.44E-02	1.29E-02
Fe II	4556	3.94E-01	9.45E-02	1.72E+00	2.78E-02	5.76E-02	1.94E-02	9.49E-02	3.21E-02	1.54E-01
Fe II	4584	2.12E-01	2.63E-01	5.13E-01	2.09E-02	4.99E-02	6.73E-02	3.58E-02	8.01E-02	6.45E-02
He II	4686	4.70E-01	1.54E-01	1.79E+00	1.91E-01	8.98E-02	1.80E-01	3.68E-01	2.32E-01	4.59E-01
H I	4861	1.00E+00	1.00E+00	0.00E+00	1.00E+00	1.00E+00	0.00E+00	1.00E+00	1.00E+00	0.00E+00
He I + Fe II	4924	9.16E-02	3.72E-02	1.82E-01	3.89E-02	4.47E-01	5.30E+00	8.98E-02	1.86E-01	3.95E-01
He I + Fe II	5016	1.17E-01	7.32E-03	1.16E+00	4.71E-02	2.48E-01	4.16E+00	1.37E-01	3.21E-02	4.70E-01
He I	5048	1.72E-01	1.32E-01	1.98E-01	1.35E-01	1.01E-01	1.64E-01	5.31E-02	7.89E-02	5.23E-02
Fe II	5169	2.81E-01	1.41E-01	3.02E-01	2.49E-02	4.96E-01	5.24E+00	8.63E-02	2.13E-01	7.30E-01
Fe II	5198	4.10E-01	3.24E-01	1.66E-01	1.37E-02	1.01E-01	6.36E-01	4.07E-02	5.92E-02	1.18E-02
Fe II	5235	2.87E-01	1.61E-01	1.13E+00	1.07E-02	3.80E-01	3.82E+00	5.55E-02	9.62E-02	2.41E-02
Fe II	5276	3.74E-01	2.16E-01	4.32E-01	1.01E-02	2.38E-01	6.82E-01	4.50E-02	5.55E-02	1.65E-03
[Fe XIV]	5303	3.75E-01	2.35E-01	2.82E-01	1.25E-01	3.31E-01	6.51E-01	3.02E-01	1.21E-01	6.53E-01
Fe II	5317	4.17E-01	6.10E-03	4.00E+00	7.78E-02	1.69E-01	1.89E-01	9.70E-02	1.52E-01	1.83E-01
Fe II	5363	7.77E-02	2.38E-02	4.61E-01	8.43E-03	2.55E-01	7.15E+00	3.50E-02	5.30E-02	4.51E-02
He II	5412	6.33E-02	2.20E-02	1.68E-01	3.82E-02	8.67E-02	3.97E-02	7.90E-02	4.56E-02	4.07E-02
Fe II	5535	5.91E-02	1.28E-02	1.01E-01	2.60E-02	9.21E-02	1.07E-01	2.05E-01	1.74E-01	5.87E-02
N II	5679	2.54E-01	1.88E-01	3.14E-01	5.97E-03	6.52E-02	5.03E-01	4.80E-03	7.89E-02	6.68E-02
He I	5876	3.07E-01	3.42E-01	1.37E-01	1.03E-01	6.45E-02	2.39E-02	6.12E-01	1.14E+00	8.00E+00
Fe II	5991	1.44E-02	5.73E-02	2.44E-01	6.66E-03	5.68E-02	8.94E-02	3.48E-02	6.41E-02	1.35E-02
[Fe VII]	6087	3.63E-02	5.79E-02	4.87E-02	2.89E-03	1.77E-02	8.59E-03	4.80E-02	1.85E-01	2.15E-01
He II	6310	6.42E-02	4.76E-02	1.86E-01	6.89E-03	1.01E-01	3.88E-01	2.88E-02	5.06E-02	2.17E-02
Si II	6347	3.98E-02	8.54E-03	3.10E-02	1.27E-02	8.52E-02	1.84E-01	4.69E-02	3.82E-02	2.84E-03
[Fe X]	6374	2.43E-01	1.43E-01	1.72E-01	1.02E-01	7.37E-02	1.18E-02	1.56E+00	1.49E+00	1.16E-01
H I	6563	5.12E+00	5.73E+00	5.35E+00	8.46E-01	1.58E+00	8.94E+00	6.95E+00	7.23E+00	5.15E+00
He I	6678	3.77E-01	2.22E-01	6.96E-01	8.77E-02	4.68E-02	2.44E-01	5.36E-01	1.57E-01	3.38E+00
O VI	6828	3.85E-02	1.06E-01	3.77E-01	2.91E-02	4.07E-02	1.01E-02	1.38E-01	3.70E-02	1.29E-01
[A XI]	6919	2.29E-02	6.83E-02	2.21E-01	1.55E-02	5.45E-02	1.93E-02	7.01E-02	1.73E-02	1.20E-01
He I	7065	4.09E-01	2.20E-01	7.36E-01	1.09E-01	2.38E-02	7.12E-01	1.04E+00	1.34E+00	5.89E+00
C II	7235	3.87E-02	1.48E-01	1.61E-01	3.27E-03	3.91E-02	3.88E-02	–	–	–
He I	7281	1.26E-01	2.20E-01	8.94E-01	2.97E-02	4.91E-02	6.98E-03	1.65E-01	4.13E-01	1.32E+00
Fe II	7712	6.51E-02	2.36E-01	1.46E+00	1.31E-02	3.91E-02	2.96E-02	8.76E-02	7.77E-02	1.37E-03
[Fe XI]	7892	1.65E-01	3.29E-02	2.28E-01	5.26E-02	2.46E-02	1.17E-02	1.49E+00	1.65E+00	9.75E-01
Ca II	8498	2.47E-01	3.11E-02	1.22E+00	4.71E-02	4.99E-03	4.64E-02	4.80E-01	2.90E-01	3.70E+00
Ca II + H I	8542	2.40E-01	6.89E-02	4.30E-01	4.64E-02	4.76E-02	1.30E-04	4.56E-01	7.87E-01	2.46E+00
H I	8598	1.48E-01	3.35E-02	7.80E-01	2.40E-02	4.69E-02	6.56E-02	2.78E-01	2.69E-01	2.48E-03
Ca II + H I	8665	2.26E-01	5.30E-02	6.82E-01	3.82E-02	7.67E-03	1.09E-02	1.10E-01	3.33E-02	8.09E-02
H I	8750	1.47E-01	1.46E-02	3.52E-01	2.61E-02	6.14E-02	2.64E-02	2.29E-01	4.07E-02	1.20E+00
H I	8863	1.66E-01	7.07E-02	8.52E-01	5.53E-02	7.67E-03	3.04E-02	2.88E-01	6.44E-01	1.81E+00
H I	9015	1.70E-01	7.99E-02	8.93E-01	3.45E-02	8.44E-02	4.07E-02	3.83E-01	3.26E-01	1.43E-01

[a]Relative to Hβ

Table 6.20: Observed and best-fit CLOUDY model line flux ratios[a] for day 43 of 2019 outburst of V3890 Sgr

Line ID	λ (Å)	**Observed**	**Modelled**	χ^2
He I	4026	3.21E-02	8.52E-02	3.20E-01
H I	4102	1.86E-01	2.22E-01	3.01E-02
Fe II	4179	8.24E-02	3.28E-02	4.93E-02
Fe II	4233	2.50E-02	1.26E-02	1.01E-02
H I	4340	2.87E-01	4.11E-01	2.29E-01
He I	4471	1.86E-02	1.25E-01	2.88E-01
Fe II	4517	7.79E-02	4.15E-02	1.77E-02
He II	4686	4.14E-01	1.10E+00	5.72E+00
H I	4861	1.00E+00	1.00E+00	0.00E+00
He I + Fe II	5016	3.06E-01	2.09E-01	1.06E-01
He I	5048	8.31E-02	1.26E-02	6.08E-02
Fe II	5169	7.32E-02	6.60E-02	1.81E-03
Fe II	5198	5.27E-02	1.36E-02	3.82E-02
Fe II	5235	4.74E-02	1.75E-02	1.94E-02
Fe II	5276	2.31E-01	5.29E-02	3.00E+00
[Fe XIV]	5303	6.29E-02	2.67E-02	2.04E-02
Fe II	5317	7.50E-02	3.55E-02	2.26E-01
Fe II	5363	1.66E-01	1.47E-02	6.11E-01
He II	5412	4.85E-02	1.02E-01	7.80E-02
Fe II	5535	8.53E-02	2.62E-02	1.52E-01
[N II]	5755	2.79E-01	1.60E-01	1.71E-01
He I	5876	4.49E-01	1.40E+00	1.21E+01
Fe II	5991	3.88E-02	3.60E-02	1.84E-04
[Fe VII]	6087	4.25E-02	9.83E-03	5.06E-02
He II	6310	7.72E-02	1.31E-02	7.75E-02
Si II	6347	3.76E-02	1.97E-02	5.40E-03
[Fe X]	6374	7.35E-01	1.08E+00	3.00E+00
H I	6563	9.85E+00	9.56E+00	1.58E+00
He I	6678	1.15E-01	3.61E-01	7.08E-01
O VI	6828	5.23E-02	4.04E-02	1.04E-02
[A XI]	6919	9.04E-03	6.00E-03	2.69E-04
He I	7065	2.40E-01	8.62E-02	1.77E+00

[a] Relative to Hβ

O refers to observed flux ratios

M refers to modelled flux ratios

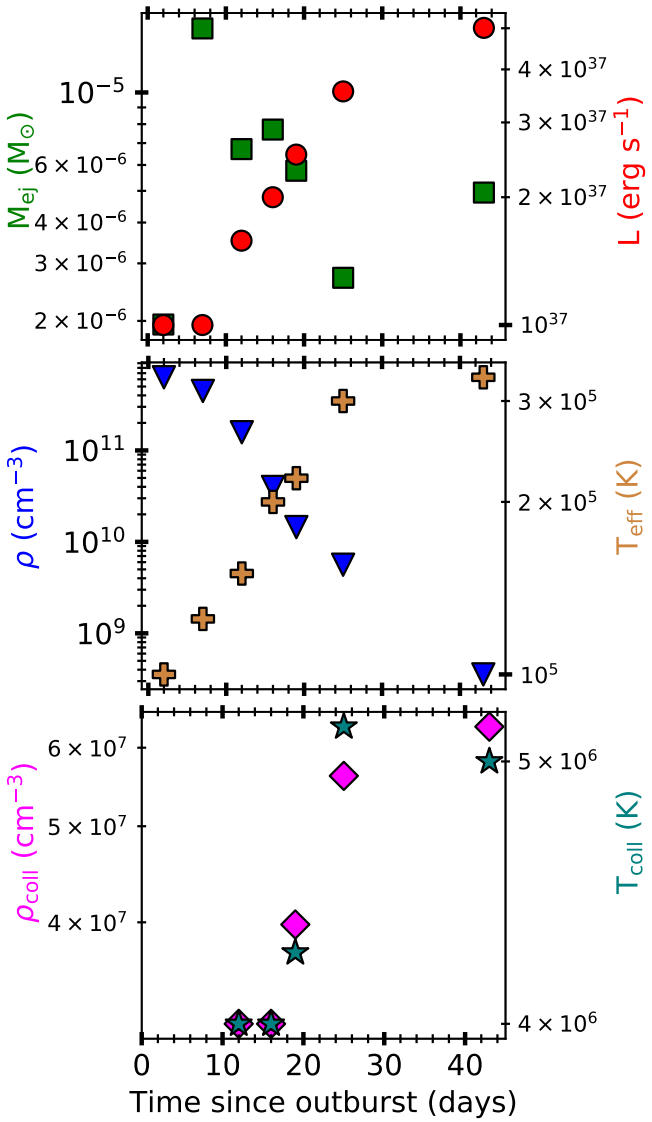

Figure 6.36: Variation of best-fit parameters obtained from CLOUDY from day 2 to 43 such as luminosity (L), effective temperature ($T_{\rm eff}$), density (ρ), temperature ($T_{\rm coll}$) and density ($\rho_{\rm coll}$) in collisionally excited region, ejected mass ($M_{\rm ej}$).

43. It was found to be bipolar with equatorial rings and ellipsoidal shell (Fig. 6.37). The equatorial rings became more prominent as the system evolved. Hα and Hβ are present in all the regions. The He I and He II lines are from the inner regions and Fe II from the equatorial rings. The coronal lines are coming from the ellipsoidal shell which is 0.2–0.5 AU from the red giant surface. The inclination angle of the system was found to 68° $\pm$ 1.35°. The details on the extent and distance from the central source of all the components in the morphology of the ejecta for all the epochs are given in Table 6.21.

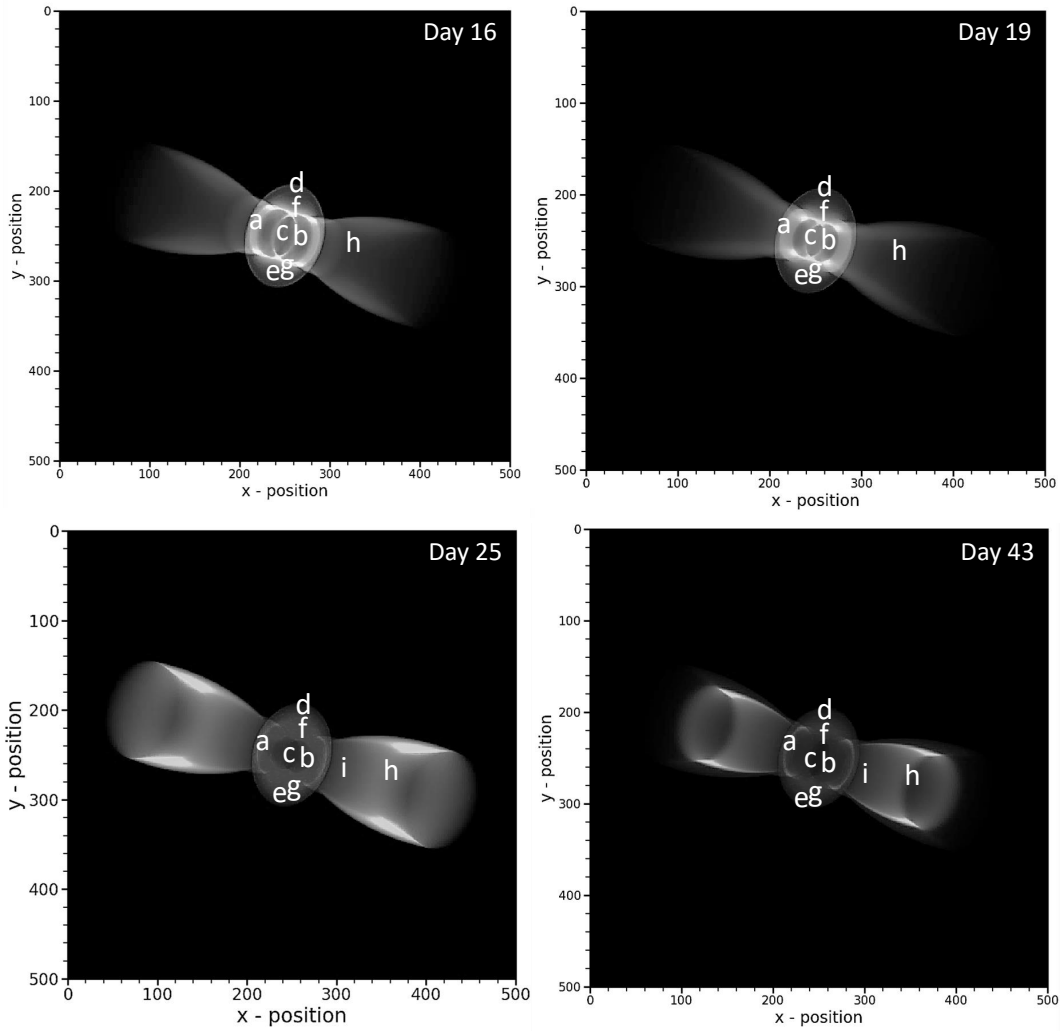

Figure 6.37: Morphology of the ejecta of V3890 Sgr during its 2019 outburst obtained using the optical spectrum in the two-dimensional plane with X-axis being the line-of-sight direction and Y being the axis perpendicular to that of the plane of sky and line-of-sight. Here, x_{16} and $y_{16} = 5.62 \times 10^{11}$ cm; x_{19} and $y_{19} = 8.13 \times 10^{11}$ cm; x_{25} and $y_{25} = 8.71 \times 10^{11}$ cm and x_{43} and $y_{43} = 1.86 \times 10^{12}$ cm. The labels marked represent a: Fe II, b: He I, c: He II, d: [Fe VII], e: [Fe X], f: [Fe XI], g: [Fe XIV], h: H I, i: [N II].

6.5.2 Radio light curve

The radio observations for 2019 outburst of V3890 Sgr were in standard continuum mode of GMRT with a bandwidth of 33 MHz split into 256 channels and using upgraded GMRT (uGMRT) at band 3 (250–500 MHz), band 4 (550–900 MHz) and band 5 (1000–1450 MHz). The sampling for recording data was 16 sec. The flux density and band-pass calibrators used were 3C286, 3C48 and 3C468.1 and phase calibrator were 1822-096 (J2000). The multi-epoch observation was carried out from

Table 6.21: Details of the morphology of the ejecta on different epochs for V3890 Sgr

Epoch	**Component**	**Extent**[a] **(cm)** ($\times 10^{13}$ **cm**)	**Radius (cm)** ($\times 10^{13}$ **cm**)	**Distance**[b] **(cm)** ($\times 10^{13}$ **cm**)	**Angle**[c] (°)
Day 7	Cone	2.14 ± 0.11	1.92 ± 0.08	0.21 ± 0.01	80.5 ± 0.92
	Equatorial ring	-	1.92 ± 0.10	1.07 ± 0.07	-
	Bipolar (enhanced)	5.12 ± 0.17	-	2.14 ± 0.11	-
Day 16	Cone	1.24 ± 0.09	1.48 ± 0.07	0.25 ± 0.02	59 ± 1.13
	Equatorial ring	-	2.97 ± 0.13	1.61 ± 0.11	-
	Bipolar (enhanced)	11.9 ± 1.31	-	4.08 ± 0.09	-
	Ellipsoid	3.96 ± 0.13	-	2.23 ± 0.09	-
Day 19	Cone	2.44 ± 0.12	2.76 ± 0.11	0.33 ± 0.01	68 ± 0.79
	Equatorial ring	-	3.58 ± 0.13	1.46 ± 0.11	-
	Bipolar (enhanced)	14.6 ± 1.23	-	5.20 ± 0.98	-
	Ellipsoid	3.90 ± 0.11	-	2.60 ± 0.10	-
Day 25	Cone	1.46 ± 0.11	1.71 ± 0.09	0.24 ± 0.01	73.5 ± 1.09
	Equatorial ring	-	2.68 ± 0.12	2.19 ± 0.10	-
	Bipolar (enhanced)	17.1 ± 1.43	-	4.39 ± 0.14	-
	Ellipsoid	4.15 ± 0.14	-	2.68 ± 0.11	-
Day 43	Cone	2.76 ± 0.11	3.26 ± 0.13	0.35 ± 0.02	77.25 ± 1.11
	Equatorial ring	-	5.02 ± 0.15	4.02 ± 0.13	-
	Bipolar (enhanced)	2.41 ± 0.10	-	8.04 ± 0.20	-
	Ellipsoid	7.03 ± 0.21	-	4.02 ± 0.16	-

[a]Extent of the component along the ejecta axis

[b]Distance from the centre to the component along the ejecta axis

[c]Outer opening angle of the cone

2019 Sept 06 (day 10) to 2020 Feb 17 (day 174) with each observing run of 1–3 hr duration.

No radio emission was observed until day 5.7 by Nyamai et al. (2019) at 1.28 GHz. The radio emission from this object was observed from Karl G. Jansky Very Large Array (VLA) and the VLA Low-band Ionosphere and Transient Experiment (VLITE) by Polisensky et al. (2019) on day 26. It was reported that the radio spectrum was consistent with that of the self-absorbed synchrotron emission. The spectral index value being -0.3 at 1.26–7.0 GHz changing over to +0.7 at 0.34–1.26 GHz. They suggested that the radio synchrotron is connected to shock. The radio light curve obtained at multi-frequency is as shown in Fig. 6.38. The radio light curve also includes the values reported by Nyamai et al. (2019) and Polisensky et al. (2019).

The radio light curves of different RNe similar to that of V3890 Sgr such as RS Oph and V745 Sco are plotted together in Fig. 6.39 for comparison. The evolution of radio emission of the 2019 outburst of V3890 Sgr appears to be lying in between

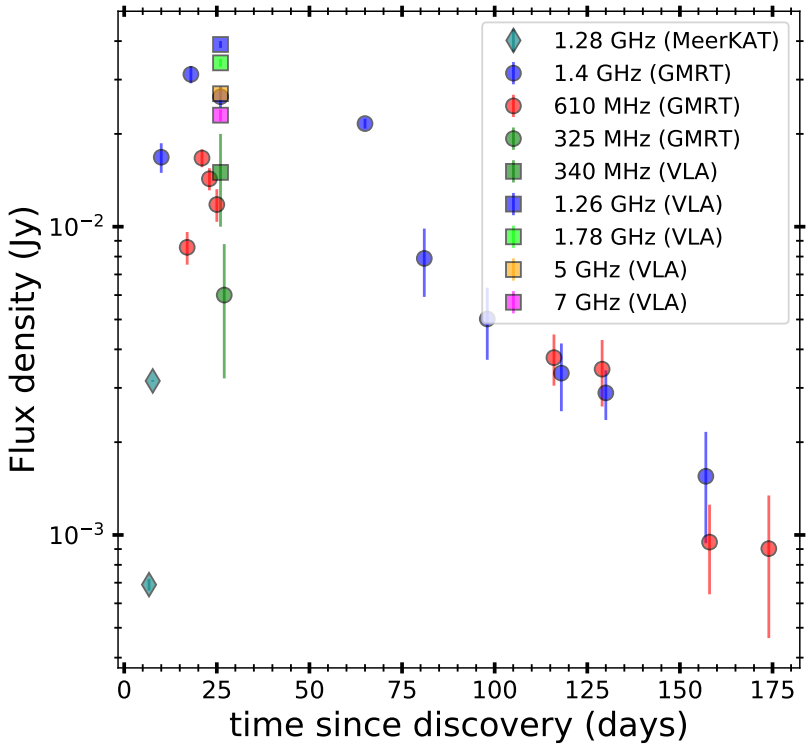

Figure 6.38: Radio light curve of V3890 Sgr during its 2019 outburst. The light curve is generated using GMRT, MeerKAT and VLA data points.

the radio emission of RS Oph and V745 Sco. Also, the flux density values of V3890 Sgr lies in between that of RS Oph and V745 Sco.

The radio light curve obtained using GMRT at 325, 610 and 1420 MHz was modelled to obtain physical parameters of the system. The model based on Weiler et al. (2002) was used for the same. It is given by

$$S\,(\mathrm{mJy}) = K_1 \left(\frac{\nu}{1\,\mathrm{GHz}}\right)^{\alpha} \left(\frac{t-t_0}{20\,\mathrm{days}}\right)^{\beta} \times \exp(-\tau_{\mathrm{homog}}^{\mathrm{CSM}}) \left[\frac{1-\exp(-\tau_{\mathrm{clumps}}^{\mathrm{CSM}})}{\tau_{\mathrm{clumps}}^{\mathrm{CSM}}}\right] \tag{6.1}$$

where

$$\tau_{\mathrm{homog}}^{\mathrm{CSM}} = K_2 \left(\frac{\nu}{1\ \mathrm{GHz}}\right)^{-2.1} \left(\frac{t-t_0}{20\ \mathrm{days}}\right)^{\delta}, \tag{6.2}$$

$$\tau_{\mathrm{clumps}}^{\mathrm{CSM}} = K_3 \left(\frac{\nu}{1\ \mathrm{GHz}}\right)^{-2.1} \left(\frac{t-t_0}{20\ \mathrm{days}}\right)^{\delta'} \tag{6.3}$$

The term $t - t_0$ refers to time since outburst and t_0 corresponds to 2019 Aug 28. The term K_1 represents the flux density, K_2 is attenuation by a homogeneous absorbing medium at 1 GHz after 20 days of nova outburst and K_3 is attenuation by a clumpy

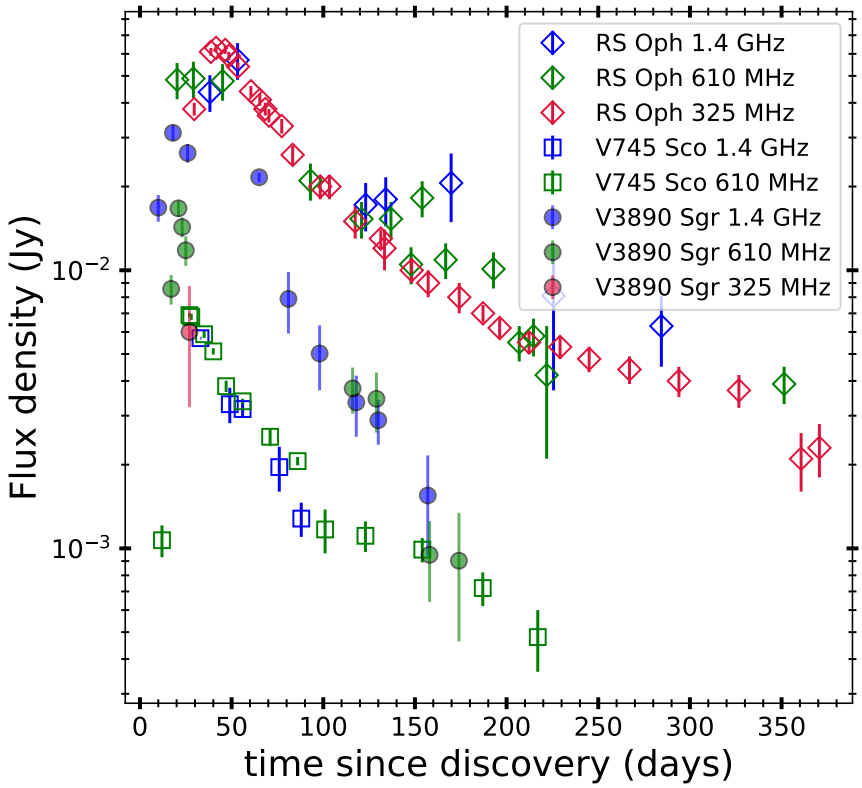

Figure 6.39: Radio light curves of RS Oph (Kantharia et al., 2007, 2016), V745 Sco (Hjellming, 1989; Kantharia et al., 2016) and V3890 Sgr [GMRT] at multi-frequency bands.

or filamentary medium at 1 GHz after 20 days of nova outburst. The terms $\tau^{\rm CSM}_{\rm homog}$ and $\tau^{\rm CSM}_{\rm clumps}$ are the optical depths due to the ionized circumstellar medium (CSM) to the homogeneous and clumpy emitting regions respectively. The term α is the spectral index while the term β is the rate of decline in the optically thin phase. The optical depths in the homogeneous and clumpy CSM is given by δ and δ' respectively. The radio emission obtained at different frequencies from GMRT along with the MeerKAT and VLA data points were simultaneously non-linearly fitted using the Levenberg-Marquardt algorithm (Press et al., 2002) and the best-fit parameters obtained are as shown in Table 6.22. The modelled light curve is as shown in Fig. 6.40. Based on the model light curve, the radio emission peaked at $\sim$17.8 mJy on $\sim$day 31 at 610 MHz and $\sim$30.4 mJy on day 17 at 1420 MHz. The variation in the optical depths at 610 and 1420 MHz frequencies is as shown in the Fig. 6.41. $\tau_{\rm clumps}$ shows a slower decline while $\tau_{\rm homog}$ falls rapidly. The $\tau_{\rm clumps}$ drops to unit opacity within 17 and 30 days for 610 and 1420 MHz respectively corresponding to the peaks and taking longer than that of $\tau_{\rm homog}$ which took 5.8 and 11.9 days at 610

Table 6.22: Best-fit parameters obtained from radio data modelling of the 2019 outburst of V3890 Sgr

Parameter	**Values**
K_1	48.59
K_2	0.10
K_3	1.32
α	-0.32
β	-1.44
δ	-2.43
δ'	-3.13

and 1420 MHz respectively. The time of peak of the emission at both frequencies is coincident with the time of unit opacity values in the clumpy medium indicating that the turn-on of the synchrotron emission at low radio frequency is primarily by the optical thickness of clump density gas rather than the uniform dense gas. During the 2014 outburst of V745 Sco and 1985 outburst of RS Oph, time of peak emission at low frequencies corresponds to the time of unit opacity in the uniform medium suggesting that the synchrotron turn-on is primarily due to the uniform density gas (Kantharia et al., 2016). During the 2006 outburst of RS Oph, an early turn-on of

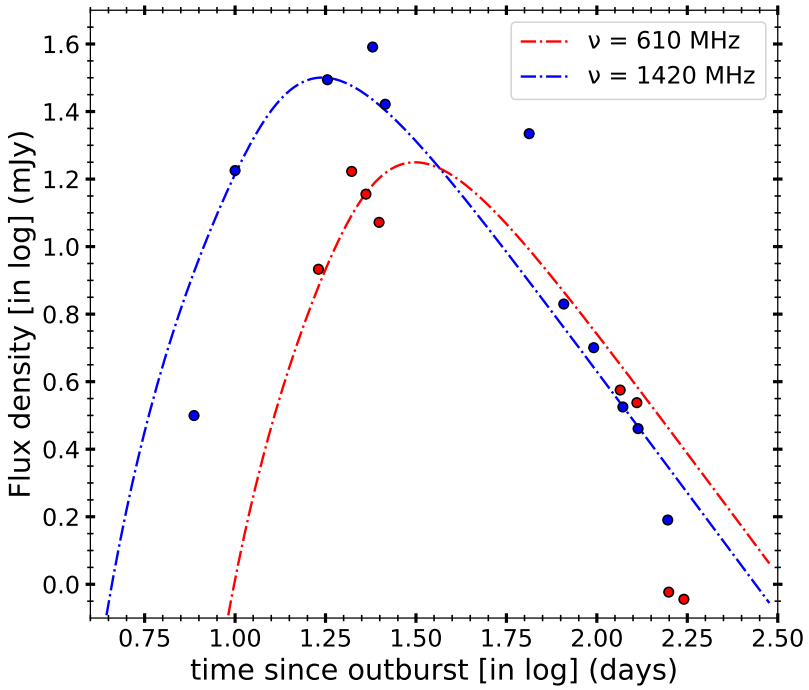

Figure 6.40: The observed radio data points and the modelled light curve generated using parameters in Table 6.22 for the 2019 outburst of V3890 Sgr.

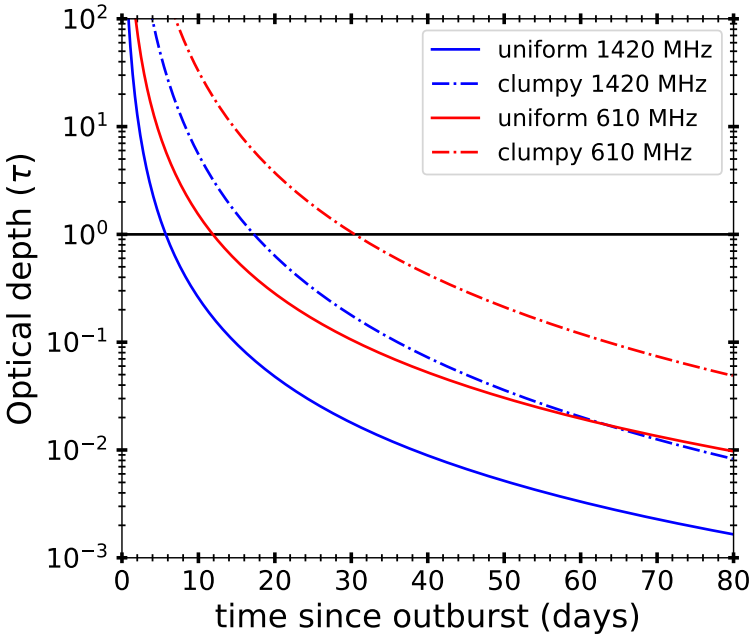

Figure 6.41: The optical depth evolution due to the homogeneous and clumpy medium during the 2019 outburst of V3890 Sgr. The black horizontal line refers to the opacity value equal to one.

synchrotron emission is observed and it driven by both the uniform and clump density gas as opacity in the both medium fall to unity around the same time (Kantharia et al., 2007, 2016).

6.5.3 Soft X-ray emission

V3890 Sgr was observed with the *AstroSat* SXT instrument on 2019 Sept 05.68 UT (day 8.2) to 06.85 UT (day 9.98) and on 2019 Sept 12.78 UT (day 15.7) to 16.30 UT (day 19.2). The SXT light curve obtained at energy range 0.3–1.0 keV (soft band) and 1.0–7.0 keV (hard band) is as shown in Fig. 6.42. The count rates in the soft band are fluctuating while those in the hard band are almost constant. The hardness ratios reveal that during the onset of the SSS phase and around the peak of SSS phase the hardness ratio is more. Also, noted is the anti-correlation between the hardness ratio and that of the soft band count rates.

The spectral analysis during these two observations shows that two plasma components are dominating at energies above 1 keV and a soft blackbody component at lower energies. The hotter plasma at $\sim$4 keV is less abundant compared to solar

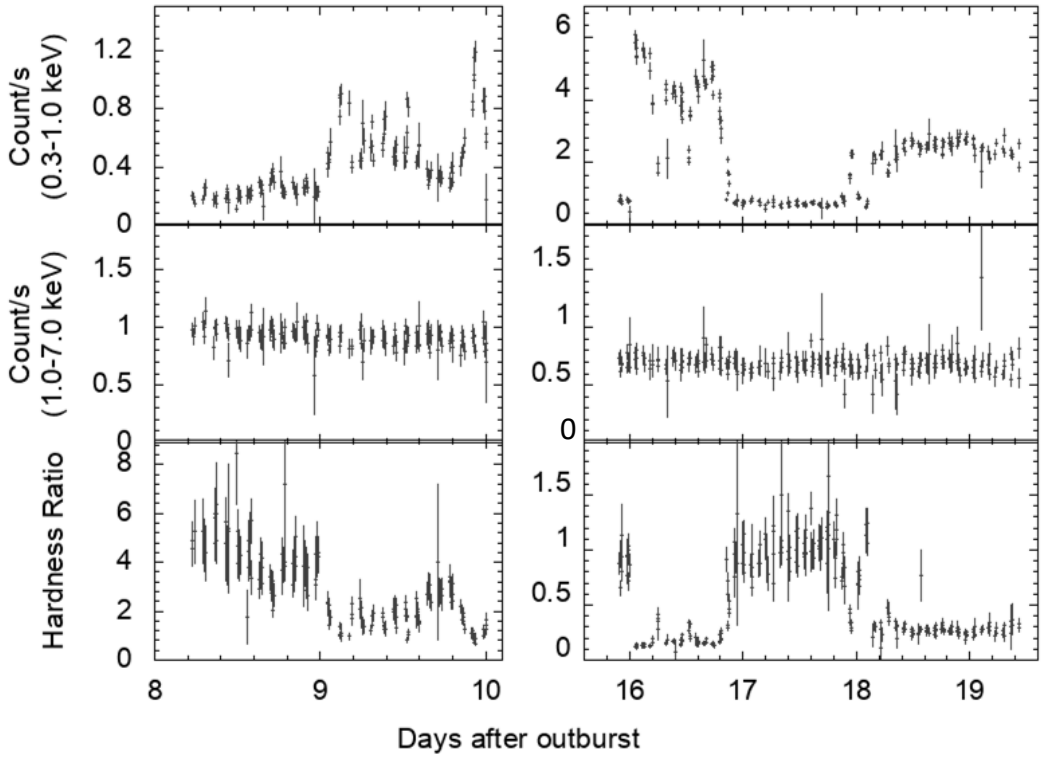

Figure 6.42: Soft X-ray light curve of V3890 Sgr in the energy range 0.3–1.0 keV (*top-panels*) and 1.0–7.0 keV (*middle-panels*). The hardness ratios are also plotted in the *bottom-panels*.

while the cooler plasma at ∼0.9 keV is overabundant compared to solar. This is consistent with that of *Chandra* high resolution X-ray spectral analysis 2 days post outburst (Orio et al., 2020). The absorbing column density is also consistent with that of *Chandra* data analyses and is found to be $\sim 10^{22}$ cm^{-2} for both the plasma components from days 8.1–9.9. The soft blackbody component is the cause for the variations seen in the light curve, and it dominates the spectra from ∼day 8.5. The hot plasma is weaker, and the column density is of the value 0.7×10^{22} cm^{-2} from day 15.7. A similar trend of decrease in column density was also seen in RS Oph and V745 Sco (Bode et al., 2006; Page et al., 2015). From the spectral analysis of day 15.7 to 19.2 observations, it was noticed that several emission lines like O VII, N VII, O VIII and Mg XI were present. Note that O VI emission along with many iron coronal lines were seen in the optical spectrum. This suggests that the plasma components present are complex and might indicate the presence of clumpy multi-temperature plasma around these epochs as the optical depth decreases.

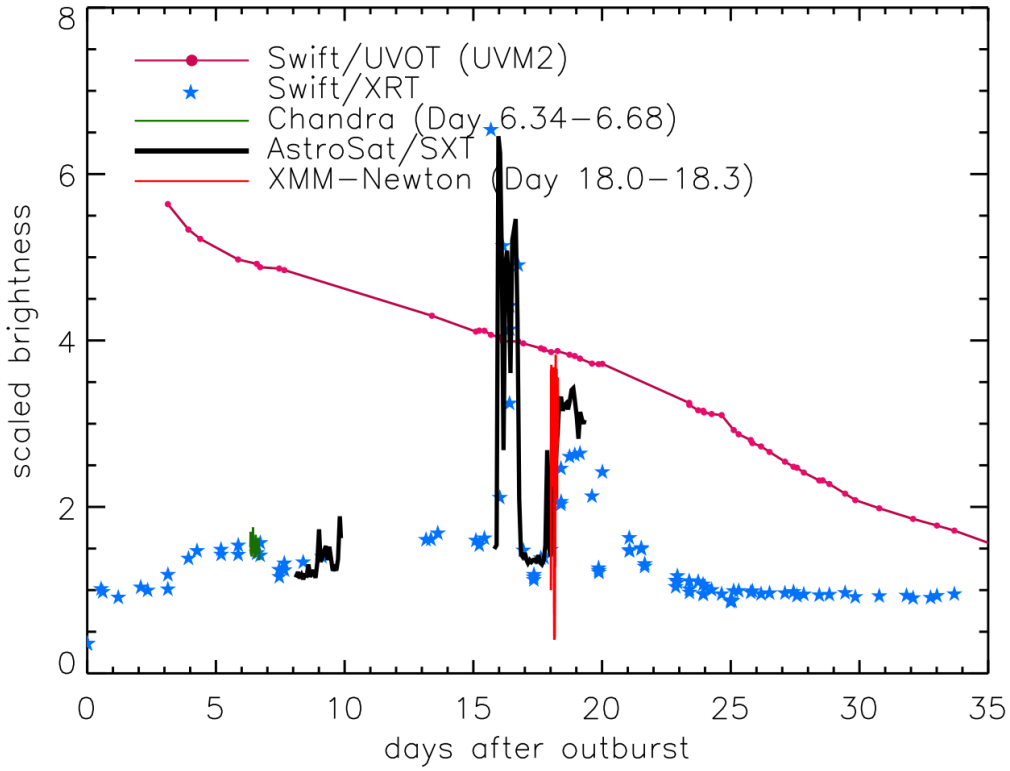

Figure 6.43: X-ray (0.5–10.0 keV) and UV light curve of V3890 Sgr during its 2019 outburst from *Swift* XRT and UVOT. The *AstroSat* observations are represented using black continuous line. The light curve obtained from *Chandra*/ACIS (zero order, ObsID 22845) is in green continuous line and from $XMM-Newton$/MOS2 (ObsID 0821560201) is in red continuous line.

The intensity strengthening is seen in the X-ray spectrum <0.7 keV ∼day 8.57 coincident with that of the onset of SSS phase on day 8.36 as reported by Page et al. (2019b). It peaked around day 15–20 and turned off on day 26.18 (Page et al., 2019a). Using the relation 3.7, the ejected mass was estimated to be 2×10^{-6} $M_{\odot}$ and the accretion rate of $\sim 2 \times 10^{-7}$ $M_{\odot}$ yr^{-1} was estimated using the relations in Henze et al. (2014) and Page et al. (2015), and by adopting super-Eddington luminosity as suggested by Gonzalez-Riestra (1992) for the 1990 outburst. These values suggest that not all the accreted material is ejected during the outburst.

The Fig. 6.43 is adopted from our paper Singh et al. 2020 [in MNRAS review], it shows the X-ray and UV light curves from different telescopes. There is presence of dips in the *Swift* XRT light curve on days 7, 17 and 27. It is noticed that the

first dip of day 7 is coincident with the beginning of the formation of narrow core in the optical emission lines (Figs. 6.31 and 6.32) and the ejected mass calculated using optical spectral data is found to be significantly high of the order of 10^{-5} $M_{\odot}$ (Section 6.5.1) on this epoch. Also, it is coincident with the radio detection at 1.28 GHz on day 6.7 (Nyamai et al., 2019). The dip around day 17 in the XRT light curve is coincident with the radio detection at 610 MHz from GMRT. The dip around day 27 in the XRT light curve is coincident with the radio detection at 325 MHz from GMRT and emergence of forbidden line [N II] around the same time. The onset of γ-ray emission (Buson et al., 2019) is coincident with that of the optical peak. The presence of coronal lines and narrowing of the emission lines in the optical spectrum, detection of soft X-ray emission and non-thermal radio emission in the RNe with a giant donor usually arise from a shock heated plasma due to the shock interaction of the ejecta with RG wind (Anupama & Mikołajewska, 1999). Evidence of clumpy nature in the environment of this system is seen in all the wavelengths analysed-optical: presence of clumpy density medium was necessary to obtain the synthetic spectrum; radio: the synchrotron turn-on was driven mainly by the clumpy medium, with radio emission peaks in the both the frequencies occurring around the same day as the system reaching unit opacity values in clumpy medium; X-ray: presence of complex plasma components suggesting a clumpy nature.

6.6 Summary

Analysis of five hybrid class of novae were discussed. The temporal evolution of spectra of four novae were presented in detail, also discussed were the morphology of the ejecta obtained for all the novae.

The evolution of the 2011 outburst of T Pyx is similar to that of the previous outbursts. The emission lines during the early pre-maximum phase have P-Cygni profiles with deep and narrow absorption components and sharp emission peaks, with the ejecta velocity decreasing from 2500 km s^{-1} to 1000 km s^{-1} until $\sim$day 12. The rise to optical maximum and early decline phase have P-Cygni profiles with

round peaked emission components and slowly fading absorption components, with the ejecta velocity increasing from 1000 km s^{-1} to 2000 km s^{-1} until ∼day 68. The emission lines in the nebular phase are broad and double peaked with wing-like structures on both the sides. The emission lines in the late post-outburst phase are narrow, and [O III] lines show a blue-shift by $\sim$ 780 km s^{-1} beyond day 1721.

V612 Sct is an unusual nova with many rebrightenings composed of five maxima. The $t_2(V)$ and $t_3(V)$ values are found to be 18 and 105 days respectively. The mass of the WD is found to be 0.66 $M_\odot$. The optical spectra consist of He, N, Fe, Ca and O lines initially and followed by appearance of coronal lines. The lines profiles change from P-Cygni to emission and back to P-Cygni. During the rise and peak period, the lines are P-Cygni profiles while during the decline, they have emission profiles. The ionization states are higher at the minima than at maxima. The lines profiles are boxy or rectangular and evolve into smoother profiles with time.

Using the optical and NIR data from AAVSO and SMARTS of V906 Car, $t_2(V)$ and $t_3(V)$ were estimated to be 50 and 70 days respectively, indicating V906 Car belongs to the class of moderately fast novae. The reddening, $E(B-V)$ was estimated to be about 0.75 and distance to the nova was found to be 1.3 kpc. The mass of the WD was estimated to be 0.7 $M_\odot$. The optical spectral line profiles evolved from P-Cygni with broad emission and narrow absorption components to emission ones with boxy and structured profiles. The nova evolved from an Fe II to He/N spectral class. According to the available spectral data, this transition occurred post the period of re-brightening observed in the optical and NIR light curve, and the γ-ray emission and shock detection period.

During the 2019 outburst of V3890 Sgr, multi-wavelength analyses were carried out. From the optical light curve, $t_2(V)$ and $t_3(V)$ were estimated to be 2.89 and 8.6 days respectively. The mass of the WD was found to be 1.37 $M_\odot$. The optical spectra consist of He, N, O, C, Si, Fe and Ca lines. The broader profiles seen initially evolve into narrower core emission line profiles. Also, present are the coronal lines as the system evolves. The onset of γ-ray emission is coincident with that of the optical peak. The modelling of the radio light curve show that the intrinsic spectra index

was found to be -0.32 with a decline rate in the optically thin phase of 1.44. The evolution of the optical depth from both the clumpy and uniform density gas suggest that the turn-on of the synchrotron emission at the low frequency is primarily driven by the optical depth in the clump density gas. The complex plasma components that were seen during the soft X-ray emission suggest the presence of clumpy multi-temperature plasma. The presence of coronal lines and narrowing of the emission lines in the optical spectrum with time, the detection of soft X-ray emission and non-thermal radio emission suggest shock interaction of the ejecta with the evolved secondary in this system.

The morphology of the ejecta was obtained for all the hybrid novae in the sample. V5588 Sgr and T Pyx have bipolar cones with equatorial rings. V906 Car has a bipolar structure with equatorial rings appearing in the late phase. V3890 Sgr has enhanced bipolar structures with cones and equatorial rings similar to He/N novae. In all the novae, Fe II emission is from the rings and He lines are from the inner cone regions. The high ionization forbidden lines like [N II] and [O III] if present are from the outer regions.

7

Summary and future work

7.1 Summary

In this work, observational data analysis of several novae are discussed. Novae serve as valuable astrophysical laboratories in the physics of accretion onto the compact objects. The observational spectra of novae are useful in deriving and understanding the physical conditions in the envelope and also the evolution of these conditions as the system evolves. The emission lines present in the spectra reveal a varying range of physical conditions such as ionization parameters and densities as seen in this work.

This work includes detailed analysis of nine Fe II, two He/N and five hybrid novae as discussed in Chapters 4, 5 and 6. Among these, three belong to RNe while the rest belong to the CNe. The list of novae discussed are given in Table 7.1.

Chapter 1 provides an introduction to nova systems and their observational properties. The motivation for the thesis is also provided in this Chapter. The methodology to reduce the data are discussed in Chapter 2. Ten different instruments were used to obtain multiwavelength data of the nova systems used in this study. The details of all these instruments along with reduction methodology are discussed in Chapter 2.

Chapter 3 presents the detailed methodology used to analyze the data and obtain

Table 7.1: List of novae discussed in this work

Object	**Type**	**Spectral class**
V477 Sct	Classical nova	He/N
V2362 Cyg	Classical nova	Fe II
V5587 Sgr	Classical nova	Fe II
V5588 Sgr	Classical nova	Hybrid
T Pyx	Recurrent nova	Hybrid
V2676 Oph	Classical nova	Fe II
V339 Del	Classical nova	Fe II
V1369 Cen	Classical nova	Fe II
V2944 Oph	Classical nova	Fe II
V5856 Sgr	Classical nova	Fe II
M31N 2008-12a	Recurrent nova	He/N
V612 Sct	Classical nova	Hybrid
V3665 Oph	Classical nova	Fe II
V906 Car	Classical nova	Hybrid
V5857 Sgr	Classical nova	Fe II
V3890 Sgr	Recurrent nova	Hybrid

ejecta morphology of different novae. The spectral synthesis and plasma simulation code CLOUDY was used to obtain synthetic spectra of different novae and estimate the ejecta physical conditions like effective blackbody temperature and luminosity of the central ionizing source, shell radius, density of the ejecta components, (clump and diffuse) and chemical abundances. The 3D code pyCloudy was used to obtain the pseudo-3D morphology of the nova ejecta and also the inclination of the system. The morphokinematic application SHAPE was used to obtain the 3D morphology of the nova ejecta and also understand the asymmetry in the geometry of the ejecta.

Chapter 4 deals with the Fe II class of novae namely V2362 Cyg, V5587 Sgr, V2676 Oph, V339 Del, V1369 Cen, V2944 Oph, V5856 Sgr, V3665 Oph and V5857 Sgr. Detailed temporal evolution of V339 Del and V5856 Sgr systems were discussed in this chapter. Chapter 5 includes analysis of He/N nova V477 Sct and detailed multiwavelength analysis of He/N nova M31N 2008-12a. Chapter 6 deals with the hybrid novae, namely V5588 Sgr, T Pyx, V612 Sct, V906 Car and V3890 Sgr. Detailed temporal evolution of T Pyx, V612 Sct, V906 Car and V3890 Sgr are discussed.

The morphology of the ejecta obtained for all the novae is given in Table 7.2. The

ejected mass and details on abundance values obtained for different nova systems using spectral synthesis and plasma simulation code CLOUDY is given in Table 7.3. The summary of the objects studied in this work is as follows:

1. V477 Sct: The emission line profiles were complex with the presence of multiple components. The morphology of the ejecta was found to be a slightly asymmetric bipolar structure with cones and equatorial rings inclined at an angle of about 83°. The forbidden lines originated from the outer regions while He lines came from the inner regions.

2. V2362 Cyg: The morphology of the ejecta was found to be bipolar cones with equatorial rings and bipolar frustum of prolate spheroid inclined at an angle of about 48°. The forbidden lines originated from the outer regions while He lines came from the inner regions and the spheroidal frustum was formed due to [N II] line.

3. V5587 Sgr: The morphology of the ejecta using Hα was found to be almost symmetric with bi-layered bipolar cones inclined at an angle of about 54°.

4. V5588 Sgr: The morphology of the ejecta was found to be bipolar cones with equatorial rings and bipolar frustum of prolate spheroid inclined at an angle of about 63°. [O I] and Fe II are from the rings, He from inner regions and the spheroidal frustum from the [N II] line.

5. T Pyx: The temporal evolution of spectra from day 1 to 2415 was studied in detail. The line profiles evolve from P-Cygni to round peaked emission ones and then to broad double-peaked emission structures. The morphological evolution of the ejecta was also obtained, and morphology was found to be bipolar cones with equatorial rings inclined at an angle of about 15°.

6. V2676 Oph: The morphology of the ejecta in the nebular phase was found to be bipolar cones with faint equatorial rings inclined at an angle of about 65°.

7. V339 Del: The temporal evolution of spectra from day 13 to 210 was studied in detail. The morphology of the ejecta using Hα was found to be slightly asymmetric bipolar cones inclined at an angle of about 58°.

8. V1369 Cen: The morphology of the ejecta using Hα was found to be asymmetric bipolar cones inclined at an angle of about 50°.

9. V2944 Oph: The morphology of the ejecta was found to be bipolar cones with equatorial rings inclined at an angle of about 51°. The forbidden lines originated from the outer regions while He lines came from the inner regions.

10. V5856 Sgr: The temporal evolution of spectra from day 11 to 1358 was studied in detail. The line profiles evolve from absorption to P-Cygni to round peaked emission ones and then to broad double-peaked emission structures. The morphological evolution of the ejecta was also obtained, and morphology was found to be asymmetric bipolar cones with equatorial rings inclined at an angle of about 9°.

11. M31N 2008-12a: Optical photometry and spectroscopy of the 2016 and 2018 outburst were studied. The UV and X-ray light curves during the 2018 outburst were used for a multiwavelength analysis of the outburst. The morphology of the ejecta was found to be slightly asymmetric with bipolar structures with cones and an equatorial ring inclined at an angle of about 81°.

12. V612 Sct: The temporal evolution of spectra from day 14 to 1062 was studied in detail. The structure of the line profiles varied consistently with that of the rebrightenings seen in the light curve.

13. V3665 Oph: The morphology of the ejecta using Hα was found to be asymmetric bipolar cones with an equatorial ring inclined at an angle of about 45°.

14. V906 Car: The temporal evolution of spectra from day 6 to 316 was studied in detail. The optical spectral line profiles evolved from P-Cygni with broad emission and narrow absorption components to emission ones with boxy and

Table 7.2: Morphology of the ejecta obtained for different nova systems in the sample

Object	Type	i°	Morphology
V477 Sct	He/N	83	Enhance bipolar with cones and equatorial rings
V2362 Cyg	Fe II	48	Bipolar cones with frustum of prolate spheroid and equatorial rings
V5587 Sgr	Fe II	54	Bipolar cones
V5588 Sgr	Hybrid	63	Bipolar cones with frustum of prolate spheroid and equatorial rings
T Pyx	Hybrid	15	Bipolar cones with equatorial rings
V2676 Oph	Fe II	65	Bipolar cones with equatorial rings
V339 Del	Fe II	58	Bipolar cones
V1369 Cen	Fe II	50	Bipolar cones
V2944 Oph	Fe II	51	Bipolar cones with equatorial rings
V5856 Sgr	Fe II	8.5	Bipolar cones with equatorial rings
M31N 2008-12a	He/N	81	Enhance bipolar with cones and an equatorial ring
V3665 Oph	Fe II	45	Bipolar cones with an equatorial ring
V906 Car	Hybrid	50	Dumbbell-like
V5857 Sgr	Fe II	41	Bipolar cones with an equatorial ring
V3890 Sgr	Hybrid	68	Enhance bipolar with cones, equatorial rings and an ellipsoidal shell

structured profiles. The nova evolved from Fe II to He/N. The morphological evolution was studied, and it was found to be asymmetry dumbbell-like structure inclined at an angle of about 50°.

15. V5857 Sgr: The morphology of the ejecta using Hα was found to be asymmetric bipolar cones with an equatorial ring inclined at an angle of about 41°.

16. V3890 Sgr: The temporal evolution of the system in optical, radio and X-ray were studied in detail from day 2 to 262. The morphological evolution, along with the evolution of physical conditions using the optical spectra was studied in detail. The morphology of the ejecta in optical was found to be bipolar one with equatorial rings and ellipsoidal shell with most of the coronal emission arising from the ellipsoid inclined at an angle of about 68°. The detailed analysis of the radio light curve suggested that the turn-on of the synchrotron emission was primarily driven by the clump density gas rather than the uniform density gas.

7.2 Discussion and future prospects

A detailed study of the temporal evolution of some novae in the sample such as T Pyx, V339 Del, V5856 Sgr, M31N 2008-12a, V612 Sct, V906 Car and V3890 Sgr

Table 7.3: Ejected mass and abundances of the nova ejecta

Object	**t[a](days)**	**Ejected mass ($M_\odot$)**	**Elements[b]**
V477 Sct	43	1.67×10^{-5}	Helium, nitrogen, oxygen
V2362 Cyg	480	8.08×10^{-6}	Helium, nitrogen, oxygen
V5588 Sgr	43	1.12×10^{-6}	Iron, helium, nitrogen, oxygen, calcium
T Pyx	68	2.74×10^{-5}	Iron, helium, nitrogen, oxygen, calcium, carbon
	224	4.60×10^{-7}	Helium, nitrogen, oxygen, neon
	252	1.52×10^{-6}	Helium, nitrogen, oxygen, neon
	336	2.13×10^{-6}	Helium, nitrogen, oxygen
	1064	3.64×10^{-6}	Helium, nitrogen, oxygen
V2676 Oph	1138	1.42×10^{-5}	Helium, oxygen, sulphur, argon
V339 Del	13	3.25×10^{-5}	Iron, oxygen, nitrogen, calcium
	20	6.43×10^{-5}	Iron, carbon, oxygen, nitrogen, calcium
	53	1.09×10^{-4}	Iron, helium, oxygen, nitrogen
V2944 Oph	699	9.13×10^{-6}	Helium, oxygen, nitrogen
V5856 Sgr	25	8.43×10^{-4}	Iron, calcium
	127	3.43×10^{-4}	Iron, oxygen, nitrogen
	533	3.40×10^{-4}	Helium, oxygen, nitrogen
M31N 2008-12a	1.52	7.21×10^{-8}	Helium
V906 Car	96	6.07×10^{-4}	Iron, helium, oxygen, nitrogen
V3890 Sgr	2	1.95×10^{-6}	Iron, helium, nitrogen, calcium
	7	1.57×10^{-5}	Iron, helium, nitrogen, calcium, silicon
	12	6.71×10^{-6}	Iron, helium, nitrogen, calcium, silicon
	16	7.70×10^{-6}	Iron, helium, nitrogen, calcium, silicon
	19	5.76×10^{-6}	Iron, helium, nitrogen, calcium, silicon
	25	2.71×10^{-6}	Iron, helium, nitrogen, calcium, silicon
	43	4.94×10^{-6}	Iron, helium, nitrogen, silicon

[a]Time since discovery in days

[b]Abundance values of the elements more than that of solar abundance values

was carried out. The study revealed that these novae show evolutionary behaviour similar to their respective spectral class. However, V612 Sct showed unusual behaviour with several maxima and a corresponding change in the ionization states. The chemical composition in the ejecta discussed for some novae during their evolution (Table 7.3) reveals that the elemental composition is not the same during the early and late phase as also suggested by Starrfield et al. (2016). There is presence of a range of elements in the ejecta of novae in the sample like helium, carbon, nitrogen, oxygen, neon, silicon, sulphur, argon, calcium and iron whose abundance values are more than that of solar abundance values.

All the Fe II class of novae in the sample have bipolar cone-like structures with or without equatorial rings with an inclination angle in the range of 40°–65° except for V5856 Sgr which has an inclination angle of about 9°. The presence of cones and

rings can be explained to be due to the wind interaction with the secondary or interaction of the ejecta with a pre-existing circumbinary material (Gill & O'Brien, 1999; O'Brien et al., 1995) or as an interaction between multiple shells ejected during the outburst. Origin of the forbidden lines like [O III] and [N II] are found to be from the outer regions implying that they are coming from the optically thin expanding shell. The helium lines are coming from the inner regions. The forbidden oxygen lines and Fe II present in the ejecta of any nova is predominantly contributed by the equatorial rings. The Fe II might be contributed mainly from the circumbinary material. [N II] lines when present, are coming either from the conical bases or the spheroidal frustum and are formed either due to the frictional interaction between multiple ejecta, or interaction of the ejecta wind with the secondary (Lloyd et al., 1997).

Both the He/N novae in the sample have enhanced bipolar structures along the ejecta axis with cones and equatorial rings at an inclination angle of about 80°. The [O III] lines are from the outer regions, and [N II] lines are from equatorial rings indicating that they are arising from the optical thin regions and He lines are coming from the cones in the inner regions of the bipolar structures. The morphokinematic analysis of few He/N novae in the previous studies was as follows. Ribeiro et al. (2013b) suggested that morphology of He/N type, Nova Mon 2012 is a bipolar structure with a high inclination angle of $82^\circ \pm 6^\circ$. The best-fitting remnant morphology of He/N type, Nova Cyg 2008 #2 was found to be polar blobs and an equatorial ring with a high inclination angle of 80° by Ribeiro et al. (2011). The best-fit Hα profile corresponding to the observed profile of KT Eri obtained by Ribeiro et al. (2013a) resulted in the dumbbell-shaped structure with an inclination angle of 58°.

Hybrid novae in the sample have the morphology of the ejecta and the system's inclination angle seen in that of Fe II and He/N type of novae. It is noticed that all the novae in the sample have bipolar conical structures irrespective of the spectral class. From the numerical calculations and suggestions in the literature by Gill & O'Brien (1999) and O'Brien et al. (1995), cones are generated as a consequence of frictional interaction of wind with the secondary. In some cases, a fast wind sweeps up the density distribution forming a ring near the density enhanced regions where

the double cones are present (Lloyd et al., 1997). It is noticed that [N II] emission is coming from equatorial ring components in the case of V477 Sct and also T Pyx (Pavana et al., 2019a) rather than bipolar regions as in the case of other novae. This might be due to the variation in ionization rather than the density as also seen and suggested in the case of V705 Cas by Gill & O'Brien (1999).

The presence of cones and rings in general can also be explained due to the wind interaction with the secondary or interaction of the ejecta with the pre-existing circumbinary material in the case of some novae. For example in the case of V2944 Oph, there was observational evidence for the presence of pre-existing circumstellar medium (Munari & Walter, 2016) hence, the presence of equatorial rings could be due to the interaction of the outflow with this CSM.

The morphology and elemental distribution of the nova ejecta presented here indicate the presence of equatorial rings to be common in the Fe II and hybrid class, while they are absent or weak in the He/N class. This implies that the He/N class novae are the ones with either no, or a very low circumbinary material, while the Fe II class are the ones with a significant amount of circumbinary material. The bipolar nature and similarity in the morphology of the systems irrespective of the spectral class and also identical elemental distribution might hint that the systems are inherently He/N. It was suggested by Shore (2012) that there is no distinction between the different spectral classes and it is more relevant to the expansion phase of nova. It was proposed that some novae have already passed the optical thick phase when detected while some are still in optical thick phase.

Multiwavelength monitoring of novae is very crucial for a better understanding of the nova systems in terms of ionization, processes involving emission line formation, the evolution of the system and observational properties of the system. It is well-known that CNe behave similarly in most cases, and the detailed study of some novae in this work reveals that there are unusual systems like V612 Sct. In this work, an effort has been made to use different available instruments and analysis for these data has been carried out. In future, more focus will be on obtaining high resolution

data throughout the evolution of different novae to investigate the chemical composition in detail and also study and analyze the line profiles to obtain any complex morphology of the ejecta with or without the availability of spatially resolved images. Due to good high resolution coverage of V906 Car at different phases, a more profound understanding of the evolution of the morphology of ejecta with respect to asymmetry in the system was well understood.

It is essential to carry out the analysis for a larger sample to verify if any different morphology is present in nova ejecta than what is obtained during this sample study. Also, increasing the sample will result in obtaining a well-understood exhaustive model for all class of novae. It is also essential to model novae in their late post-outburst phase to understand the characteristic properties of the accretion disc and the secondary which is not well understood. It is interesting to note that the novae with massive WDs ($\gtrsim$1.3 $M_{\odot}$) such as V477 Sct, M31N 2008-12a and V3890 Sgr have enhanced bipolar structures. Unless and until this analysis is considered for a larger sample, it cannot be concluded that the mass of the WD is playing a significant role in the morphology of the ejecta. Also, a larger sample of massive WD might confirm if the WD mass is having any role in the spectral class of nova as well as the morphology of the ejecta.

The study of quiescence phase of nova systems reveals the properties of the central binary system and the accretion process. Also, information on the emission line fluxes which eventually leads to the understanding of changes in the physical conditions in the line forming regions which could be due to accretion rates or binary motion. It also helps in understanding the property and type of secondary present in the system. In this study, detailed work on quiescence phase was carried out only on T Pyx, and the recent novae that are studied in detail are still in their nebular phase. The quiescence phase of novae such as V5856 Sgr, V612 Sct, V906 Car and V3890 Sgr will be studied and analyzed in detail to obtain the observational properties and morphology of the ejecta as a part of future work of this study.

It is important to note that different spectra are revealed at different times based on the optical depth at that particular wavelength. It is essential to understand the

line profiles at different phases of multiwavelength spectra similar to the analysis carried out for some novae in this work in the optical regime. However, modelling multiwavelength spectrum is essential to understand if there is any non-uniform distribution of elements, to get a complete picture on the chemical abundance values at a particular phase as well as the ejected mass, any difference or similarity in the ejecta geometries in different wavelengths, any effect on the morphology with a change in physical conditions due to various phenomena in different wavelength regime, if density distribution is dominated by the clump or uniform medium in the ejecta, any contribution from the accretion disc, secondary or primary on the morphology, and any impact of shock interactions on the morphology of the ejecta as well as the physical conditions.

The current availability of all-sky survey like the All Sky Automated Survey for SuperNovae (ASAS-SN) has increased the discovery rate of novae. For example, two of the novae V5856 Sgr (ASASSN-16ma) and V906 Car (ASASSN-18fv) used in this sample study were discovered by this survey. It is essential to monitor many such new novae from its pre-maximum to late post-outburst phase to understand the evolution of the outburst. Also, with an increase in discovery rate and eventually studying the evolution of unusual classical novae (like V612 Sct in our sample) might result in getting better insight into the behaviour of these systems in general. Further, with surveys such as the Rubin Observatory Legacy Survey of Space and Time (LSST), the information about progenitors during pre-outburts can be obtained in the pre-outburst period, something that is currently not well understood. With the upcoming large and highly sensitive telescope such as Thirty Meter Telescope (TMT), high resolution monitoring can be carried out with ease during the late post-outburst and quiescence phases of novae. This would eventually help better understand not only the binary nature but also the nature of accretion disc and the secondary. There is no detailed study or understanding of extragalactic novae except few studies of novae in Local Group of galaxies. Spectroscopy of extragalactic novae has been very challenging with the available facilities because of the distance. Temporal spectral evolution of these extragalactic novae will be easily possible with a large facility like

TMT. It was noted that galaxies like M33 in the Local Group had a higher population of fast novae unlike in M31 and our galaxy and it was attributed to the younger population in the galaxy (Shafter et al., 2012). Hence, the study of extragalactic novae in such galaxies would provide evidence to whether or not the star formation history of the host galaxy result in a different population of novae. Also, spectropolarimetric observations of novae is essential. It will not only provide information on the geometry of the shell and its interaction with the environment but will also provide information on the inclination of the system and degree of asymmetry in the shell.

Bibliography

Abdo, A. A., Ackermann, M., Ajello, M., et al. 2010, Science, 329, 817

Ackermann, M., Ajello, M., Albert, A., et al. 2014, Science, 345, 554

Ak, T., Retter, A., & Liu, A. 2005, Publications of the Astronomical Society of Australia, 22, 298

Amelio, G. F., Tompsett, M. F., & Smith, G. E. 1970, The Bell System Technical Journal, 49, 593

Anderson, G., Fender, R., Chomiuk, L., & Staley, T. 2013, The Astronomer's Telegram, 5428, 1

Anupama, G. C. 2008, in Astronomical Society of the Pacific Conference Series, Vol. 401, RS Ophiuchi (2006) and the Recurrent Nova Phenomenon, ed. A. Evans, M. F. Bode, T. J. O'Brien, & M. J. Darnley, 31

Anupama, G. C. & Kamath, U. S. 2012, Bulletin of the Astronomical Society of India, 40, 161

Anupama, G. C. & Mikołajewska, J. 1999, Astronomy & Astrophysics , 344, 177

Anupama, G. C. & Sethi, S. 1994, Monthly Notices of the Royal Astronomical Society , 269, 105

Arai, A. & Imamura, K. 2011, IAU Circ., 9196, 2

Arai, A., Nagashima, M., Kajikawa, T., & Naka, C. 2011, IAU Circ., 9203, 2

Arai, A., Uemura, M., Kawabata, K. S., et al. 2010, Publications of the Astronomical Society of Japan, 62, 1103

Ayani, K. & Fujii, M. 2015a, Central Bureau Electronic Telegrams, 4086, 3

Ayani, K. & Fujii, M. 2015b, Central Bureau Electronic Telegrams, 4086, 4

Aydi, E., Sokolovsky, K. V., Chomiuk, L., et al. 2020, Nature Astronomy, 4, 776

Barnes, S. & MacQueen, P. 2008, in Society of Photo-Optical Instrumentation Engineers (SPIE) Conference Series, Vol. 7014, Proceedings of SPIE , 70141H

Bath, G. T. & Shaviv, G. 1976, Monthly Notices of the Royal Astronomical Society , 175, 305

Beals, C. S. 1931, Monthly Notices of the Royal Astronomical Society , 91, 966

Berardi, P., Sims, W., & Sollecchia, U. 2017, The Astronomer's Telegram, 10558, 1

Bhattacharyya, J. C. 1987, Bulletin of the Astronomical Society of India, 15, 121

Bode, M. F. & Evans, A. 2008, Classical Novae, Vol. 43

Bode, M. F., O'Brien, T. J., Osborne, J. P., et al. 2006, Astrophysical Journal , 652, 629

Bode, M. F., Seaquist, E. R., & Evans, A. 1987, Monthly Notices of the Royal Astronomical Society , 228, 217

Boyle, W. S. & Smith, G. E. 1970, The Bell System Technical Journal, 49, 587

Bramall, D. G., Schmoll, J., Tyas, L. M. G., et al. 2012, in Society of Photo-Optical Instrumentation Engineers (SPIE) Conference Series, Vol. 8446, Proceedings of SPIE , 84460A

Bramall, D. G., Sharples, R., Tyas, L., et al. 2010, in Society of Photo-Optical Instrumentation Engineers (SPIE) Conference Series, Vol. 7735, Proceedings of SPIE , 77354F

Breeveld, A. A., Landsman, W., Holland, S. T., et al. 2011, in American Institute of Physics Conference Series, Vol. 1358, American Institute of Physics Conference Series, ed. J. E. McEnery, J. L. Racusin, & N. Gehrels, 373–376

Brocklehurst, M. 1972, Monthly Notices of the Royal Astronomical Society , 157, 211

Buson, S., Jean, P., & Cheung, C. C. 2019, The Astronomer's Telegram, 13114, 1

Camenzind, M. 2007, Compact objects in astrophysics : white dwarfs, neutron stars, and black holes

Cao, Y., Kasliwal, M. M., Neill, J. D., et al. 2012, Astrophysical Journal , 752, 133

Chesneau, O., Meilland, A., Banerjee, D. P. K., et al. 2011, Astronomy & Astrophysics , 534, L11

Cheung, C. C., Jean, P., Shore, S. N., & Fermi Large Area Telescope Collaboration. 2013, The Astronomer's Telegram, 5649

Chomiuk, L., Linford, J., Finzell, T., et al. 2013, The Astronomer's Telegram, 5382, 1

Chomiuk, L., Nelson, T., Mukai, K., et al. 2014, Astrophysical Journal , 788, 130

Clayton, D. D. & Hoyle, F. 1974, Astrophysical Journal Letters , 187, L101

Clegg, R. E. S. 1987, Monthly Notices of the Royal Astronomical Society , 229, 31P

Combi, M. R., Bertaux, J.-L., Quemerais, E., Maekinen, J. T. T., & Ferron, S. 2013, IAU Circ., 9266

Corbett, H., Law, N., Goeke, E., et al. 2018, The Astronomer's Telegram, 11467, 1

Crause, L. A., Sharples, R. M., Bramall, D. G., et al. 2014, in Society of Photo-Optical Instrumentation Engineers (SPIE) Conference Series, Vol. 9147, Proceedings of SPIE , 91476T

Crawford, S. M., Still, M., Schellart, P., et al. 2010, in Society of Photo-Optical Instrumentation Engineers (SPIE) Conference Series, Vol. 7737, Proceedings of SPIE , 773725

Csák, B., Kiss, L. L., Retter, A., Jacob, A., & Kaspi, S. 2005, Astronomy & Astrophysics , 429, 599

Danilet, A. B., Holoien, T. W. S., Wagner, R. M., et al. 2015, The Astronomer's Telegram, 7339, 1

Darnley, M. J., Bode, M. F., Smith, R. J., & Evans, A. 2013, The Astronomer's Telegram, 5279, 1

Darnley, M. J., Henze, M., Bode, M. F., et al. 2016, Astrophysical Journal , 833, 149

Darnley, M. J., Henze, M., Shafter, A. W., et al. 2018, The Astronomer's Telegram, 12177

Darnley, M. J., Henze, M., Steele, I. A., et al. 2015, Astronomy & Astrophysics , 580, A45

Darnley, M. J., Hounsell, R., Godon, P., et al. 2017a, Astrophysical Journal , 849, 96

Darnley, M. J., Hounsell, R., Godon, P., et al. 2017b, Astrophysical Journal , 847, 35

Darnley, M. J., Hounsell, R., O'Brien, T. J., et al. 2019, Nature, 565, 460

Darnley, M. J., Ribeiro, V. A. R. M., Bode, M. F., Hounsell, R. A., & Williams, R. P. 2012, Astrophysical Journal , 746, 61

Das, R. & Mondal, A. 2015, New Astronomy, 39, 19

Das, R. K., Ashok, N. M., & Banerjee, D. P. K. 2005, IAU Circ., 8617, 2

De Gennaro Aquino, I., Schröder, K. P., Mittag, M., et al. 2015, Astronomy & Astrophysics , 581, A134

De Gennaro Aquino, I., Shore, S. N., Schwarz, G. J., et al. 2014, Astronomy & Astrophysics , 562, A28

della Valle, M. & Livio, M. 1995, Astrophysical Journal , 452, 704

della Valle, M. & Livio, M. 1996, Astrophysical Journal , 473, 240

Denisenko, D. & Masi, G. 2013, IAU Circ., 9258, 3

Downes, R. A. & Duerbeck, H. W. 2000, The Astronomical Journal, 120, 2007

Duerbeck, H. W. 1981, Publications of the Astronomical Society of the Pacific , 93, 165

Duerbeck, H. W. 1987, Space Science Reviews, 45, 1

Duerbeck, H. W. & Benetti, S. 1996, Astrophysical Journal Letters , 468, L111

Duerbeck, H. W. & Seitter, W. C. 1979, The Messenger, 17, 1

Evans, A., Banerjee, D. P. K., Gehrz, R. D., et al. 2017, Monthly Notices of the Royal Astronomical Society , 466, 4221

Evans, A., Gehrz, R. D., Helton, L. A., et al. 2012, Monthly Notices of the Royal Astronomical Society: Letters, 424, L69

Eyres, S. P. S., O'Brien, T. J., Beswick, R., et al. 2009, Monthly Notices of the Royal Astronomical Society , 395, 1533

Ferland, G. J., Chatzikos, M., Guzmán, F., et al. 2017, Revista Mexicana de Astronomía y Astrofísica, 53, 385

Fujii, M. & Yamaoka, H. 2005, IAU Circ., 8617, 3

Gehrz, R. D. 1988, Annual Review of Astronomy and Astrophysics, 26, 377

Gehrz, R. D. 2008, Infrared studies of classical novae, 2nd edn., ed. M. F. Bode & A. Evans, Cambridge Astrophysics (Cambridge University Press), 167–193

Gill, C. D. & O'Brien, T. J. 1999, Monthly Notices of the Royal Astronomical Society , 307, 677

Godon, P., Sion, E. M., Williams, R. E., & Starrfield, S. 2018, Astrophysical Journal , 862, 89

Gonzalez-Riestra, R. 1992, Astronomy & Astrophysics , 265, 71

Guarro, J., Berardi, P., Sollecchia, U., et al. 2017, The Astronomer's Telegram, 10737, 1

Hachisu, I. & Kato, M. 2006, The Astrophysical Journal Supplement Series, 167, 59

Hachisu, I. & Kato, M. 2007, Astrophysical Journal , 662, 552

Hachisu, I. & Kato, M. 2014, Astrophysical Journal , 785, 97

Harrison, T. E., Johnson, J. J., & Spyromilio, J. 1993, , 105, 320

Hellier, C. 2001, Cataclysmic Variable Stars

Helton, L. A., Woodward, C. E., Walter, F. M., et al. 2010, The Astronomical Journal, 140, 1347

Henze, M., Darnley, M. J., Williams, S. C., et al. 2018, Astrophysical Journal , 857, 68

Henze, M., Ness, J. U., Darnley, M. J., et al. 2014, Astronomy & Astrophysics , 563, L8

Henze, M., Ness, J.-U., Darnley, M. J., et al. 2015, Astronomy & Astrophysics , 580, A46

Henze, M., Pietsch, W., Haberl, F., et al. 2011, Astronomy & Astrophysics , 533, A52

Hernanz, M., Ferri, C., & Sala, G. 2007, The Astronomer's Telegram, 1226, 1

Hjellming, R. M. 1989, IAU Circ., 4853, 2

Hjellming, R. M. & Wade, C. M. 1970, Astrophysical Journal Letters , 162, L1

Hjellming, R. M., Wade, C. M., Vandenberg, N. R., & Newell, R. T. 1979, Astronomical Journal, 84, 1619

Hummer, D. G. & Storey, P. J. 1987, Monthly Notices of the Royal Astronomical Society , 224, 801

Hutchings, J. B. 1972a, Publications of the Dominion Astrophysical Observatory Victoria, 14, 59

Hutchings, J. B. 1972b, Monthly Notices of the Royal Astronomical Society , 158, 177

Itagaki, K., Gao, X., Darnley, M. J., et al. 2016, The Astronomer's Telegram, 9848, 1

Izzo, L., Della Valle, M., Mason, E., et al. 2015, Astrophysical Journal Letters , 808, L14

Izzo, L., Ederoclite, A., Della Valle, M., et al. 2012, Mem. Societa Astronomica Italiana , 83, 830

Izzo, L., Molaro, P., Mason, E., et al. 2018, The Astronomer's Telegram, 11468, 1

Jean, P., Cheung, C. C., Ojha, R., van Zyl, P., & Angioni, R. 2018, The Astronomer's Telegram, 11546, 1

Jones, A. & Pearce, A. 1990, IAU Circ., 5004, 3

Joshi, V., Banerjee, D. P. K., & Ashok, N. M. 2014, Monthly Notices of the Royal Astronomical Society , 443, 559

Joshi, V., Srivastava, M., & Banerjee, D. P. K. 2018, The Astronomer's Telegram, 11570

Kajikawa, T., Arai, A., Nagashima, M., et al. 2015, Acta Polytechnica CTU Proceedings, 2, 242

Kantharia, N. G., Anupama, G. C., Prabhu, T. P., et al. 2007, Astrophysical Journal Letters , 667, L171

Kantharia, N. G., Dutta, P., Roy, N., et al. 2016, Monthly Notices of the Royal Astronomical Society , 456, L49

Kasliwal, M. M., Cenko, S. B., Kulkarni, S. R., et al. 2011, Astrophysical Journal , 735, 94

Kato, M., Saio, H., & Hachisu, I. 2015, Astrophysical Journal , 808, 52

Kato, T., Nakajima, K., Maehara, H., & Kiyota, S. 2009, arXiv e-prints [[arXiv]0904.2228]

Kaur, A., Rajagopal, M., Hartmann, D. H., et al. 2018, The Astronomer's Telegram, 12205

Kawakita, H., Ootsubo, T., Arai, A., Shinnaka, Y., & Nagashima, M. 2017, Astronomical Journal, 153, 74

Kenyon, S. J. & Fernandez-Castro, T. 1987, , 93, 938

Kimeswenger, S., Dalnodar, S., Knapp, A., et al. 2006, The Astronomer's Telegram, 963, 1

King, A. R. 1989, in Classical Novae, 17–37

Kiyota, S., Kato, T., & Yamaoka, H. 2004, Publications of the Astronomical Society of Japan, 56, S193

Krauss, M. I., Chomiuk, L., Rupen, M., et al. 2011, Astrophysical Journal Letters , 739, L6

Krautter, J. 2008, X-ray emission from classical novae in outburst, 2nd edn., ed. M. F. Bode & A. Evans, Cambridge Astrophysics (Cambridge University Press), 232–251

Krautter, J., Oegelman, H., Starrfield, S., Wichmann, R., & Pfeffermann, E. 1996, Astrophysical Journal , 456, 788

Kuin, N. P. M., Page, K. L., Williams, S. C., et al. 2017, The Astronomer's Telegram, 10636, 1

Kurtenkov, A., Napetova, M., & Tomov, T. 2017a, The Astronomer's Telegram, 10725, 1

Kurtenkov, A., Tomov, T., & Pessev, P. 2017b, The Astronomer's Telegram, 10527, 1

Kuulkers, E., Page, K. L., Osborne, J. P., et al. 2013, The Astronomer's Telegram, 5283, 1

Kwok, S. 1983, Monthly Notices of the Royal Astronomical Society , 202, 1149

Li, K.-L., Chomiuk, L., & Strader, J. 2016, The Astronomer's Telegram, 9736

Li, K.-L., Metzger, B. D., Chomiuk, L., et al. 2017, Nature Astronomy, 1, 697

Liller, W. & Vina del Mar. 1990, IAU Circ., 5010, 2

Livio, M. 1992, Astrophysical Journal , 393, 516

Lloyd, H. M., O'Brien, T. J., & Bode, M. F. 1997, Monthly Notices of the Royal Astronomical Society , 284, 137

Luckas, P. 2016, The Astronomer's Telegram, 9678

Luckas, P. 2018, The Astronomer's Telegram, 11460, 1

Lynch, D. K., Woodward, C. E., Gehrz, R., et al. 2008, Astronomical Journal, 136, 1815

MacDonald, J. 1996, Astrophysics and Space Science Library, Vol. 208, Classical nova evolution: clues from soft X-ray emission, ed. A. Evans & J. H. Wood, 281

Martin, P. G. 1989, in Classical Novae, 73–92

Martini, P., Wagner, R. M., Tomaney, A., et al. 1999, Astronomical Journal, 118, 1034

Mason, E., Diaz, M., Williams, R. E., Preston, G., & Bensby, T. 2010, Astronomy & Astrophysics , 516, A108

Mason, E., Shore, S. N., Kuin, P., & Bohlsen, T. 2020, Astronomy & Astrophysics , 635, A115

Mazuk, S., Lynch, D. K., Rudy, R. J., et al. 2005, IAU Circ., 8644, 1

Mazuk, S., Rudy, R. J., Lynch, D. K., et al. 2006, IAU Circ., 8731, 2

McLaughlin, D. B. 1960, The Spectra of Novae, 585

McLoughlin, D., Blundell, K. M., & Lee, S. 2020, Monthly Notices of the Royal Astronomical Society , 494, 743

McMullin, J. P., Waters, B., Schiebel, D., Young, W., & Golap, K. 2007, in Astronomical Society of the Pacific Conference Series, Vol. 376, Astronomical Data Analysis Software and Systems XVI, ed. R. A. Shaw, F. Hill, & D. J. Bell, 127

Mondal, A., Anupama, G. C., Kamath, U. S., et al. 2018, Monthly Notices of the Royal Astronomical Society , 474, 4211

Morisset, C. 2013, pyCloudy: Tools to manage astronomical Cloudy photoionization code, Astrophysics Source Code Library

Munari, U., Hambsch, F. J., & Frigo, A. 2017a, Monthly Notices of the Royal Astronomical Society , 469, 4341

Munari, U., Hambsch, F. J., Frigo, A., et al. 2017b, The Astronomer's Telegram, 10572, 1

Munari, U., Henden, A., Banerjee, D. P. K., et al. 2015a, Monthly Notices of the Royal Astronomical Society , 447, 1661

Munari, U., Henden, A., Dallaporta, S., & Cherini, G. 2013, Information Bulletin on Variable Stars, 6080, 1

Munari, U., Maitan, A., Moretti, S., & Tomaselli, S. 2015b, New Astronomy, 40, 28

Munari, U., Ochner, P., Hambsch, F. J., et al. 2017c, The Astronomer's Telegram, 10736, 1

Munari, U., Ochner, P., Siviero, A., Dallaporta, S., & Valisa, P. 2015c, The Astronomer's Telegram, 7367, 1

Munari, U., Siviero, A., Henden, A., et al. 2008, Astronomy & Astrophysics , 492, 145

Munari, U., Siviero, A., Navasardyan, H., & Dallaporta, S. 2006, Astronomy & Astrophysics , 452, 567

Munari, U., Traven, G., Hambsch, F. J., et al. 2017d, The Astronomer's Telegram, 10641, 1

Munari, U. & Walter, F. M. 2016, Monthly Notices of the Royal Astronomical Society , 455, L57

Munari, U. & Zwitter, T. 1997, Astronomy & Astrophysics , 318, 269

Nakano, S., Nishimura, H., Kiyota, S., & Yusa, T. 2011, IAU Circ., 9196, 1

Nakano, S., Nishimura, H., Miles, R., & Yamaoka, H. 2006, IAU Circ., 8697, 1

Nakano, S., Sakurai, Y., & Schmeer, P. 2015, Central Bureau Electronic Telegrams, 4086, 1

Nauenberg, M. 1972, Astrophysical Journal , 175, 417

Neckel, T. & Klare, G. 1980, Astronomy and Astrophysics, Suppl. Ser., 42, 251

Nelson, T., Chomiuk, L., Roy, N., et al. 2014, Astrophysical Journal , 785, 78

Nelson, T., Mukai, K., Chomiuk, L., & Sokoloski, J. 2013a, The Astronomer's Telegram, 5593, 1

Nelson, T., Mukai, K., Chomiuk, L., et al. 2013b, The Astronomer's Telegram, 5305, 1

Nelson, T., Mukai, K., Sokoloski, J. L., et al. 2018, The Astronomer's Telegram, 11608, 1

Ness, J. U., Starrfield, S., Schwarz, G., et al. 2006a, Central Bureau Electronic Telegrams, 696, 1

Ness, J. U., Starrfield, S., Schwarz, G., et al. 2006b, Central Bureau Electronic Telegrams, 783, 1

Nishimura, H., Kaneda, H., Kojima, T., & Yusa, T. 2012, Central Bureau Electronic Telegrams, 3072, 1

Nishiyama, K. & Kabashima, F. 2008, CBAT IAU, http://www.cbat.eps.harvard.edu/iau/CBAT_M31.html#2008-12a

Nishiyama, K., Kabashima, F., Maehara, H., & Kiyota, S. 2011, IAU Circ., 9203

Nyamai, M. M., Woudt, P. A., Ribeiro, V. A. R. M., & Chomiuk, L. 2019, The Astronomer's Telegram, 13089, 1

O'Brien, T. J., Lloyd, H. M., & Slavin, A. J. 1995, in Annals of the Israel Physical Society, Vol. 11, Asymmetrical Planetary Nebulae, ed. A. Harpaz & N. Soker, 258

Orio, M., Drake, J. J., Ness, J. U., et al. 2020, Astrophysical Journal , 895, 80

Osborne, J. P., Page, K., Beardmore, A., et al. 2013, The Astronomer's Telegram, 5505, 1

Osterbrock, D. E. & Ferland, G. J. 2006, Astrophysics of gaseous nebulae and active galactic nuclei (Sausalito, CA: University Science Books)

Page, K. L., Beardmore, A. P., Osborne, J. P., et al. 2019a, The Astronomer's Telegram, 13137, 1

Page, K. L., Beardmore, A. P., Osborne, J. P., et al. 2019b, The Astronomer's Telegram, 13084, 1

Page, K. L., Kuin, N. P., Osborne, J. P., et al. 2014, The Astronomer's Telegram, 5967, 1

Page, K. L., Osborne, J. P., Kuin, N. P. M., et al. 2015, Monthly Notices of the Royal Astronomical Society , 454, 3108

Page, K. L., Osborne, J. P., Kuin, N. P. M., et al. 2013, The Astronomer's Telegram, 5470, 1

Patterson, J., Kemp, J., Shambrook, A., et al. 1998, Publications of the Astronomical Society of the Pacific , 110, 380

Patterson, J., Oksanen, A., Kemp, J., et al. 2017, Monthly Notices of the Royal Astronomical Society , 466, 581

Pavana, M., Anche, R. M., Anupama, G. C., Ramaprakash, A. N., & Selvakumar, G. 2019a, Astronomy & Astrophysics , 622, A126

Pavana, M., Anupama, G. C., & Pramod, K. S. 2019b, The Astronomer's Telegram, 13060, 1

Pavana, M., Anupama, G. C., Selvakumar, G., & Kiran, B. S. 2017, The Astronomer's Telegram, 10613, 1

Pavana, M., Raj, A., Bohlsen, T., et al. 2020, Monthly Notices of the Royal Astronomical Society , 495, 2075

Payne-Gaposchkin, C. 1964, The galactic novae

Piano, G., Lucarelli, F., Pittori, C., et al. 2018, The Astronomer's Telegram, 11553, 1

Poggiani, R. 2008, Astrophysics and Space Science, 315, 79

Poggiani, R. 2009, New Astronomy, 14, 4

Poggiani, R. 2017, in The Golden Age of Cataclysmic Variables and Related Objects IV, 49

Pojmanski, G., Yamaoka, H., Haseda, K., et al. 2005, IAU Circ., 8617

Polisensky, E., Linford, J. D., Giacintucci, S., et al. 2019, The Astronomer's Telegram, 13185, 1

Poole, T. S., Breeveld, A. A., Page, M. J., et al. 2008, Monthly Notices of the Royal Astronomical Society , 383, 627

Pottasch, S. 1959, Annales d'Astrophysique, 22, 412

Prabhu, T. P., Anupama, G. C., & Surendiranath, R. 1998, Bulletin of the Astronomical Society of India, 26, 383

Press, W. H., Teukolsky, S. A., Vetterling, W. T., & Flannery, B. P. 2002, Numerical recipes in C++ : the art of scientific computing

Rabus, M. & Prieto, J. L. 2018, The Astronomer's Telegram, 11506, 1

Raj, A., Das, R. K., & Walter, F. M. 2017, Astrophysical Journal , 835, 274

Raj, A., Pavana, M., Kamath, U. S., Anupama, G. C., & Walter, F. M. 2018, Acta Astronomica, 68, 79

Rayner, J., Rudy, R. J., Lynch, D. K., et al. 2006, IAU Circ., 8788, 1

Ribeiro, V. A. R. M., Bode, M. F., Darnley, M. J., et al. 2013a, Monthly Notices of the Royal Astronomical Society , 433, 1991

Ribeiro, V. A. R. M., Darnley, M. J., Bode, M. F., et al. 2011, Monthly Notices of the Royal Astronomical Society , 412, 1701

Ribeiro, V. A. R. M., Munari, U., & Valisa, P. 2013b, Astrophysical Journal , 768, 49

Roy, N., Chomiuk, L., Sokoloski, J. L., et al. 2012, Bulletin of the Astronomical Society of India, 40, 293

Roy, N., Kantharia, N. G., Dutta, P., et al. 2013, The Astronomer's Telegram, 5376, 1

Rudy, R. J., Crawford, K. B., & Russell, R. W. 2016, The Astronomer's Telegram, 9849

Rupert, J., Wagner, R. M., Woodward, C. E., & Starrfield, S. 2018, The Astronomer's Telegram, 11528

Ryder, S. D., Kool, E. C., & Chomiuk, L. 2018, The Astronomer's Telegram, 11504, 1

Schaefer, B. E. 2018, Monthly Notices of the Royal Astronomical Society , 481, 3033

Schaefer, B. E., Landolt, A. U., Linnolt, M., et al. 2013, Astrophysical Journal , 773, 55

Schaefer, B. E., Pagnotta, A., & Shara, M. M. 2010, Astrophysical Journal , 708, 381

Schaefer, G. H., Brummelaar, T. T., Gies, D. R., et al. 2014, New Astronomyt, 515, 234

Schlafly, E. F. & Finkbeiner, D. P. 2011, Astrophysical Journal , 737, 103

Schwarz, G. J. 2002, Astrophysical Journal , 577, 940

Schwarz, G. J., Shore, S. N., Starrfield, S., et al. 2001, Monthly Notices of the Royal Astronomical Society , 320, 103

Schwarz, G. J., Shore, S. N., Starrfield, S., & Vanlandingham, K. M. 2007a, Astrophysical Journal , 657, 453

Schwarz, G. J., Woodward, C. E., Bode, M. F., et al. 2007b, Astronomical Journal, 134, 516

Seaquist, E. R. 2008, Radio emission from novae, 2nd edn., ed. M. F. Bode & A. Evans, Cambridge Astrophysics (Cambridge University Press), 141–166

Seaquist, E. R., Duric, N., Israel, F. P., et al. 1980, Astronomical Journal, 85, 283

Seaquist, E. R. & Palimaka, J. 1977, Astrophysical Journal , 217, 781

Selvelli, P., Cassatella, A., Gilmozzi, R., & González-Riestra, R. 2008, Astronomy & Astrophysics , 492, 787

Shafter, A. W., Darnley, M. J., Bode, M. F., & Ciardullo, R. 2012, Astrophysical Journal , 752, 156

Shakhovskoy, D. N., Antonyuk, K. A., & Belan, S. P. 2017, Astrophysics, 60, 19

Shapiro, S. L. & Teukolsky, S. A. 1986, Black Holes, White Dwarfs and Neutron Stars: The Physics of Compact Objects

Shara, M. M. 1981, Astrophysical Journal , 243, 926

Shara, M. M., Moffat, A. F. J., Williams, R. E., & Cohen, J. G. 1989, Astrophysical Journal , 337, 720

Shara, M. M., Zurek, D. R., Williams, R. E., et al. 1997, Astronomical Journal, 114, 258

Shore, S. N. 2008, Optical and ultraviolet evolution, 2nd edn., ed. M. F. Bode & A. Evans, Cambridge Astrophysics (Cambridge University Press), 194–231

Shore, S. N. 2012, Bulletin of the Astronomical Society of India, 40, 185

Shore, S. N., De Gennaro Aquino, I., Scaringi, S., & van Winckel, H. 2014, Astronomy & Astrophysics , 570, L4

Shore, S. N., Schwarz, G. J., De Gennaro Aquino, I., et al. 2013, Astronomy & Astrophysics , 549, A140

Siviero, A., Munari, U., Valentini, M., & Valisa, P. 2006, IAU Circ., 8702, 2

Skopal, A., Drechsel, H., Tarasova, T., et al. 2014, Astronomy & Astrophysics , 569, A112

Sokoloski, J. L., Crotts, A. P. S., Lawrence, S., & Uthas, H. 2013, Astrophysical Journal Letters , 770, L33

Sokoloski, J. L., Rupen, M. P., & Mioduszewski, A. J. 2008, Astrophysical Journal Letters , 685, L137

Sokolovsky, K. V., Orio, M., Page, K. L., et al. 2019, The Astronomer's Telegram, 13050, 1

Sriram, S., Kumar, A., Surya, A., et al. 2018, in Society of Photo-Optical Instrumentation Engineers (SPIE) Conference Series, Vol. 10702, Ground-based and Airborne Instrumentation for Astronomy VII, 107026K

Stanek, K. Z., Holoien, T. W. S., Kochanek, C. S., et al. 2018, The Astronomer's Telegram, 11454, 1

Stanek, K. Z., Kochanek, C. S., Brown, J. S., et al. 2016, The Astronomer's Telegram, 9669

Stanek, K. Z., Kochanek, C. S., Chomiuk, L., et al. 2017, The Astronomer's Telegram, 10523, 1

Starrfield, S., Iliadis, C., & Hix, W. R. 2016, Publications of the Astronomical Society of the Pacific , 128, 051001

Starrfield, S., Timmes, F. X., Hix, W. R., et al. 2004, Astrophysical Journal Letters , 612, L53

Steffen, W., Koning, N., Wenger, S., Morisset, C., & Magnor, M. 2011, IEEE Transactions on Visualization and Computer Graphics, 17, 454

Strader, J., Chomiuk, L., Aydi, E., et al. 2019, The Astronomer's Telegram, 13047, 1

Strader, J., Chomiuk, L., Holoien, T. W. S., et al. 2018, The Astronomer's Telegram, 11456, 1

Strittmatter, P. A., Woolf, N. J., Thompson, R. I., et al. 1977, Astrophysical Journal , 216, 23

Strope, R. J., Schaefer, B. E., & Henden, A. A. 2010, Astronomical Journal, 140, 34

Surina, F., Hounsell, R. A., Bode, M. F., et al. 2014, Astronomical Journal, 147, 107

Tajitsu, A., Sadakane, K., Naito, H., Arai, A., & Aoki, W. 2015, New Astronomyt, 518, 381

Tajitsu, A., Sadakane, K., Naito, H., et al. 2016, Astrophysical Journal , 818, 191

Tan, H. & Gao, X. 2018, The Astronomer's Telegram, 12200

Tanaka, J., Nogami, D., Fujii, M., Ayani, K., & Kato, T. 2011a, Publications of the Astronomical Society of Japan, 63, 159

Tanaka, J., Nogami, D., Fujii, M., et al. 2011b, Publications of the Astronomical Society of Japan, 63, 911

Tang, S., Bildsten, L., Wolf, W. M., et al. 2014, Astrophysical Journal , 786, 61

Tarasova, T. N. & Skopal, A. 2016, Astronomy Letters, 42, 10

Taylor, A. R., Pottasch, S. R., Seaquist, E. R., & Hollis, J. M. 1987, Astronomy & Astrophysics , 183, 38

Toraskar, J., Mac Low, M.-M., Shara, M. M., & Zurek, D. R. 2013, Astrophysical Journal , 768, 48

Tylenda, R., Kamiński, T., Schmidt, M., Kurtev, R., & Tomov, T. 2011, Astronomy & Astrophysics , 532, A138

van den Bergh, S. & Younger, P. F. 1987, Astronomy and Astrophysics, Suppl. Ser., 70, 125

Vanlandingham, K. M., Schwarz, G. J., Shore, S. N., Starrfield, S., & Wagner, R. M. 2005, Astrophysical Journal , 624, 914

Waagen, E. O. 2013, AAVSO Alert Notice, 489

Walter, F. M., Battisti, A., Towers, S. E., Bond, H. E., & Stringfellow, G. S. 2012, Publications of the Astronomical Society of the Pacific , 124, 1057

Warner, B. 1989, in Classical Novae, 1–16

Warner, B. 1995, Astrophysics and Space Science, 232, 89

Warner, B. 2008, Properties of novae: an overview, 2nd edn., ed. M. F. Bode & A. Evans, Cambridge Astrophysics (Cambridge University Press), 16–33

Weiler, K. W., Panagia, N., Montes, M. J., & Sramek, R. A. 2002, Annual Review of Astronomy and Astrophysics, 40, 387

Williams, R. 2012, Astronomical Journal, 144, 98

Williams, R. E. 1992, Astronomical Journal, 104, 725

Williams, R. E. 1994, Astrophysical Journal , 426, 279

Williams, R. E., Hamuy, M., Phillips, M. M., et al. 1991, Astrophysical Journal , 376, 721

Williams, S. C. & Darnley, M. J. 2017, The Astronomer's Telegram, 10542, 1

Williams, S. C., Darnley, M. J., & Healy, M. W. 2018, The Astronomer's Telegram, 11398

Yamaoka, H., Kinugasa, K., Naito, H., Ozaki, S., & Fujii, M. 2006, IAU Circ., 8698, 1

Zwicky, F. 1936, Publications of the Astronomical Society of the Pacific , 48, 191